IR LASER SPECTROSCOPY OF REACTIVE INTERMEDIATES AND COMPLEXES TRAPPED IN SUPERFLUID HELIUM NANODROPLETS

by

CHRISTOPHER PEDRAM MORADI

(Under the Direction of Assoc. Prof. Gary E. Douberly)

ABSTRACT

Helium nanodroplets are used to trap and stabilize a variety of reactive species including alkyl radicals, organic carbenes, and clusters containing Cl atoms. The vibrational spectra of these systems are investigated, predominantly in the C–H stretching region, and rotational fine-structure is observed for many of the smaller systems. The ro-vibrational spectra of C_3H_3, C_3H_5, and *n,i*-C_3H_7 become increasingly congested as the degree of unsaturation of the radical is reduced, and the spectra are modeled using both low- and high-accuracy computational methods in conjunction with a local-mode Hamiltonian approach. Preliminary results of the local-mode model indicate that coupling between C–H stretching vibrations and overtones/combinations of scissor modes lead to the observed spectral congestion. Several vibrational bands of the HCOH and HOCOH carbenes are measured in the C–H and O–H stretching regions. The He droplet spectra are consistent with the isolation of the *trans*-HCOH isomer and both the *trans,trans*- and *trans,cis*-HOCOH isomers. Vibrational frequencies, rotational constants, and permanent electric dipole moments (extracted from Stark spectroscopic measurements of HOCOH isomers) obtained for the He-solvated carbenes are compared with results of Ar matrix experiments, gas-phase results (when available), and anharmonic frequency computations. Finally, Cl atoms were

generated *via* the thermal decomposition of Cl_2 and were solvated in He droplets alongside either HCl or NH_3 molecules. The Cl–HCl van der Waals complex that aggregates in He droplets is demonstrated to have an L-shaped geometry (rather than a linear, H-bonded or Cl-bonded geometry) on the basis of both vibrational frequency of the HCl stretch and predictions of the transition dipole moment. The $ClNH_3$ adduct, on the other hand, has a much stronger 2-center, 3-electron bond, which is confirmed computationally. There is no spectroscopic evidence for either NH_3Cl or $Cl–HNH_2$ geometries despite both being stable minima on the CCSD(T) potential energy surface.

INDEX WORDS: HELIUM NANODROPLETS, INFRARED SPECTROSCOPY, VIBRATIONAL SPECTROSCOPY, STARK, HYDROCARBON RADICALS, CARBENE, CHLORINE ATOMS

IR LASER SPECTROSCOPY OF REACTIVE INTERMEDIATES AND COMPLEXES TRAPPED IN SUPERFLUID HELIUM NANODROPLETS

by

CHRISTOPHER PEDRAM MORADI

B.S., University of Georgia, 2010

A Dissertation Submitted to the Graduate Faculty of The University of Georgia in Partial Fulfillment of the Requirements for the Degree

DOCTOR OF PHILOSOPHY

ATHENS, GEORGIA

2016

IR LASER SPECTROSCOPY OF REACTIVE INTERMEDIATES AND COMPLEXES TRAPPED IN SUPERFLUID HELIUM NANODROPLETS

by

CHRISTOPHER PEDRAM MORADI

Major Professor:	Gary E. Douberly
Committee:	Michael A. Duncan
	Geoffrey D. Smith

Electronic Version Approved:

Suzanne Barbour
Dean of the Graduate School
The University of Georgia
May 2016

ACKNOWLEDGEMENTS

First and foremost, I have to give thanks to my advisor, Professor Gary Douberly. As a senior undergrad, I wasn't even considering going to graduate school until he stood in the hallway with me and explained that I would actually *get paid* to continue my education. I chose to stay at UGA and work in his group because of how genuinely excited he was by science, and that made me equally excited and motivated to learn. This has continued over my entire 5+ years in his research group, and I couldn't have asked for a better advisor. Also, I'd like to give a huge thank you to my committee members, Professors Geoff Smith and Mike Duncan, for imparting me with their knowledge throughout both my undergraduate and graduate work.

Secondly, I would like to thank all of the scientists with whom we collaborated. Many thanks to Drs. Stephen Klippenstein, Franklin Goldsmith, Ned Sibert, John Stanton, and Hua Guo for all of their assistance. Without their theoretical expertise and willingness to help, it would have been insurmountably difficult to attain the quality of work presented herein.

I was also fortunate enough to have worked alongside two amazing post-docs. Early in my graduate studies, Dr. Paul Raston joined the group and taught me so much about spectroscopy and being laid back. He fielded all the questions that I had deemed too simple to ask Gary, and he didn't make me feel too dumb in the process. Shortly after Paul left, Dr. Chris Leavitt joined the group, and lightning had struck again. By this point, I kind of knew what was going on in the lab, and he and I joined forces to do a lot of good science and drink a lot of good beer. Cheers and thanks to you guys.

Finally, I owe several fellow graduate students significant gratitude because they helped keep me sane. Dr. Tao Liang for enduring sitting at the computer next to me, and trying to teach me theory. And also for playing all that terrible pop music that we laughed and sang to. Dr. Brian Sanders for the video games, brew days, and pub conversations about science and football and life and pretty much everything. Future Drs. Ellen Broering, Melody Walter, Phan Truong, and Ramsey Steiner for all the baked goods, cardio, coffee, and bleating. You all rock.

TABLE OF CONTENTS

Page

LIST OF TABLES

Page

LIST OF FIGURES

Page

CHAPTER 1

INTRODUCTION

1.1 A Brief History of Matrix Isolation and Early He Droplet Work

The spectroscopy of radicals trapped in cryogenic matrices has been studied for several decades with seminal work appearing in 1954.[1,2] In the work of Whittle, Dows, and Pimentel,[1] they attempted to measure infrared spectra of well-studied molecules trapped in several types of matrices including CO_2, CCl_4 (both at 85 K), and Xe (at 66 K). While they did not have success with the inert gas Xe at the time of writing, they did note that preliminary experiments at a lower temperature of 29 K appeared promising. Their matrix isolation technique proved to be so successful that, within only four years, it was used to trap and measure the infrared spectrum of the highly reactive methylene molecule (CH_2), generated from the photolysis of diazomethane (CH_2N_2), in Ar and N_2 matrices at a temperature of 20 K.[3,4] Since these pioneering experiments, a variety of experimental methods have used different matrices, especially noble gas matrices, to study ions, radicals, and complexes.[5-11] Solid noble gas matrices are used primarily due to their chemical inertness, however there are significant drawbacks which can include doubling and/or inhomogeneous broadening of spectral lines due to the presence of matrix sites as well as significant red-shifting of vibrational band origins relative to gas phase values.[9] Furthermore, rotational structure is usually not observed for molecules in solid matrices, limiting the possibility for structural assignments or distinguishing between isomers.

The use of solid parahydrogen (SPH) as a matrix overcomes some of the disadvantages of rare gas matrix isolation. SPH is often referred to as a "quantum solid" because of its large zero-point motion and delocalization of the H_2 molecules.[12] The tetrahexacontapole-induced (64-pole) $J = 6 \leftarrow 0$ rotational transition of SPH was found to be very narrow with a half-width, half-maximum linewidth of only about 180 MHz,[13] and this discovery stimulated the application of high-resolution spectroscopy to study molecules embedded in SPH matrices. Indeed, rotational fine structure was observed in the vibrational spectrum of methane trapped in a 5 K SPH matrix with the unfortunate side effect, however, that the *M* degeneracy of the rotational wavefunctions was lifted by the crystal effects of the hydrogen cage and the transitions were consequently split.[12] Atoms and small hydrocarbon radicals have also been generated and stabilized via the photolysis of suitable precursors that have been trapped in a hydrogen matrix.[12,14-16] The hydrogen matrix is not inert however, and there exists the possibility for reaction between the matrix and the generated radicals either through direct reaction, vibrational and/or electronic pumping of reactants over a reaction barrier, or tunneling. For instance, photolytically generated H atoms are able to react with CO_2 within a 5 K parahydrogen matrix to form OH and CO, and the nascent OH radicals undergo a secondary reaction with the matrix H_2 molecules to form water,[17] thereby precluding the spectroscopic study of the hydroxyl radical in SPH.

The helium droplet methodology, which would prove to largely overcome the downsides of both solid noble gas and SPH matrices, was developed during the early 1990s. Although interesting properties of liquid helium droplets themselves had been investigated previously by electron impact ionization,[18] Scheidemann, Toennies, and Northby demonstrated that it was possible to use He clusters to pick up Ne atoms in a crossed-beam experiment.[19] These results paved the way for the seminal work of Scoles and co-workers who were able to use droplets

consisting of a few thousand He atoms to pick up a SF_6 probe molecule, and they reported the measurement of two infrared absorptions near 946 cm^{-1}.[20] These absorptions were located very near gas-phase measurements of the triply-degenerate antisymmetric stretching vibration. Furthermore, the same experiment demonstrated the possibility for the pickup of two SF_6 molecules by the He cluster. Two additional vibrational absorptions were again found to be very near those observed for the gas-phase SF_6 dimer.[20] Thus, this lone experiment demonstrated the possibility for the infrared spectroscopic interrogation of He-solvated molecules and clusters (although at the time it was unclear whether the foreign molecule was solvated by the droplet or resided on its surface). The initial studies on SF_6 were performed using line-tunable N_2O and CO_2 lasers,[20,21] allowing for spectral resolution of only ~0.25 cm^{-1}, but rotational fine-structure was observed for the first time for He-solvated SF_6 by switching to a tunable, continuous-wave diode laser having a linewidth of 30 MHz.[22,23] From the obtained spectrum, the authors extracted rotational constants, which were found to be significantly reduced relative to the gas-phase values, and a rotational temperature of 0.37 ± 0.05 K for the embedded SF_6.[22] At this point, it likely became clear that several of the glaring drawbacks of traditional matrix isolation spectroscopy had been overcome. Indeed, by 1995, helium nanodroplets had been shown to solvate the molecules encountered, cool the degrees of freedom of the dopant(s) significantly below the temperatures attainable in other noble gas matrices, and allow for the (perturbed) rotation of the molecule enabling the use of spectroscopy to study rovibrational dynamics and superfluidity on the microscopic scale.

Following the proof-of-principle experimental work of the early 1990s, several groups began to study the spectroscopy of He-solvated molecules. This was not limited to vibrational spectroscopy however, and in fact, the electronic spectroscopy of He-solvated glyoxal ($C_2H_2O_2$)

served as the first evidence that He nanodroplets were indeed superfluid.[24] Electronic excitations tend to be more affected by the He environment than are vibrational excitations due to stronger repulsion between the excited electron and the He atoms. Owing to this effect, the frequency of a molecule's zero-phonon line in He droplets may be red- or blue-shifted by 10 to 100 cm^{-1} relative to its gas-phase value, however the frequency shifts observed in liquid He are still much smaller than those reported for molecules in solid matrices.[25] Further evidence for superfluidity in ^{4}He droplets was demonstrated in the so-called "microscopic Andronikashvili experiment."[26] In summary, OCS was doped into droplets of ^{3}He and the C–O vibration was found to be a featureless absorption. Upon the addition of ~60 ^{4}He atoms to the ^{3}He droplets, forming droplets of heterogeneous composition, the C–O vibration displayed the expected rotational fine-structure indicating that the ^{4}He atoms formed a small superfluid region, within the ^{3}He droplet, which was able to solvate the OCS molecule and allow it to "freely" rotate.

1.2 Vibrational Spectroscopy of Stable Molecules and Clusters

There have been many infrared spectroscopic studies of closed-shell molecules solvated in He nanodroplets. It was estimated, again using SF_6 as a probe molecule, that the dissipation rate of the He environment is on the order of 10^{16} K/s,[27] although this is likely an upper limit given that commonly obtained ~1 GHz linewidths of vibrational spectra indicate vibrational cooling occurs on a slower timescale on the order of 10^{12} K/s. Thus, many experiments were performed in order to study the dynamics of relaxation processes in this cold, highly dissipative He droplet environment. One interesting result is that vibrationally excited HF does not relax on the timescale of the measurement, despite being in a 0.4 K He droplet. Its detection was enabled

by an increase in the average kinetic energy of the droplet beam upon vibrational resonance rather than by depletion of the droplet beam intensity.[28] Nonetheless, the HF $R(0)$ transition observed in He droplets is broad, having a full-width, half-maximum linewidth of 0.43 cm^{-1} and suggesting that the excited state lifetime is reduced relative to the gas phase. On the contrary, the $R(0)$ transition of the acetylenic CH stretch of He-solvated HCN has a linewidth of only 0.0067 cm^{-1} (200 MHz) despite also being a small, linear molecule.[29] Both HF and HCN access the same final rotational state within a high-frequency vibrational state, but the difference lies in the magnitude of their rotational energies. HF in $J = 1$ has ~40 cm^{-1} of rotational energy whereas the heavier HCN rotor has only ~3 cm^{-1} in the same state. The slower rotational motion of the HCN molecule falls in the "phonon gap," and hence HCN cannot effectively couple to the droplet's elementary excitations.[24] On the other hand, multiple quanta of droplet phonons can couple to the higher rotational energy of HF and influence the rate of rotational relaxation. Therefore, the broad linewidth of the HF transition is dominated by He-facilitated rotational relaxation from $J = 1$ to $J = 0$ in the vibrationally excited manifold,[28] while the HCN transition linewidth is predominantly due to slower vibrational relaxation. Infrared rovibrational spectra and associated relaxation dynamics have now been explored for a variety of molecular systems.[28,30-38]

Helium droplets are capable of picking up as many molecules as they encounter as long as the cooling process does not result in the complete evaporation of the He droplet. This leads to the possibility of studying both homogeneous and heterogeneous molecular clusters. The measurement of cluster spectra is just as straightforward as measuring monomer spectra because the droplet pickup process is statistical.[39] As illustrated graphically in Chapter 2, when the number density is optimized for the pickup of one molecule, there is a relatively large probability

of pickup of a second molecule. Two molecules captured by a single droplet will feel each other's presence due to electrostatic and/or dispersion forces and very quickly become trapped in a stable geometry on the potential energy surface (PES). There are excellent review articles that discuss cluster growth dynamics in He droplets, clusters comprised of polar and/or nonpolar molecules, water clusters and "hydrated" biomolecule clusters, metal atom clusters, and even the deposition of clusters formed in He droplets onto a surface.[39,40]

1.3 Vibrational Spectroscopy of Radicals and Open-Shell Clusters

Of course, small molecules that are stable over a wide range of temperatures can often be investigated using straightforward techniques, and many of these systems are now tractable computationally as well. However, the spectroscopic study of small reactive systems such as radicals and carbenes is far more challenging in both of those aspects. The reason for this is the increased number of intramolecular interactions possible due to the presence of unpaired electron(s). For instance, an unpaired electron's magnetic moment can couple to its own orbital angular momentum, the spin angular momentum of other unpaired electrons, the rotation of the molecule itself, and so on, and these interactions greatly enrich the spectrum of the molecule.[41] Thus, there is much to be learned from the analysis of high-resolution rovibrational spectra of open-shell molecules in the gas phase. However, the gas-phase spectrum can very quickly become overwhelming as the radical grows in size, and the ability to extract meaningful chemical physics may be diminished. Helium nanodroplets, as mentioned above, provide a much colder environment in which radicals can be studied, serving to reduce the number of quantum states occupied by the radical and simplify the rovibrational spectrum.

The spectroscopic interrogation of transient radicals is difficult also because of the need for a sufficient radical number density such that an experimental technique can be sensitive to their detection. Indeed, this is a major benefit of solid matrix isolation techniques because the radicals can be trapped in a chemically inert environment, and the radical concentration can accumulate to the required level. In the case of liquid helium nanodroplets, a droplet beam is formed by skimming the droplet expansion, and this droplet beam can be doped with radicals of interest. A convenient way to generate gas-phase radicals is by thermal decomposition of a precursor molecule,[42] and the nascent radicals immediately enter the droplet beam trajectory. Anti-parallel alignment of an infrared laser beam with the droplet beam provides for the laser interaction with many radical-containing droplets, making the helium droplet technique viable for their detection.

Open-shell clusters consisting of a radical that is weakly-bound to a closed-shell molecule are also of fundamental interest. The radical-molecule complex may not be reactive, as for the collision between Ar/He and OH,[43] and inelastic scattering of nonreactive molecules is important in the study of energy transfer and equilibrium dynamics. Often however, the radical may be able to undergo reaction with its partner molecule, and there may exist stable minima on the PES corresponding to entrance- and exit-channel complexes that are located between the separated reactants/products and the transition state. Prereactive, entrance-channel complexes have been shown to have a substantial effect on the outcome of a chemical reaction, specifically with regard to low-temperature chemistry, because of their orientation effect as the reactants approach one another. For instance, the Cl + HD reaction studied in a crossed molecular beam experiment shows a strong preference for the formation of DCl rather than HCl (over the 5-7 kcal/mol collision energy range).[44] This result is reproduced computationally only when long-

range van der Waals forces are included on the reactive PES.[44] These van der Waals complexes are difficult to study in the gas-phase because they not only have small binding energies, but they also often have low barriers to reaction. Helium nanodroplets have the advantage of being able to sequentially solvate and cool individual atoms and molecules to 0.4 K allowing for their aggregation and the investigation of these stable but elusive complexes. The remainder of this dissertation focuses on the infrared spectroscopy, mostly in the hydrogen stretching region, of a variety of small, reactive molecules and entrance-channel complexes that have been isolated in He nanodroplets.

References

(1) Whittle, E.; Dows, D. A.; Pimentel, G. C. *J. Chem. Phys.* **1954**, *22*, 1943-1943.

(2) Norman, I.; Porter, G. *Nature* **1954**, *174*, 508-509.

(3) Milligan, D. E.; Pimentel, G. C. *J. Chem. Phys.* **1958**, *29*, 1405-1412.

(4) DeMore, W. B.; Pritchard, H. O.; Davidson, N. *J. Am. Chem. Soc.* **1959**, *81*, 5874-5879.

(5) Sander, W.; Bucher, G.; Wierlacher, S. *Chem. Rev.* **1993**, *93*, 1583-1621.

(6) Dunkin, I. R. *Chem. Soc. Rev.* **1980**, *9*, 1-23.

(7) Bondybey, V. E.; Smith, A. M.; Agreiter, J. *Chem. Rev.* **1996**, *96*, 2113-2134.

(8) Andrews, L. *Annu. Rev. Phys. Chem.* **1979**, *30*, 79-101.

(9) Andrews, L. *Annu. Rev. Phys. Chem.* **1971**, *22*, 109-132.

(10) H Frei, a.; Pimentel, G. C. *Annu. Rev. Phys. Chem.* **1985**, *36*, 491-524.

(11) Nagarajan, R.; Maier, J. P. *Int. Rev. Phys. Chem.* **2010**, *29*, 521-554.

(12) Momose, T.; Shida, T. *Bull. Chem. Soc. Jpn.* **1998**, *71*, 1-15.

(13) Okumura, M.; Chan, M.-C.; Oka, T. *Phys. Rev. Lett.* **1989**, *62*, 32-35.

(14) Kettwich, S. C.; Paulson, L. O.; Raston, P. L.; Anderson, D. T. *J. Phys. Chem. A* **2008**, *112*, 11153-11158.

(15) Fushitani, M.; Miyamoto, Y.; Hoshina, H.; Momose, T. *J. Phys. Chem. A* **2007**, *111*, 12629-12634.

(16) Fushitani, M.; Momose, T.; Shida, T. *Chem. Phys. Lett.* **2002**, *356*, 375-382.

(17) Fushitani, M.; Shida, T.; Momose, T.; Räsänen, M. *J. Phys. Chem. A* **2000**, *104*, 3635-3641.

(18) Stephens, P. W.; King, J. G. *Phys. Rev. Lett.* **1983**, *51*, 1538-1541.

(19) Scheidemann, A.; Toennies, J. P.; Northby, J. A. *Phys. Rev. Lett.* **1990**, *64*, 1899-1902.

(20) Goyal, S.; Schutt, D. L.; Scoles, G. *Phys. Rev. Lett.* **1992**, *69*, 933-936.

(21) Goyal, S.; Schutt, D. L.; Scoles, G. *J. Phys. Chem.* **1993**, *97*, 2236-2245.

(22) Hartmann, M.; Miller, R. E.; Toennies, J. P.; Vilesov, A. *Phys. Rev. Lett.* **1995**, *75*, 1566-1569.

(23) Fröchtenicht, R.; Toennies, J. P.; Vilesov, A. *Chem. Phys. Lett.* **1994**, *229*, 1-7.

(24) Hartmann, M.; Mielke, F.; Toennies, J. P.; Vilesov, A. F.; Benedek, G. *Phys. Rev. Lett.* **1996**, *76*, 4560-4563.

(25) Toennies, J. P.; Vilesov, A. F. *Angew. Chem., Int. Ed.* **2004**, *43*, 2622-2648.

(26) Grebenev, S.; Toennies, J. P.; Vilesov, A. F. *Science* **1998**, *279*, 2083-2086.

(27) Scheidemann, A.; Schilling, B.; Toennies, J. P. *J. Phys. Chem.* **1993**, *97*, 2128-2138.

(28) Nauta, K.; Miller, R. E. *J. Chem. Phys.* **2000**, *113*, 9466-9469.

(29) Nauta, K.; Miller, R. E. *Phys. Rev. Lett.* **1999**, *82*, 4480-4483.

(30) Lindsay, C. M.; Douberly, G. E.; Miller, R. E. *J. Mol. Struct.* **2006**, *786*, 96-104.

(31) Nauta, K.; Miller, R. E. *J. Chem. Phys.* **2001**, *115*, 8384-8392.

(32) Nauta, K.; Miller, R. E. *Chem. Phys. Lett.* **2001**, *350*, 225-232.

(33) Lindsay, C. M.; Miller, R. E. *J. Chem. Phys.* **2005**, *122*, 104306.

(34) von Haeften, K.; Rudolph, S.; Simanovski, I.; Havenith, M.; Zillich, R. E.; Whaley, K. B. *Phys. Rev. B* **2006**, *73*, 054502.

(35) Grebenev, S.; Havenith, M.; Madeja, F.; Toennies, J. P.; Vilesov, A. F. *J. Chem. Phys.* **2000**, *113*, 9060-9066.

(36) Callegari, C.; Reinhard, I.; Lehmann, K. K.; Scoles, G.; Nauta, K.; Miller, R. E. *J. Chem. Phys.* **2000**, *113*, 4636-4646.

(37) Behrens, M.; Buck, U.; Fröchtenicht, R.; Hartmann, M.; Huisken, F.; Rohmund, F. *J. Chem. Phys.* **1998**, *109*, 5914-5920.

(38) Slipchenko, M. N.; Vilesov, A. F. *Chem. Phys. Lett.* **2005**, *412*, 176-183.

(39) Choi, M. Y.; Douberly, G. E.; Falconer, T. M.; Lewis, W. K.; Lindsay, C. M.; Merritt, J. M.; Stiles, P. L.; Miller, R. E. *Int. Rev. Phys. Chem.* **2006**, *25*, 15-75.

(40) Toennies, J. P.; Vilesov, A. F. *Angew. Chem. Int. Ed.* **2004**, *43*, 2622-2648.

(41) Herzberg, G. *Molecular spectra and molecular structure*, 2d ed.; Van Nostrand: New York, 1950.

(42) Küpper, J.; Merritt, J. M.; Miller, R. E. *J. Chem. Phys.* **2002**, *117*, 647-652.

(43) Sarma, G.; Marinakis, S.; ter Meulen, J. J.; Parker, D. H.; McKendrick, K. G. *Nat. Chem.* **2012**, *4*, 985-989.

(44) Skouteris, D.; Manolopoulos, D. E.; Bian, W.; Werner, H.-J.; Lai, L.-H.; Liu, K. *Science* **1999**, *286*, 1713-1716.

CHAPTER 2

EXPERIMENTAL METHODOLOGY

2.1 Droplet Formation

A schematic of the helium droplet apparatus is shown in Figure 2.1. Helium nanodroplets are formed in the high-pressure region of an expansion of ^{4}He gas through a nozzle having a 5 μm diameter orifice. The nozzle assembly is attached to a two-stage cold head, and it is cooled to cryogenic temperatures ranging from 14-20 K. The nozzle temperature and the stagnation pressure of the He gas within the nozzle are two of three adjustable criteria that determine the mean droplet size (with the remaining "variable" being the nozzle diameter, which is much more difficult to change). The adjustment of any of these three parameters allows for the "tuning" of the mean droplet size and the tailoring of the droplet beam composition to a specific application. Typical experimental conditions, at which much of the data presented in this dissertation was collected, are 35 bars backing pressure and 17.000 ± 0.005 K nozzle temperature. Substitution of these parameters into an empirical equation yields a mean droplet size equal to ~4800 atoms, according to published scaling laws.[1] However, the droplet beam is far from monodisperse; indeed, the droplet size distribution is quite broad, having a half-width that is equal to ~87% of the mean droplet size, and can be described using a log-normal equation.[2,3]

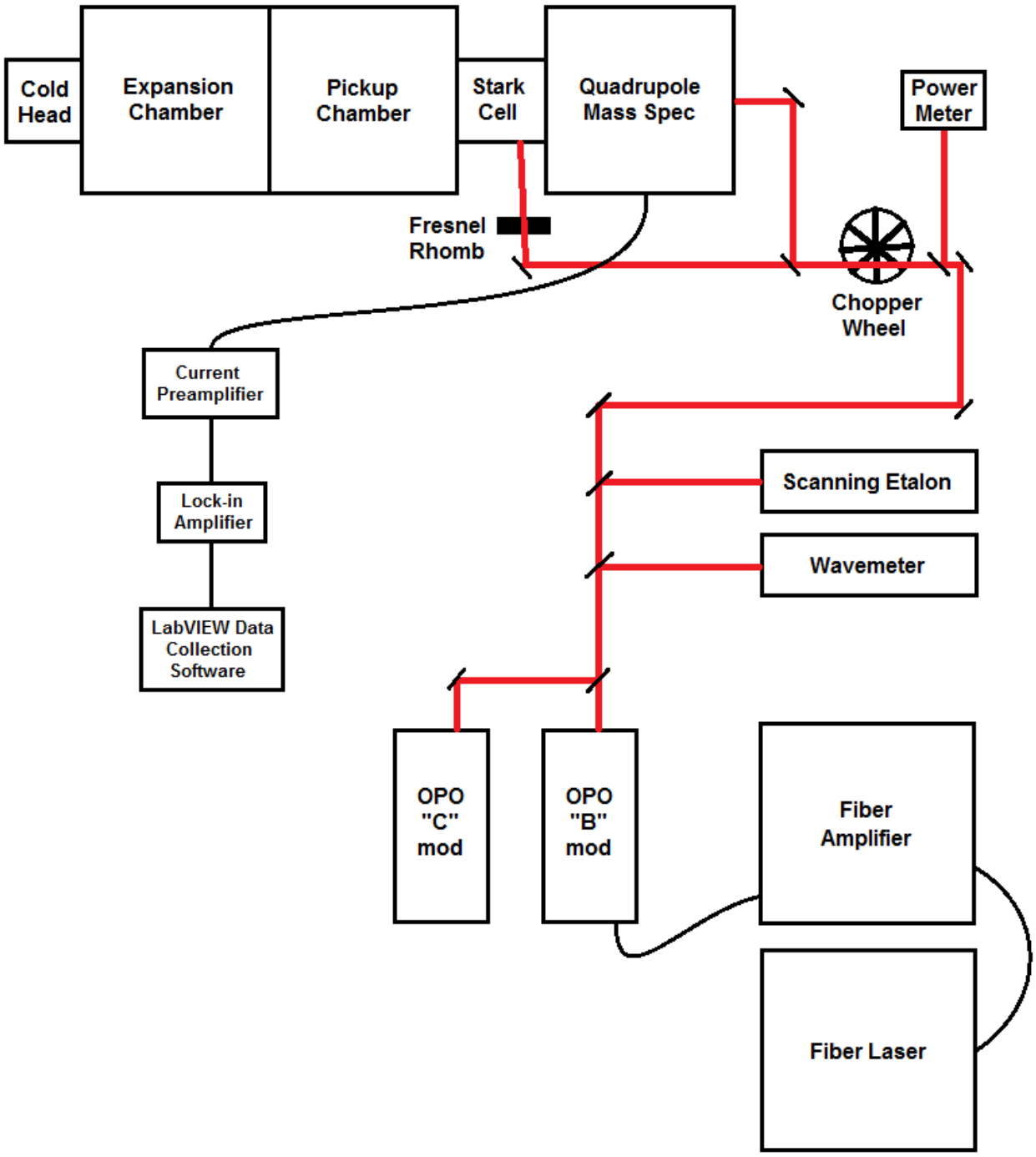

Figure 2.1: Architecture of the He nanodroplet experimental setup. The various components are discussed within this chapter.

Droplets of the size discussed above are ideal for capturing and cooling the internal degrees of freedom of single molecules and small clusters, as discussed in the next section. However, droplet size is not limited to only thousands of He atoms. Lowering the nozzle temperature below 11 K results in the expansion of a liquid jet of He through the nozzle orifice.[4,5] Breakup of the liquid jet leads to the formation of orders of magnitude larger droplets than those obtained through the gas-phase homogeneous nucleation mechanism. Ultralarge droplets having mean sizes greater than 10^9 He atoms have been detected using an extremely low temperature, small diameter nozzle, and in fact, the formed droplets are no longer nanodroplets, as they have diameters on the order of micrometers.[6] Droplets consisting of millions or billions of He atoms, while not useful for measuring the types of IR depletion spectra discussed herein, have been used to study electron capture and solvation,[7] the formation of lattices of quantum vortices within the droplet,[8] and photoionization dynamics.[9]

As the He atoms aggregate into droplets, they are expanding into the vacuum chamber which is kept at a background pressure of approximately 10^{-5} torr (under experimental conditions). At distances exceeding about 1000 nozzle diameters (5 mm in the current configuration) collisions of He cease, and the droplets evaporatively cool in the vacuum environment.[10,11] The evaporative cooling process is exponential as a function of time, and the temperature of ^{4}He droplets levels out at ~0.4 K after about a microsecond.[12] The droplet beam velocity is usually on the order of 200 – 400 m/s,[2,10] and so equilibrium of the droplet temperature occurs over sub-millimeter distances. Finally, the nascent droplets are skimmed by a cone having a 0.4 mm aperture (~1 cm downstream from the nozzle) to yield a beam of He droplets.

2.2 Droplet Pickup

After the He droplets are skimmed into a beam, they pass into a "pickup chamber" that contains a low pressure of the molecule(s) of interest. Collisions between the droplets and atoms/molecules, with some exceptions, lead to solvation by the droplet.[13] The majority of molecules have been determined to be solvated by the droplets, however certain open-shell atoms have been shown to either exist on the surface of the droplet or are not captured by the droplets at all. The alkali and alkaline earth metals reside on the surface of the droplet because the small free energy gain resulting from the He–impurity pair potential does not overcome the larger cost of creating a cavity within the He droplet.[14] Atomic hydrogen is unable to exist within a He droplet due to its large de Boer parameter, which describes the "quantumness" of the system,[14] however molecular hydrogen is readily solvated.

Given that the pickup of a molecule has no effect on the pickup of subsequent molecules, the droplet pickup process obeys Poisson statistics.[15] This is defined by the equation

$$P(n) = \frac{(\alpha L)^n e^{-\alpha L}}{n!} \qquad \textbf{(Eq. 2.1)}$$

where $P(n)$ is the probability of a droplet picking up n molecules as it passes through the pickup chamber having length L. The quantity α describes the adjustable properties of the experiment and is given by the product $\alpha = \rho\sigma$ where ρ is the number density of the gas in the chamber, and σ is the geometric cross-section of the droplet. Figure 2.2 shows the pickup probability as a function of pickup chamber pressure, and from this it is seen that it is possible to optimize for the pickup of a certain number of molecules by adjusting the chamber pressure. It is also clear that even if the chamber pressure is optimized for pickup of a specific number of dopants, there is always nonzero probability that the droplets will pickup more and/or less molecules. This is

accounted for in spectroscopic studies by measuring the signal intensity as a function of the pick-up chamber pressure, allowing for the assignment of cluster sizes.

Gas-phase radicals are generated by allowing the vapor of a suitable precursor molecule to effuse through a heated pyrolysis tube. The pyrolysis tube is heated either indirectly or directly, and different tubes are used in both methods. In the first type of pyrolysis source, a quartz tube is indirectly heated by passing current through a coil of Ta wire wrapped around the end of the tube. Approximately 30 Amps of current is passed through this Ta wire under normal operating conditions, and the resistive heating warms the walls of the quartz tube to temperatures

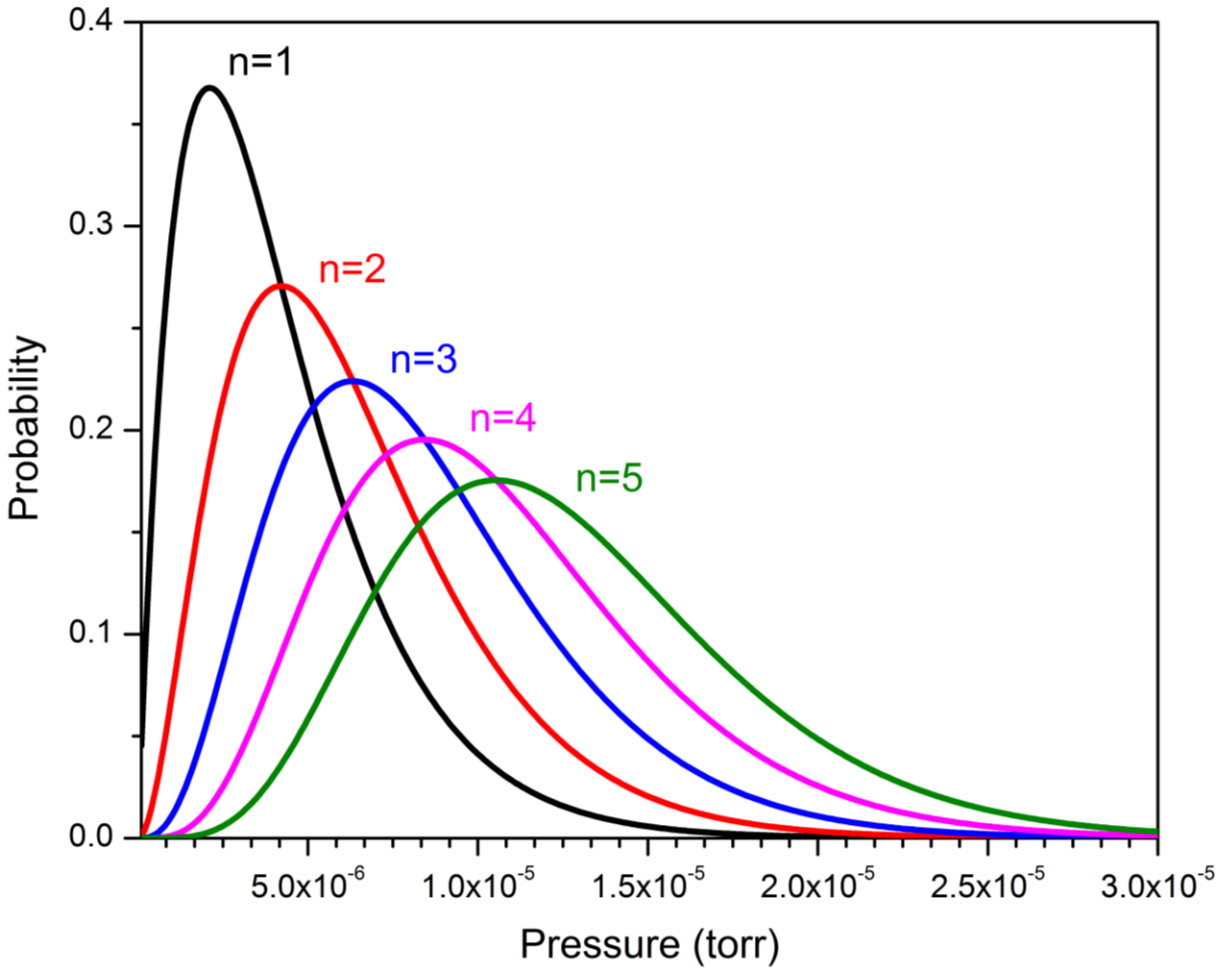

Figure 2.2: Poisson curves generated using Equation 2.1. The number of molecules picked up by the droplets is denoted by n. In the simulation, the droplets have a mean radius of 3.75 nm and pass through a 30 cm pickup chamber.

approaching 1000 K. This temperature is high enough that molecules such as peroxides (ROOR′) and organic nitrites (RONO) decompose when they collide with the hot tube wall. The decomposition products, which are often a mix of radicals and stable molecules, exit the quartz tube directly into the droplet beam trajectory. The second pyrolysis source is constructed with a quartz tube coupled to a ~1" section of 1 mm I.D. SiC tube. Electrodes are clamped onto the SiC tube, as shown in Figure 2.3, and current is passed directly through the walls of the tube. Temperatures of ~1600 K are attained in the "hot zone" at power levels of only tens of Watts, allowing for the pyrolysis of more stable molecules.[16] The SiC has the additional advantage of being more robust than the Ta wire which becomes labile at high temperatures and can break.

2.3 Stark Cell

After passing through the pickup chamber, the droplet beam enters a chamber containing a removable Stark cell, as depicted in Figure 2.4. The Stark cell is comprised of two flat stainless steel electrodes positioned above and below the droplet beam and separated by 3.1(0) mm. High voltage, on the order of several kV, is applied to one of the electrodes while the other is kept grounded. Therefore, DC fields up to ~40-50 kV/cm have been attained using the current setup. On either side of the electrodes are two Au-coated mirrors which are used to multipass infrared light from an optical parametric amplifier (*vide infra*). The light intersects the droplet beam approximately 20-30 times, between the steel electrodes, before being dumped into the wall of the vacuum chamber. The polarization of the laser beam can be rotated using a Fresnel rhomb in order to align or misalign the laser polarization with the Stark field. The laser polarization is usually aligned to be either parallel or perpendicular to the Stark field to take

advantage of the different selection rules in the two cases. For a molecule in a strong electric field, this interaction is

$$H_{Stark} = -\boldsymbol{\mu} \cdot \boldsymbol{E} = -|\mu||E|cos(\theta) \quad \textbf{(Eq. 2.2)}$$

where $\boldsymbol{\mu}$ is the permanent electric dipole of the molecule, **E** is the applied electric field, and θ is the angle between the two vectors. The rotational Hamiltonian is then the sum of the Stark Hamiltonian and the rigid-rotor rotational Hamiltonian (given here for an asymmetric top):

$$H_{rot} = A\hat{J}_z^2 + B\hat{J}_x^2 + C\hat{J}_y^2 - |\mu||E|cos(\theta). \quad \textbf{(Eq. 2.3)}$$

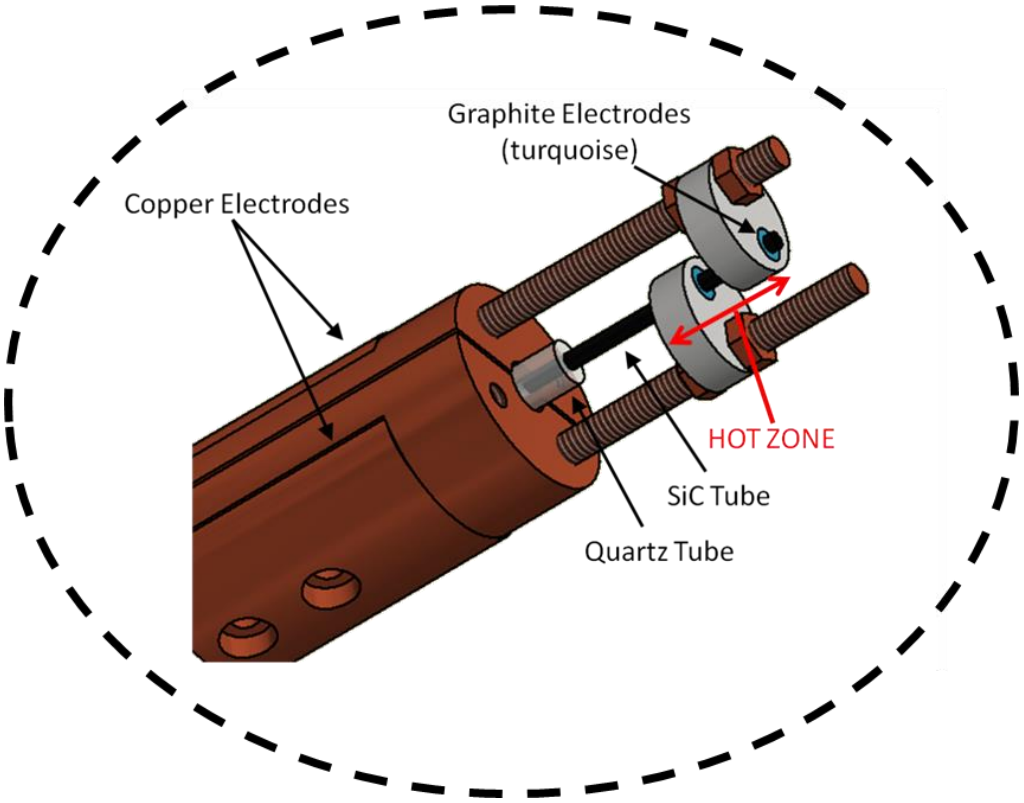

Figure 2.3: Pyrolysis region of the SiC source. Precursor molecules effuse the length of the quartz tube before entering the SiC pyrolysis tube. Typically 3.5 Amps of alternating current pass through the "hot zone," which is variable in length but set to ~0.75" for pyrolysis of Cl_2. The copper electrodes are water-cooled. The He droplet beam trajectory is orthogonal to the tube axis and passes just outside the tube exit.

J is no longer a good quantum number because the rotational states of the molecule are mixed due to the partial alignment of the molecular dipole with the applied field. However, the *M* quantum number (the projection of *J* onto the electric field axis) remains good, and the parallel configuration leads to the $\Delta M = 0$ selection rule whereas the perpendicular configuration leads to $\Delta M = \pm 1$. These selection rules along with the modification of the field-free rotational Hamiltonian by the Stark term generate shifts and splittings in the rotational fine structure allowing for the determination of the vibrationally averaged permanent electric dipole moment of the He-solvated molecule.

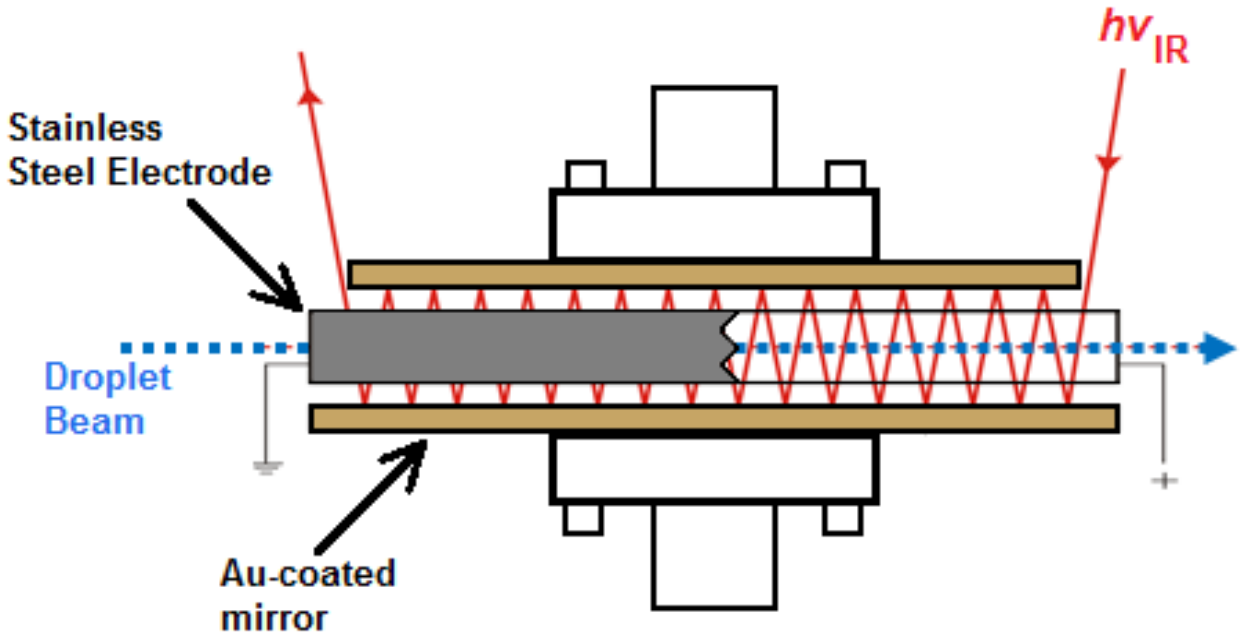

Figure 2.4: Stark cell schematic. The droplet beam passes between a pair of electrodes, one of which has several kV of applied voltage while the other is grounded. A pair of Au-coated mirrors reflects the infrared radiation 20-30 times between the electrodes so that Stark spectra of He-solvated polar molecules may be obtained.

2.4 Infrared Optical Parametric Oscillator and Laser Depletion

The source of infrared radiation is the idler output from a continuous-wave optical parametric oscillator (cw-OPO) manufactured by Lockheed-Martin Aculight (ARGOS 2400-SF-15). The cw-OPO is pumped by a Yb-doped fiber laser (Koheras Adjustik) that outputs 15 mW of 1064 nm light with a linewidth of <100 kHz. The fiber laser wavelength is both temperature tunable (20° C to 50° C) and piezo tunable (0 – 200V). These two parameters may be adjusted individually, each allowing for continuous tuning of the pump frequency by ~3 cm^{-1}, giving a net tuning range of ~6 cm^{-1}. The light is then coupled into a fiber amplifier (IPG Photonics) which amplifies the output of the fiber laser up to a maximum output power of 15 W. Finally, the 15 W, 1064 nm light is coupled into a bow-tie cavity that is the resonator for the OPO module. Conversion of the pump beam into signal and idler beams is achieved using a magnesium-oxide-doped periodically-poled lithium niobate (MgO:PPLN) crystal. The bow-tie cavity is resonant for the signal beam, and therefore tuning of the pump wavelength (via temperature or piezo) consequently tunes the idler wavelength. Two of these non-linear crystals in two separate OPO modules are used for their different tuning ranges. The idler beam from module "B" covers the frequency region 3150 – 4000 cm^{-1}, and module "C" covers the range 2600 – 3150 cm^{-1}. The PPLN crystals have a "fan-out" design of their periodic poling which enables translation of the crystal and results in coarse ~1 cm^{-1} tuning over the aforementioned ranges. The idler beam has >1 W of power over the entire tuning range of both modules.

The residual pump and the generated signal beam are dumped into beam stops, while the idler output is used for the collection of IR spectra. Along its path toward the vacuum chamber, fractions of the beam are reflected from the surfaces of CaF_2 windows and directed into various

diagnostic devices. At each of three window interfaces, approximately 10-20 mW is reflected into a wavemeter, a Fabry-Perot scanning etalon, and a power meter. The wavemeter reading and the laser power are both recorded, using custom Labview software, as the OPO is scanned, and the scanning etalon is monitored by the operator to ensure that the idler beam stays in a single longitudinal mode. The beam is focused into either the quadrupole mass spectrometer (QMS) in a collinear arrangement or the Stark cell in a multipass arrangement. In the collinear arrangement, the idler beam overlaps spatially with the entirety of the droplet beam, whereas in the multipass arrangement, the idler beam intersects the droplet beam only ~30 times within the electric field generated by the electrodes discussed above.

Droplet beam flux is detected using a quadrupole mass spectrometer (QMS) and electron impact ionization. As the He droplets enter the QMS, collisions between droplets and high-energy electrons form He^+ ions. These may aggregate into He_n^+ clusters, and/or they may encounter a dopant and undergo electron transfer, ionizing the dopant and forming neutral He. Because the dopant's ionization energy is always much less than that of He, electron transfer comes with large energy release, often resulting in fragmentation of the molecular dopant. The nascent ions pass into the quadrupole mass filter, which can be set to allow only ions of a specific mass-to-charge ratio to pass. This is useful for differentiating between droplets containing precursor molecules and those containing decomposition products because they often ionize into different mass channels. For instance, the mass spectra shown in Chapter 3 (Figure 3.3) demonstrate that ionization of the propargyl (C_3H_3) radical results in intense m/z = 38 u signal, whereas the propargyl peroxy radical (C_3H_3OO) significantly ionizes into m/z = 27 u. Alternatively, the QMS may be set to RF-only mode, which allows all ions to pass, forgoing any

benefits of mass selectivity but enabling the detection of spectroscopic signal on many mass channels simultaneously.

A droplet that contains a dopant that does not interact with the incident infrared radiation will simply stay the same size from the time after dopant pickup/cooling until detection. However, when a dopant becomes ro-vibrationally excited by the infrared light, the absorbed energy is quickly quenched by the cold He environment. This occurs through the evaporation of He atoms from the surface of the droplet with each individual He atom carrying ~5 cm^{-1} of translational energy as it leaves.[12] Given the frequencies of vibrations that can be probed with the two OPO modules mentioned above, several hundred He atoms are ejected from the droplet following photon absorption and relaxation of the dopant. Droplets containing dopants that have been vibrationally excited now contain roughly 10-20% fewer helium atoms and a correspondingly smaller geometric cross-section than when the laser was not on resonance. The smaller droplet cross-section reduces the efficiency with which the droplets are electron-impact-ionized, and so the MS ion signal is reduced upon ro-vibrational excitation of the dopant. This reduction is termed "laser-induced depletion" or simply "laser depletion" and corresponds to spectroscopic signal. The infrared light is mechanically chopped at 80 Hz such that the ion signal can be measured when the laser is both blocked and unblocked at each wavelength. The modulated multiplier current is converted into a voltage (Stanford Research SR570 current preamplifier) and processed with a lock-in amplifier before being sent to LabVIEW data collection software.

References

(1) Knuth, E.; Schilling, B.; Toennies, J. P. *Proceedings of the 19th International Symposium on Rarefied Gas Dynamics* (Oxford University Press, London, 1995).

(2) Lewerenz, M.; Schilling, B.; Toennies, J. P. *Chem. Phys. Lett.* **1993**, *206*, 381-387.

(3) Harms, J.; Toennies, J. P.; Dalfovo, F. *Phys. Rev. B* **1998**, *58*, 3341-3350.

(4) Knuth, E. L.; Henne, U. *J. Chem. Phys.* **1999**, *110*, 2664-2668.

(5) Jiang, T.; Northby, J. A. *Phys. Rev. Lett.* **1992**, *68*, 2620-2623.

(6) Grisenti, R. E.; Toennies, J. P. *Phys. Rev. Lett.* **2003**, *90*, 234501.

(7) Henne, U.; Toennies, J. P. *J. Chem. Phys.* **1998**, *108*, 9327-9338.

(8) Gomez, L. F.; Ferguson, K. R.; Cryan, J. P.; Bacellar, C.; Tanyag, R. M. P.; Jones, C.; Schorb, S.; Anielski, D.; Belkacem, A.; Bernando, C.; Boll, R.; Bozek, J.; Carron, S.; Chen, G.; Delmas, T.; Englert, L.; Epp, S. W.; Erk, B.; Foucar, L.; Hartmann, R.; Hexemer, A.; Huth, M.; Kwok, J.; Leone, S. R.; Ma, J. H. S.; Maia, F. R. N. C.; Malmerberg, E.; Marchesini, S.; Neumark, D. M.; Poon, B.; Prell, J.; Rolles, D.; Rudek, B.; Rudenko, A.; Seifrid, M.; Siefermann, K. R.; Sturm, F. P.; Swiggers, M.; Ullrich, J.; Weise, F.; Zwart, P.; Bostedt, C.; Gessner, O.; Vilesov, A. F. *Science* **2014**, *345*, 906-909.

(9) Fröchtenicht, R.; Henne, U.; Toennies, J. P.; Ding, A.; Fieber-Erdmann, M.; Drewello, T. *J. Chem. Phys.* **1996**, *104*, 2548-2556.

(10) Buchenau, H.; Knuth, E. L.; Northby, J.; Toennies, J. P.; Winkler, C. *J. Chem. Phys.* **1990**, *92*, 6875-6889.

(11) Buchenau, H.; Toennies, J. P.; Northby, J. A. *J. Chem. Phys.* **1991**, *95*, 8134-8148.

(12) Brink, D. M.; Stringari, S. *Z. Phys. D* **1990**, *15*, 257-263.

(13) Lewerenz, M.; Schilling, B.; Toennies, J. P. *J. Chem. Phys.* **1995**, *102*, 8191-8207.

(14) Ancilotto, F.; Lerner, P. B.; Cole, M. W. *J. Low. Temp. Phys.* **1995**, *101*, 1123-1146.

(15) Choi, M. Y.; Douberly, G. E.; Falconer, T. M.; Lewis, W. K.; Lindsay, C. M.; Merritt, J. M.; Stiles, P. L.; Miller, R. E. *Int. Rev. Phys. Chem.* **2006**, *25*, 15-75.

(16) Kohn, D. W.; Clauberg, H.; Chen, P. *Rev. Sci. Instrum.* **1992**, *63*, 4003-4005.

CHAPTER 3

PROPARGYL + O_2 REACTION IN HELIUM DROPLETS: ENTRANCE CHANNEL BARRIER OR NOT?

A combination of liquid He droplet experiments and multireference electronic structure calculations is used to probe the potential energy surface for the reaction between the propargyl radical and O_2. Infrared laser spectroscopy is used to probe the outcome of the low temperature, liquid He-mediated reaction. Bands in the spectrum are assigned to the acetylenic CH stretch (ν_1), the symmetric CH_2 stretch (ν_2) and the antisymmetric CH_2 stretch (ν_{13}) of the acetylenic-*trans* propargyl peroxy radical ($^{\cdot}OO\text{-}CH_2\text{-}C{\equiv}CH$). The observed band origins are in excellent agreement with previously reported anharmonic frequency computations for this species.[1] The Stark spectrum of the ν_1 band provides further evidence that the reaction leads only to the *trans*-acetylenic species. There are no other bands in the CH_2 stretching region that can be attributed to any of the other three propargyl peroxy isomers/conformers that are predicted to be minimum energy structures (*gauche*-acetylenic, *cis*-allenic and *trans*-allenic). There is also no evidence for the kinetic stabilization of a van der Waals complex between propargyl and O_2. A combination of multireference and coupled-cluster electronic structure calculations is used to probe the potential energy surface in the neighborhood of the transition state connecting reactants with the acetylenic adduct. The multireference based evaluation of the doublet-quartet splitting added to the coupled-cluster calculated quartet state energies yields what are likely the most accurate predictions for the doublet potential curve. This calculation suggests that there is no saddle point

for the addition process, in agreement with the experimental observations. Other calculations suggest the possible presence of a small submerged barrier.

3.1 Introduction

The formation of soot in hydrocarbon combustion is an ongoing and active area of research that is driven by its harmful effects to humans and the environment. There are several recent reviews on the mechanism of soot formation.[2-6] The general mechanism consists of the breakdown of aliphatic fuel molecules to unsaturated hydrocarbon radicals that react to form an aromatic ring. From this first ring, larger polycyclic aromatic hydrocarbons (PAHs) are formed through various addition mechanisms. Ultimately, the largest PAHs dimerize through either physical or chemical interactions, and the coupling of such dimerizations with further surface growth reactions leads to the formation of macroscopic particles. The explicit steps in each of these stages are still the subject of intense debate. Nevertheless, it is generally accepted that the rate-limiting step in the overall mechanism is the formation of the first ring. The importance of resonantly stabilized free radicals (RSFRs) in the formation of the first aromatic ring has now been established by a large body of experimental and theoretical work.[7-22]

The propargyl radical ($HCCCH_2$) is an example of a RSFR that is central to the mechanism of soot formation.[9,17,18,20,22] Indeed, the potential energy surface (PES) for the recombination of two propargyl radicals has multiple reaction paths that lead to benzene with no intrinsic barriers.[7,8,17] For propargyl, quantum chemistry (CCSD(T)/ANO) predicts that 35% of the electron spin density resides on the terminal acetylenic carbon while the remaining 65% is on the methylenic carbon.[23] The resonance stabilization energy associated with this electron

delocalization has been computed to be ≈11 kcal·mol^{-1}.[23] Because this stabilization energy is lost upon C–O bond formation, the C_3H_3–OO (propargyl peroxy) radical is less strongly bound than typical alkylperoxy radicals,[24] and unlike alkyl + O_2, the propargyl + O_2 reaction is predicted to proceed over a small entrance channel barrier (≈1–4 kcal·mol^{-1}).[24] Hence, the propargyl radical is less reactive with O_2 and is therefore oxidized less effectively in comparison to nonresonantly stabilized radicals, leading to high concentrations in combustion environments. Indeed, the high-pressure limit rate coefficient for self-reaction is >10^2 times larger than it is for oxidation.[9] Here we report the outcome of the propargyl + O_2 reaction carried out in the low-temperature, dissipative environment of a He nanodroplet. We employ infrared (IR) laser spectroscopy and electronic structure theory to address the issue of whether or not the previously predicted entrance barriers[24] are true features on the C_3H_3–O_2 PES.

The propargyl peroxy C–O bond energy (ΔH_{298}) was determined to be 18.9 ± 1.4 kcal·mol^{-1} in the seminal work of Slagle and Gutman.[25] In comparison, hydrocarbon radicals with much smaller (or no) resonance character such as methyl, ethyl and vinyl radicals have much higher O_2 binding energies of 29, 34 and 45 kcal·mol^{-1}, respectively.[24] Oxygen may add to either the terminal methylenic or acetylenic carbon atoms of propargyl, resulting in either an acetylenic ($^{\cdot}$OO-CH_2-C≡CH) or an allenic (CH_2=C=CH-OO$^{\cdot}$) isomer, respectively. In the ground electronic state, both isomers are predicted to have two conformers.[26] The four propargyl peroxy isomer-conformer species that will be discussed here are the *trans*- acetylenic, *gauche*- acetylenic, *cis*- allenic, and *trans*- allenic species (Figure 3.1). Hereafter, we adopt the naming convention used previously by Miller and co-workers and abbreviate these as ace-T, ace-G, all-C, and all-T, respectively. The barrier heights associated with the formation of ace-T and all-T from separated C_3H_3 and O_2 were computed by various methods to be 2.5–4.9 and 4.3–8.2

kcal·mol^{-1}, respectively.[24,27] The larger barrier for allenic isomer formation reflects the smaller spin density on the acetylenic carbon, in comparison to the methylenic carbon. Moreover, the transition state in the entrance channel leading to all-T is above the $C_3H_3 + O_2$ asymptotic limit, whereas the barrier in the entrance channel associated with the formation of ace-T is slightly "submerged" (shown schematically in Figure 3.2), as determined empirically.[9]

Jochnowitz *et al*. reported the solid-Ar matrix (20 K) isolation IR spectrum of the codeposited propargyl + O_2 system, which contains bands that can be unambiguously assigned to the ace-T propargyl peroxy radical.[1] This observation seems to indicate that there is at most a small barrier in the channel associated with O_2 addition to the methylenic carbon center. Alternating deposition of propargyl radicals and O_2 resulted in the observation and assignment of most of the ace-T bands predicted by CCSD(T)/VPT2 anharmonic frequency computations; however, there was no attempt to assign bands to the *gauche* conformer of the acetylenic isomer (ace-G). None of the allenic isomers were observed in the Ar matrix, consistent with the predicted barrier of 4–8 kcal·mol^{-1} *above* the separated reactants. Thomas *et al*. produced gas-phase propargyl peroxy radicals via the photolysis of propargyl chloride in the presence of O_2.[26] Room temperature near-IR cavity ringdown spectroscopy of the gas-phase species revealed $\tilde{A} \leftarrow \tilde{X}$ vibronic bands assigned to the ace-T isomer, and some weak, featureless absorptions were tentatively assigned to ace-G and all-C. Quantum chemistry computations from the same group predicted nearly isoenergetic ace-G and ace-T conformers (ΔH_0 = 0.3 kcal·mol^{-1}) separated by a small barrier to interconversion (≈0.3 kcal·mol^{-1} for ace-G to ace-T interconversion). From 1D variational calculations, it was found that below the torsional interconversion barrier, only 2 and 4 bound states are supported in the ace-G and ace-T wells, respectively.[26]

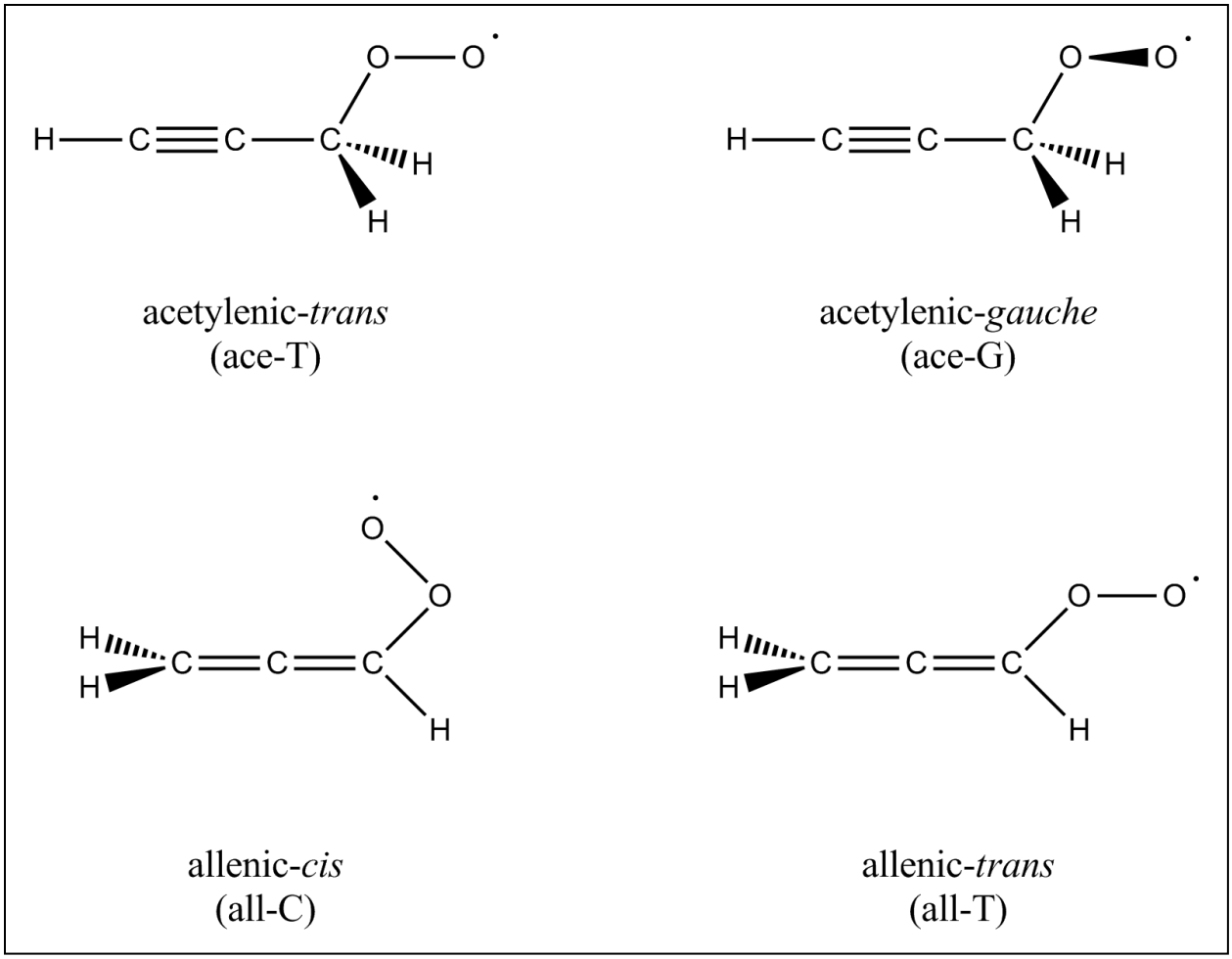

Figure 3.1: Schematic representation of the ground electronic state equilibrium structures of propargyl peroxy radicals. Structures denoted as *cis*, *gauche*, and *trans* have OOCC dihedral angles of 0°, ±128°, and 180°, respectively.

It is interesting to consider the condensation of C_3H_3 and O_2 within a He nanodroplet at 0.4 K. There are three possible outcomes; one, the rapid cooling associated with He atom evaporation will lead to the kinetic stabilization of the metastable entrance channel species; two, the reaction will proceed over the small barrier and be quenched at the intermediate peroxy radical well on the potential, as observed in solid-Ar and in the room temperature gas-phase spectra; or, three, both outcomes are observed within the ensemble of reactive encounters. On the basis of previous He droplet work,[28-33] we expect to observe the entrance channel C_3H_3–O_2

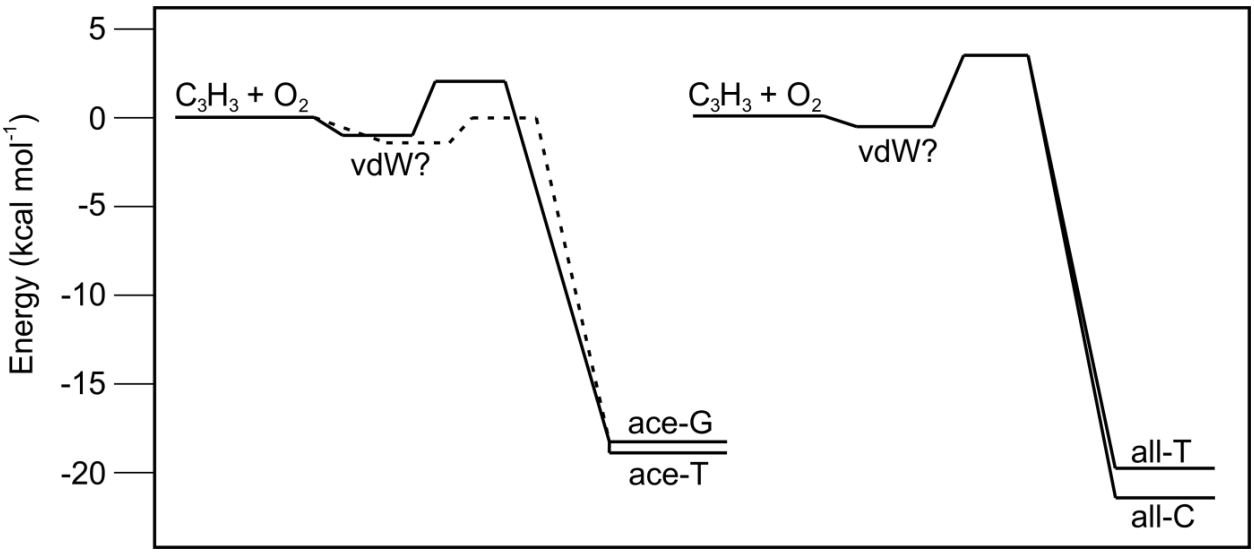

Figure 3.2: Schematic of the addition of O_2 to the two terminal carbon atoms of C_3H_3. Solid black lines represent theoretical predictions of the barrier heights, and the dashed line represents the energy surface fitted to agree with the experimentally determined rate coefficient for the $C_3H_3 + O_2$ addition reaction.[9,24]

van der Waals complex, provided the barrier in the entrance channel is sufficiently large. Indeed, there are a few examples where the stabilization of prereactive species occurs even when the barriers in the entrance valley lie submerged below the asymptotic dissociation energy,[30,32,33] as is the case here for the $C_3H_3 + O_2$ methylenic addition pathway. This expectation is best justified with a specific example from the He droplet literature. Miller and co-workers used IR laser spectroscopy to study the reaction between HCN and Ga in He droplets.[33] They observed the weakly bound HCN–Ga complex. The energies of the HCN–Ga complex, the transition state to Ga insertion into the H–C bond, and the HGaCN product are –4, –2 and –13 kcal·mol^{-1}, respectively (zero is defined as the infinitely separated HCN and Ga fragments). Therefore, for this metal atom insertion reaction, the He cooling rate along with the ≈2 kcal·mol^{-1}submerged barrier in the entrance channel is sufficient to kinetically trap the entrance channel HCN–Ga species. However, it is unknown if any of the reactive encounters lead to the insertion product,

given that there was no laser coverage available to probe for HGaCN. Although we have come to expect He-mediated kinetic trapping of metastable species to be a rather general result,[34] in this study, we find that the sequential addition of C_3H_3 and O_2 to the droplet leads exclusively to the *trans*-acetylenic propargyl peroxy radical (ace-T), and there is no spectroscopic evidence for an entrance channel complex stabilized by electrostatic and dispersion forces in the long-range part of the potential. Multireference based methods are employed to characterize the entrance channel regions of the potential, and we discuss the origin of what appears to be a spurious barrier in the channel associated with O_2 addition to the methylenic carbon center, leading directly to the barrierless formation of the ace-T peroxy radical. These results are consistent with a previous study,[24] in which the barrier in the entrance channel had to be significantly reduced (+3.7 to –0.2 kcal·mol^{-1}) to obtain quantitative agreement between the predictions of a time-dependent master equation model and the experimental rate coefficients.[9,25]

3.2 Experimental Methods

The He droplet apparatus used here has been described in detail previously.[34] Droplets are formed in a continuous expansion of high-purity He (20 bar) into vacuum through a cold (14–24 K), ≈5 μm diameter pinhole nozzle. The droplets have sizes that follow a log-normal distribution,[35,36] and those sizes reported here are the mean sizes obtained from published scaling laws.[37] A mean droplet size of 3700 ± 1000 He atoms is obtained under the conditions 20 bar, 15 K, and a nozzle with a 5 ± 1 μm diameter.[35] The droplet expansion is collimated by a ≈0.4 mm diameter skimmer, and the droplet beam passes into a differentially pumped pick-up chamber containing an effusive, continuous-flow pyrolysis source.[34,38] Propargyl radicals are

produced within this pyrolysis source via the thermal decomposition of either 1-butyn-4-nitrite ($HCC(CH_2)_2ONO$) or propargyl bromide ($HCCCH_2Br$). Operation of the source near 700 K results in the fragmentation of 1-butyn-4-nitrite into one propargyl radical, one NO molecule, and one formaldehyde molecule. Pyrolysis of propargyl bromide requires a higher temperature and does not result in 100% decomposition at the highest possible source temperature; it was therefore used only to confirm the assignments of bands in the survey spectrum measured using the nitrite precursor. The droplet beam passes close to the tip of the pyrolysis source and a fraction of the droplets subsequently pick-up and solvate the pyrolytic decomposition products. The 1-butyn-4-nitrite pressure is kept low ($\approx 10^{-4}$ Torr) to avoid recombination reactions within the pyrolysis source and to optimize for the pick-up of single molecules. At this pressure, it is estimated that ≈12% of all droplets pick-up a single C_3H_3 radical.[39] Following pick-up, the molecular degrees of freedom of the hot propargyl radical are cooled to the droplet temperature (0.4 K) via He atom evaporation.[40] The droplet beam then passes through a pick-up cell containing O_2 at $\approx 10^{-6}$ Torr and a fraction of propargyl-doped droplets will additionally pick-up an O_2 molecule. Only ≈5% of the droplet ensemble picks up both C_3H_3 and a single O_2 molecule, and the remaining droplets are either devoid of dopants or pick up other combinations of C_3H_3, NO, CH_2O and O_2. Because the time scale between pick-up events (tens of microseconds) is longer than the cooling timescale (< 1 ns), the addition of O_2 to droplets containing C_3H_3 leads to the formation of $C_3H_3O_2$ via the interaction of cold monomer fragments. On the basis of the ≈20 kcal·mol^{-1} (≈7000 cm^{-1}) C–O bond energy, the He-mediated $C_3H_3 + O_2 \rightarrow C_3H_3O_2$ reaction leads to the evaporation of approximately 1400 He atoms per droplet (≤ 5 cm^{-1} of energy removed per evaporated He atom).[41]

The droplets pass into a differentially pumped chamber where they are electron-impact ionized and detected with a quadrupole mass spectrometer. Figure 3.3 shows the mass spectra of undoped (A) and doped (B-D) droplet beams as experimental conditions are adjusted to produce He-solvated propargyl peroxy radicals. With the pyrolysis source off, the mass spectrum (Figure 3.3A) consists of a series of intense He_n^+ peaks.[42] The mass spectrum in Figure 3.3B is obtained as 1-butyn-4-nitrite is allowed to flow through the room-temperature pyrolysis source. Peaks in Figure 3.3B associated with the He-solvated precursor, most notably m/z = 39 u, arise from its ionization via He^+ charge transfer and its subsequent fragmentation. Apparently the dominate precursor fragmentation channel upon ionization is the formation of $C_3H_3^+$. When the pyrolysis source is heated to ≈700 K (Figure 3.3C), the peak at m/z = 39 u ($C_3H_3^+$) diminishes while peaks at m/z = 29 u ($C_2H_5^+$), 30 u (CH_2O^+ and NO^+), and m/z = 38 u ($C_3H_2^+$) gain intensity. This indicates the thermal, pyrolytic decomposition of 1-butyn-4-nitrite and the introduction of propargyl, NO, and formaldehyde to the droplets. Figure 3.3D shows the mass spectrum obtained with the heated pyrolysis source and the addition of O_2 to the downstream gas pick-up cell. Other than the appearance of m/z = 32 u, the mass spectrum remains relatively unchanged.

The output from a continuous-wave IR optical parametric oscillator (OPO) overlaps the He droplet beam either collinearly or perpendicularly in a Stark/multipass cell which is described elsewhere.[43-45] The tuning and calibration of this OPO laser system is likewise described elsewhere.[46] Rovibrational excitation of the He-solvated molecular species is followed by energy transfer to the collective excitations of the droplet, which leads to the evaporation of several hundred He atoms. This laser induced reduction in the geometric cross section of the droplets is detected as a depletion of ion signal in individual mass channels, which are chosen to discriminate against complexes of propargyl with other pyrolysis products (e.g. NO, CH_2O).

The OPO beam is mechanically chopped at 80 Hz, and the ion signal is processed by a lock-in amplifier as the OPO frequency is continuously tuned with ≈10 MHz resolution. The resulting spectra are normalized to the laser power.

3.3 Theoretical Methods

The present theoretical analysis is focused on the potential energy surface in the neighborhood of the transition state for the addition to form the acetylenic $C_3H_3O_2$ adduct. A series of constrained optimizations were performed for CO separations ranging from 1.8 to 3.0 Å. This range of separations extends from the strongly attractive region where chemical bonding is dominant to the region where van der Waals interactions are dominant. A saddle point for the addition process, if present, would be expected to lie between these two limits.

The interaction energies in this region of configuration space are not well described with single reference methods. Thus, the constrained optimizations were performed with multireference second order perturbation theory (PT2)[47] employing an 11 electron 9 orbital (11e,9o) complete active space (CAS) wave function and Dunning's correlation-consistent polarized valence triple-zeta (cc-pVTZ) basis set.[48] This (11e,9o) active space consisted of the (6e,4o) π-space of O_2 and the (5e,5o) π-space of C_3H_3. With this method, the *cis* orientation of the OOCC dihedral angle provides the minimum energy geometry, at least at the saddle-point, and this orientation was employed throughout the present minimum energy path (MEP) analysis.

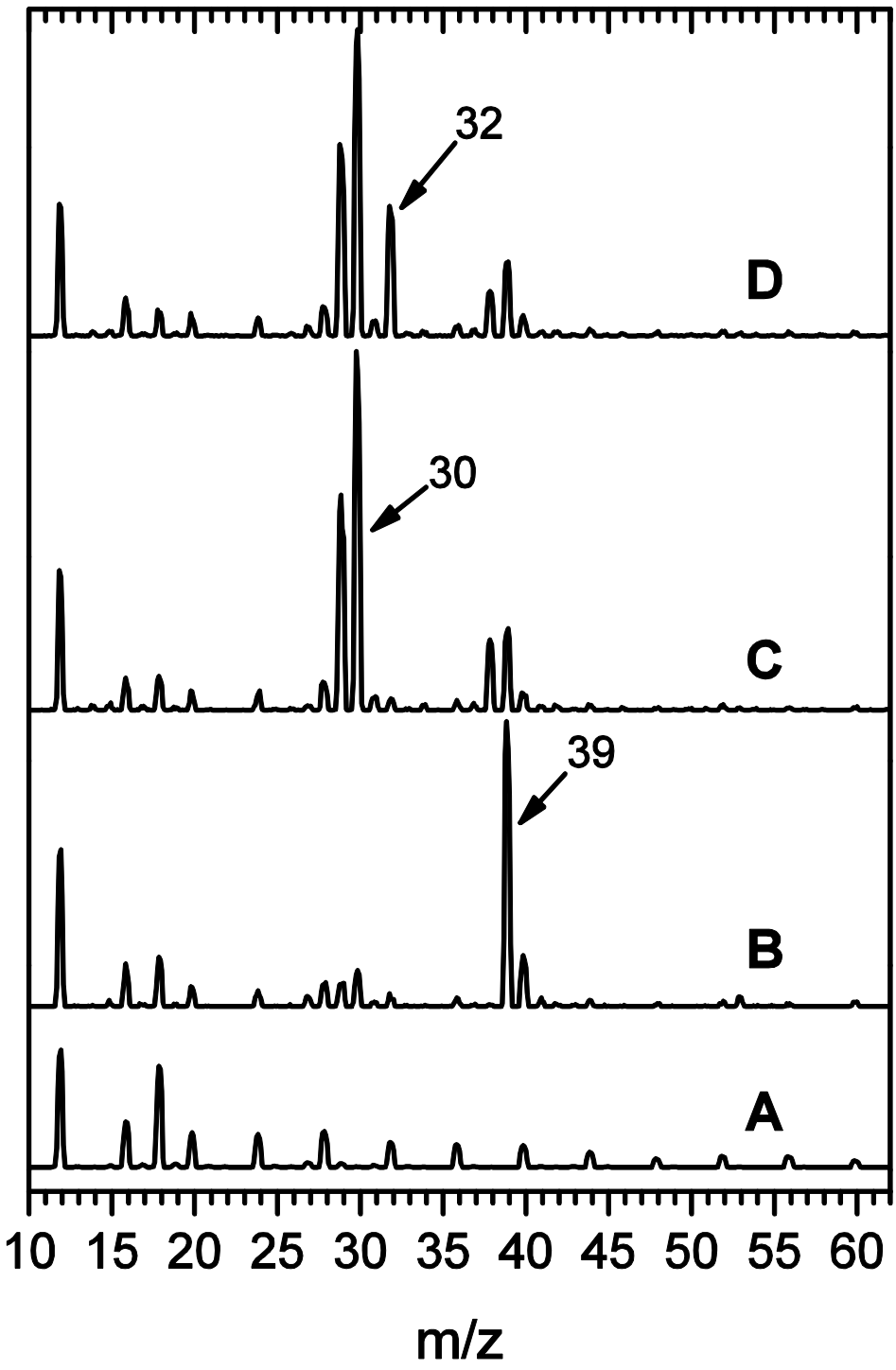

Figure 3.3: (A) Mass spectrum of the neat He beam. (B) Flowing room temperature 1-butyn-4-nitrite through the *cold* pyrolysis source. (C) Flowing room temperature 1-butyn-4-nitrite through the *hot* pyrolysis source yielding a temperature at the tip of the quartz tube of ≈700 K. (D) Addition of O_2 to the pick-up cell while flowing 1-butyn-4-nitrite through the hot pyrolysis source.

Single point energy calculations were performed at the geometries along this distinguished coordinate MEP by employing either the CASPT2 or the multireference singles and double configuration interaction (CAS+1+2) method. The CASPT2 analysis was performed both with and without an ionization potential-electron affinity (IPEA) shift,[49] which is designed to improve the treatment of the transformation from bonded to unbonded situations and is also commonly employed to remove intruder state problems. This shift of the diagonal elements of the Fock operator is motivated by the overestimate of the correlation energy for open-shell systems in the original CASPT2 zeroth order Hamiltonian. Meanwhile the Davidson correction for higher order excitations was also evaluated for the CAS+1+2 analysis and is labeled here as CAS+1+2+QC. These multireference single point calculations were performed for both the ground doublet and quartet states. The quartet state was also analyzed with the CCSD(T) coupled cluster method.

In each instance, the calculations were performed for both the cc-pVQZ and cc-pV5Z basis sets, and the results were extrapolated to the complete basis set (CBS) limit via a simple two point $1/(l+1)^4$ extrapolation.[50] For the case of l=4 this yields:

$$E_{CBS} = E_{5Z} + 0.93\,(E_{5Z} - E_{QZ}). \qquad \textbf{(Eq. 3.1)}$$

All of the present electronic structure calculations were performed with the MOLPRO electronic structure code.[51]

3.4 Results and Discussion

3.4.1 Infrared Spectroscopy

With the pyrolysis source at 300 K, a survey scan (mass channel 39 u) in the 3300 cm^{-1} region (acetylenic CH stretch region) reveals only a single band at ≈3332 cm^{-1}, which is assigned to the acetylenic CH stretching mode of the 1-butyn-4-nitrite precursor. As shown in Figure 3.4, heating the pyrolysis source to ≈700 K attenuates this 3332 cm^{-1} band to essentially zero and leads to the appearance of an expected propargyl band at 3322 cm^{-1}.[38] Difference mass spectra (with and without the laser present at a fixed frequency), obtained with the laser frequency fixed to the peak of both of these bands (Figures 3.5A and 3.5B), indicates that significant laser-induced depletion signal on m/z = 38 u exists only for the propargyl radical and not for the precursor. The measurement of ion depletion in the 38 u channel therefore discriminates against nonpyrolyzed precursor molecules. Scanning the OPO frequency on this mass channel with the heated pyrolysis source and the addition of O_2 to the downstream pick-up cell, a partially resolved rovibrational band appears at about the same frequency as the cold precursor band (≈3332 cm^{-1}), which is clearly absent without the addition of O_2. A difference mass spectrum with the laser fixed to the peak of this new band (see Figure 3.5C) reveals intense laser depletion signal in channel m/z = 27 u. This is attributed to the protonated acetylene ion $(C_2H_3)^+$, which apparently results from rearrangement and dissociation of $(C_3H_3–O_2)^+$ following the electron impact ionization of the droplet and the subsequent $He^+ + C_3H_3O_2$ charge transfer reaction (neutral CO_2 is also formed as a result of this).[42,52,53]

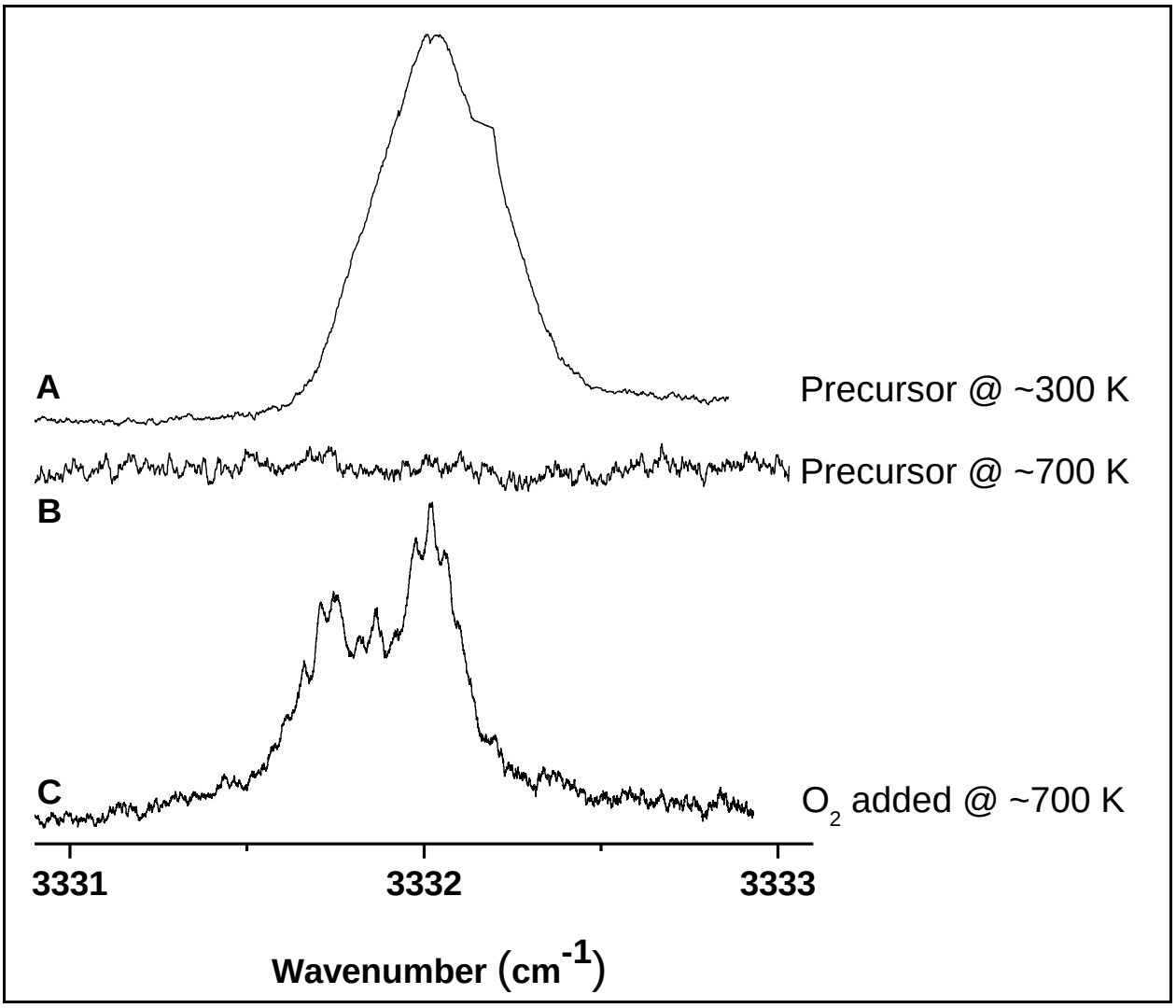

Figure 3.4: Spectrum of the acetylenic CH stretching region of A) the unpyrolyzed precursor, B) the pyrolyzed precursor, and C) the pyrolyzed precursor with O_2 added to the pick-up-cell.

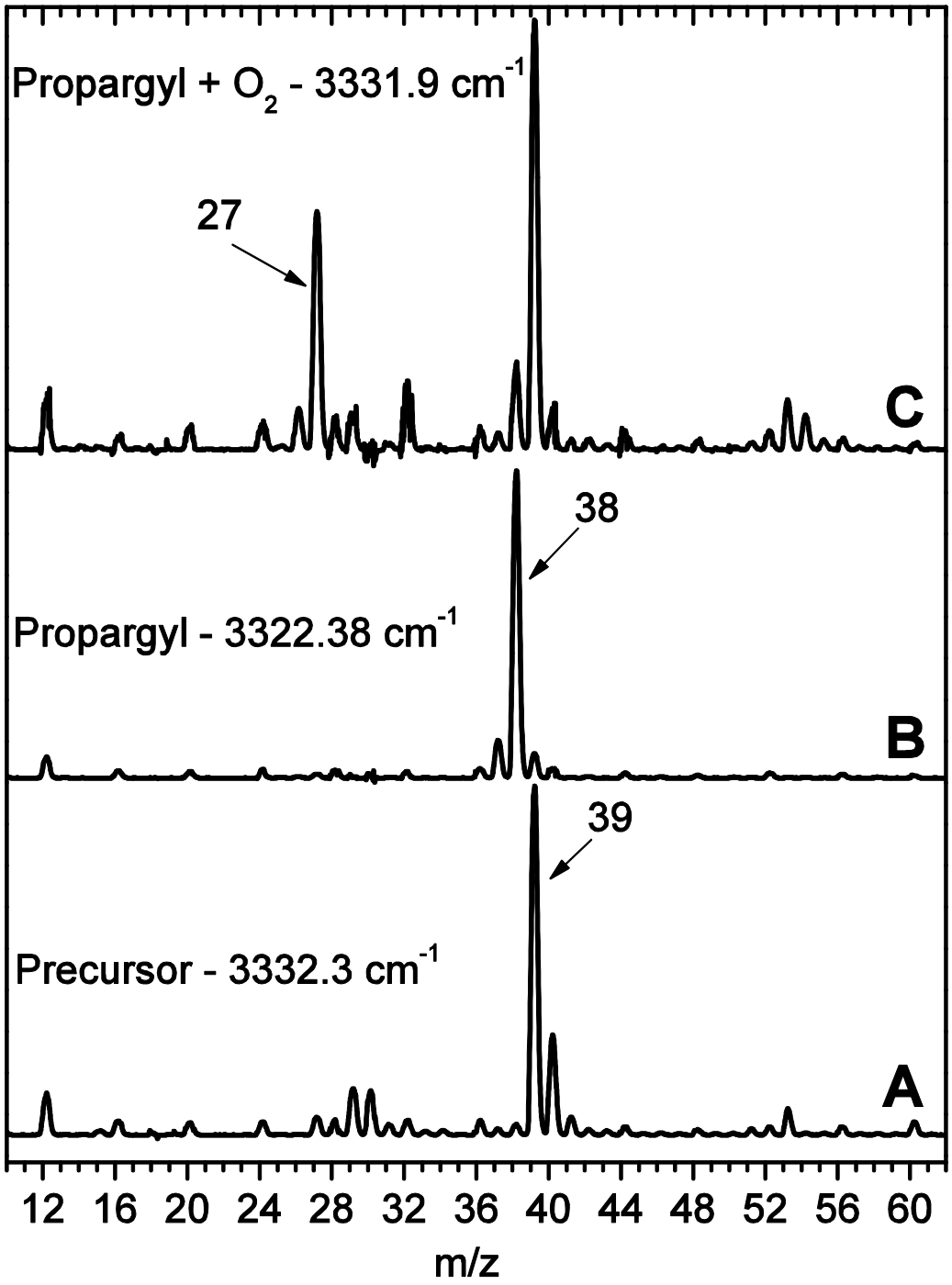

Figure 3.5: Difference mass spectra (Laser OFF – Laser ON) obtained by scanning the mass spectrometer quadrupole with the OPO frequency set to the indicated peaks. (A) Precursor flowing through the *cold* pyrolysis source. (B) Precursor flowing through the *hot* pyrolysis source. (C) O_2 is present in the pick-up cell while the precursor flows through the *hot* pyrolysis source.

Comparing the difference mass spectra in Figure 3.5, it is apparent that m/z = 27 u is the cleanest mass channel on which to search for propargyl peroxy radical bands, because it discriminates against both unpyrolyzed precursor and propargyl radical bands. Moreover, this channel discriminates against droplets that have not picked up an O_2 molecule and those that have picked up either CH_2O or NO. A survey scan with the detection channel set to 27 u is shown in Figure 3.6, and the most intense band in the spectrum is centered at 3332 cm^{-1}. The signal intensity of this band as a function of O_2 pick-up cell pressure peaks at $\approx 3 \times 10^{-6}$ Torr, and this is consistent with the pickup of a single O_2 molecule. Furthermore, as noted above, this band disappears entirely at lower pyrolysis source temperatures. Given that this new band falls in the acetylenic CH stretch region, it seems likely that at least some of the droplet-mediated $C_3H_3 + O_2$ reactions lead to the acetylenic isomer of the propargyl peroxy radical and that the 3332 cm^{-1} band is the ν_1 acetylenic CH stretching mode of either ace-T or ace-G.

An expanded view of the 3332 cm^{-1} band is shown in Figure 3.7A along with simulated spectra for ace-T and ace-G (Figures 3.7B and 3.7C, respectively). Simulations are made with PGOPHER[54] using rotational constants computed at the CCSD(T)/6-311++G** level for both the C_s symmetry ace-T and C_1 symmetry ace-G peroxy radicals (Table 3.1). The rotational constants are reduced by a factor of 3 to account for the increased effective moment of inertia that is common for He-solvated molecules of this size.[55,56] In an attempt to extract rotational constants from the spectrum with a contour fitting routine, we found that the fitting parameters were too correlated to determine quantitatively the solvent effect for rotation about each inertial axis; however, the fitted constants are consistent with the commonly observed reduction from the gas phase values ($B_{He} \cong B_{gas}/3$), assuming the computed constants for ace-T (Table 3.1). The

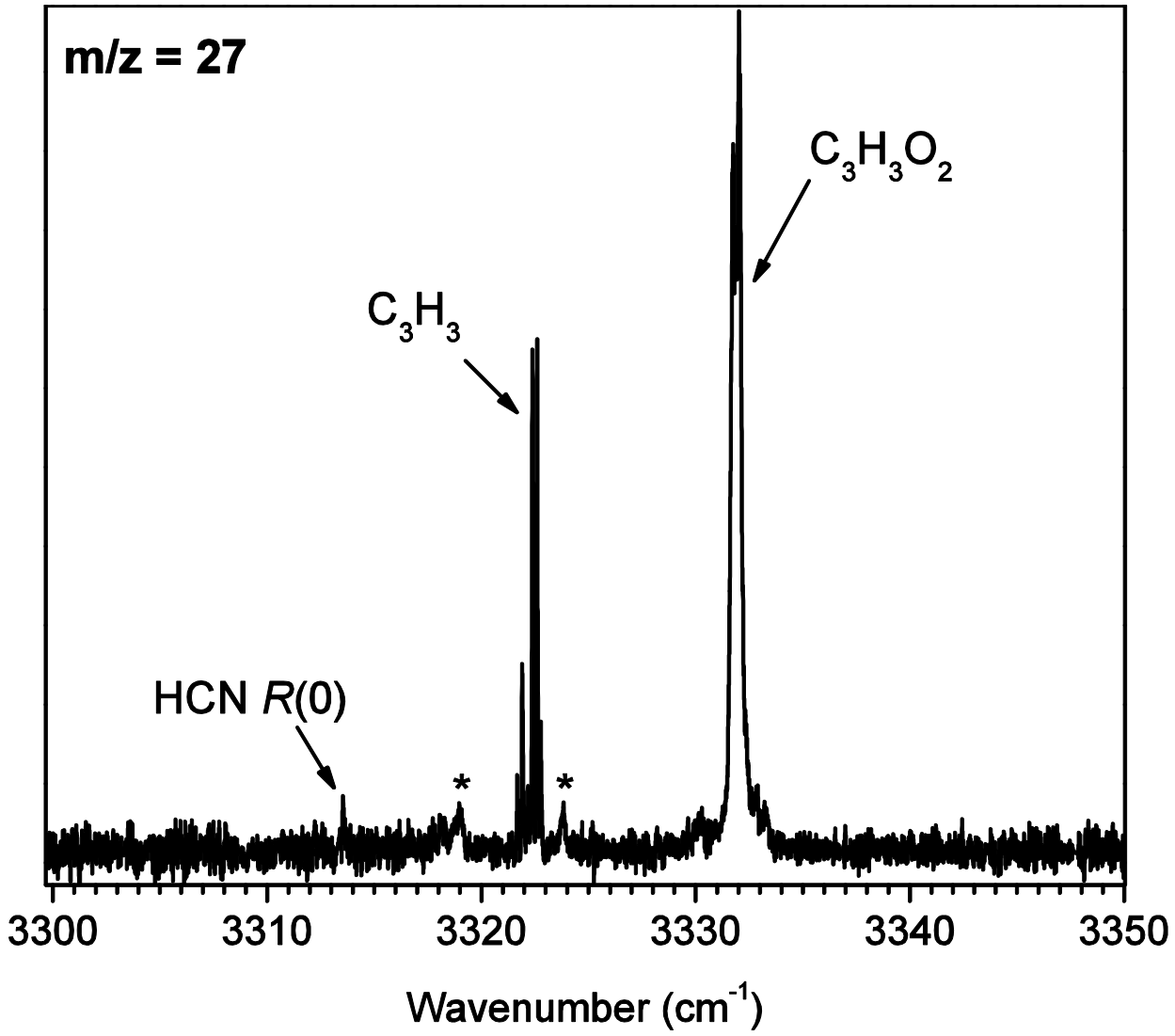

Figure 3.6: Survey scan on mass channel 27 u of the pyrolyzed precursor with O_2 added to the pick-up cell. Asterisked peaks are attributed to decomposition/recombination of the precursor (see text). The HCN *R*(0) transition at 3313.6 cm^{-1} is due to residual HCN in the chamber, which was used to optimize the laser's spatial overlap with the droplet beam prior to beginning the scan.

asymmetry parameters for ace-T and ace-G using the computed constants are –0.99 and –0.91, respectively. Therefore, both are near-prolate tops, and it is expected that the spacing between transitions within the *P* and *R* branches will be slightly greater for ace-G, given the larger (*B*+*C*)/2 constant for ace-G in comparison to ace-T. The most striking feature in the comparison of the two simulations is the larger intensity of the *Q* branch for ace-G, which is expected because the rotational term values are dependent on $(A - (B+C)/2)K^2$. Indeed, the *A* constant is reduced by roughly half and (*B*+*C*)/2 is increased by ≈25% in going from ace-T to ace-G. Therefore, in comparison to ace-T, ace-G levels with $K > 0$ are shifted down in energy, allowing more of them to be populated at the droplet temperature (0.4 K), which results in an increased *Q* branch intensity. It is evident that the agreement between the experimental spectrum and the ace-T simulation is relatively good, and that the agreement with the *P*, *Q*, and *R* branches in the ace-G simulation is overall poorer. We therefore assign this band to ace-T, although this assignment is based on the assumption that the helium effect is to reduce all three rotational constants by a factor of 3. We note that there seems to be weak structure along the wings of the simulation for ace-G that is evident in the experimental spectrum. It could be the case that there is a weaker band due to ace-G that is washed out by the ace-T band, but as discussed below, we do not observe any CH_2 stretches that can be attributed to the ace-G peroxy radical.

A Stark spectrum was obtained (see Figure 3.8) for the 3332 cm^{-1} band, which is assigned above to the acetylenic CH stretch of the ace-T propargyl peroxy radical. An electric field of 5,490 (53) V/cm was generated between two parallel, stainless steel electrodes separated by 3.10(2) mm. The linearly polarized IR beam can be rotated via a Fresnel rhomb to be either parallel or perpendicular to this Stark field, resulting in selection rules of $\Delta M = 0$ and $\Delta M = \pm 1$, respectively.[43] The experimental spectrum in Figure 3.8A corresponds to the Stark field being

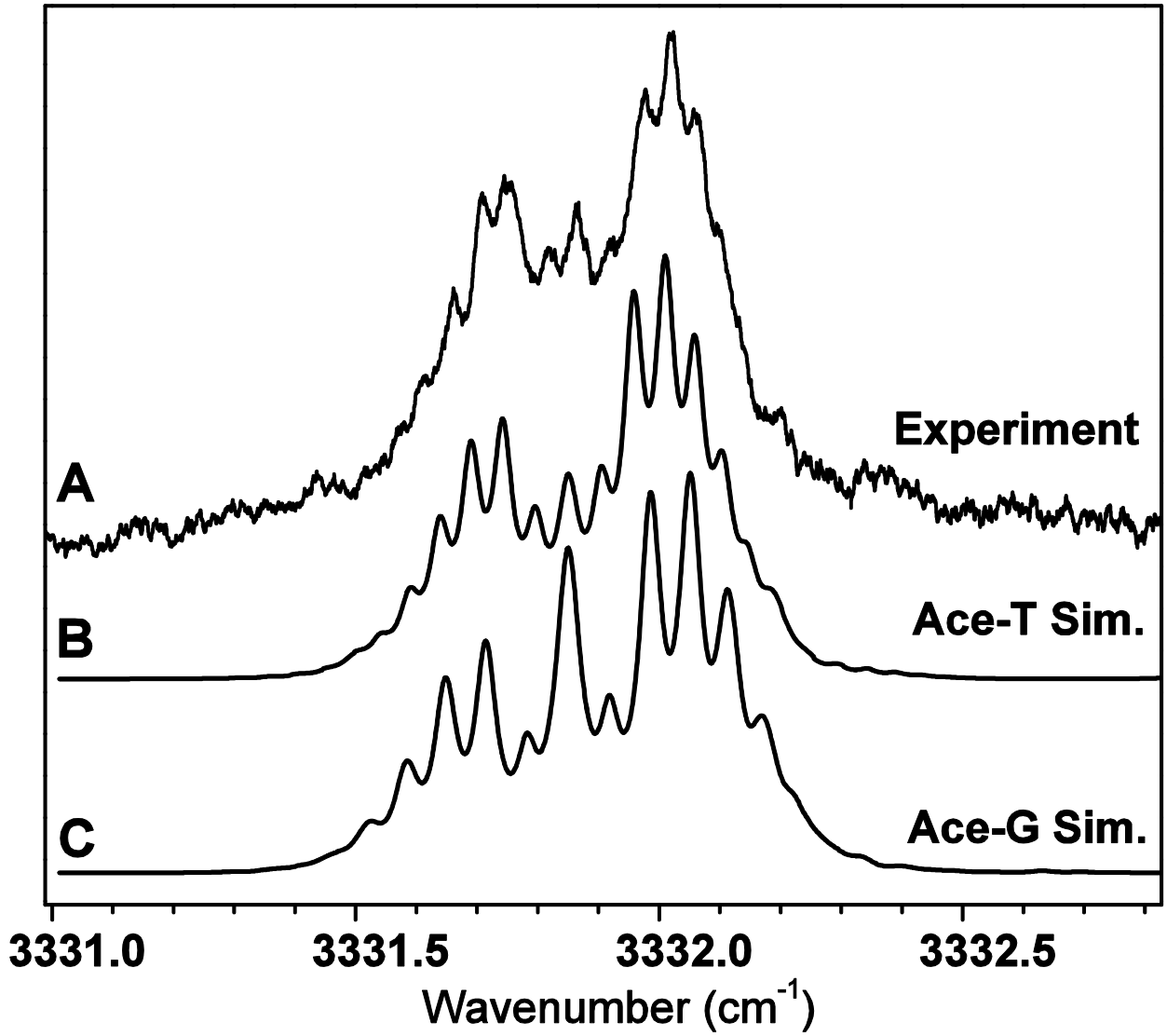

Figure 3.7: (A) Expanded view of the band assigned to the ace-T propargyl peroxy radical ν_1 CH stretch. (B) Ace-T simulation obtained by reducing the *ab initio* constants by a factor of 3. (C) Ace-G simulation obtained by reducing the *ab initio* constants by a factor of 3. Geometries and rotational constants were computed at the CCSD(T) level with a 6-311++G** basis set.

aligned parallel to the IR beam polarization. Also shown in Figures 3.8B and 3.8C are Stark simulations for ace-T and ace-G, respectively, obtained with PGOPHER[54] using the electric field magnitude, laser polarization relative to the electric field, the computed rotational constants (reduced 3-fold to account for the He), and the computed permanent electric dipole components along the molecule-fixed axes (Table 3.1). It is clear that the simulation for ace-T more closely resembles the experimental spectrum than does the ace-G simulation, thus lending additional support to the assignment of this band to ace-T. There are weak features present in the experimental spectrum, which are unaccounted for in the Stark simulations; we attribute many of these to the impurities discussed below. Adjustment of the permanent electric dipole component

Table 3.1: Computed rotational constants for the ace-T and ace-G propargyl peroxy conformers.[a]

	ace-T [b]	**ace-G** [b]	**fitted** [c]
A	1.1	0.45	0.28(1)
B	0.084	0.11	0.029(1)
C	0.079	0.095	0.026(1)
μ_a	2.379	1.964	
μ_b	1.362	1.703	
μ_c	0	0.542	

[a] CCSD(T)/6-311++G** level of theory. All rotational constants have units of wavenumbers (cm^{-1}), and all permanent electric dipole components have units of Debye.

[b] For the simulations shown in Figure 3.7, the computed rotational constants reported here for ace-T and ace-G are reduced by a factor of 3 to account for the coupling of the heavy rotor to the He droplet.

[c] Constants that result from a contour fit of the 3332 cm^{-1} band. Numbers in parentheses are 1σ errors.

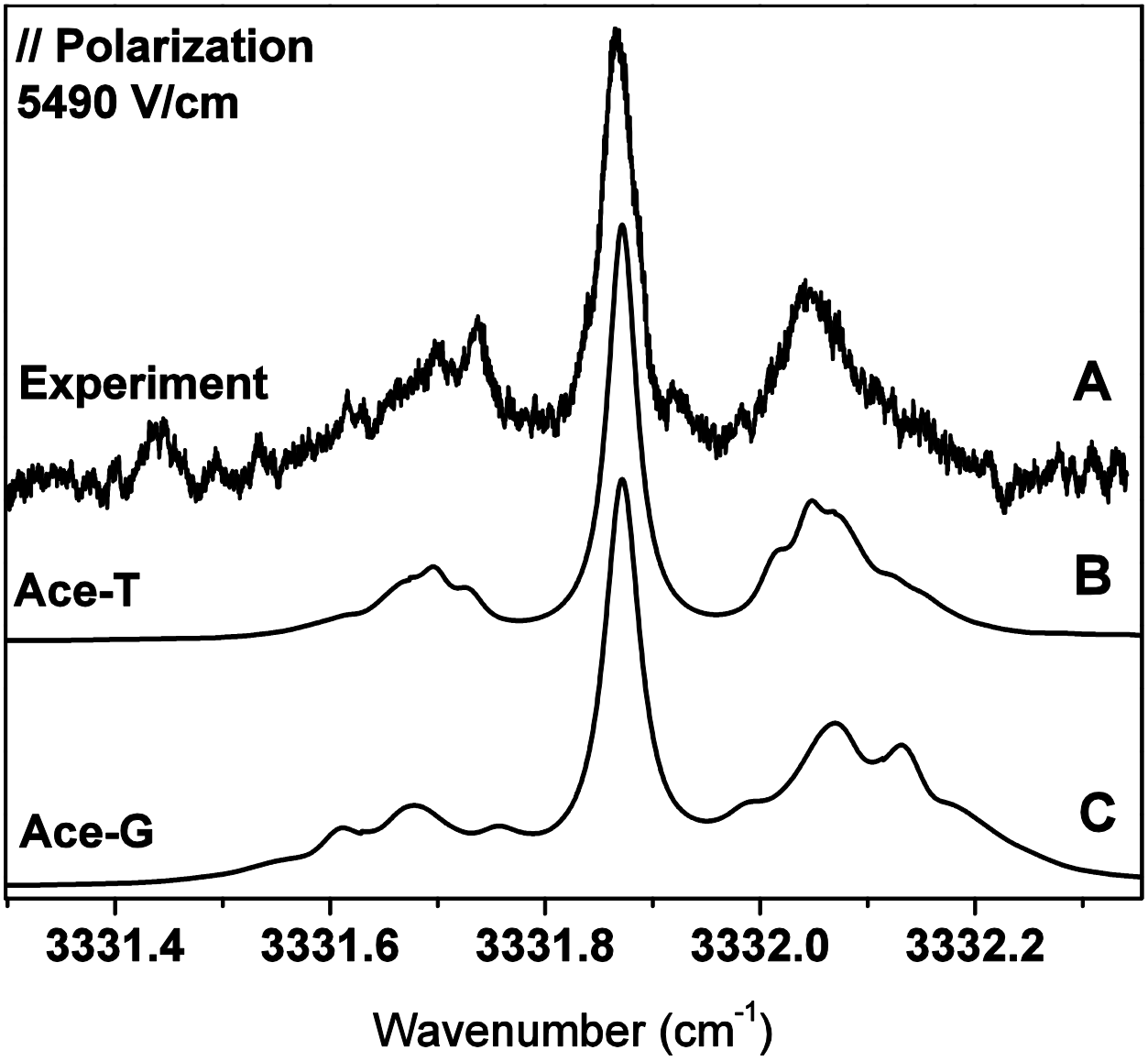

Figure 3.8: (A) Stark spectrum of the 3332 cm^{-1} band with an applied electric field of 5490 V/cm. The polarization of the IR light is rotated by 90° by means of a Fresnel rhomb such that it is parallel with the Stark field. Also shown are simulations using the (renormalized) constants and dipole components from Table 3.1 for (B) ace-T and (C) ace-G.

along the *a* inertial axis (μ_a) from 1.5 to 3.5 D in the ace-T simulation results in only a small blue shift (red shift) of the *R* (*P*) branches of roughly 0.07 cm^{-1}, and the line shapes do not dramatically change in the simulated spectra. Thus it is not possible here to deduce an accurate value of μ_a with reasonably small error bars given the present resolution. The simulated spectrum is even less sensitive to the adjustment of μ_b, and we are likewise unable to report an experimental value for μ_b.

Having located the acetylenic CH stretch of ace-T, a survey scan from 2940 to 3115 cm^{-1} was measured to locate the corresponding symmetric and antisymmetric CH_2 stretches and to search for the ace-G and all-C/T vibrations that are predicted in this region (see Figures 3.9 and 3.10). Harmonic frequency calculations indicate blue shifts of 10–20 cm^{-1} in going from ace-T to ace-G for both the symmetric and antisymmetric CH_2 stretches.[26] Additionally, the symmetric CH_2 stretches of all-C/T are predicted near the antisymmetric CH_2 stretches of ace-G/T.[26] We observe two bands at roughly 2959.8 and 2988.6 cm^{-1}. These lack resolved rotational structure from which we could estimate a band origin, but center frequencies agree well with anharmonic calculations for the symmetric (ν_2) and antisymmetric (ν_{13}) CH_2 stretches of ace-T, respectively.[1] We do not observe any bands in this region that can be attributed to any other peroxy radical structure based on the predicted frequency shifts between conformers. The only other signal in this region appears at 3104 cm^{-1}; however, this signal disappears and the *b*-type band of ethylene is observed when O_2 is removed from the pick-up region.[57] A scan of this region with only ethylene and oxygen in the pick-up region, shown in Figure 3.10, indicates the C_2H_4–O_2 complex is the likely source of this band. Helium droplet band assignments are compared to previous theoretical and experimental results in Table 3.2.

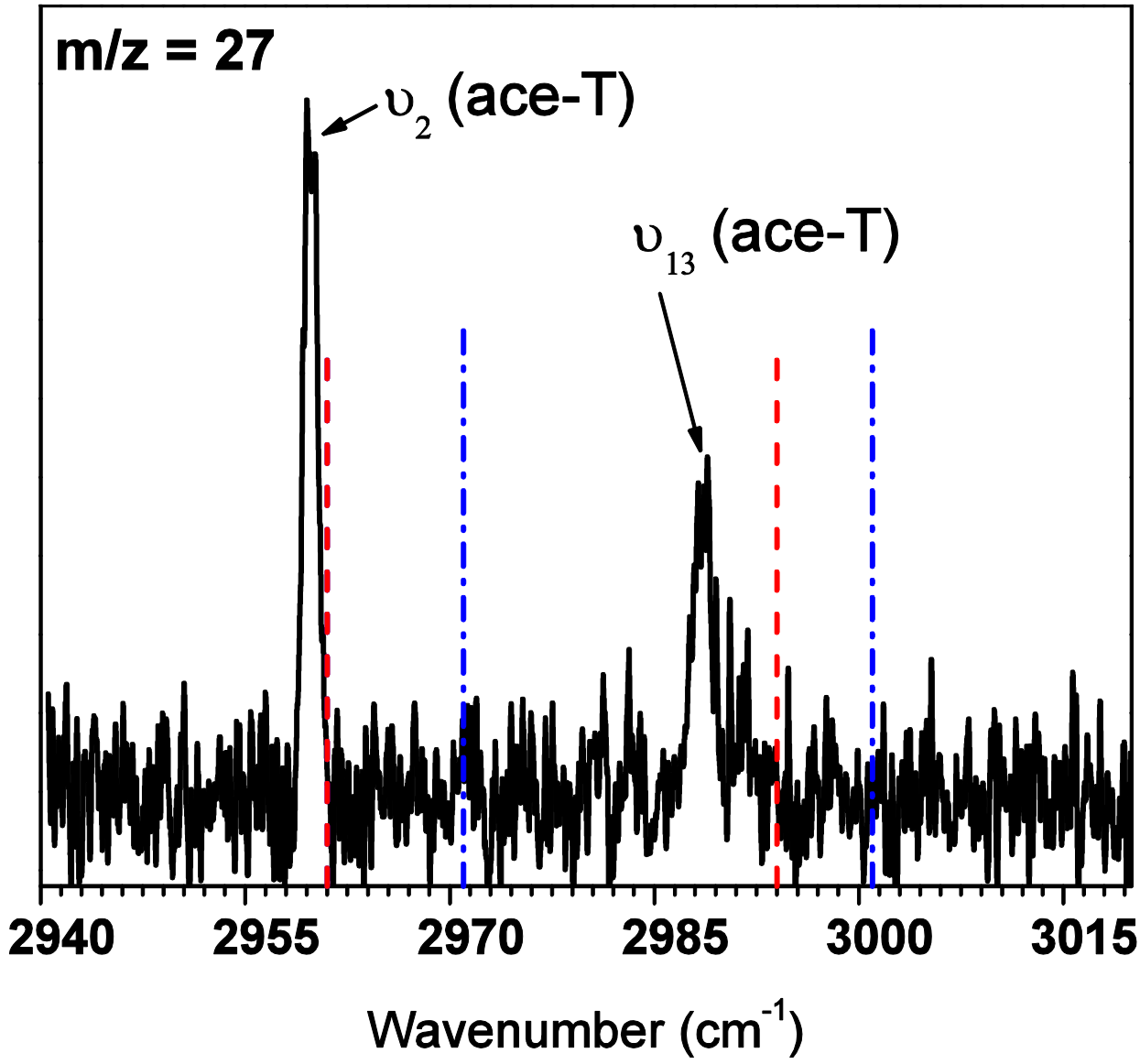

Figure 3.9: Scan of the symmetric and antisymmetric stretch regions for ace-T and ace-G (no observed stretches for ace-G). This region may also include the symmetric stretches of all-C and all-T, neither of which are observed. The higher frequency region where the antisymmetric stretches of all-C and all-T are predicted is shown in Figure 3.10. The dashed lines (red) are the computed anharmonic frequencies of the symmetric (lower frequency) and antisymmetric (higher frequency) CH_2 stretches of the ace-T peroxy radical at the CCSD(T)/ANO0 level of theory.[1] The dash-dot lines (blue) are the frequencies obtained for the ace-G conformer's symmetric (lower frequency) and antisymmetric (higher frequency) stretches by adding the harmonic frequency shifts between the ace-T and ace-G peroxy radicals[26] to the computed anharmonic frequencies (dashed lines, red).[1]

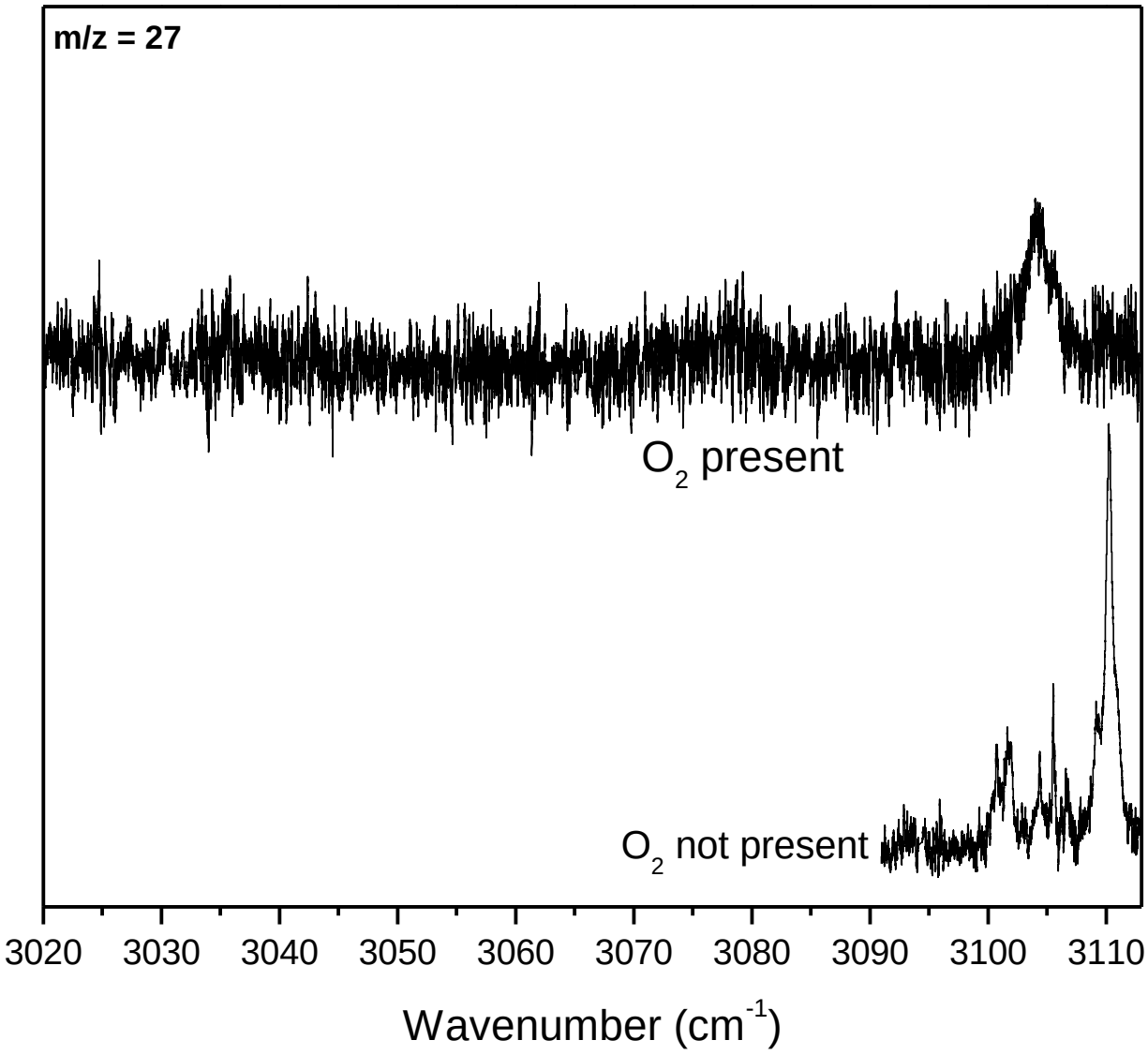

Figure 3.10: Survey spectrum of the region where the allenic conformers' asymmetric CH_2 stretches should be located. The lone signal at 3104 cm^{-1} is attributed to ethylene + O_2. When O_2 is removed from the pick-up cell, the *b*-type band of ethylene is observed.

Table 3.2. Comparison of predicted and experimentally determined band origins (cm^{-1}).

Mode	Type	Theory (ANO0/ANO1)[a,b]	Ar matrix[a]	Helium[c]
ν_1	CH stretch	3332/3337	3326 ± 3	3331.865
ν_2	CH_2 sym.	2961/2951	2960 ± 3	2959.8
ν_{13}	CH_2 asym.	2994/2980	--	2988.6

[a] Reference 22.

[b] Level of theory is CCSD(T), and the basis sets are atomic natural orbitals (ANO).

[c] The band origin of the ν_1 mode was fitted "by eye" using PGOPHER.[54] The frequencies given for the ν_2 and ν_{13} bands are determined from their centers of gravity.

We now discuss the weaker signals that are present in the survey scan near 3300 cm^{-1} (Figures 3.5 and 3.11). In addition to the ace-T ν_1 band, the acetylenic CH stretch of the propargyl radical is also observed on m/z = 27 u. This is not unexpected because propargyl radicals are picked up by droplets first, and the propargyl-doped droplets must travel ~5 cm (~7% of the total distance to the entrance of the mass spectrometer) before they can pick up O_2, form propargyl peroxy, and rearrange as described above. During this transit time between pick-up zones, the propargyl doped droplets are irradiated by the OPO beam, leading to the observed band at 3322 cm^{-1}. It is interesting to note that the 10 cm^{-1} blue shift of the acetylenic CH stretch of the propargyl radical upon reaction with O_2 to form ace-T is a direct result of the loss of resonance and the terminal acetylenic carbon adopting more *sp* character. If the condensation of propargyl and O_2 were to instead lead to a stabilized entrance channel complex, we expect to find the associated acetylenic CH stretch band of the complex only slightly shifted from the propargyl band as a result of the weak interaction. There are indeed weak signals to both the red

and blue of the propargyl band, and these are in the region expected for the acetylenic CH stretch of a weakly-bound C_3H_3–O_2 complex. The signal to the red of the propargyl band actually increases in intensity as O_2 is pumped out of the pick-up cell, indicating that it is derived from the complexation of propargyl with a decomposition and/or recombination product. However, the band to the blue of propargyl (3323.8 cm^{-1}) exhibits a strong dependence on O_2 pressure and disappears when the O_2 pressure is reduced to zero. This pressure dependence reveals that the signal at this frequency optimizes at $\approx 3 \times 10^{-6}$ Torr, consistent with the pick-up of one O_2 molecule.

Figure 3.11 also shows an expanded view of the region around the propargyl band with the propargyl radical being generated from a different precursor. When we attempted to replicate the results using C_3H_3Br as the propargyl precursor, no corresponding O_2 dependent signal was located at 3323.8 cm^{-1}. This signal must therefore be an impurity that contains the propargyl radical, yet also contains a single O_2. For example, because the 3323.8 cm^{-1} band appears only with the nitrite precursor, an assignment to a C_3H_3–CH_2O–O_2 complex seems realistic. Perhaps the complexation of C_3H_3 with formaldehyde enhances the propargyl + O_2 reaction barrier, preventing the formation of a peroxy radical and the 10 cm^{-1} blue shift of the acetylenic CH stretch. From a comprehensive analysis of the experimental spectra, the propargyl + O_2 reaction within a He droplet apparently leads only to the ace-T peroxy radical, and there is no evidence for a weakly bound complex stabilized in the entrance channel on the PES.

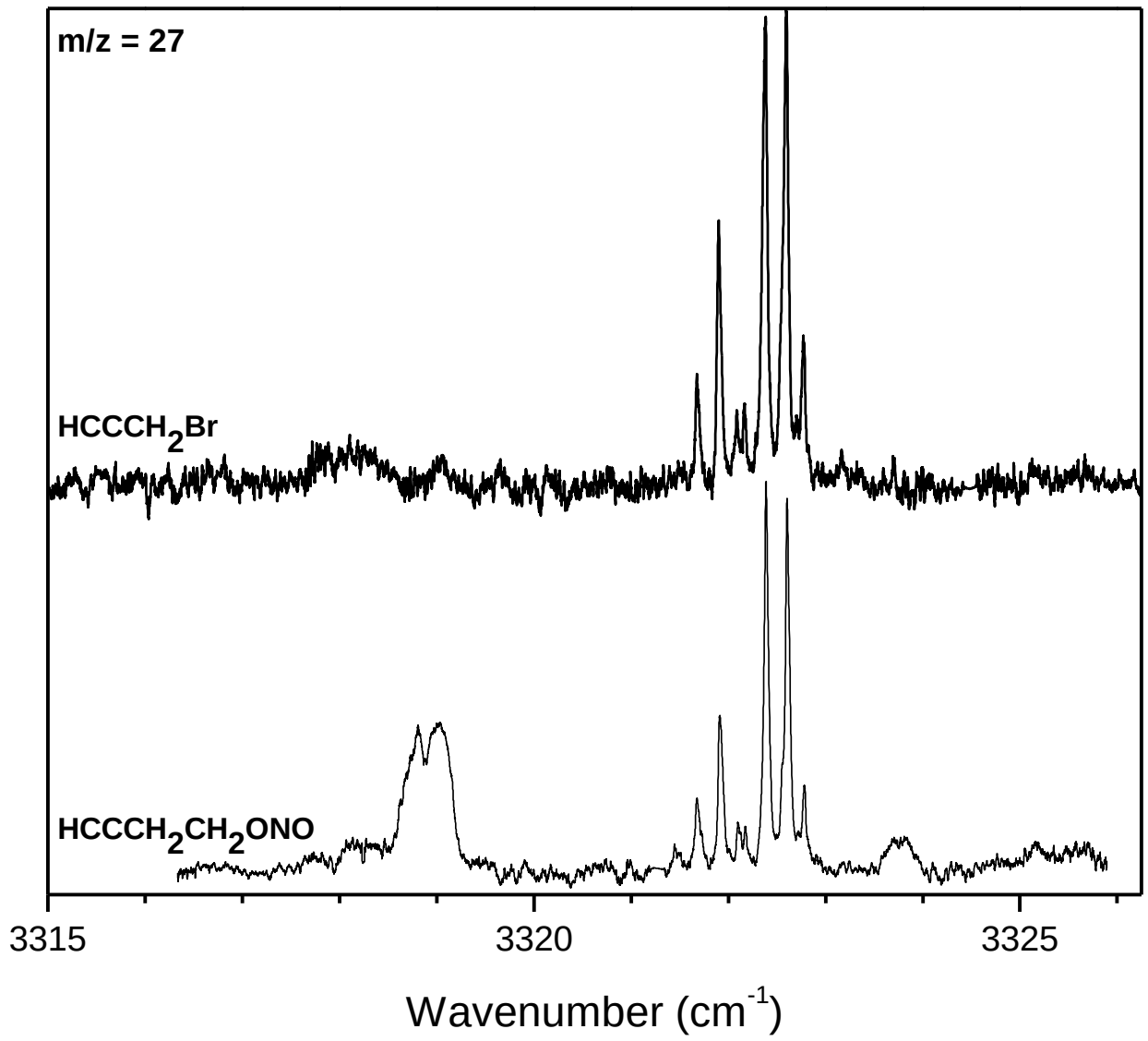

Figure 3.11: Expanded view of the rotationally resolved propargyl radical accompanied by impurity signals. Both spectra were recorded with O_2 present. The impurity signals in the lower spectrum are attributed to a slow decomposition of the precursor nitrite over time.

3.4.2 *Ab Initio* Computations

The present theoretical predictions for the interaction energy for the ground doublet state along the distinguished coordinate MEP are illustrated in Figure 3.12. The CAS+1+2 predictions show a fairly significant barrier of ≈2 kcal·mol^{-1}, and inclusion of the Davidson correction reduces this barrier to near zero and perhaps even removes it all together. This reduction in barrier height with the physical improvement from the CAS+1+2 to the CAS+1+2+QC method is commonplace for addition reactions and the lower value is generally in better agreement with experiment. Similarly, the inclusion of the IPEA shift completely removes the barrier predicted by the raw CASPT2 method.

The discrepancy of 1–2 kcal·mol^{-1} between the interaction energies for the CAS+1+2+QC and CASPT2 with IPEA shift MEPs indicates a significant level of uncertainty. This uncertainty would have a strong effect on any predicted rate constants and could perhaps affect the prediction for the presence or absence of a saddle point. We have recently been exploring an alternative approach for estimating the reaction path energies that appears to reduce these discrepancies dramatically.[58] This approach begins with the realization that open-shell low-spin states cannot be represented with a single determinant, whereas open-shell high-spin states can be. Correspondingly, the CCSD(T) method is inappropriate for treating bond dissociation curves for low-spin states, but it is perfectly appropriate for high-spin states. A direct indication of the appropriateness of the CCSD(T) method for high-spin bond dissociation curves is provided by the smallness of the T1 diagnostic along the curve. Meanwhile, multireference electronic structure methods might be expected to provide a more accurate treatment of the high-spin to low-spin energy splitting than of the absolute interactions.

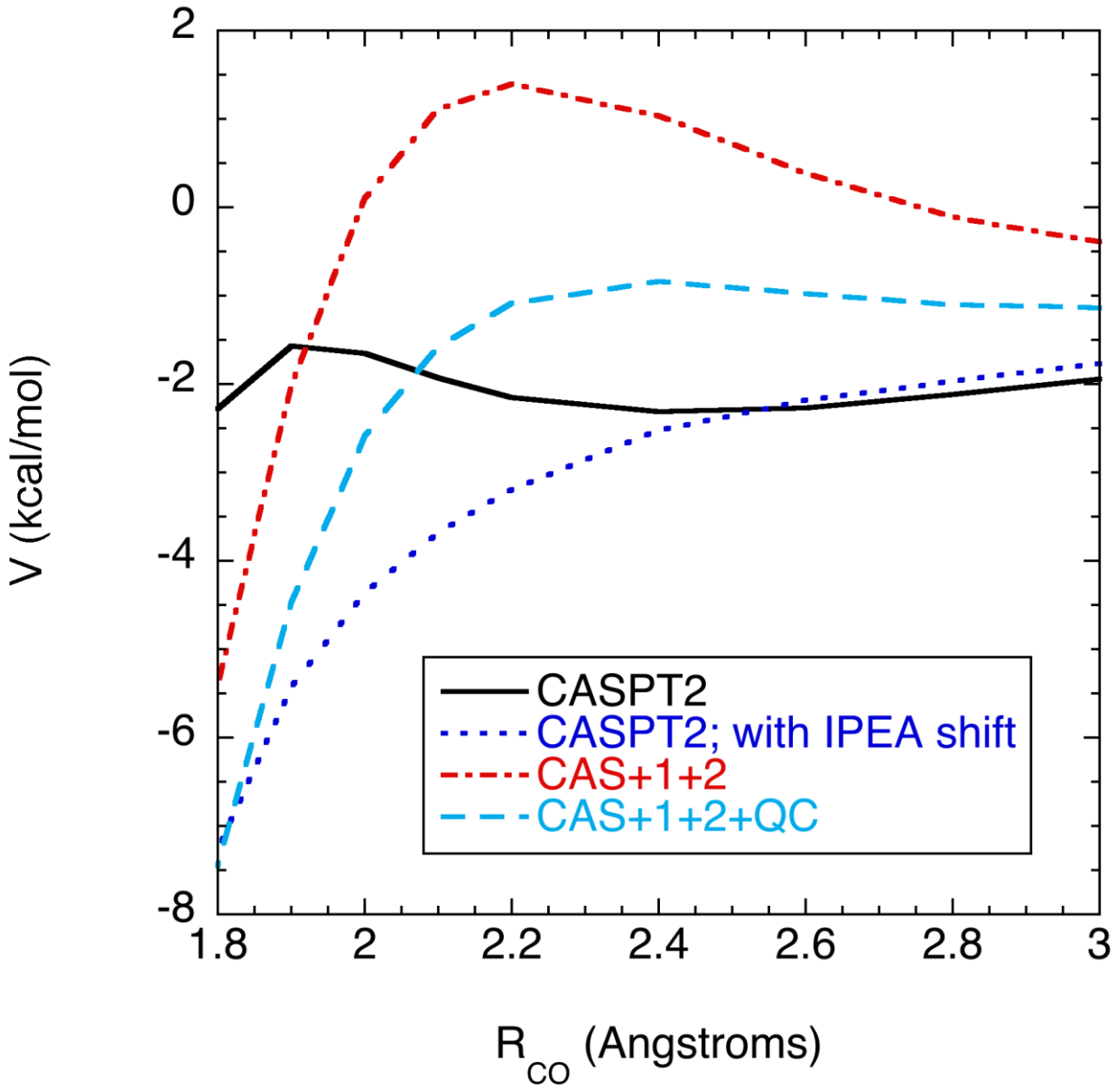

Figure 3.12: Plot of a variety (as indicated in the inset) of theoretically predicted distinguished coordinate MEP interaction energies for the addition of O_2 to C_3H_3 to form the acetylenic peroxy radical. The calculations directly evaluate the ground state doublet energy for the *cis* CCOO configuration, which is the lowest energy torsional state in this region.

Correspondingly, it is interesting to evaluate the interaction energies through the consideration of both the quartet (high-spin) and doublet (low-spin) interaction potentials. In particular, for the present system, the doublet MEP can be evaluated as the sum of the CCSD(T) evaluated quartet energy and the multireference evaluated doublet-quartet splitting. Related approaches to estimating saddle point energies were found useful in prior studies of the CH + N_2[58] and C_3H_3 + C_3H_5[60] reactions. The corresponding predictions for the MEP interaction energies are illustrated in Figure 3.13. Notably, three of the predictions are now in close correspondence over the whole MEP. Meanwhile, the deviations for the raw CASPT2 method arise only at shorter separations, where the increasing chemical interactions tend to make CASPT2 predictions inaccurate. These curves are expected to be considerably more reliable than those presented in Figure 3.12. The uncertainty in the CAS+1+2+QC curve is probably less than 1.0 kcal·mol^{-1}.

Thus, the present theoretical analysis suggests that there is most likely no barrier for the addition of O_2 to C_3H_3 to form the ace-T/G peroxy radicals. Any barrier that does exist is likely to be very small (i.e., < 0.5 kcal·mol^{-1}) and submerged below the asymptotic reactant energy. This finding is in accord with the present experimental finding that no van der Waals complexes are formed during the low temperature reaction in a He droplet. It is also in at least qualitative agreement with the prior observation that the initially predicted barrier of 3 kcal·mol^{-1} had to be reduced to less than zero to obtain agreement between theory and experiment for the addition kinetics.[24]

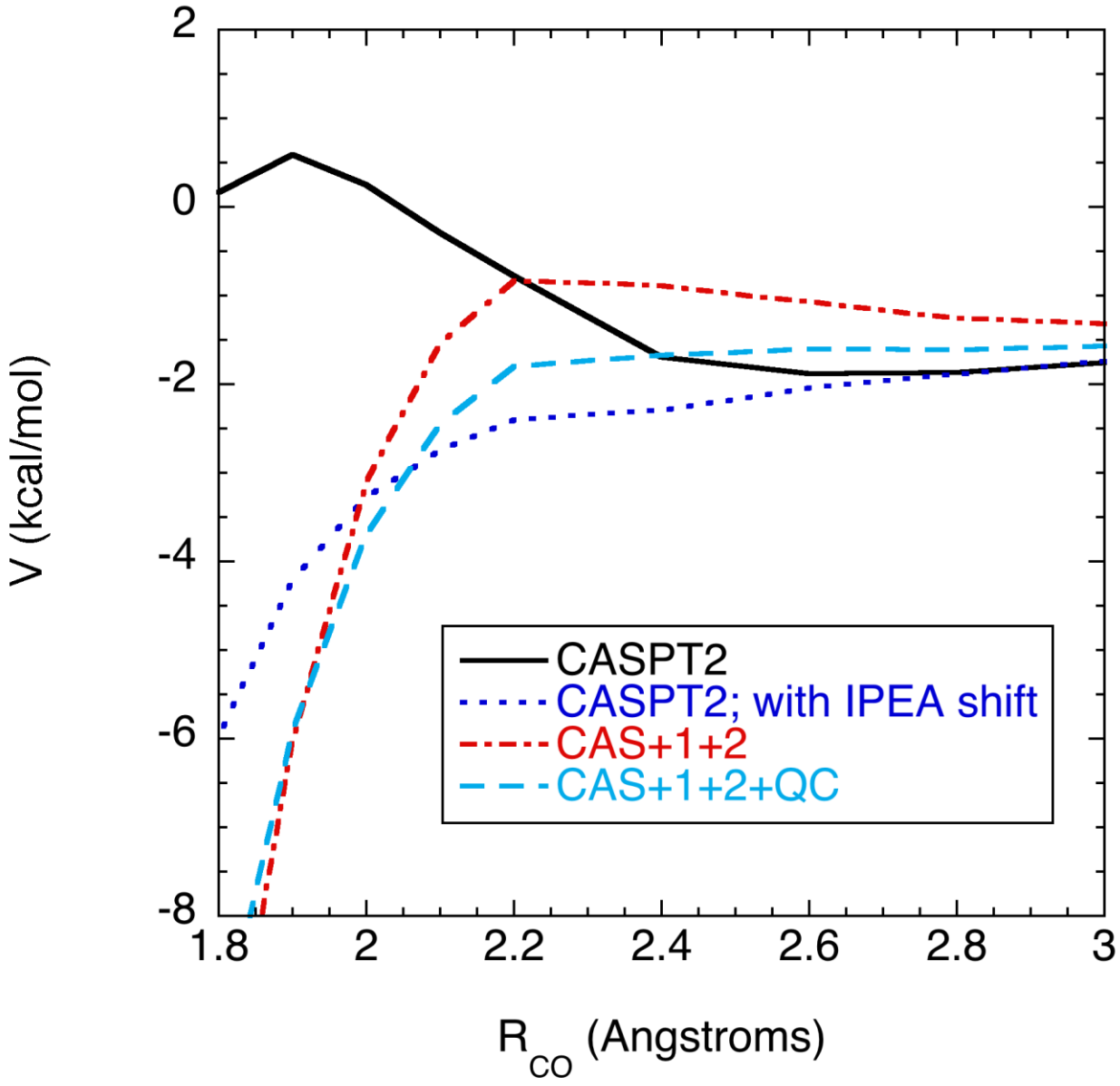

Figure 3.13: Plot of a variety of theoretically predicted distinguished coordinate MEP interaction energies for the addition of O_2 to C_3H_3 to form the acetylenic peroxy radical. The energies are evaluated from the sum of the CCSD(T)/CBS calculated quartet state energy and the doublet-quartet splitting evaluated with the method described in the inset.

3.5 Summary

The propargyl radical is generated via the pyrolysis of 1-butyn-4-nitrite ($HCCCH_2CH_2ONO$) and doped into liquid He nanodroplets. The sequential addition of single O_2 molecules to the droplets leads to the propargyl + O_2 reaction at low temperature. The outcome of this reaction is probed with IR laser spectroscopy in the fundamental CH stretch region. From an analysis of the spectrum, the *trans*-acetylenic (ace-T) propargyl peroxy radical ($^{\cdot}OO\text{-}CH_2\text{-}C{\equiv}CH$) appears to be the only product of the reaction at 0.4 K. We observe a band with partially resolved rotational structure at 3332 cm^{-1}, which is assigned to the acetylenic CH stretch (ν_1) of ace-T. Further support for this assignment comes from the experimental Stark spectrum of this band, which is satisfactorily reproduced in a simulation that assumes the computed inertial dipole moment components for ace-T. Two bands that lack rotational fine structure are observed at 2959.8 and 2988.6 cm^{-1} and are in excellent agreement with previously reported anharmonic frequency computations for the symmetric (ν_2) and antisymmetric (ν_{13}) CH_2 stretches of the ace-T species.[1] The ace-T conformer has been computed to be roughly 100 cm^{-1} lower in energy than the *gauche* conformer (ace-G).[26] For the acetylenic CH stretch, the predicted band origins for the two conformers are similar (within ≈1 cm^{-1}); however, for the symmetric and antisymmetric CH_2 stretches, conformational interconversion is predicted to result in frequency shifts of as much as 10 – 20 cm^{-1}.[26] The presence of only two bands in the CH_2 stretch region therefore suggests the presence of a facile interconversion mechanism for the higher energy *gauche* species. This is perhaps not too surprising, given that the ace-G to ace-T interconversion barrier has been computed to be only ≈0.3 $kcal{\cdot}mol^{-1}$,[26] and that there are only 2 bound states supported in the ace-G potential well. Two conformations of an allenic isomer are

predicted to be stable ($H_2C=C=CHOO^{\cdot}$, *cis*-allenic and *trans*-allenic),[26] in which the O_2 binds to the acetylenic end of propargyl rather than the methylenic end. There is also no evidence for the formation of one of these allenic isomers. This is consistent with the measurement of this system in solid-Ar and is likely due to the presence of a barrier in the entrance channel to formation of the allenic isomer, which is above the asymptotic energy of the separated reactants.[24]

Finally, we see no evidence for a van der Waals complex between propargyl and O_2, which has been previously predicted in the entrance valley to the reaction. A small shift in the acetylenic CH stretch origin of propargyl radical is expected, given the presence of a weakly interacting O_2 molecule. However, this expected spectral feature is not observed, indicating that the barrier (if any) is too small to allow for the kinetic stabilization of this species as the system condenses in the dissipative droplet environment. The present theoretical analysis confirms this finding with an indication that there is likely no saddle point for the addition of oxygen to propargyl to form the ace-peroxy radical. The analysis employing a CCSD(T)/CBS computation of the quartet state coupled with multireference predictions for the doublet-quartet splitting provides a remarkably consistent picture of the MEP while employing different multireference methods. Overall, it appears that there is a shelf in the potential for separations ranging from about 2.2 to 3.0 Å at a potential value of about –2.0 kcal·mol^{-1} relative to reactants. If present, any saddle point for the addition process is submerged well below reactants and likely lies within 0.5 kcal·mol^{-1} of the corresponding van der Waals minima.

References

(1) Jochnowitz, E. B.; Zhang, X.; Nimlos, M. R.; Flowers, B. A.; Stanton, J. F.; Ellison, G. B. *J. Phys. Chem. A* **2010**, *114*, 1498-1507.

(2) Richter, H.; Howard, J. B. *Phys. Chem. Chem. Phys.* **2002**, *4*, 2038-2055.

(3) Frenklach, M. *Phys. Chem. Chem. Phys.* **2002**, *4*, 2028-2037.

(4) D'Anna, A.; Violi, A.; D'Alessio, A. *Combust. Flame* **2000**, *121*, 418-429.

(5) Miller, J. A.; Pilling, M. J.; Troe, J. *Proc. Combust. Inst.* **2005**, *s30*, 43-88.

(6) McEnally, C. S.; Pfefferle, L. D.; Burak, A.; Kohse-Hoinghaus, K. *Prog. Energy Combust. Sci.* **2006**, *32*, 247-294.

(7) Miller, J. A.; Melius, C. F. *Combust. Flame* **1992**, *91*, 21-39.

(8) Melius, C. F.; Miller, J. A.; Evleth, E. M. *Proc. Combust. Inst.* **1992**, *24*, 621-628.

(9) Atkinson, D. B.; Hudgens, J. W. *J. Phys. Chem. A* **1999**, *103*, 4242-4252.

(10) Stein, S. E.; Walker, J. A.; Suryan, M. M.; Fahr, A. *Proc. Combust. Inst.* **1991**, *23*, 85-90.

(11) Lindstedt, R. P.; Rizos, K. A. *Proc. Combust. Inst.* **2002**, *29*, 2291-2298.

(12) Kern, R. D.; Singh, H. J.; Wu, C. H. *Int. J. Chem. Kinet.* **1988**, *20*, 731-747.

(13) Westmoreland, P. R.; Dean, A. M.; Howard, J. B.; Longwell, J. P. *J. Phys. Chem.* **1989**, *93*, 8171-8180.

(14) Marinov, N. M.; Pitz, W. J.; Westbrook, C. K.; Castaldi, M. J.; Senkan, S. M. *Combust. Sci. Technol.* **1996**, *116*, 211-287.

(15) Castaldi, M. J.; Marinov, N. M.; Melius, C. F.; Huang, J.; Senkan, S. M.; Pitz, W. J.; Westbrook, C. K. *Proc. Combust. Inst.* **1996**, *26*, 693-702.

(16) Marinov, N. M.; Castaldi, M. J.; Melius, C. F.; Tsang, W. *Combust. Sci. Technol.* **1997**, *128*, 295-342.

(17) Miller, J. A.; Klippenstein, S. J. *J. Phys. Chem. A* **2003**, *107*, 7783-7799.

(18) Georgievskii, Y.; Miller, J. A.; Klippenstein, S. J. *Phys. Chem. Chem. Phys.* **2007**, *9*, 4259-4268.

(19) DeSain, J. D.; Jusinski, L. E.; Taatjes, C. A. *Phys. Chem. Chem. Phys.* **2006**, *8*, 2240-2248.

(20) Miller, J. A.; Klippenstein, S. J. *J. Phys. Chem. A* **2001**, *105*, 7254-7266.

(21) DeSain, J. D.; Taatjes, C. A. *J. Phys. Chem. A* **2003**, *107*, 4843-4850.

(22) Howe, P. T.; Fahr, A. *J. Phys. Chem. A* **2003**, *107*, 9603-9610.

(23) Jochnowitz, E. B.; Zhang, X.; Nimlos, M. R.; Varner, M. E.; Stanton, J. F.; Ellison, G. B. *J. Phys. Chem. A* **2005**, *109*, 3812-3821.

(24) Hahn, D. K.; Klippenstein, S. J.; Miller, J. A. *Faraday Discuss.* **2001**, *119*, 79-100.

(25) Slagle, I. R.; Gutman, D. *Proc. Combust. Inst.* **1986**, *21*, 875-883.

(26) Thomas, P. S.; Kline, N. D.; Miller, T. A. *J. Phys. Chem. A* **2010**, *114*, 12437-12446.

(27) Dong, F.; Wang, S. F.; Kong, F. A. *J. Phys. Chem. A* **2003**, *107*, 9374-9379.

(28) Nauta, K.; Miller, R. E. *Science* **2000**, *287*, 293-295.

(29) Nauta, K.; Miller, R. E. *J. Chem. Phys.* **2001**, *115*, 10138-10145.

(30) Douberly, G. E.; Miller, R. E. *J. Phys. Chem. B* **2003**, *107*, 4500-4507.

(31) Madeja, F.; Havenith, M.; Nauta, K.; Miller, R. E.; Chocholousova, J.; Hobza, P. *J. Chem. Phys.* **2004**, *120*, 10554-10560.

(32) Douberly, G. E.; Miller, R. E. *J. Chem. Phys.* **2005**, *122*, 024306.

(33) Merritt, J. M.; Douberly, G. E.; Stiles, P. L.; Miller, R. E. *J. Phys. Chem. A* **2007**, *111*, 12304-12316.

(34) Choi, M. Y.; Douberly, G. E.; Falconer, T. M.; Lewis, W. K.; Lindsay, C. M.; Merritt, J. M.; Stiles, P. L.; Miller, R. E. *Int. Rev. Phys. Chem.* **2006**, *25*, 15-75.

(35) Lewerenz, M.; Schilling, B.; Toennies, J. P. *Chem. Phys. Lett.* **1993**, *206*, 381-387.

(36) Harms, J.; Toennies, J. P.; Dalfovo, F. *Phys. Rev. B* **1998**, *58*, 3341-3350.

(37) Knuth, E.; Schilling, B.; Toennies, J. P. *Proceedings of the 19th International Symposium on Rarefied Gas Dynamics*; Oxford University Press: London, 1995; Vol. 19.

(38) Kupper, J.; Merritt, J. M.; Miller, R. E. *J. Chem. Phys.* **2002**, *117*, 647-652.

(39) Lewerenz, M.; Schilling, B.; Toennies, J. P. *J. Chem. Phys.* **1995**, *102*, 8191-8207.

(40) Hartmann, M.; Miller, R. E.; Toennies, J. P.; Vilesov, A. *Phys. Rev. Lett.* **1995**, *75*, 1566-1569.

(41) Chin, S. A.; Krotscheck, E. *Phys. Rev. B* **1995**, *52*, 10405-10428.

(42) Scheidemann, A.; Schilling, B.; Toennies, J. P. *J. Phys. Chem.* **1993**, *97*, 2128-2138.

(43) Nauta, K.; Miller, R. E. *Phys. Rev. Lett.* **1999**, *82*, 4480-4483.

(44) Stiles, P. L.; Nauta, K.; Miller, R. E. *Phys. Rev. Lett.* **2003**, *90*, 135301.

(45) Nauta, K.; Moore, D. T.; Miller, R. E. *Faraday Discuss.* **1999**, 261-278.

(46) Morrison, A. M.; Liang, T.; Douberly, G. E. *Rev. Sci. Instrum.* **2013**, *84*, 013102.

(47) Celani, P.; Werner, H. J. *J. Chem. Phys.* **2000**, *112*, 5546-5557.

(48) Dunning, T. H. *J. Chem. Phys.* **1989**, *90*, 1007-1023.

(49) Ghigo, G.; Roos, B. O.; Malmqvist, P. A. *Chem. Phys. Lett.* **2004**, *396*, 142-149.

(50) Martin, J. M. L.; Uzan, O. *Chem. Phys. Lett.* **1998**, *282*, 16-24.

(51) Werner, H.-J. K., P. J.; Knizia, G.; Manby, F. R.; Schutz, M.; Celani, P.; Korona, T.; Lindh, R.; Mitrushenkov, A.; Rauhut, G.; Shamasundar, K. R.; Adler, T. B.; Amos, R. D.; Bernhardsson, A.; Berning, A.; Cooper, D. L.; Deegan, M. J. O.; Dobbyn, A. J.; Eckert, F.; Goll, E.; Hampel, C.; Hesselmann, A.; Hetzer, G.; Hrenar, T.; Jansen, G.; Koppl, C.; Liu, Y.; Lloyd, A. W.; Mata, R. A.; May, A. J.; McNicholas, S. J.; Meyer, W.; Mura, M. E.; Nicklass, A.; O'Neill, D. P.; Palmieri, P.; Peng, D.; Pfluger, K.; Pitzer, R.; Reiher, M.; Shiozaki, T.; Stoll, H.; Stone, A. J.; Tarroni, R.; Thorsteinsson, T.; Wang, M. MOLPRO, version 2012.1, a package of ab initio programs; 2012. 1 ed.; see http://www.molpro.net

(52) Buchenau, H.; Toennies, J. P.; Northby, J. A. *J. Chem. Phys.* **1991**, *95*, 8134-8148.

(53) Callicoatt, B. E.; Mar, D. D.; Apkarian, V. A.; Janda, K. C. *J. Chem. Phys.* **1996**, *105*, 7872-7875.

(54) PGOPHER, a Program for Simulating Rotational Structure, C. M. Western, University of Bristol, http://pgopher.chm.bris.ac.uk.

(55) Toennies, J. P.; Vilesov, A. F. *Angew. Chem., Int. Ed.*. **2004**, *43*, 2622-2648.

(56) Callegari, C.; Lehmann, K. K.; Schmied, R.; Scoles, G. *J. Chem. Phys.* **2001**, *115*, 10090-10110.

(57) Lindsay, C. M.; Miller, R. E. *J. Chem. Phys.* **2005**, *122*, 104306.

(58) Harding, L. B.; Klippenstein, S. J.; Miller, J. A. *J. Phys. Chem. A* **2008**, *112*, 522-532.

CHAPTER 4

INFRARED LASER SPECTROSCOPY OF THE HELIUM-SOLVATED ALLYL AND ALLYL PEROXY RADICALS

Infrared spectra in the C–H stretch region are reported for the allyl (CH_2CHCH_2) and allyl peroxy (CH_2=CH–$CH_2OO\cdot$) radicals solvated in superfluid helium nanodroplets. Nine bands in the spectrum of the allyl radical have resolved rotational substructure. We have assigned three of these to the ν_1 (a_1), ν_3 (a_1) and ν_{13} (b_2) C–H stretch bands and four others to the $\nu_{14}/(\nu_{15}+2\nu_{11})$ (b_2) and $\nu_2/(\nu_4+2\nu_{11})$ (a_1) Fermi dyads, and an unassigned resonant polyad is observed in the vicinity of the ν_1 band. Experimental coupling constants associated with Fermi dyads are consistent with quartic force constants obtained from density functional theory computations. The peroxy radical was formed within the He droplet *via* the reaction between allyl and O_2 following the sequential pick-up of the reactants. Five stable conformers are predicted for the allyl peroxy radical, and a computed two-dimensional potential surface for rotation about the CC–OO and CC–CO bonds reveal multiple isomerization barriers greater than $\approx$300 cm^{-1}. Nevertheless, the C–H stretch infrared spectrum is consistent with the presence of a *single* conformer following the allyl + O_2 reaction within helium droplets.

4.1 Introduction

As a resonantly stabilized radical, allyl (CH_2CHCH_2) plays an important role in the molecular weight growth chemistry that leads to the formation of ring-containing compounds and ultimately soot in combustion environments.[1-8] The resonance stabilization[9] is estimated to be ≈10 kcal·mol^{-1}, and the initially formed adducts in reactions involving allyl are therefore less strongly bound in comparison to analogous alkyl radical reactions. In general, product formation in reactions between allyl and closed shell molecules occurs relatively slowly, as these involve pathways with barriers above the reactants.[10] This is indeed the case for the allyl + O_2 addition reaction, in which the barrier to dissociation is lowest among the reaction channels involving the energized peroxy adduct (CH_2=CH–CH_2OO·). Therefore, the primary loss channels for allyl in combustion systems are self-reaction (allyl + allyl) or reactions between it and other molecular radicals. For example, the rate coefficient for self-reaction is ≈10^2 times larger than the allyl + O_2 association reaction.[7,10-12] In this study, we investigate the mid-infrared (IR) spectroscopy of both the allyl radical and the product of the allyl + O_2 addition reaction within the cryogenic environment of a helium nanodroplet.

There is a rich history associated with the spectroscopy of the $\tilde{X}\,^2A_2$ allyl radical, and this has been most recently summarized by Ellison[13] and Curl[14] and co-workers. Solid-Ar matrix isolation spectra along with polarization spectroscopy provided approximate band origins and rather definitive assignments for all IR active vibrations.[13] High resolution jet-cooled gas-phase IR spectra have been reported for the five C–H stretch fundamentals and the CH_2 symmetric wagging mode, providing accurate values for vibrational band origins and rotational constants.[14-16] From the C–H stretch gas-phase spectra, it was determined that the upper states are all

perturbed, although no definitive explanation was provided as to the nature of the perturbing states. Curl and co-workers noted that some of these perturbations are so global that the determination of rotational constants *via* least-squares fitting was significantly affected.[14] The low temperature of helium droplets allows for a reinvestigation of the C–H stretch region with sufficient resolution and sensitivity to disentangle the spectral complexity that leads to the perturbations observed in the gas-phase spectra.

Unlike allyl, the spectroscopy of the peroxy adduct is almost completely unknown. The only spectroscopic study on the allyl peroxy radical was carried out recently by Thomas and Miller,[17] where near-IR cavity ringdown spectroscopy was used to measure the $\tilde{A} \leftarrow \tilde{X}$ vibronic spectrum. Computations of torsional isomerization potentials and Frank-Condon factors for sequence band transitions allowed for rather definitive assignments to a Boltzmann distribution of at least three torsional conformers. Density functional theory (DFT) computations revealed that the conformational flexibility of allyl peroxy results in the presence of five distinct conformational isomers.[17] As an extension of this previous study in the near-IR, we report the IR spectrum in the C–H stretch region for the ground $\tilde{X}$ state of the allyl peroxy radial formed *via* the reaction between allyl and O_2 *within* a helium droplet. A *single* conformer is observed, despite large computed torsional isomerization barriers, and this is discussed in terms of the expected cooling dynamics associated with the energized peroxy adduct.

4.2 Experimental Methods

Helium droplets ($\langle N \rangle \cong 4000$) are formed in a cryogenic (T=15–17 K) nozzle expansion of high-purity He gas (30 bar) through a 5 μm diameter pinhole nozzle.[18,19] The skimmed droplet

beam passes in front of an effusive pyrolysis source,[20,21] which generates the allyl radical, formaldehyde (CH_2O) and nitric oxide (NO) *via* the thermal dissociation of 3-butenyl nitrite ($H_2C{=}CHCH_2CH_2ONO$). The pyrolysis source consists of a quartz tube heated to ≈800 K by a tantalum filament connected to water-cooled copper electrodes. With optimized conditions, the fraction of droplets doped with a single allyl radical is approximately 12%, assuming complete precursor dissociation and no radical recombination within the source, which was maintained at a relatively low pressure ($\approx 10^{-5}$ Torr). The other 88% of the droplet ensemble is either devoid of dopants or picks up other combinations of allyl, CH_2O and NO. For the allyl peroxy measurements, high-purity O_2 gas is added to a downstream, differentially pumped pick-up cell at 2×10^{-6} Torr. The fraction of droplets that sequentially pick up one allyl radical and one O_2 molecule is ≈4%.[22] The helium-solvated dopants are rapidly (<1 ns) cooled to ≈0.4 K *via* He atom evaporation.[23,24] In addition to the ≈500 He atoms required to dissipate the internal energy of the allyl and O_2 monomers, the droplet mediated allyl + O_2 addition reaction between cold reactants ($\Delta H \cong -18$ kcal·mol^{-1})[12,25-28] leads to the evaporation of ≈1250 atoms, producing an allyl peroxy radical cooled to 0.4 K.

The doped droplet beam is irradiated with the idler output from a continuous-wave optical parametric oscillator (Aculight, ARGOS 2400-SF-15), the tuning and calibration of which are described elsewhere.[29] Vibrational excitation of a helium-solvated dopant near 3000 cm^{-1} is followed by vibrational quenching and the evaporation of an additional ≈600 He atoms (≤5 cm^{-1} per evaporating He atom).[30] This laser-induced geometric cross section reduction is detected as an ion dip on selected mass channels (*vide infra*) as the depleted droplets enter into a quadrupole mass spectrometer. The idler wave of the OPO is amplitude modulated at 80 Hz with

a mechanical chopper, and the ion signal is demodulated with a lock-in amplifier and normalized to laser power, producing quasi-mass-selective, background free IR spectra.

4.3 Quantum Chemistry Computations

Geometry optimizations and harmonic frequency computations were carried out for the allyl radical and allyl peroxy conformers using Gaussian 09 at the B3LYP/cc-pVTZ level of theory.[31] The optimized geometries are shown in Figure 4.1, and the labeling scheme for the allyl peroxy conformers is adopted from that employed previously by Thomas and Miller.[17] The T, C, and G labels indicate *trans*, *cis*, and *gauche* conformations, respectively; the 1, and 2 labels indicate the OOCC (G/T ≅ ±60°/180°) and OCCC (G/C ≅ ±120°/0°) dihedral angles, respectively. The results from frequency computations are summarized in Table 4.1. The 0.964 scaling factor is the average scale factor necessary to bring into agreement the harmonic frequencies and the gas-phase C–H stretch fundamentals of the allyl radical. Cubic and quartic force constants were computed for the allyl radical at the same level using second-order vibrational perturbation theory (VPT2), as implemented in Gaussian 09.[32,33]

In previous B3LYP/cc-pVDZ computational work by Thomas and Miller,[17] relaxed potential scans were obtained by fixing the OCCC dihedral angle to either ≈0° (C_2 conformers) or ≈120° (G_2 conformers) and scanning the OOCC dihedral angle (rotation about the CC–OO bond).[17] These potential scans revealed five stable allyl peroxy conformations. We have reproduced and extended these computations at the B3LYP/cc-pVTZ level in the form of a relaxed, two-dimensional potential surface for two allyl peroxy torsional isomerization coordinates (OCCC and OOCC dihedral angles; Figure 4.2). The relative zero-point corrected

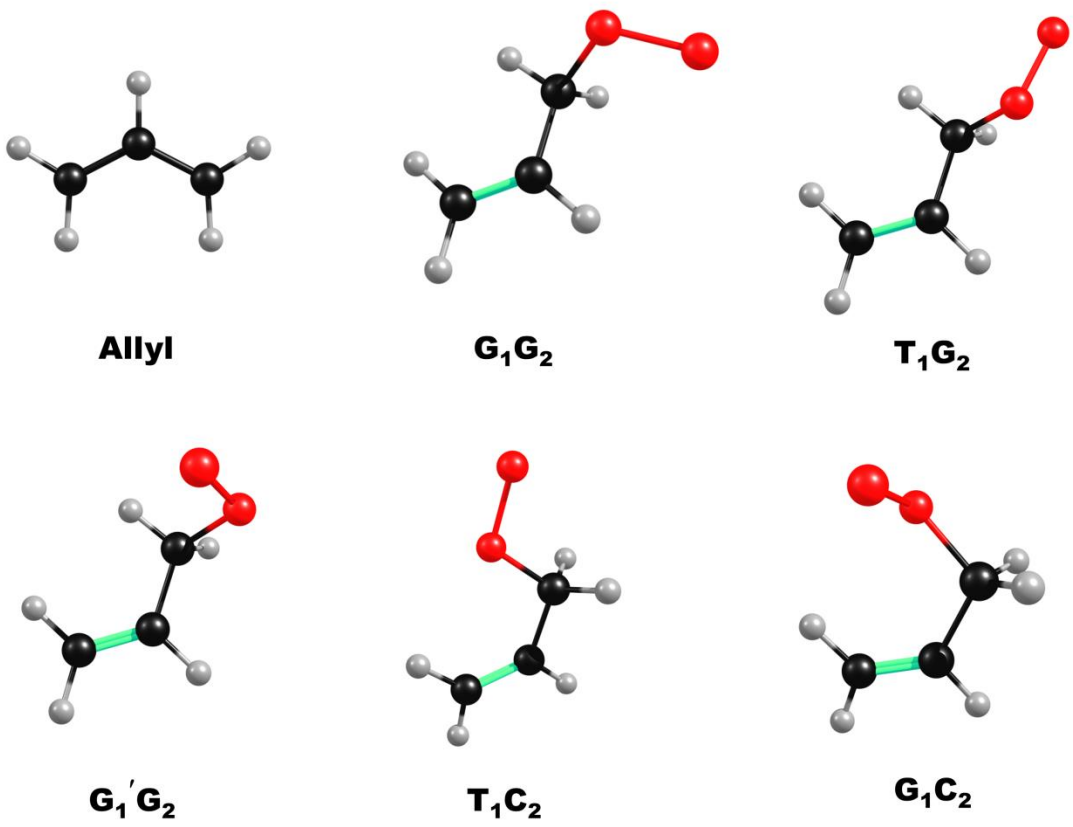

Figure 4.1: The allyl radical and allyl peroxy radicals computed at the B3LYP/cc-pVTZ level of theory. **T**, **C**, and **G** labels indicate *trans*, *cis*, and *gauche* conformations, respectively; **1** and **2** labels indicate the OOCC (**G**/**T** ≅ ±60°/180°) and OCCC (**G**/**C** ≅ ±120°/0°) dihedral angles, respectively.

energies of the conformers at this level of theory are given in Table 4.1. The relative energies of the five conformers are within ≈310 cm^{-1} (0.88 $kcal \cdot mol^{-1}$), with the G_1G_2 conformer representing the lowest energy configuration. Given this relatively small energy range, it is reasonable to question whether or not the energy ordering is accurately predicted at this level of theory. However, simulations that assume conformer Boltzmann weights computed at the composite G2 level of theory[34] qualitatively reproduce the near-IR spectra obtained with room

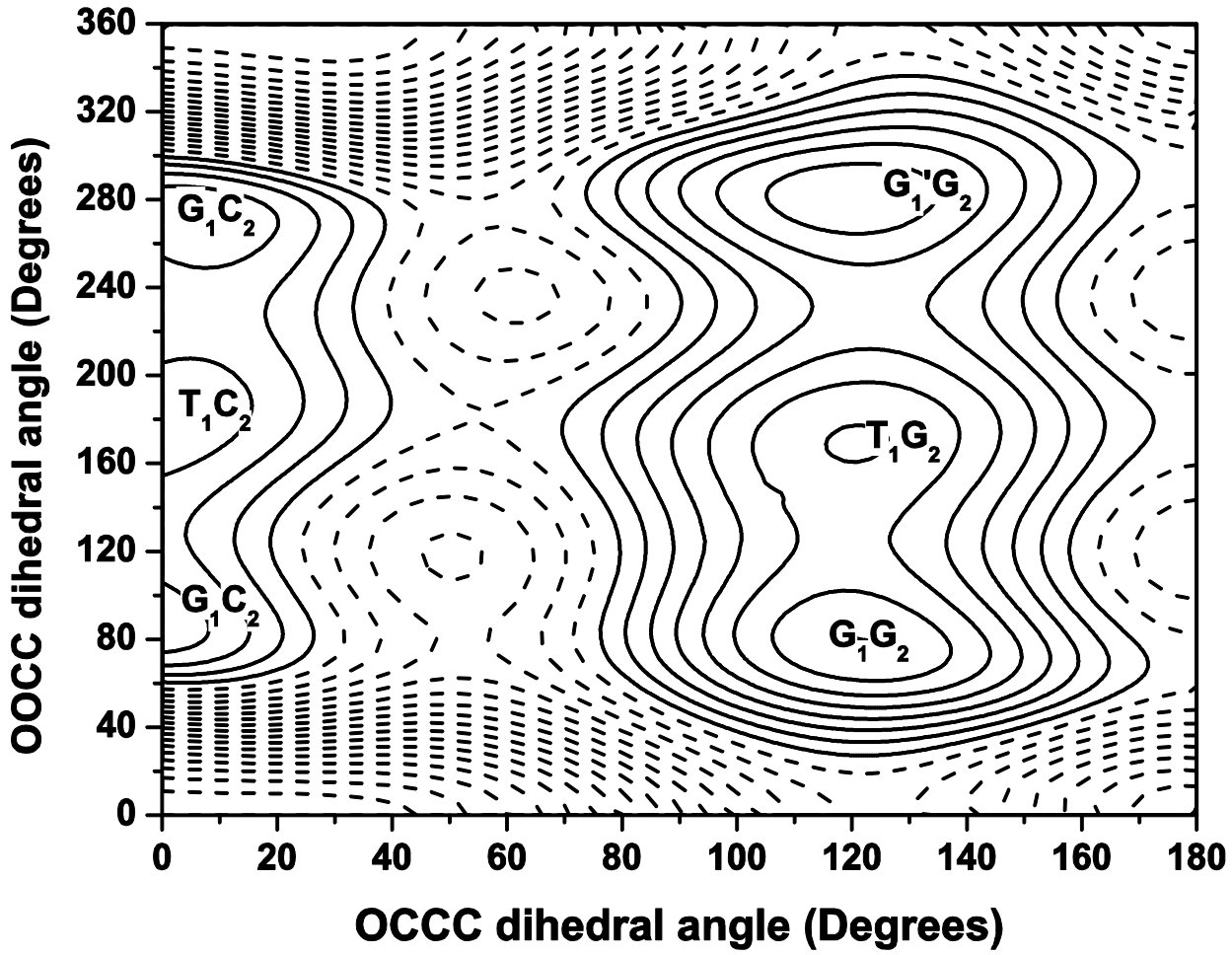

Figure 4.2: B3LYP/cc-pVTZ, two-dimensional, relaxed (geometry optimized at each point) potential energy surface for rotation about the CC–CO and CC–OO bonds in the allyl peroxy radical. The contour spacing is 100 cm^{-1}. The $\mathbf{G_1G_2}$ minimum is at 0 cm^{-1}, and contours above 700 cm^{-1} are shown as dashed lines. **T**, **C**, and **G** labels indicate *trans*, *cis*, and *gauche* conformations, respectively; **1** and **2** labels indicate the OOCC (**G**/**T** ≅ ±60°/180°) and OCCC (**G**/**C** ≅ ±120°/0°) dihedral angles, respectively.

Table 4.1: C–H stretching band frequencies (cm^{-1}) at the B3LYP/cc-pVTZ level of theory.

Allyl Peroxy								
			G_1G_2	T_1G_2	$G_1'G_2$	T_1C_2	G_1C_2	
			ΔE = 0	49	126	284	308	
Allyl			(0) [a]	(83)	(105)	(258)	(186)	
ω_{scaled} [b]	Γ_v	ν_0 gas [c]	ω_{scaled} [b,d]					ν_0 He [e]
3016 (12)	a_1	3023.46	2948 (16)	2941 (10)	2946 (19)	2923 (12)	2929 (18)	2952 (0.82)
3024 (8)	b_2	3020.32	3005 (5)	2992 (8)	3006 (4)	2958 (11)	2973 (5)	3003 (0.93)
3030 (5)	a_1	3033.87	3021 (7)	3023 (7)	3024 (8)	3027 (8)	3023 (10)	3030 (0.29)
3118 (5)	b_2	3110.60	3045 (2)	3040 (5)	3039 (7)	3041 (4)	3041 (3)	
3120 (17)	a_1	3113.98	3103 (9)	3105 (10)	3105 (10)	3120 (5)	3119 (5)	3101 (1)

[a] Zero-point corrected relative energies of peroxy radical conformers (cm^{-1}). The relative energies at the CCSD(T)/cc-pVTZ//B3LYP/cc-pVTZ level are given in parentheses. The harmonic frequencies obtained at the B3LYP/cc-pVTZ level were used to zero-point correct the relative CCSD(T) energies.

[b] Scaling factor: 0.964; Intensities in parentheses (km/mol).

[c] References 14 and 15.

[d] Γ_v=*a*.

[e] The most intense bands observed in the droplet spectrum (allyl + O_2; Figures 4.4d and 4.4e) with relative intensities presented in parentheses.

temperature cavity ringdown spectroscopy.[17] At the G2 level, the G_1G_2 conformer is also the lowest energy structure and the five conformers again span an energy range of ≈310 cm^{-1}.[17] At the B3LYP/cc-pVTZ equilibrium geometries, single point energy computations at the CCSD(T)/cc-pVTZ level indicate that the global minimum and relative energy spacing is qualitatively preserved with the more accurate treatment of electron correlation effects, although the ordering of the higher energy conformers is changed (Table 4.1). The isomerization barriers at the B3LYP/cc-pVTZ level are relatively small for rotation about the CC–OO bond, with the $G_1'G_2$ to G_1G_2 interconversion barrier being the largest at ≈300 cm^{-1}. However, the minimum energy pathway for rotation about the CC–CO bond (G_1C_2 to G_1G_2 interconversion) has an associated barrier that is considerably larger at ≈900 cm^{-1}.

4.4 Results

The scheme by which conditions are optimized for the spectroscopic study of allyl and allyl peroxy radicals is illustrated in Figure 4.3 (mass spectra) and Figure 4.4 (IR spectra). Electron impact ionization of the neat droplet beam results in a series of peaks in the mass spectrum associated with He_n^+ cluster ions (blue curve, Figure 4.3a).[35] The upper mass spectrum in Figure 4.3a (black curve) is measured with the 3-butenyl nitrite precursor flowing effusively through the room-temperature pyrolysis source. Helium solvation of the precursor and its subsequent transport into the mass spectrometer leads to additional peaks that arise from the charge transfer ionization reaction:

$$He^+ + CH_2{=}CHCH_2CH_2ONO$$

$$\rightarrow (CH_2{=}CHCH_2CH_2ONO)^+ + He$$

$$\rightarrow (CH_2{=}CHCH_2CH_2ONO)^+_{fragments} + He. \qquad \textbf{(Eq. 4.1)}$$

The He^+ ion is formed upon electron bombardment of the droplet and subsequently ionizes the solvated dopant molecule. Because the difference in the 3-butenyl nitrite and He ionization potentials is ≈15 eV, fragmentation of the hot molecular ion is expected, and these fragments are desolvated from the droplets and detected in the mass spectrometer. The most notable fragments of the ionized precursor molecule are *m*/*z*=27 $(C_2H_3)^+$, 29 $(C_2H_5)^+$, 30 $(CH_2O)^+/(NO)^+$, 39 $(C_3H_3)^+$, and 41 u $(C_3H_5)^+$. Figures 4.3b and 4.3c show the evolution of the mass spectrum as the pyrolysis source is heated from 300 to ≈800 K. As observed previously in our study of the propargyl peroxy radical,[21] the signature of near complete pyrolytic decomposition of the nitrite precursor is the appearance of an intense peak at *m*/*z*=30 u, which results from the droplet pickup and ionization of NO or CH_2O. Moreover, the mass spectrum obtained with high-temperature pyrolysis conditions contains peaks at *m*/*z*=27, 28, 29 and 39 u, which are due apparently to the He^+ charge transfer ionization of helium-solvated allyl radicals, whereas *m*/*z*=41 u is depleted by about a factor of three upon heating the source. Other than the appearance of an intense peak at 32 u, the mass spectrum is relatively unchanged following the addition of O_2 to the downstream pick-up cell (Figure 4.3d).

Near complete dissociation of the precursor within the pyrolysis source is also evident from the IR spectra measured on mass channel *m*/*z*=39 u. The bands observed in the 2910 to 3120 cm^{-1} region are associated with the various C–H stretch vibrations of the nitrite precursor (Figure 4.4a), and these are clearly depleted as the source temperature is increased from 300 to

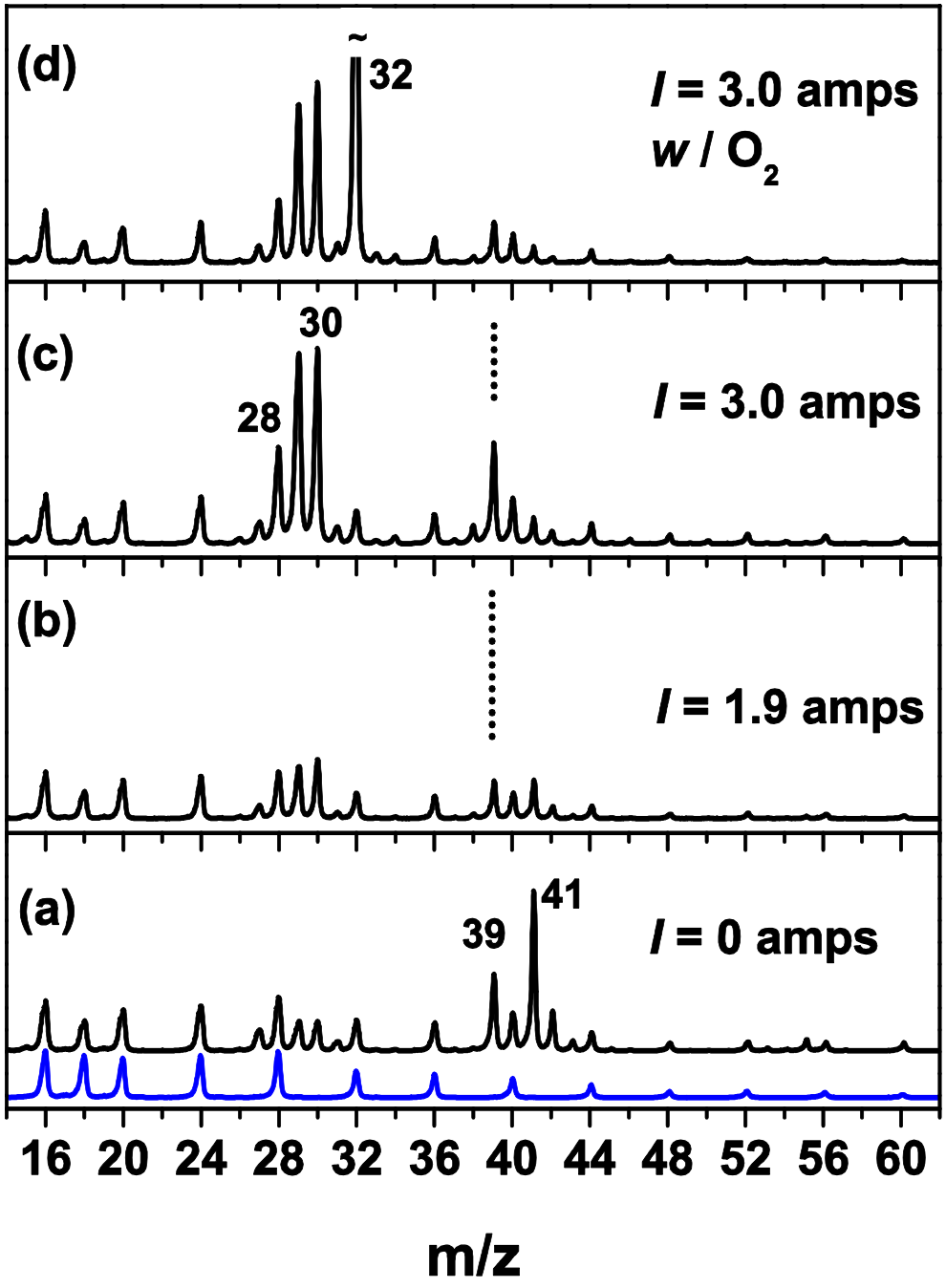

Figure 4.3: Evolution of droplet beam mass spectrum as conditions are adjusted to produce helium-solvated allyl and allyl peroxy radicals. (a) mass spectra of the neat droplet beam (blue) and the droplet beam with 2-butenyl nitrite flowing effusively through the room temperature pyrolysis source (black). (b) Mass spectrum upon passing 1.9 amps through the pyrolysis source tantalum filament (≈500 K). (c) Mass spectrum with the pyrolysis source at 3.0 amps (≈800 K). (d) Mass spectrum with the pyrolysis source at 3.0 amps and with O_2 added to the downstream pick-up cell (2×10^{-6} Torr).

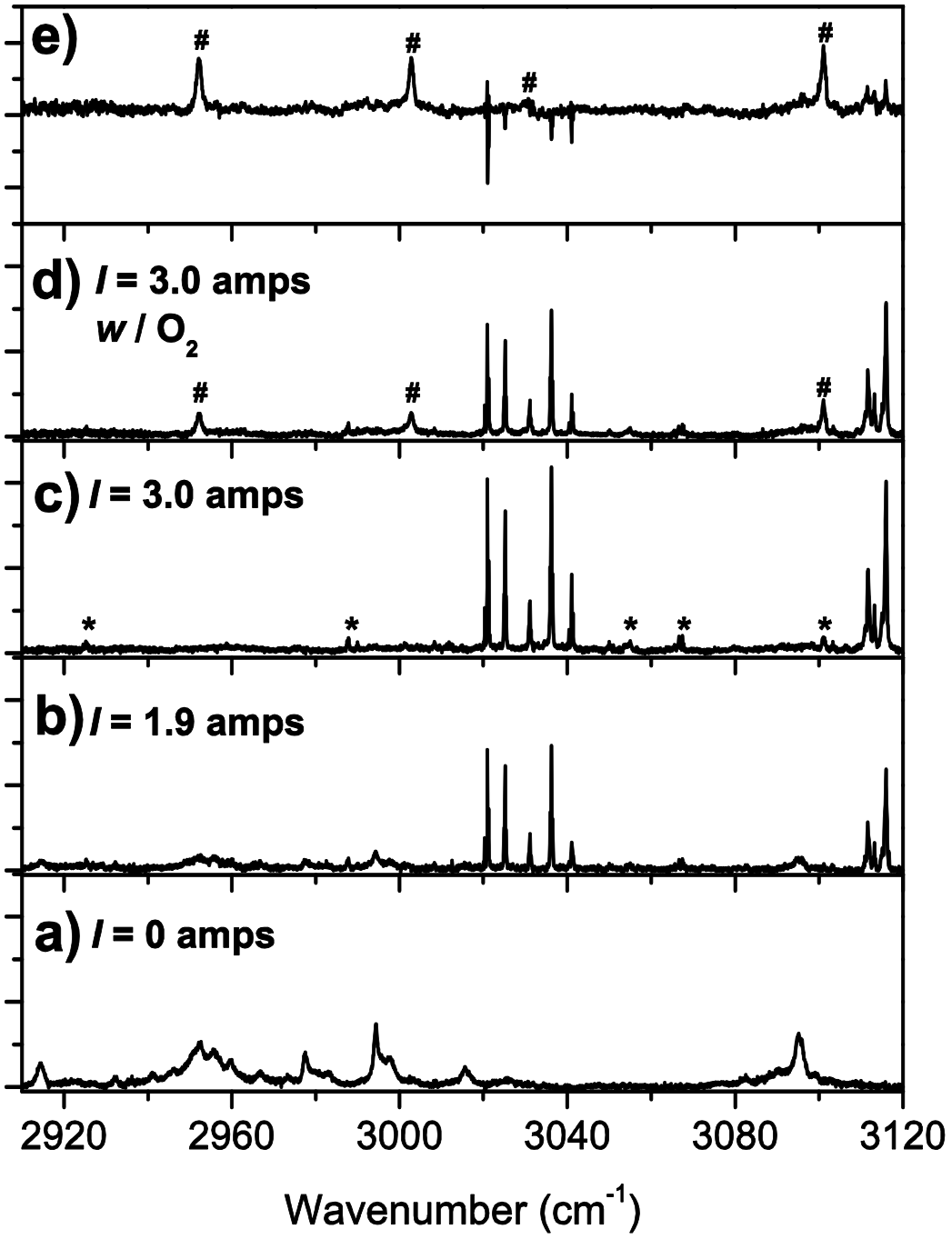

Figure 4.4: Infrared spectra of the droplet beam measured as ion depletion in mass channel *m*/*z* = 39 u. Each spectrum, (a) through (d), was obtained under identical experimental conditions used to record the mass spectra in Figures 4.3a through 4.3d. Bands associated with allyl + NO (or CH_2O) adducts are marked by *, and bands assigned to the allyl peroxy radical are marked by #. The difference spectrum (e) is obtained by subtracting (c) from (d); both (c) and (d) spectra were normalized to the most intense allyl transition located at 3034.28 cm^{-1}. There is some residual transition intensity from allyl bands in (e) due to the performed subtraction.

≈800 K (Figures 4.4b and 4.4c). Upon thermal decomposition of the precursor, a sharper series of bands in the 3020 to 3040 cm^{-1} and 3110 to 3120 cm^{-1} regions appear (Figures 4.4b and 4.4c), and some of these are within 1 cm^{-1} of the band origins previously reported for the gas-phase[14,15,36] allyl radical. A number of weaker features are observed that can be assigned to the allyl nitrosyl[37] or allyl + CH_2O reaction products, as about 5-10% of the droplet ensemble is expected to sequentially pick up the allyl radical and either NO or CH_2O. These features are marked by asterisks in Figure 4.4c. The addition of O_2 to the downstream pick-up cell leads to a series of relatively intense bands in the IR spectrum that are shifted from the allyl radical transitions (*e.g.* 2952, 3002 and 3102 cm^{-1}), and these are assigned to allyl peroxy radicals (*vide infra*) (Figure 4.4d). Test scans on several different mass channels indicate that ion-signal depletion on m/z=39 u provides the highest sensitivity spectra for both the allyl and allyl peroxy radicals. Furthermore, we found that mass channels 38 u and 41 u were also satisfactory for the allyl and 3-butenyl nitrite precursor spectra, respectively.

With the C_{2v}(M) permutation inversion group, it is readily shown that, at 0.4 K, the ensemble of allyl radicals is cooled mostly to the lowest rotational levels of each nuclear spin isomer, namely the 0_{00} and 1_{01} levels. The spin degeneracies of these rotational levels are 10 (K_a+K_c=even) and 6 (K_a+K_c=odd), respectively. At the droplet temperature, the 2_{02} level has a Boltzmann weight ($N(2_{02})/N(0_{00})$) equal to 0.03, whereas all other rotational levels have weights less than 0.0003. For each vibrational band, we therefore expect any resolved rotational structure to be rather simple, consisting of only a few intense transitions. Because the *b*-inertial axis lies along the C_2 axis of the allyl radical and the *a*-axis is in the plane of the molecule (Figure 4.5 inset), the a_1 and b_2 symmetry vibrational bands are *b*-type and *a*-type, respectively. Higher resolution scans of features in Figure 4.4c reveal nine vibrational bands that can be

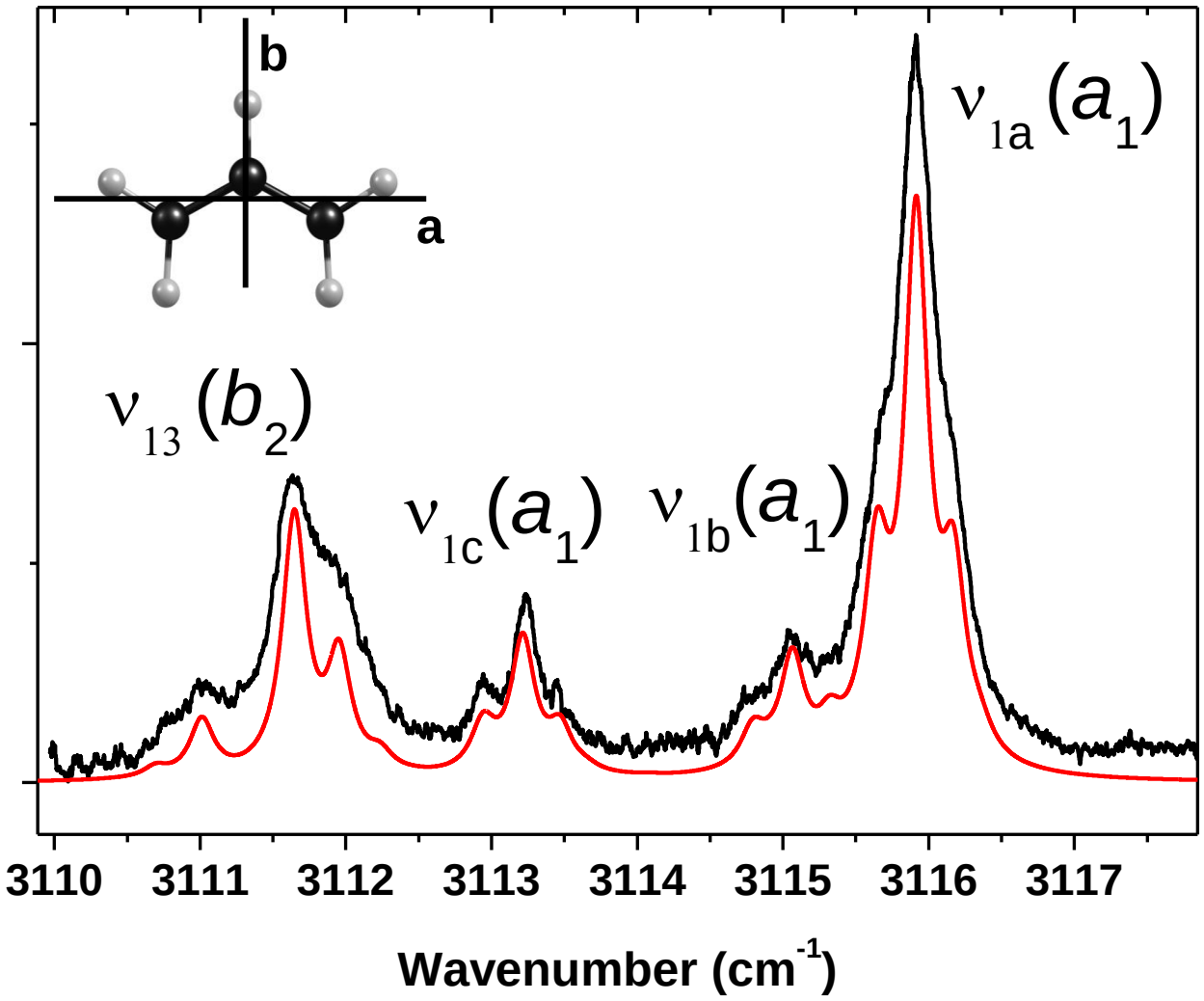

Figure 4.5: Higher resolution scan in the region of the ν_1 and ν_{13} fundamental bands of the allyl radical. The smooth red line is a composite simulation of all four bands using the constants reported in Table 4.2. The symmetry of each vibration is determined by the band type (a_1: *b*-type, b_2: *a*-type). The inset shows the inertial axes of the allyl radical.

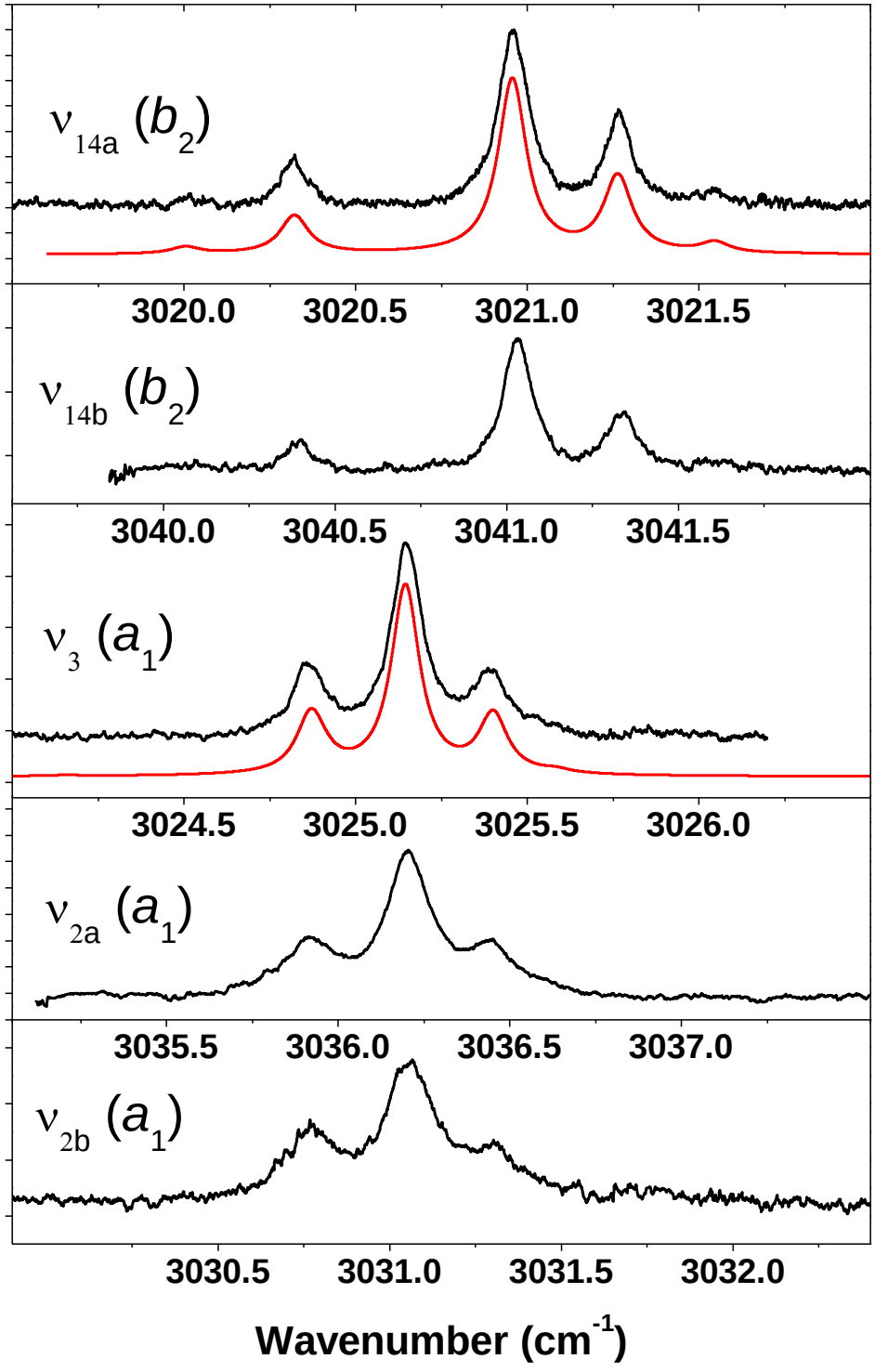

Figure 4.6: Higher resolution scans in the region of the ν_2, ν_3, and ν_{14} fundamental bands of the allyl radical. The smooth red lines are simulations using the constants reported in Table 4.2. The symmetry of each vibration is determined by the band type (a_1: *b*-type, b_2: *a*-type).

assigned to the allyl radical, and each of these bands is given a symmetry label based on the associated rotational substructure. The 3110 to 3118 cm^{-1} region is shown in Figure 4.5 and contains four bands, two of which can be assigned to the ν_1 (a_1) and ν_{13} (b_2) fundamental bands. These two bands correspond to the excitation of in-phase and out-of-phase antisymmetric stretching of the CH_2 subunits, respectively. These assignments are motivated by the small band origin shifts from the gas-phase spectra (<1 cm^{-1}) and the partially resolved rotational substructure that clearly indicates each band type. Higher resolution scans of the other five bands assigned to the allyl radical are shown in Figure 4.6. The bands centered at 3020.64, 3023.25, and 3034.28 cm^{-1} are very close to the origins of gas-phase bands previously assigned to the ν_{14} (b_2), ν_3 (a_1), and ν_2 (a_1) fundamental bands associated with the excitation of the out-of-phase symmetric CH_2, lone CH, and in-phase symmetric CH_2 stretching motions, respectively.[14] The symmetry types of these three bands in the droplet spectrum are completely consistent with an assignment that follows the frequency ordering determined previously from the gas-phase study,[14] and this again implies that the allyl radical band origins are shifted by less than 1 cm^{-1} upon helium-solvation. In addition to the five bands assigned to fundamentals in the gas-phase study, the other four bands in Figures 4.5 and 4.6 can also be confidently assigned to the allyl radical (3029.48 (a_1), 3040.72 (b_2), 3111.30 (a_1), and 3113.15 cm^{-1} (a_1)). Indeed, the rotational substructure of all nine bands can be satisfactorily simulated with a consistent set of rotational constants (*vide infra*), which provides strong support to the assignment of these four previously unreported bands to the allyl radical. Tentative assignments of two of these four bands are suggested on the basis of DFT force field computations, as discussed below. The assignments, band origins, and parameters used for the band simulations are summarized in Table 4.2.

The spectrum in Figure 4.4d was measured with O_2 (2×10^{-6} Torr) added to the differentially pumped pick-up cell located downstream from the pyrolysis source. The O_2 pressure was adjusted slightly below the optimal pressure for the pick-up of single O_2 molecules, which renders cluster formation (pick-up of multiple O_2 molecules) essentially negligible. Based on Poisson statistics,[22] at the experimental pressure of the pick-up cell, the probability associated with doping of a single droplet with an allyl radical and multiple O_2 molecules is <0.5%. Three distinct spectral features at 2952, 3003, and 3101 cm^{-1} grow in upon O_2 addition, along with weaker features in the baseline around these bands. Moreover, broader features are also observed in the 3020-3040 cm^{-1} region underneath the allyl radical bands. The spectra with (Figure 4.4d) and without (Figure 4.4c) the addition of O_2 were subtracted, revealing more clearly the bands that are associated with the allyl peroxy radicals (Figure 4.4e). All of these bands lack resolved rotational substructure and are instead nearly Lorentzian with full-width at half-maximum line widths of ≈1 cm^{-1}. These line widths are all broader than the expected rotational contours for allyl peroxy radicals at ≈0.4 K and are likely due to a homogeneous broadening mechanism associated with the inelastic/elastic decay of the vibrational resonance (τ ≈ 5 ps). Bands assigned to allyl peroxy radicals are compared to scaled harmonic frequency computations for the five lowest energy conformations in Table 4.1.

4.5 Discussion

4.5.1 $\tilde{X}\ ^2A_2$ Allyl radical spectrum

Because of the low rotational temperature and limited number of transitions, it is difficult to determine with much precision the effective rotational constants for the helium-solvated allyl radical. For example, the *A* rotational constant cannot be determined because there is effectively no population in rotational levels with $K_a \geq 1$. Moreover, combination differences do not allow for a determination of $(B+C)/2$ (abbreviated $\bar{B}$). Nevertheless, we have estimated the effective $\bar{B}'$ constant for each band by fixing $(B'-C')$ to its gas-phase value, in order to reduce the number of adjustable parameters. To obtain satisfactory agreement between the experimental and simulated spectra, the $\bar{B}'$ constants must be reduced to half the value of $\bar{B}'_{\text{gas}}$. This factor of two reduction is consistent with the $B_{\text{gas}}/B_{\text{He}}$ ratios observed for many other small helium-solvated molecules.[38-40] Including a single D_J' distortion constant brings both the *a*- and *b*-type simulations into excellent agreement with experiment. Despite the limited number of transitions, the vibrational band origins are determined to better than ± 0.01 cm^{-1} for the three *a*-type bands, although the reported band origins for the six *b*-type bands necessarily represent lower limits (we assume $A_{\text{He}}=A_{\text{gas}}$). Reducing the A_{He} rotational constant to $A_{\text{gas}}/2$ has the effect of increasing the *b*-type band origins by ≈ 0.3 cm^{-1}. The relative intensities of transitions within each band are consistent with a rotational temperature of 0.35 K, and the individual transitions are approximately Lorentzian with ≈ 0.1 cm^{-1} line widths.

Table 4.2: Allyl radical rotational constants and vibrational band origins (cm^{-1}).

	Γ_v	$\nu_0^{He,a}$	$\bar{B}^{He}$	$(B-C)^{He}$	D_J^{He}		$\nu_0^{gas,b}$	$\bar{B}^{gas,b}$	$(B-C)^{gas,b}$	$\nu^{matrix\ c}$
ν_{1a}	a_1	3114.00 [0.57]	0.165	0.055	0.006	ν_1	3113.98	0.318	0.056	3109
ν_{1b}	a_1	3113.15 [0.13]	0.165	0.055	0.006					
ν_{1c}	a_1	3111.30 [0.13]	0.165	0.055	0.006					
ν_{2a} [d]	a_1	3034.28 [1]	0.165	0.055	0.006	ν_2	3033.87	0.318	0.056	3052
ν_{2b} [d]	a_1	3029.48 [0.16]	0.165	0.055						
ν_3	a_1	3023.25 [0.26]	0.165	0.055	0.006	ν_3	3023.46	0.318	0.055	3027
ν_{13}	b_2	3111.33 [0.39]	0.159	0.055	0.0003	ν_{13}	3110.60	0.318	0.056	3107
ν_{14a} [e]	b_2	3020.64 [0.31]	0.159	0.055	0.0003	ν_{14}	3020.32	0.318	0.054	3020
ν_{14b} [e]	b_2	3040.72 [0.16]	0.159	0.055	0.0003					3040 [f]

[a] Band origins of a_1 symmetry vibrations (*b*-type bands) are determined by assuming the *A* rotational constant is unchanged in going from the gas-phase to helium and therefore represent lower limits. Band origins of b_2 symmetry vibrations (*a*-type bands) have an uncertainty less than $\pm 0.01\ cm^{-1}$. Relative intensities are given in square brackets.

[b] References 14 and 15.

[c] Reference 13.

[d] $\nu_2/(\nu_4+2\nu_{11})$ Fermi dyad.

[e] $\nu_{14}/(\nu_{15}+2\nu_{11})$ Fermi dyad.

[f] Assigned previously to the cyclopropyl radical.[13]

Along with the five bands assigned to the allyl radical C–H stretch fundamentals (ν_1, ν_2, ν_3, ν_{13}, ν_{14}), the relative intensities of the four other partially resolved bands behave similarly with experimental conditions. Furthermore, the rotational structure strongly suggests an assignment of these previously unreported bands to the allyl radical. Although the gas-phase spectra in the C–H stretch region have been assigned *only* to the five fundamentals, the rotationally resolved bands of the isolated species exhibit both local and global perturbations. These, however, were not assigned definitively to specific interactions, although it was noted that the ν_1 (a_1) and ν_{13} (b_2) levels can interact *via* a *c*-axis Coriolis perturbation.[14,15,36]

As a possible alternative assignment of the four previously unreported bands, we have considered the impurities that may arise due to allyl radical recombination reactions within the pyrolysis source. For example, under high-temperature conditions, Ellison and co-workers found that the pyrolysis of allyl iodide produced weak features in the solid-Ar matrix IR spectrum that could be assigned to 1,5-hexadiene, allene, and propene.[13] The allene and propene impurities are due to the disproportionation of two allyl radicals, and 1,5-hexadiene is the allyl dimerization product. We have systematically ruled out all three of these species as possible carriers of the four unassigned bands *via* the known gas-phase IR spectra of these species, and in general, with our low pressure source conditions, the production of these species from the pyrolysis of 3-butenyl nitrite appears to be largely negligible. Interestingly, Ellison and co-workers observed a strong feature at 3040 cm^{-1} in the matrix spectrum that they assigned to the cyclopropyl radical,[13] a cyclic C_3H_5 isomer, which forms presumably *via* ring closing in the hot pyrolysis source. Indeed, the *a*-type band in the droplet spectrum centered at 3040.72 cm^{-1} is within 0.1 cm^{-1} of the $\nu_7^+ \leftarrow 0^+$ band origin of the jet-cooled cyclopropyl radical (3040.676 cm^{-1}).[41] However, this cyclopropyl band is purely *b*-type, and we can therefore rule out this assignment.

It is also interesting to note that the linear dichroism spectra[13] of the matrix isolated sample indicates that this 3040 cm^{-1} band has b_2 symmetry, assuming an assignment to a C_{2v} species, which is consistent with the *a*-type rotational substructure observed in the droplet spectrum. It is more difficult to compare other weaker features in the matrix spectrum to the bands observed here due to unknown matrix shifts and line broadening effects.

Given the observed rotational substructure and other experimental evidence, it is reasonable to assign the four newly observed bands to the allyl radical, and these are therefore likely to be derived from either strong combination/overtone bands or transitions that gain intensity *via* resonance interactions between the fundamental modes and nearby dark levels. From the matrix isolation spectrum, we can estimate the wavenumbers (neglecting anharmonicity) of the highest energy overtone and combination bands that consist of two quanta of excitation, namely $2\nu_4$ (a_1, 2956 cm^{-1}) and $\nu_4+\nu_{15}$ (b_2, 2942 cm^{-1}), which are associated with the symmetric (ν_4 (a_1)) and antisymmetric (ν_{15} (b_2)) CH_2 scissor modes. Assuming the ν_4 and ν_{15} fundamentals are not significantly red shifted by the matrix (no more than ≈30 cm^{-1}), the bands to the blue of 3020 cm^{-1} in the droplet spectrum are well above the combination and first overtone levels of ν_4 and ν_{15}. The four newly observed bands must therefore be associated with combination or overtone levels consisting of three or more quanta of excitation. However, in the absence of resonance interactions, these higher-order combination and overtone bands might not be expected to have nearly half the average intensity of the C–H stretch fundamentals, as observed experimentally. It is more likely that the weaker bands in the droplet spectrum are the result of anharmonic resonance interactions involving the dark levels and the bright C–H stretch fundamentals.

From the relative intensities of the two lower energy *a*-type bands and their energy separation, the magnitude of the matrix element coupling the b_2 symmetry dark level to the ν_{14} fundamental is estimated to be ≈8 cm^{-1} (assuming a two-state interaction). Similarly, the *b*-type band at 3029.5 cm^{-1} can be rationalized by the coupling of an a_1 symmetry dark level to either the ν_2 or ν_3 fundamental with a matrix element equal to ≈2 cm^{-1}. It is difficult to pin down the exact levels involved in these apparent Fermi type perturbations, because the state density in the 3020 to 3120 cm^{-1} region is ≈1.2 states per cm^{-1}, and there are many symmetry allowed interactions involving states that differ by several quanta in the zeroth order description. We can, however, suggest assignments that are based on anharmonic frequency computations at the B3LYP/cc-pVTZ level of theory. The lowest order, symmetry allowed, nearly resonant interactions involving C–H stretch fundamentals are $\nu_2/(\nu_4+2\nu_{11})$ and $\nu_{14}/(\nu_{15}+2\nu_{11})$, and the φ_{iijk} quartic force constants associated with the coupling of these levels are computed to be ≈10 cm^{-1}. This suggests an assignment of the *a*-type bands at 3020.64 and 3040.72 cm^{-1} to the $\nu_{14}/(\nu_{15}+2\nu_{11})$ (b_2) Fermi dyad, and these are labeled in Figure 4.6 and Table 4.2 as ν_{14a} and ν_{14b}. Similarly, the 3029.48 and 3034.28 cm^{-1} *b*-type bands are assigned to the $\nu_2/(\nu_4+2\nu_{11})$ (a_1) Fermi dyad (ν_{2a} and ν_{2b}). The appearance of multiple *b*-type bands in the 3111 to 3116 cm^{-1} range perhaps indicates a multiple resonance involving the ν_1 (a_1) fundamental (ν_{1a}, ν_{1b}, and ν_{1c}). However, there are relatively few states with three quanta of excitation in this vicinity to which the ν_1 mode can resonantly couple *via* an interaction of the form $\langle 210|\varphi_{iijk}|001\rangle$, and provided the limited information available from the VPT2 computation (third and semi-diagonal fourth derivatives of the potential), we are left to speculate as to the origin of the resonance polyad evident in this spectral region.

4.5.2 $\tilde{X}\ ^2A$ Allyl peroxy radical spectrum

The approximately 1 cm^{-1} broad bands in Figures 4.4d and 4.4e are assigned to the C–H stretch fundamentals of the allyl peroxy radical. In comparison to the allyl radical, the peroxy radical C–H stretch bands are broader by about a factor of 10. The comparatively broader peroxy radical bands are consistent with the larger vibrational state density in this energy regime, which apparently results in efficient vibrational energy decay (either elastic or inelastic) that is fast in comparison to the rotational period of the molecule. Unfortunately, the lack of rotational fine structure makes the spectral assignments somewhat less definitive, in comparison to the allyl radical spectrum. Indeed, the assignments reported here are simply derived from the results of harmonic frequency and relative energy computations for the various conformers, as well as the response of the bands to the presence of O_2.

The scaled harmonic frequencies for the five allyl peroxy conformers are given in Table 4.1. Each conformer has five C–H stretch vibrations, and these can be described as symmetric CH_2 (sp^3 carbon), antisymmetric CH_2 (sp^3 carbon), symmetric CH_2 (sp^2 carbon), lone CH (sp^2 carbon), and antisymmetric CH_2 (sp^2 carbon), from low to high energy, respectively. Bands at 2952, 3003, 3030, and 3101 cm^{-1} in the droplet spectrum agree rather well with the scaled harmonic frequencies computed for the above vibrations, especially for the conformers that have OCCC dihedral angles equal to approximately ±120° (*i.e.* the G_1G_2, T_1G_2 and $G_1'G_2$ conformers; G_2-conformers). Given the line widths of the allyl peroxy bands in the droplet spectrum, we expect the bands associated with the C_2 and G_2 type conformers to be resolved, assuming the computed isomerization induced frequency shifts. For example, isomerization from a C_2 to G_2 configuration results in a ≈20 cm^{-1} blue shift of the lowest frequency C–H

stretch band. Based on the agreement between the experimental bands and scaled harmonic frequency computations, an assignment of the spectrum in Figure 4.4e to a G_2 type allyl peroxy conformer is reasonable, and the relative intensities suggest specifically an assignment to the T_1G_2 conformer. We emphasis again that the relative energetics of the three G_2 conformers are computed to be within 100 cm^{-1}, making it rather difficult to justify any assignment to a specific conformer. Moreover, some of the predicted conformer to conformer frequency shifts (*e.g.* between G_1G_2 and $G_1'G_2$) are rather small. Nevertheless, from the difference spectrum shown in Figure 4.4e, it appears that a *single conformation* dominates the ensemble, although we note that there are a few reproducible, weaker features near the more prominent ones. Therefore, although we assign here the allyl peroxy spectrum to a *single* helium-solvated G_2-conformer, we cannot completely rule out the presence of a smaller fraction of the other conformers.

Given the magnitude of the barrier heights for torsional isomerization, it is perhaps surprising that the allyl + O_2 reaction carried out *within* a He droplet leads to a single conformer, which is presumably the lowest energy conformer. Of course, in the limit of slow vibrational cooling, the system would "anneal" to the global minimum, and only the lowest energy conformer would be present at equilibrium in the 0.4 K droplet ensemble. However, the rate of energy dissipation *via* He atom evaporation has been shown to be sufficiently rapid to kinetically trap non-global minimum conformations of many other species, such as 2-chloroethanol,[42] tryptophan,[43] and tyrosine.[43] In these cases, the intact gas-phase molecules were picked-up by the droplets, and the equilibrium conformer distribution at the vapor temperature was largely preserved upon cooling to 0.4 K.[44,45] Moreover, as molecular *cluster* systems condense within He droplets, metastable structures are often kinetically trapped behind small isomerization barriers (greater than about 100 cm^{-1}),[39,40,46-48] although there are notable exceptions.[49,50] For

these systems, the sequential pick-up process results in *cold* monomers that condense and produce relatively small amounts of intermolecular vibrational kinetic energy, which can be effectively dissipated prior to cluster rearrangement.

The bond-forming reaction discussed here is quite different from either of the above processes. The reaction between allyl and O_2 produces ≈18 kcal·mol^{-1} (9100 K) of internal vibrational energy. The IR spectrum suggests that the peroxy radical is *funneled* into a G_2-type conformation as this vibrational energy is dissipated by He atom evaporation. We postulate that this results from the more closely spaced (<100 cm^{-1}) torsional levels being more efficiently relaxed (as a result of stronger coupling to droplet phonon modes) in comparison to the higher frequency stretching/bending vibrations. This is motivated by recent spectroscopic studies of vibronic bands of substituted anthracene derivatives[51] and hydridotrioxygen (HOOO)[52] in which torsional excitation was accompanied by a homogeneous line broadening consistent with dampening on the sub-ps timescale. Because the allyl + O_2 reaction leads to a vibrationally hot system containing multiple quanta of stretch/bend excitation, the isomerization barriers will be initially small, and if the more closely spaced torsional states relax faster, the system could funnel into one conformational minimum as it cascades down the ladder of excited stretching/bending levels. For example, in the excited ν_{18} level (largely C–O stretch; 850 cm^{-1}), the vibrationally adiabatic potential surface for rotation about the CC–OO bond is computed (B3LYP/cc-pVTZ) to be less anisotropic in comparison to the ground state surface in Figure 4.2. The minimum energy pathways for torsional isomerization are expected to become even less anisotropic with increasing C–O stretch excitation because of the larger $\langle r_{CO} \rangle$ expectation values associated with the excited vibrational levels. It is reasonable to expect bound states to appear first near the global minimum region of the ground vibrational state torsional potential as the

higher frequency vibrations of the hot system are relaxed; this could explain the dominance of a single G_2 type conformer in the droplet spectrum. It would be worthwhile to test these ideas by computing the vibrationally adiabatic potential surface for rotation about the CC–OO bond with various degrees of vibrational excitation. Of course, much of this discussion is necessarily qualitative, as the true relaxation dynamics occur on a multidimensional potential surface coupled to the bath of excitations provided by the droplet. The allyl + O_2 reaction therefore presents a particularly challenging system for theoretical methods that aim to understand the cooling dynamics of molecular systems in liquid He droplets.

4.6 Summary

The allyl radical (CH_2CHCH_2) is produced from the pyrolytic decomposition of 3-butenyl nitrite and cooled to 0.4 K in liquid He droplets. Nine partially resolved rovibrational bands are observed with IR laser spectroscopy in the C–H stretch region. Solvent induced vibrational frequency shifts are observed to be small (<1 cm^{-1}), and the $(B+C)/2$ rotational constants are reduced by about a factor of two in going from the gas phase to He droplets, both of which are consistent with previous measurements of other helium-solvated hydrocarbon radicals.[53,54] The rotational substructure allows for a definitive symmetry assignment for each band. We have assigned three of these to the ν_1 (a_1), ν_3 (a_1) and ν_{13} (b_2) C–H stretch bands and four others to the $\nu_{14}/(\nu_{15}+2\nu_{11})$ (b_2) and $\nu_2/(\nu_4+2\nu_{11})$ (a_1) Fermi dyads. For each Fermi dyad, the energy separation and intensities of component bands indicate that the coupling matrix element is approximately 2-8 cm^{-1}. Consistent with this, the φ_{iijk} quartic force constants associated with each near resonant coupling are computed to be ≈10 cm^{-1}. The two unassigned a_1 bands at

3111.30 and 3113.15 cm^{-1} are likely members of a resonance polyad involving the excited ν_1 (a_1) level, although we are unable to suggest an assignment given the information provided by the VPT2 computation.

The addition of O_2 to a differentially pumped downstream pick-up cell results in the appearance of four bands in the vicinity of the allyl C–H stretch bands. All four lack resolved rotational substructure and are instead approximately Lorentzian with full-width at half-maximum line widths of ≈1 cm^{-1}. On the basis of comparisons to frequency and intensity computations, these bands are assigned to the C–H stretch fundamentals of a G_2 type conformer of the allyl peroxy radical (CH_2=CH–CH_2OO·), which is formed *via* the allyl + O_2 reaction that occurs *within* the He droplet between sequentially picked-up and cooled monomers. A single conformation dominates the spectrum despite there being multiple isomerization barriers larger than 300 cm^{-1}. Because the helium-solvated allyl peroxy radical is born with 6300 cm^{-1} (9100 K) of internal vibrational energy, the initial barriers for internal rotation are expected to be relatively low. Indeed, the computed vibrationally adiabatic potential along the CCOO dihedral angle shows a reduced torsional anisotropy upon single quantum C–O stretch excitation. Assuming the more closely spaced torsional levels (<100 cm^{-1}) relax more efficiently in comparison to the higher frequency vibrations, the system may funnel into the lowest energy conformational minimum as it cascades down the ladder of excited stretching/bending levels.

References

(1) Miller, J. A.; Melius, C. F. *Combust. Flame* **1992**, *91*, 21-39.

(2) D'Anna, A.; Violi, A.; D'Alessio, A. *Combust. Flame* **2000**, *121*, 418-429.

(3) Miller, J. A.; Klippenstein, S. J. *J. Phys. Chem. A* **2001**, *105*, 7254-7266.

(4) Richter, H.; Howard, J. B. *Phys. Chem. Chem. Phys.* **2002**, *4*, 2038-2055.

(5) Frenklach, M. *Phys. Chem. Chem. Phys.* **2002**, *4*, 2028-2037.

(6) Miller, J. A.; Pilling, M. J.; Troe, J. *Proc. Combust. Inst.* **2005**, *s30*, 43-88.

(7) Georgievskii, Y.; Miller, J. A.; Klippenstein, S. J. *Phys. Chem. Chem. Phys.* **2007**, *9*, 4259-4268.

(8) Miller, J. A.; Klippenstein, S. J.; Georgievskii, Y.; Harding, L. B.; Allen, W. D.; Simmonett, A. C. *J. Phys. Chem. A* **2010**, *114*, 4881-4890.

(9) Ellison, G. B.; Davico, G. E.; Bierbaum, V. M.; DePuy, C. H. *Int. J. Mass Spectrom.* **1996**, *156*, 109-131.

(10) Lee, J.; Bozzelli, J. W. *Proc. Combust. Inst.* **2005**, *30*, 1015-1022.

(11) Selby, T. M.; Meloni, G.; Goulay, F.; Leone, S. R.; Fahr, A.; Taatjes, C. A.; Osborn, D. L. *J. Phys. Chem. A* **2008**, *112*, 9366-9373.

(12) Rissanen, M. P.; Amedro, D.; Eskola, A. J.; Kurten, T.; Timonen, R. S. *J. Phys. Chem. A* **2012**, *116*, 3969-3978.

(13) Nandi, S.; Arnold, P. A.; Carpenter, B. K.; Nimlos, M. R.; Dayton, D. C.; Ellison, G. B. *J. Phys. Chem. A* **2001**, *105*, 7514-7524.

(14) Han, J. X.; Utkin, Y. G.; Chen, H. B.; Hunt, N. T.; Curl, R. F. *J. Chem. Phys.* **2002**, *116*, 6505-6512.

(15) Uy, D.; Davis, S.; Nesbitt, D. J. *J. Chem. Phys.* **1998**, *109*, 7793-7802.

(16) Hirota, E.; Yamada, C.; Okunishi, M. *J. Chem. Phys.* **1992**, *97*, 2963-2970.

(17) Thomas, P. S.; Miller, T. A. *Chem. Phys. Lett.* **2010**, *491*, 123-131.

(18) Knuth, E.; Schilling, B.; Toennies, J. P. *Proceedings of the 19th International Symposium on Rarefied Gas Dynamics*; Oxford University Press: London, 1995; Vol. 19.

(19) Lewerenz, M.; Schilling, B.; Toennies, J. P. *Chem. Phys. Lett.* **1993**, *206*, 381-387.

(20) Küpper, J.; Merritt, J. M.; Miller, R. E. *J. Chem. Phys.* **2002**, *117*, 647-652.

(21) Moradi, C. P.; Morrison, A. M.; Klippenstein, S. J.; Goldsmith, C. F.; Douberly, G. E. *J. Phys. Chem. A* **2013**, *117*, 13626-13635.

(22) Lewerenz, M.; Schilling, B.; Toennies, J. P. *J. Chem. Phys.* **1995**, *102*, 8191-8207.

(23) Brink, D. M.; Stringari, S. *Z. Phys. D: At., Mol. Clusters* **1990**, *15*, 257-263.

(24) Hartmann, M.; Miller, R. E.; Toennies, J. P.; Vilesov, A. *Phys. Rev. Lett.* **1995**, *75*, 1566-1569.

(25) Ruiz, R. P.; Bayes, K. D.; Macpherson, M. T.; Pilling, M. J. *J. Phys. Chem.* **1981**, *85*, 1622-1624.

(26) Morgan, C. A.; Pilling, M. J.; Tulloch, J. M.; Ruiz, R. P.; Bayes, K. D. *J. Chem. Soc., Faraday Trans. 2* **1982**, *78*, 1323-1330.

(27) Slagle, I. R.; Ratajczak, E.; Heaven, M. C.; Gutman, D.; Wagner, A. F. *J. Am. Chem. Soc.* **1985**, *107*, 1838-1845.

(28) Bozzelli, J. W.; Dean, A. M. *J. Phys. Chem.* **1993**, *97*, 4427-4441.

(29) Morrison, A. M.; Liang, T.; Douberly, G. E. *Rev. Sci. Instrum.* **2013**, *84*, 013102.

(30) Chin, S. A.; Krotscheck, E. *Phys. Rev. B* **1995**, *52*, 10405-10428.

(31) Frisch, M. J.; Trucks, G. W.; Schlegel, H. B. et al., Gaussian Inc., Wallingford CT, 2009.

(32) Barone, V. *J. Chem. Phys.* **2005**, *122*, 014108.

(33) Bloino, J.; Barone, V. *J. Chem. Phys.* **2012**, *136*.

(34) Curtiss, L. A.; Raghavachari, K.; Trucks, G. W.; Pople, J. A. *J. Chem. Phys.* **1991**, *94*, 7221-7230.

(35) Buchenau, H.; Toennies, J. P.; Northby, J. A. *J. Chem. Phys.* **1991**, *95*, 8134-8148.

(36) DeSain, J. D.; Thompson, R. I.; Sharma, S. D.; Curl, R. F. *J. Chem. Phys.* **1998**, *109*, 7803-7809.

(37) Rissanen, M. P.; Amedro, D.; Krasnoperov, L.; Marshall, P.; Timonen, R. S. *J. Phys. Chem. A* **2013**, *117*, 793-805.

(38) Callegari, C.; Lehmann, K. K.; Schmied, R.; Scoles, G. *J. Chem. Phys.* **2001**, *115*, 10090-10110.

(39) Toennies, J. P.; Vilesov, A. F. *Angew. Chem. Int. Ed.* **2004**, *43*, 2622-2648.

(40) Choi, M. Y.; Douberly, G. E.; Falconer, T. M.; Lewis, W. K.; Lindsay, C. M.; Merritt, J. M.; Stiles, P. L.; Miller, R. E. *Int. Rev. Phys. Chem.* **2006**, *25*, 15-75.

(41) Dong, F.; Davis, S.; Nesbitt, D. J. *J. Phys. Chem. A* **2006**, *110*, 3059-3070.

(42) Skvortsov, D. S.; Vilesov, A. F. *J. Chem. Phys.* **2009**, *130*, 151101.

(43) Lindinger, A.; Toennies, J. P.; Vilesov, A. F. *J. Chem. Phys.* **1999**, *110*, 1429-1436.

(44) Choi, M. Y.; Dong, F.; Miller, R. E. *Philos. Trans. R. Soc. London, Ser. A* **2005**, *363*, 393-412.

(45) Choi, M. Y.; Miller, R. E. *J. Am. Chem. Soc.* **2006**, *128*, 7320-7328.

(46) Nauta, K.; Miller, R. E. *J. Chem. Phys.* **2001**, *115*, 10138-10145.

(47) Douberly, G. E.; Miller, R. E. *J. Phys. Chem. B* **2003**, *107*, 4500-4507.

(48) Douberly, G. E.; Miller, R. E. *J. Chem. Phys.* **2005**, *122*, 024306.

(49) Metzelthin, A.; Sanchez-Garcia, E.; Birer, O.; Schwaab, G.; Thiel, W.; Sander, W.; Havenith, M. *ChemPhysChem* **2011**, *12*, 2009-2017.

(50) Forbert, H.; Masia, M.; Kaczmarek-Kedziera, A.; Nair, N. N.; Marx, D. *J. Am. Chem. Soc.* **2011**, *133*, 4062-4072.

(51) Pentlehner, D.; Greil, C.; Dick, B.; Slenczka, A. *J. Chem. Phys.* **2010**, *133*, 114505.

(52) Raston, P. L.; Liang, T.; Douberly, G. E. *J. Chem. Phys.* **2012**, *137*, 184302.

(53) Raston, P. L.; Agarwal, J.; Turney, J. M.; Schaefer, H. F.; Douberly, G. E. *J. Chem. Phys.* **2013**, *138*, 194303.

(54) Raston, P. L.; Liang, T.; Douberly, G. E. *J. Chem. Phys.* **2013**, *138*, 174302.

CHAPTER 5

INFRARED LASER SPECTROSCOPY OF THE *N*-PROPYL AND *I*-PROPYL RADICALS IN HE DROPLETS: SIGNIFICANT BEND-STRETCH COUPLING REVEALED IN THE C–H STRETCH REGION

The *n*-propyl and *i*-propyl radicals were generated in the gas phase via pyrolysis of *n*-butyl nitrite ($CH_3(CH_2)_3ONO$) and *i*-butyl nitrite ($CH(CH_3)_2CH_2ONO$) precursors, respectively. Nascent radicals were promptly solvated by a beam of He nanodroplets, and the infrared spectra of the radicals were recorded in the C–H stretching region. In addition to a few vibrational bands previously measured in an Ar matrix,[1,2] we observe many unreported bands between 2800 and 3150, which we attribute to propyl radicals. The C–H stretching modes observed above 2960 cm^{-1} are in excellent agreement with anharmonic frequencies computed using VPT2. Between 2800 and 2960 cm^{-1}, however, the spectra of *n*-propyl and *i*-propyl radicals become quite congested and difficult to assign due to the presence of multiple anharmonic resonances. Computations employing a local mode Hamiltonian reveal the origin of the spectral congestion to be strong coupling between the high frequency C–H stretching modes and the overtones and combination bands of lower frequency bending/scissoring motions. The only significant local coupling is between stretches and bends on the same CH_2/CH_3 group.

5.1 Introduction

The combustion of propane is of significant interest because it is the smallest hydrocarbon which can be oxidized in "low-temperature" flames,[3] and these low-temperature combustion environments are important in the development of cleaner, more efficient engines.[4] Hydrogen abstraction from propane leads to the *n*-propyl ($CH_3CH_2CH_2$) and *i*-propyl (CH_3CHCH_3) radicals. These radicals can then go on to react with O_2 to form propyl peroxy radicals, and these C_3H_7OO radicals are the smallest peroxy radicals that can undergo intramolecular H-atom transfer through a geometrically favorable five- or six-membered ring transition state to form a hydroperoxyalkyl (QOOH) radical, e.g. $CH_2CH_2CH_2OOH$.[5] Indeed, many experiments and computations have been performed for the propyl + O_2 reaction.[5-9]

There is, however, a dearth of experimental and theoretical study of the propyl radicals themselves. Experimentally, aside from several electron spin resonance studies,[10-14] the only previous spectroscopic work we could find was carried out by Pacansky and co-workers in which they trapped and photodissociated dibutyryl peroxide and diisobutyryl peroxide in an Ar matrix to form the *n*- and *i*-propyl radicals (and CO_2), respectively, and measured their IR spectrum.[1,2] The C–H stretching region they reported for the *n*-propyl radical was highly congested, but they were able to assign symmetric and antisymmetric vibrational bands of the radical CH_2 group as well as one "anomalous band" corresponding to the symmetric vibration of the adjacent CH_2 group.[1] They were also able to assign several bands, including three C–H stretching vibrations, unambiguously to the *i*-propyl radical, but the majority of the spectrum could not be disentangled from the various combination/disproportionation and photoproducts.[2] In theoretical work by Li, et al., the structure of the *n*-propyl radical was investigated with high-accuracy methods, and

they provided corresponding anharmonic frequency predictions using VPT2.[15] The lack of any high-resolution experimental data and the emergence of high-level calculations for the *n*-propyl radical motivated the current work where we use He droplets to capture and study the vibrational spectrum of the *n*-propyl and *i*-propyl radicals.

5.2 Experimental Methods

The details of the helium droplet methodology has been discussed elsewhere,[16-19] and only a brief summary follows. Liquid He droplets, having a mean droplet size of 4500 He atoms, are formed in an expansion (35 bars stagnation pressure) of He gas, cooled to 17 K, through a nozzle having a 5 ± 1 um orifice.[16] The droplets evaporatively cool to an equilibrium temperature of 0.4 K before being skimmed into a beam by a 0.4 mm conical skimmer.[20] The droplet beam passes into a pickup chamber containing a low density of the molecule of interest. Stable molecules, such as propene, are introduced directly into the pickup chamber from a lecture bottle. Radicals are generated in a pyrolysis source consisting of a precursor molecule that effuses through a quartz tube; the end of the quartz tube is wrapped with a coil of Ta wire through which high current is passed, heating the wire and the quartz tube end.[18,21] A precursor molecule that collides with the hot tube wall decomposes, and the products immediately enter the droplet beam path, which is at a 90° angle to the pyrolysis source and adjacent to the quartz tube end. A collision between a droplet and a foreign molecule results in solvation by the droplet and subsequent cooling of the dopant to 0.4 K on a sub-nanosecond timescale.[20,22]

The precursor molecule used for the production of *n*-propyl radicals is *n*-butyl nitrite (*n*-BN), which was synthesized by the addition of aqueous $NaNO_2$ to an aqueous solution of *n*-

butanol and sulfuric acid at 0 °C.[23] The *i*-propyl radical precursor molecule is *i*-butyl nitrite, which was prepared by substituting *i*-butanol for the *n*-butanol in the procedure above. The pyrolysis of R−CH_2ONO nitrite molecules has been shown to lead to the formation of NO, CH_2O, and R radicals (R = C_3H_3, C_3H_5).[24,25]

The IR output of a continuous-wave optical parametric oscillator (cw-OPO) is spatially overlapped with the droplet beam trajectory and counter-propagating. The tuning and operation of the cw-OPO is discussed elsewhere.[26] IR absorption by a dopant within a droplet leads to vibrational excitation that is quickly quenched by the cold, dissipative He environment. This energy is removed via the evaporation of He atoms from the droplet, with each He atom carrying ~5 cm^{-1} of energy.[27] The loss of hundreds of He atoms reduces the geometric cross-section of the droplet and consequently reduces the probability that the droplet is electron-impact ionized by the mass spectrometer, resulting in a laser-induced depletion of the MS ion signal. The laser beam is mechanically chopped at 80 Hz as the laser frequency is slowly tuned such that at each frequency the MS ion signal can be measured while the laser is both blocked and unblocked. Any depletion in the MS ion signal is recorded as spectroscopic signal. The ion current is converted into a voltage, processed with a lock-in amplifier, and collected with custom LabVIEW software.

5.3 Results and Discussion

Mass spectra were measured for both the *n*-BN precursor flowing through the room-temperature pyrolysis source (bottom of Figure 5.1) and with the pyrolysis source being operated at a temperature of ~1000 K (top of Figure 5.1). The precursor signals at m/z = 41 and 43 u were

monitored as the pyrolysis source temperature was increased. It was found that the intensities of these two peaks decreased with increasing pyrolysis temperature, and a signal at m/z = 39 increased in intensity. An intense cluster of peaks near m/z = 30 u appear as well due to the remaining major decomposition products of *n*-BN which are CH_2O and NO. Pyrolysis of *n*-BN also leads to significant intensity on m/z = 15 and 27 u which has not been observed for the decomposition of alkyl nitrites used to generate ethyl, propargyl, and allyl radicals. The presence of these masses is indicative of the generation of CH_3 radicals and C_2H_4 molecules in the pyrolysis source, respectively. Although the presence of CH_3 was not spectroscopically verified, intense depletion signal was found at 2990.56 cm^{-1} which corresponds to a transition within the ν_{11} vibrational band of C_2H_4.

The IR laser-induced depletion spectrum of the precursor molecule, shown at the bottom of Figure 5.2, was measured with the quadrupole set to pass only ions having *m/z* = 43 u as this was one of the most intense signals in the MS. Fortunately, most of the precursor absorptions lie between 2850 and 3000 cm^{-1} and are fairly weak and broad which should reduce the presence of any unpyrolyzed precursor in the radical spectrum. Because *m/z* = 39 u was observed in the MS to have a significant increase in intensity upon *n*-BN pyrolysis, as well as being consistent with an expected ionization product of the *n*-propyl radical, this mass channel was chosen to record the depletion spectrum of the *n*-BN decomposition products (see the top spectrum of Figure 5.2). Finally, the middle spectrum of Figure 5.2 is that of the propene (C_3H_6) molecule which was recorded to ascertain the location of its vibrations in case precursor decomposition led to significant propene production.

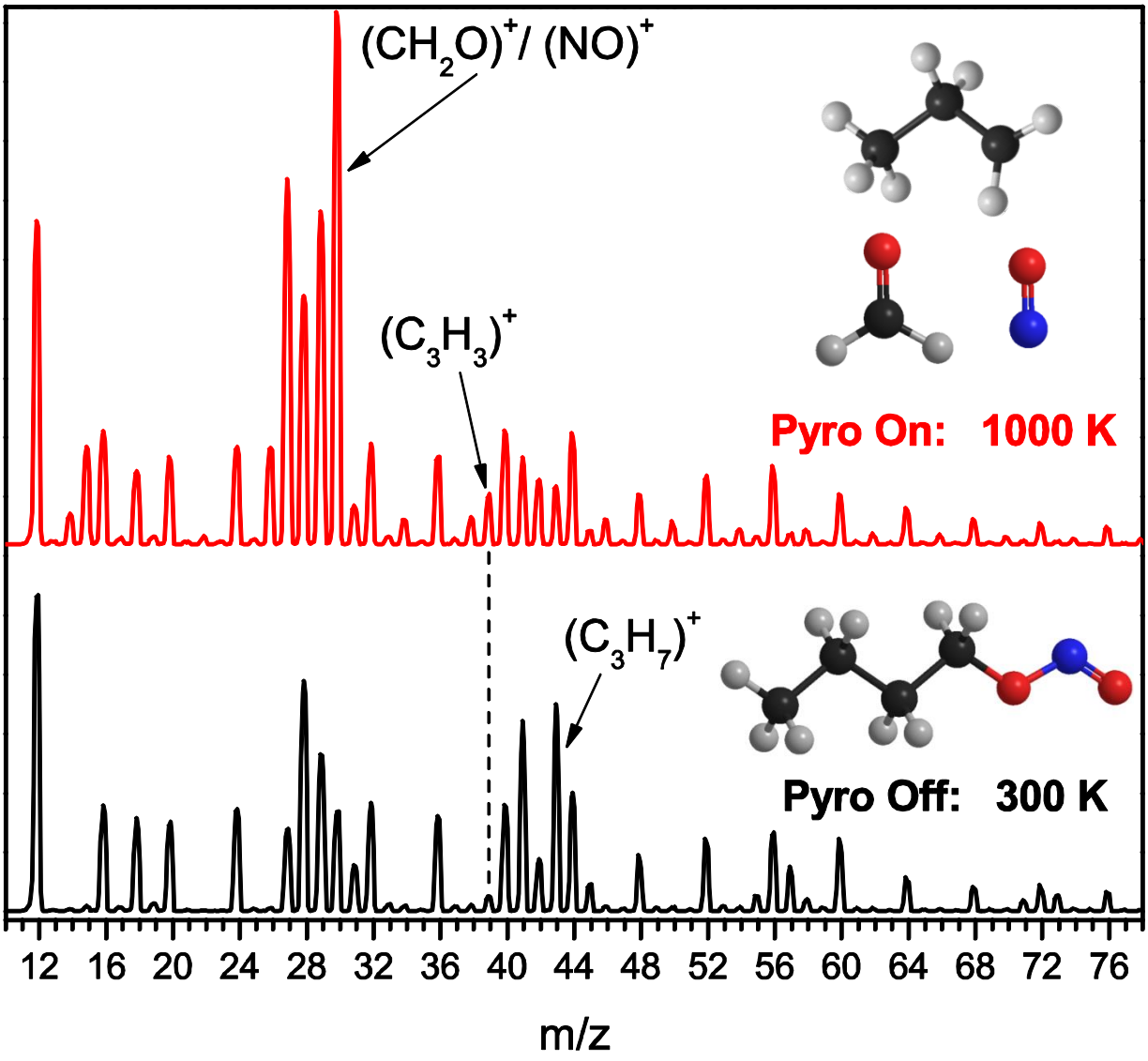

Figure 5.1: Mass spectra of the room-temperature *n*-BN precursor (bottom) and its main pyrolysates (top). The reduced ion signal in m/z = 41 and 43 u as well as the increased ion signal at masses between 27 and 30 u are indicative of precursor decomposition. The increase in the ion signal on m/z = 39 u (denoted by the dashed line) is expected to result from ionization and fragmentation of the *n*-propyl radical.

The top spectrum in Figure 5.2 shows weak signals (marked by *) that correspond to the positions of the most intense vibrations of propene, however the majority of the "pyrolysis-on" spectrum cannot be explained by either precursor or propene vibrations. Furthermore, the spectra of the He-solvated methyl radical and ethylene molecule in the CH stretching region are known,[28,29] and these decomposition products would not be expected to contribute to the spectrum anyway due to the mass selection of the quadrupole. There are two intense vibrations above 3000 cm^{-1} that are consistent with symmetric and antisymmetric CH_2 stretch vibrations that have been assigned to the *n*-propyl radical in an Ar matrix.[1] A third distinct vibration falls near 2823 cm^{-1} and is consistent with the "anomalous band" also assigned to the *n*-propyl radical in an Ar matrix.[1] The congestion between these two regions, however, is difficult to interpret. Having ruled out the possibility of other decomposition products contributing to the spectrum, we considered the possibility of a droplet picking up a *n*-propyl radical and another component of the pyrolysate. However, when the flux through the pyrolysis source is reduced by ~40%, all of the signals between 2810 and 2960 cm^{-1} decrease in intensity together (but do not disappear entirely), indicating that the spectrum arises predominantly from the pickup of a single molecule. We therefore conclude that the majority of the features in the congested "pyrolysis-on" spectrum in Figure 5.2 is due to the pickup and detection of a single *n*-propyl radical.

Figure 5.3 shows difference mass spectra (DMS) obtained by fixing the laser frequency to the peak of a vibrational band and scanning the quadrupole from 10 to 82 u in 0.01 u increments. The bottom DMS shows the laser depletion on each mass channel for the most intense precursor vibration at 2979 cm^{-1}, and there is significant depletion signal on masses greater than 43 u (the mass of the *n*-propyl radical). The top DMS was measured with the laser frequency fixed to the symmetric CH_2 stretch of *n*-propyl near 3026.9 cm-1, and this DMS

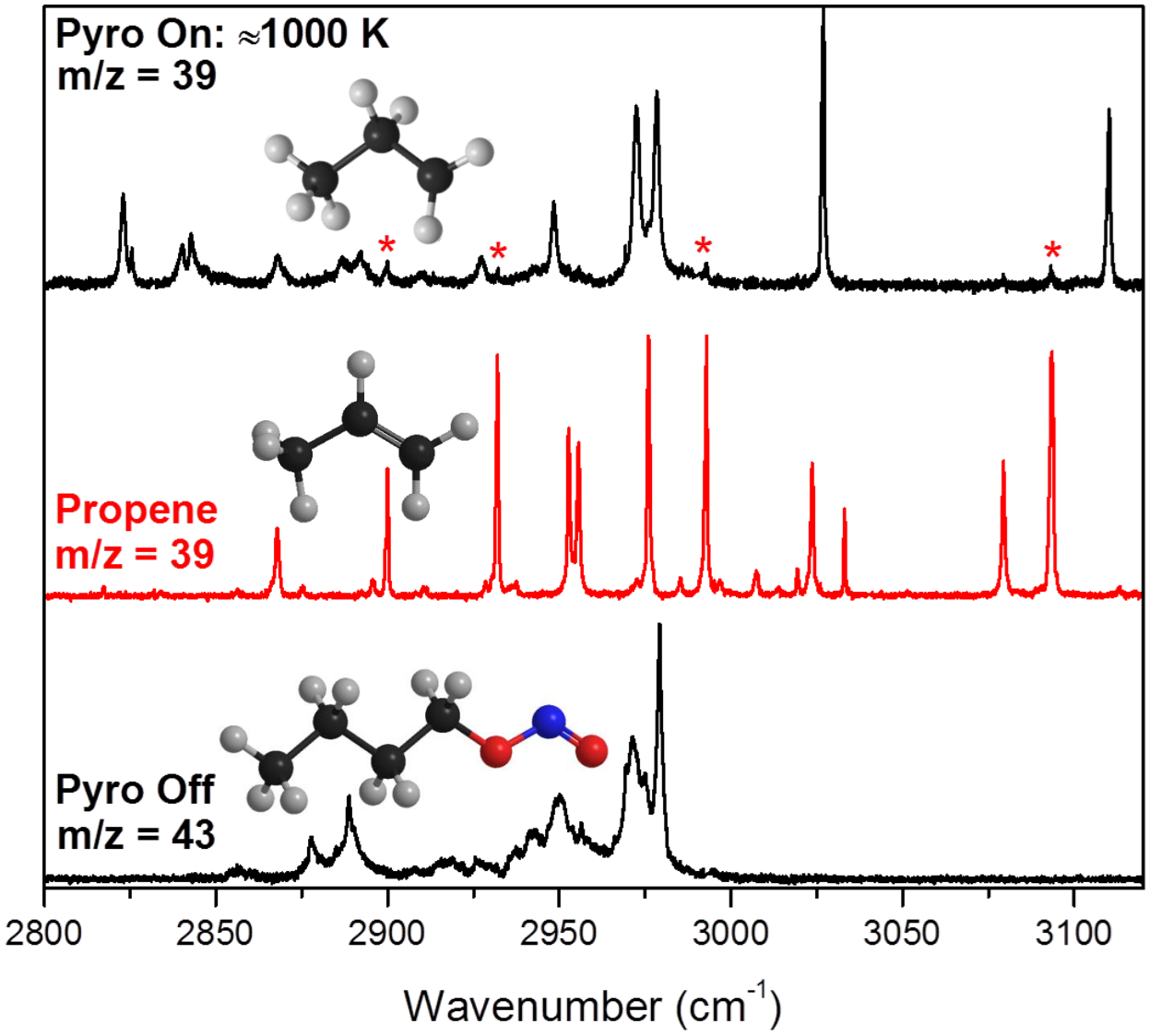

Figure 5.2: IR spectra measured in the CH stretching region. The spectrum of the precursor (bottom) was recorded with *n*-BN flowing through the room-temperature pyrolysis source. The spectrum attributed to the *n*-propyl radical (top) was measured with *n*-BN flowing through the hot (1000 K) pyrolysis source. The spectrum of propene (middle) was measured with a low pressure of propene gas, taken from a lecture bottle, in the pickup cell. Peaks marked by * in the *n*-propyl spectrum are attributed to the formation of a small fraction of propene during the precursor decomposition process.

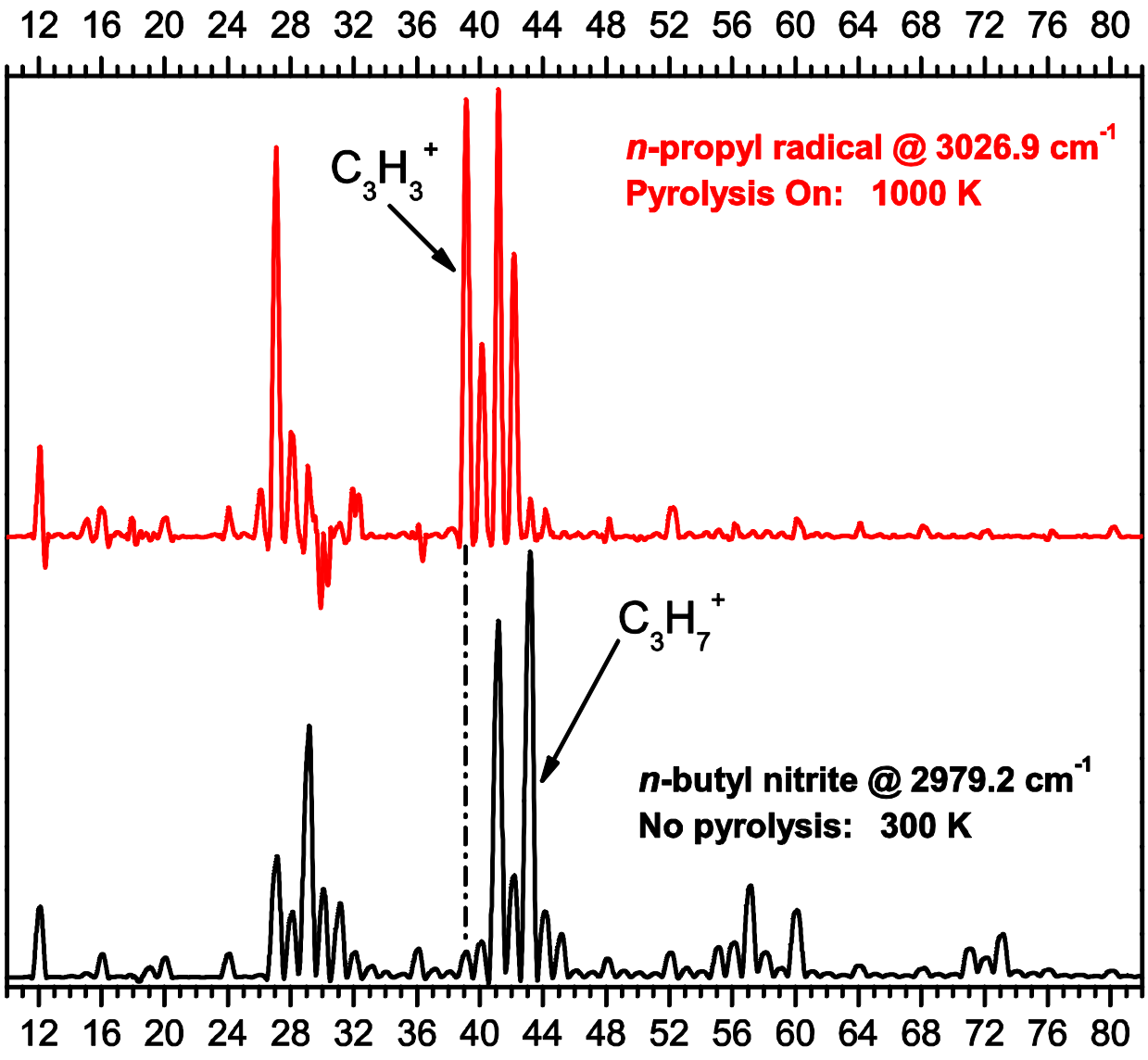

Figure 5.3: Difference mass spectra comparison of the *n*-BN precursor and the *n*-propyl radical. The precursor DMS (bottom) shows laser depletion at masses greater than that of the *n*-propyl radical (43 u), whereas the band assigned to *n*-propyl shows depletion only at masses up to 43 u.

shows no significant depletion signal beyond 43 u with the exception of He_n ($n \geq 11$) peaks. These DMS were measured for each band in the *n*-propyl radical spectrum, and each of these bands shows a similar intensity pattern between *m/z* = 39 and 42 u with no significant contribution from higher mass channels, lending further confidence that the observed spectrum is due solely to the *n*-propyl radical.

The successful detection of the *n*-propyl radical led to the expectation that pyrolysis of isobutyl nitrite (*i*-BN, $(CH_3)_2CHCH_2ONO$) under the same experimental conditions would yield a clean IR spectrum of the *i*-propyl radical. The IR spectra shown in Figure 5.4 of the precursor, propene, and "hot-pyrolysis" decomposition products (bottom, middle, and top, respectively), show this to be mostly true, although the decomposition spectrum (recorded on *m/z* = 39 u) demonstrates a much higher conversion of the (*i*-BN) precursor into propene. The decomposition spectrum contains an intense absorption at 3062 cm^{-1} consistent with the lone CH stretch of the *i*-propyl radical as assigned in a prior Ar matrix experiment.[2] The propene vibrational spectrum was scaled and subtracted out of the decomposition spectrum, and a series of DMS and pressure dependence studies on the remaining bands (as discussed above) indicates the absorptions arise predominantly from a single *i*-propyl radical. Figure 5.5 displays both the *n*-propyl (top) and the subtracted *i*-propyl (bottom) spectra with * symbols denoting residual propene features.

The first attempt to model the congested region between 2800 and 2960 cm^{-1} in the experimental spectrum of *n*-propyl is shown in the bottom of Figure 5.6. In the simulation, Li et al. computed anharmonic vibrational frequencies at the CCSD(T)/ANO0 level of theory, using a VPT2 analysis.[15] It was found that there were several anharmonic resonances predicted involving C–H stretches coupled to overtones of bending modes.[15] Diagonalization of an

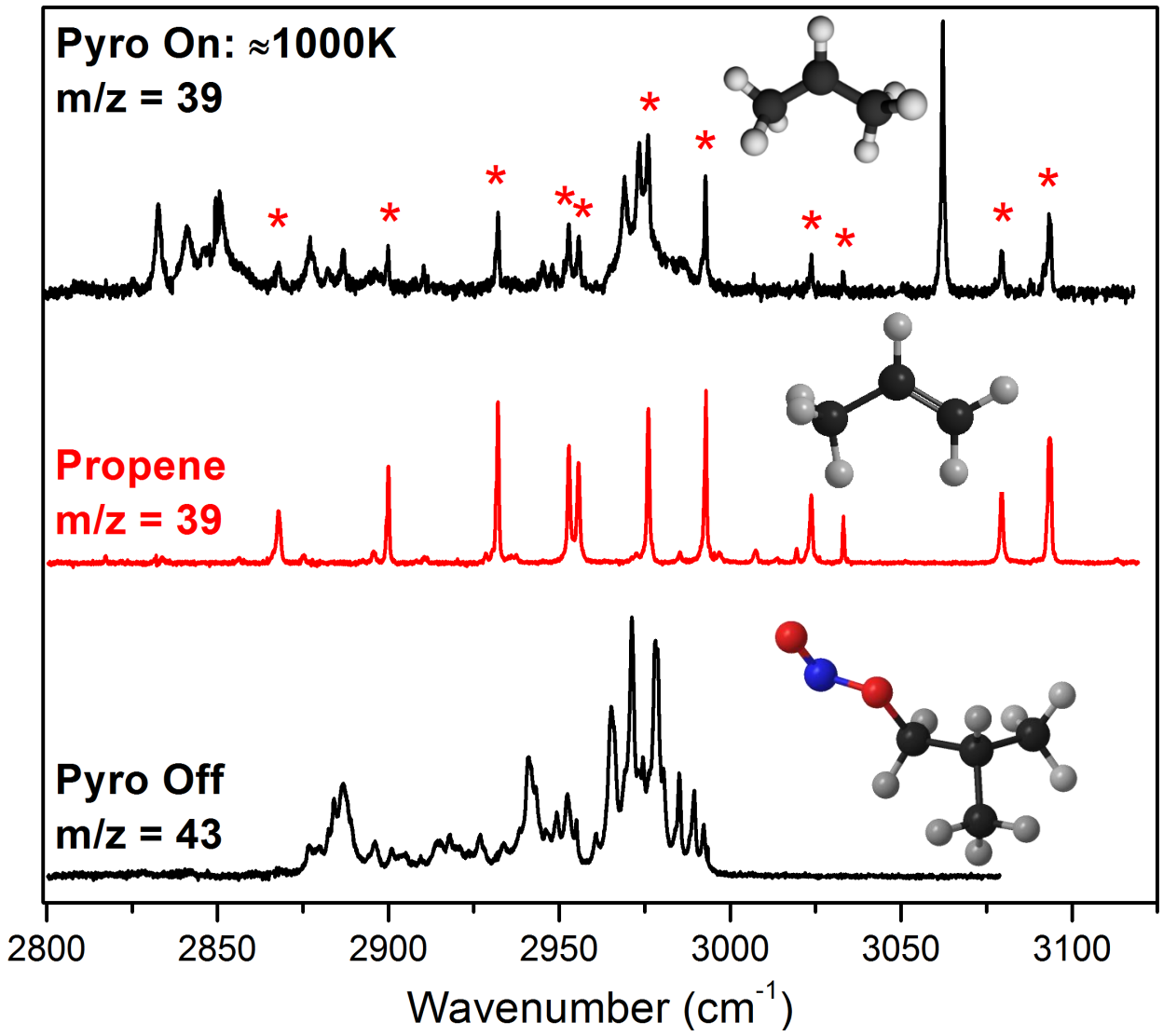

Figure 5.4: IR spectra measured in the CH stretching region. The spectrum of the precursor (bottom) was recorded with *i*-BN flowing through the room-temperature pyrolysis source. The spectrum mostly attributed to the *i*-propyl radical (top) was measured with *i*-BN flowing through the hot (1000 K) pyrolysis source. The spectrum of propene (middle) was measured with a low pressure of propene gas, taken from a lecture bottle, in the pickup cell. Peaks marked by * in the *i*-propyl spectrum are attributed to the formation of propene during the precursor decomposition process. Significantly more propene is formed during the pyrolysis of *i*-BN relative to *n*-BN.

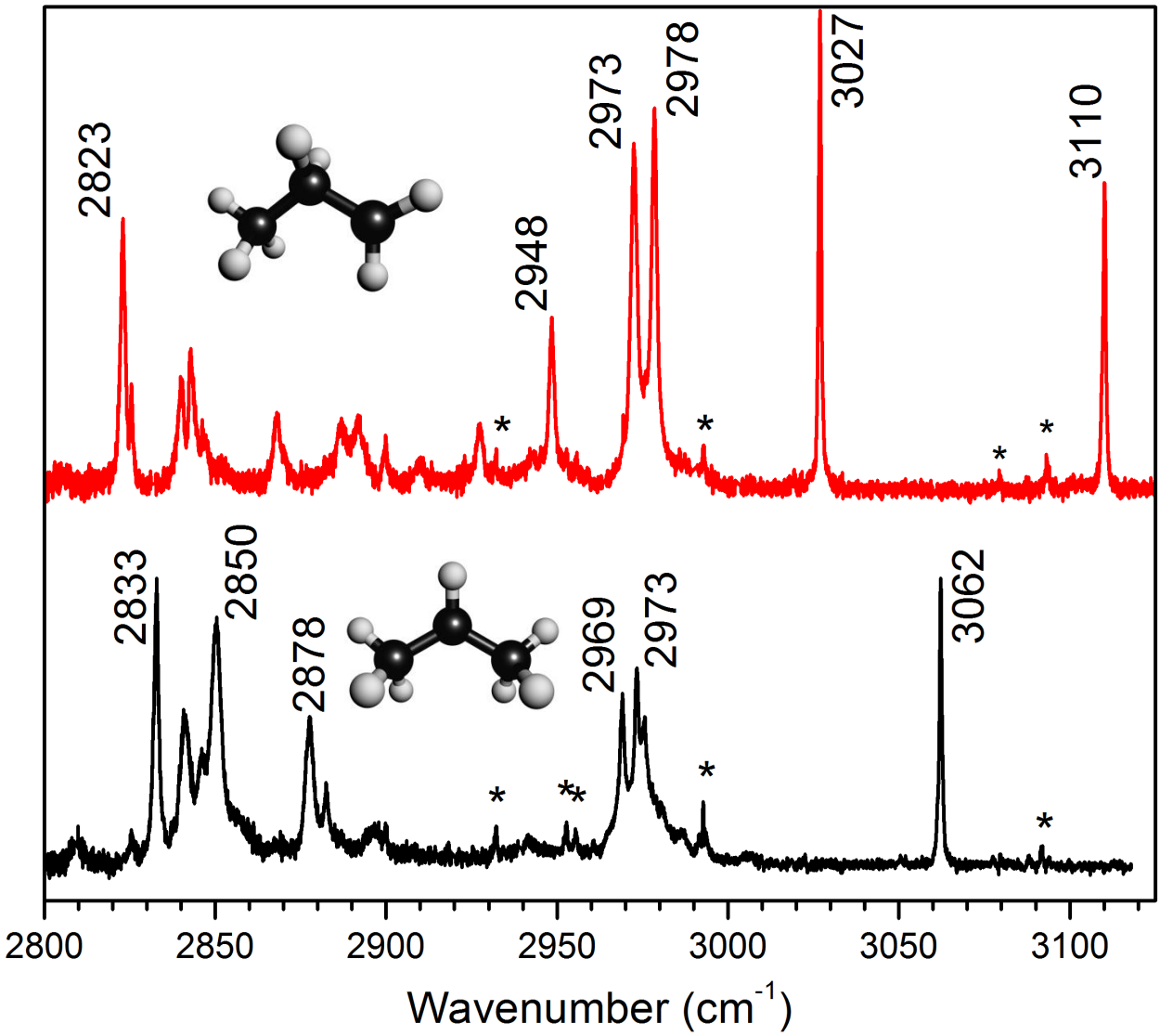

Figure 5.5: Comparison of the IR spectra of *n*-propyl (top) and *i*-propyl radicals (bottom). The wavenumber of the more intense vibrations is labeled. Most of the propene present in the *i*-propyl spectrum has been subtracted out, but residual propene absorptions are marked by *.

effective vibrational Hamiltonian matrix, which includes the anharmonic force constants , yields the eigenvalues shown as vibrational bands (marked by * and #) in the middle spectrum of Figure 5.6. Although the experimental band near 2950 cm^{-1} is accounted for by inclusion of these Fermi resonances, it is clear that even these high-level computational results do not capture the complexity inherent to the IR spectrum of the *n*-propyl radical.

We have initiated collaboration with Ned Sibert and co-workers at the University of Wisconsin who have developed a model Hamiltonian that has had good success in predicting vibrational spectra in the C–H stretching region for several hydrocarbon molecules.[30-32] They demonstrate that the C–H stretching vibrations and the overtone of the scissor vibration of a single CH_2 group can be strongly coupled. Their local-mode Hamiltonian, which incorporates these cubic stretch-bend couplings on the CH_2 groups, yields excellent agreement with measured IR spectra. Moreover, this can be accomplished using scaled harmonic DFT vibrational frequencies and cubic force constants as inputs to the model Hamiltonian, greatly reducing the computational time. The result of using this local-mode Hamiltonian approach for the *n*-propyl radical is shown in Figure 5.7. The simulation indicates that the most important interactions that are complicating the vibrational spectrum in the C–H stretching region are predominantly these bend-stretch couplings. The high-level VPT2 calculations are not yet complete for the *i*-propyl radical, at the time of this writing, but lower level computations predict a similar discrepancy between experiment and theory at C–H stretch frequencies < 2950 cm^{-1}. Thus, a preliminary vibrational spectrum is simulated using the local mode approach and shown in Figure 5.8. Again, the model appears to be capturing the most relevant interactions leading to the spectral congestion, and we are hopeful that further tweaking of the model and its parameters will result in even better agreement.

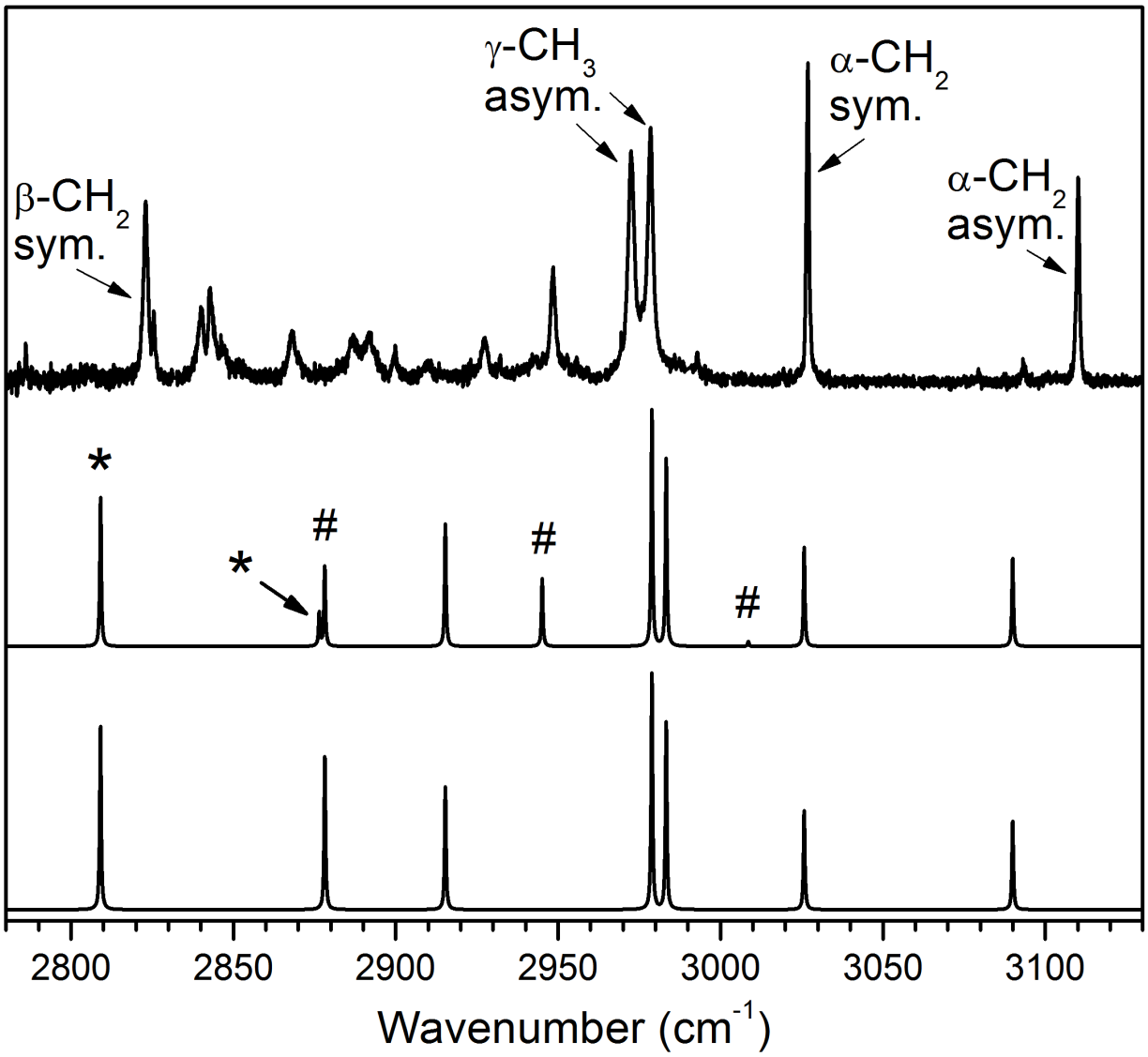

Figure 5.6: Experimental and computed vibrational spectra of the *n*-propyl radical. The anharmonic vibrational frequencies and force constants were computed at the CCSD(T)/ANO0 level of theory using a VPT2 correction (bottom). In the middle simulation, vibrations denoted by * result from Fermi coupling between ν_7 and $2\nu_{10}$, and vibrations denoted by # result from a three-state anharmonic resonance between ν_6, $2\nu_8$, and $2\nu_9$. The experimental spectrum is shown at the top of the figure.

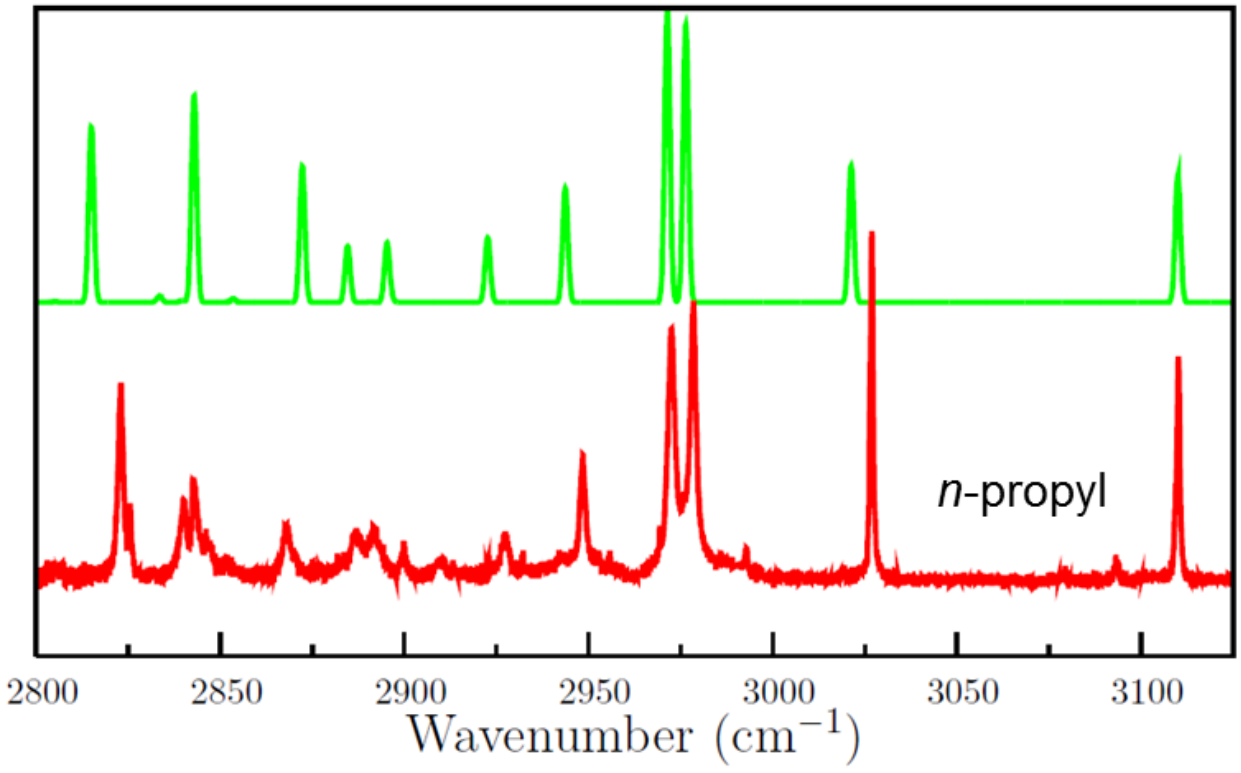

Figure 5.7: Preliminary simulation of the *n*-propyl vibrational spectrum using the local-mode Hamiltonian approach.[30] The experimental spectrum is shown on the bottom, and the simulation is shown on top.

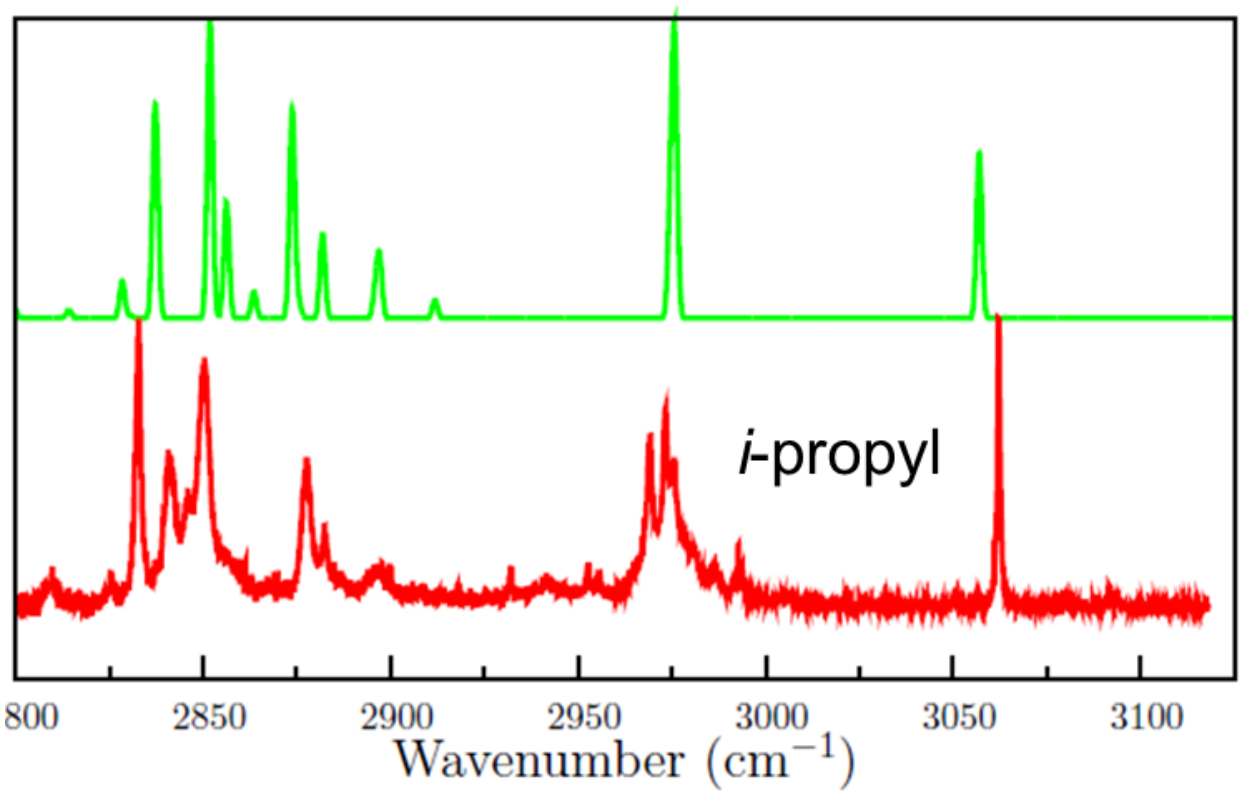

Figure 5.8: Preliminary simulation of the *i*-propyl vibrational spectrum using the local-mode Hamiltonian approach.[30] The experimental spectrum is shown on the bottom, and the simulation is shown on top.

5.4 Summary

The *n*-propyl and *i*-propyl radicals have been generated via the thermal decomposition of alkyl nitrite precursors and subsequently solvated in He nanodroplets. The vibrational spectrum in the C–H stretching region was measured for both radicals, and the *n*- and *i*-propyl spectra have high-frequency (> 3000 cm^{-1}) CH stretches that are consistent with those reported for the radicals in Ar matrix experiments.[1,2] Vibrational bands above 2960 cm^{-1} are in good agreement with the results of VPT2 calculations for both radicals (preliminary results for *i*-propyl), however the spectrum below this cutoff becomes significantly congested and is not predicted well by VPT2. Pressure dependence studies were performed in order to verify that the measured spectra result predominantly from the pickup of a single radical, and therefore the congestion cannot be due to complexes of radicals with decomposition products. Similarly, DMS studies were performed to ensure that the spectroscopic signals are present only on mass channels that would be consistent with the pickup of a C_3H_7 isomer. Preliminary results using a local-mode Hamiltonian, that includes coupling between the C–H stretches and the overtone of the scissor vibration, better predict the vibrational spectrum, indicating that the spectral complexity arises mostly from stretch-bend anharmonic couplings.

References

(1) Pacansky, J.; Horne, D. E.; Gardini, G. P.; Bargon, J. *J. Phys. Chem.* **1977**, *81*, 2149-2154.

(2) Pacansky, J.; Coufal, H. *J. Chem. Phys.* **1980**, *72*, 3298-3303.

(3) Miller, J. A.; Klippenstein, S. J. *J. Phys. Chem. A* **2013**, *117*, 2718-2727.

(4) A. McIlroy, and G. McRae, in *Report of the Basic Energy Sciences Workshop on Clean and Efficient Combustion of 21st Century Transportation Fuels* Combustion Research Facility, Sandia National Laboratories, Livermore, CA, (2007).

(5) DeSain, J. D.; Klippenstein, S. J.; Miller, J. A.; Taatjes, C. A. *J. Phys. Chem. A* **2003**, *107*, 4415-4427.

(6) Ruiz, R. P.; Bayes, K. D. *J. Phys. Chem.* **1984**, *88*, 2592-2595.

(7) DeSain, J. D.; Taatjes, C. A.; Miller, J. A.; Klippenstein, S. J.; Hahn, D. K. *Faraday Discuss.* **2002**, *119*, 101-120.

(8) Tarczay, G.; Zalyubovsky, S. J.; Miller, T. A. *Chem. Phys. Lett.* **2005**, *406*, 81-89.

(9) Baldwin, R. R.; Walker, R. W.; Yorke, D. A. *J. Chem. Soc. Faraday Trans. 1* **1973**, *69*, 826-832.

(10) Fessenden, R. W.; Schuler, R. H. *J. Chem. Phys.* **1963**, *39*, 2147-2195.

(11) Krusic, P. J.; Kochi, J. K. *J. Am. Chem. Soc.* **1971**, *93*, 846-860.

(12) Krusic, P. J.; Jesson, J. P.; Meakin, P. *J. Phys. Chem.* **1971**, *75*, 3438-3453.

(13) Adrian, F. J.; Cochran, E. L.; Bowers, V. A. *J. Chem. Phys.* **1973**, *59*, 3946-3952.

(14) Fessenden, R. *J. Chim. Phys. Phys.-Chim. Biol.* **1964**, *61*, 1570-1575.

(15) Li, C. Y.; Agarwal, J.; Wu, C. H.; Allen, W. D.; Schaefer, H. F. *J. Phys. Chem. B* **2015**, *119*, 728-735.

(16) Callegari, C.; Lehmann, K. K.; Schmied, R.; Scoles, G. *J. Chem. Phys.* **2001**, *115*, 10090-10110.

(17) Toennies, J. P.; Vilesov, A. F. *Angew. Chem., Int. Ed.* **2004**, *43*, 2622-2648.

(18) Choi, M. Y.; Douberly, G. E.; Falconer, T. M.; Lewis, W. K.; Lindsay, C. M.; Merritt, J. M.; Stiles, P. L.; Miller, R. E. *Int. Rev. Phys. Chem.* **2006**, *25*, 15-75.

(19) Stienkemeier, F.; Lehmann, K. K. *J. Phys. B* **2006**, *39*, R127-R166.

(20) Hartmann, M.; Miller, R. E.; Toennies, J. P.; Vilesov, A. *Phys. Rev. Lett.* **1995**, *75*, 1566-1569.

(21) Kupper, J.; Merritt, J. M.; Miller, R. E. *J. Chem. Phys.* **2002**, *117*, 647-652.

(22) Scheidemann, A.; Schilling, B.; Toennies, J. P. *J. Phys. Chem.* **1993**, *97*, 2128-2138.

(23) Noyes, W. A. *Org. Synth.* **1936**, *16*, 7.

(24) Moradi, C. P.; Morrison, A. M.; Klippenstein, S. J.; Goldsmith, C. F.; Douberly, G. E. *J. Phys. Chem. A* **2013**, *117*, 13626-13635.

(25) Leavitt, C. M.; Moradi, C. P.; Acrey, B. W.; Douberly, G. E. *J. Chem. Phys.* **2013**, *139*, 234301.

(26) Morrison, A. M.; Liang, T.; Douberly, G. E. *Rev. Sci. Instrum.* **2013**, *84*, 013102.

(27) Brink, D. M.; Stringari, S. *Z. Phys, D: At., Mol. Clusters* **1990**, *15*, 257-263.

(28) Morrison, A. M.; Raston, P. L.; Douberly, G. E. *J. Phys. Chem. A* **2013**, *117*, 11640-11647.

(29) Lindsay, C. M.; Miller, R. E. *J. Chem. Phys.* **2005**, *122*.

(30) Buchanan, E. G.; Dean, J. C.; Zwier, T. S.; Sibert, E. L. *J. Chem. Phys.* **2013**, *138*, 064308.

(31) Buchanan, E. G.; Sibert, E. L.; Zwier, T. S. *J. Phys. Chem. A* **2013**, *117*, 2800-2811.

(32) Sibert, E. L.; Kidwell, N. M.; Zwier, T. S. *J. Phys. Chem. B* **2014**, *118*, 8236-8245.

CHAPTER 6

REACTIVE INTERMEDIATES IN ^{4}HE NANODROPLETS: INFRARED LASER STARK SPECTROSCOPY OF HYDROXYMETHYLENE AND DIHYDROXYCARBENE

Hydroxymethylene (HCOH) and its d_1-isotopologue (HCOD) are isolated in low temperature helium nanodroplets following pyrolysis of glyoxylic acid. Transitions identified in the infrared spectrum are assigned exclusively to the *trans*-conformation based on previously reported anharmonic frequency computations. For the OH(D) and CH stretches, *a*- and *b*-type transitions are observed, and when taken in conjunction with CCSD(T)/cc-pVTZ computations, lower limits to the vibrational band origins are determined. The relative intensities of the *a*- and *b*-type transitions provide the orientation of the transition dipole moment in the inertial frame. The He nanodroplet data are in excellent agreement with anharmonic frequency computations reported here and elsewhere, confirming an appreciable Ar-matrix shift of the OH and OD stretches and strong anharmonic resonance interactions in the high-frequency stretch regions of the mid-infrared.

Singlet dihydroxycarbene (HOCOH) is produced via pyrolytic decomposition of oxalic acid, captured by helium nanodroplets, and probed with infrared laser Stark spectroscopy. Rovibrational bands in the OH stretch region are assigned to either *trans,trans*- or *trans,cis*-rotamers on the basis of symmetry type, nuclear spin statistical weights, and comparisons to electronic structure theory calculations. Stark spectroscopy provides the inertial components of the permanent electric dipole moments for these rotamers. The dipole components for

trans,trans- and *trans,cis*- rotamers are (μ_a, μ_b) = (0.00, 0.68(6)) and (1.63(3), 1.50(5)), respectively. The infrared spectra lack evidence for the higher energy *cis,cis*- rotamer, which is consistent with a previously proposed pyrolytic decomposition mechanism of oxalic acid and computations of HOCOH torsional interconversion and tautomerization barriers.

6.1 Introduction

Carbenes (R^1–C̈–R^2) are utilized as synthetic scaffolds in modern organometallic chemistry,[1-6] and they have long been recognized as reaction intermediates in organic chemistry.[7-9] Carbenes also play significant roles in many fundamental areas of chemical physics, including atmospheric,[10,11] combustion[12,13] and interstellar chemistry.[14-17] Singlet carbenes are composed of a divalent, sp^2 hybridized C atom with an out-of-plane, vacant *p*-orbital, whereas triplet carbenes possess two half-filled *p*-orbitals.[18] The relative stabilities of singlet and triplet electronic states depends partially on the propensity of substituent groups to back-donate electron density to the electron deficient C atom.[10,18]

There exists a long and rich history of the spectroscopy of carbene systems, including the seminal work on gas-phase methylene[19-22] and other triatomic carbenes.[10,23-25] Our understanding of the physical chemistry of these elusive species has profited tremendously from cryogenic matrix isolation spectroscopy,[26] with the earliest reports on matrix isolated methylene appearing shortly after the introduction of the technique in the late 1950s.[27] Indeed the structure and reactivity of an impressive range of carbene systems have been probed with this method.[16,26-33]

Hydroxymethylene (HCOH), a singlet carbene involved in the photochemistry of its tautomer, formaldehyde,[34-38] has been implicated in the formation of simple sugars (*i.e.* glycolaldehyde) in the cosmos,[39,40] and has been the subject of numerous theoretical studies.[39,41-46] Despite the large theoretical interest, experimental studies are lacking due to the highly reactive, transient nature of HCOH. The first indirect measurement of HCOH was reported by Sodeau and Lee.[47] Low temperature matrix FT-IR and photolysis experiments were performed on isotopically labeled formaldehyde (FA), where it was postulated that formation of glycolaldehyde resulted from the reaction between HCOH and FA. The heat of formation of hydroxymethylene has been measured in photodissociation experiments of hydroxymethyl radicals,[48,49] and furthermore, the energetics associated with *cis*- and *trans*-hydroxymethylene were reported using a sliced velocity map imaging technique.[50]

The first direct observation of HCOH (and HCOD) was reported recently by Schreiner and co-workers, where the pyrolysis products (*vide infra*) of glyoxylic acid (GA) were deposited in an 11 K Ar matrix.[51] The resulting FT-IR spectrum was assigned to *trans*-HCOH(D) based on high-level anharmonic frequency computations. Interestingly, at 11 K, hydroxymethylene rearranged to formaldehyde via tunneling with a half-life of approximately 2 hours, consistent with the computed 1.3 eV barrier to isomerization.[51] Concurrently with the study by Schreiner and co-workers, the anharmonic frequencies and intensities were reported for both *cis*- and *trans*-HCOH and HCOD, using vibrational configuration interaction (VCI) theory.[52] Both sets of anharmonic frequencies are in agreement with the matrix FT-IR spectra, with the exception of the OH and OD stretches, which deviate from computed values by ~70 and ~40 cm^{-1}, respectively.

Among the series of Ar matrix studies reported by Schreiner and co-workers, dihydroxycarbene, HOCOH, was shown to be similarly produced via the thermal decomposition of a readily available precursor, oxalic acid (**1a** and **1b** in Figure 6.1).[53] *Ab initio* computations show that dihydroxycarbene is stabilized by in-plane, π-electron donation from oxygen, implying production of HOCOH in its ground singlet state.[53-55] This stabilizing transfer of electron density into the vacant, out-of-plane *p*-orbital results in a rather large singlet-triplet energy splitting (computed here to be 61.7 kcal/mol) and substantial torsional interconversion barriers. Computations of the singlet potential energy surface (PES)[53,56] revealed three locally stable rotamers (**2a**, **2b** and **2c**). The matrix FTIR spectra of the pyrolytic decomposition products of oxalic acid revealed the presence of *trans,trans*- and *trans,cis*-HOCOH (**2a** and **2b**), but the higher energy *cis,cis*- rotamer (**2c**) was absent. Unlike HCOH, efficient tunneling of HOCOH to its tautomeric aldehyde, formic acid (**3**), was not observed.[53]

More recently, McCarthy and coworkers used a combination of microwave and millimeter wave spectroscopy for the structural determination of the gas-phase *trans,cis*-rotamer.[57] Here they confirmed a planar, C_s symmetry structure, consistent with previous theoretical computations. Their structural results further illustrate the critical role that the second electron-donating group in HOCOH plays in making this molecule resistant to isomerization. The apparent stability of this carbene to tunneling suggests a possible role for it in the atmospheric and astrochemistry already discussed for members of its isomeric family, formic acid and the simplest Criegee intermediate, peroxymethylene.[58-61] Extending upon these previous spectroscopic studies, the work described herein consists of an analysis of the rovibrational spectra of both He-solvated HCOH and HOCOH as well as the measurement of the permanent electric dipole moments of the latter using IR laser Stark spectroscopy.

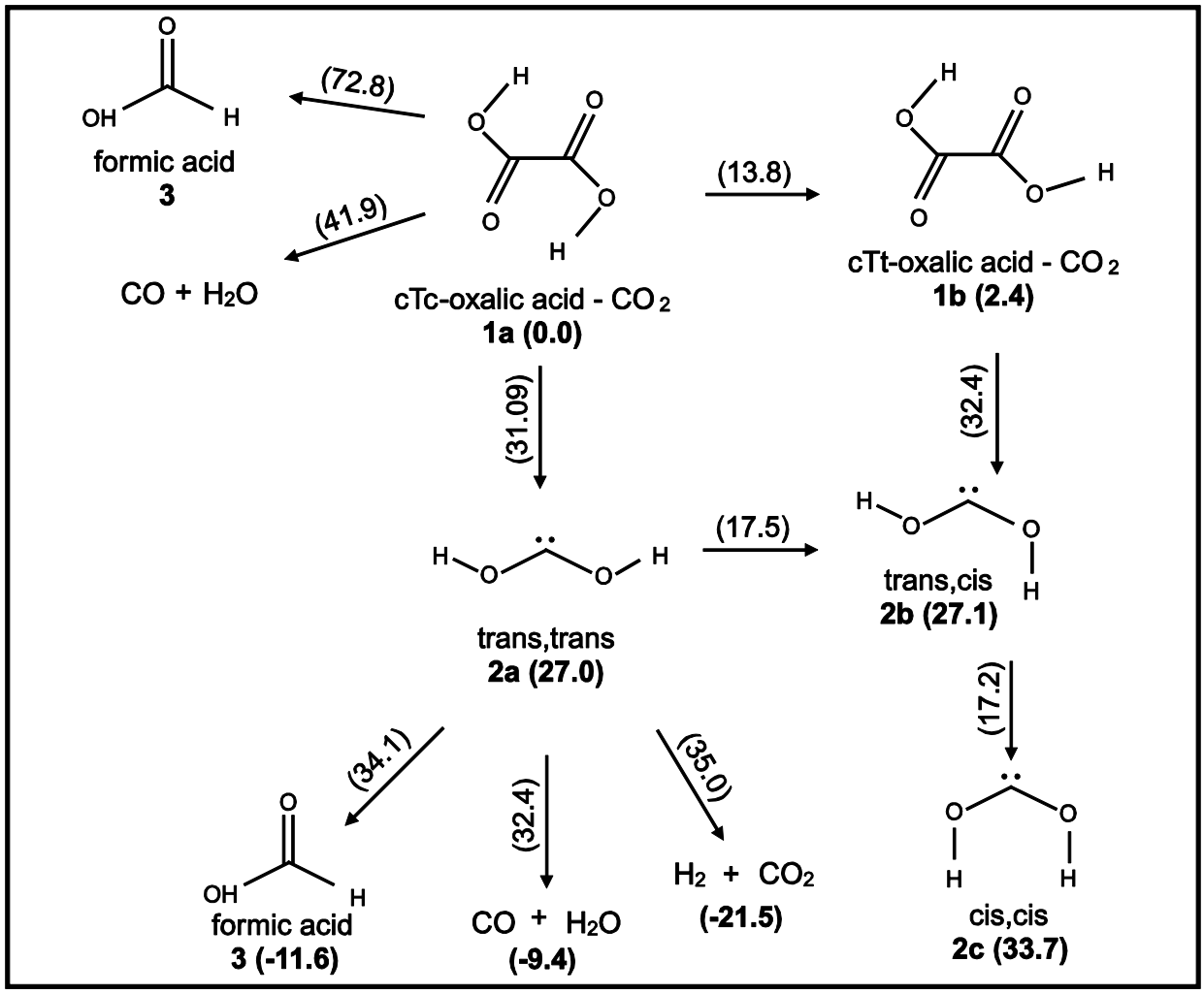

Figure 6.1: Possible products of the pyrolytic decomposition of the *cTc*, and *cTt*-oxalic acid conformers. The three lowest-lying isomers of dihydroxycarbene are *trans,trans-*, *trans,cis-*, and *cis,cis-*, although only the former two are observed, consistent with previous work.[36] Barrier heights (numbers in parentheses) and relative ΔH_0 values (bold numbers in parentheses) associated with each oxalic acid rearrangement and decomposition pathway are from Ref. 62. The barrier heights and relative ΔH_0 values associated with dihydroxymethylene rotamerization/decomposition are from Ref. 53.

6.2 Experimental Methods

The helium droplet methodology employed here has been described in detail previously.[62-65] Nanodroplets of superfluid He are generated in a subcritical, supersonic expansion of He gas (99.9995 % purity, 35 bar) through a cold (17 K), 5 μm diameter pinhole nozzle. Under these conditions, droplets consisting of 4500 He atoms on average are produced at a rate of 10^{12} s^{-1}.[62,66,67] The droplets pass into a differentially pumped "pickup" chamber, where gas-phase molecules are captured, solvated and cooled to ≈0.4 K.[68] A low-pressure, effusive pyrolysis source located in the pickup chamber produces gas-phase carbenes by thermal decomposition of organic precursor molecules.[69] Gas-phase HCOH and HOCOH was generated via pyrolysis of glyoxylic acid ($C_2H_2O_3$) and oxalic acid ($C_2H_2O_4$), respectively, analogous to the procedures reported by Schreiner and co-workers.[51,53] The pyrolysis region consisted of a 15 cm long quartz tube with an outer diameter of 0.6 cm, which is oriented perpendicular to the droplet beam. The sealed end of the tube, furthest from the beam, contained ≈1 g of oxalic acid. To achieve sufficient vapor pressure (≈10^{-5} Torr) in the pickup zone to optimize for the capture of single molecules, the sample was heated to 330 K by a Nichrome wire wrapped around the sealed end of the quartz tube. The temperature in this sample region was monitored by a K-type thermocouple. The pyrolysis region, adjacent to the droplet beam, was wrapped with a single coil of Ta wire, through which high current was passed. Pyrolysis of the precursor molecule(s) and subsequent carbene production was optimized at ≈1000 K (35 A).

The doped droplet beam passes into a Stark/multipass cell consisting of two 15 cm long, parallel, gold-coated mirrors situated on either side of the droplet beam and two parallel, stainless steel electrodes located above and below the beam axis. The electrode spacing is

3.10(2) mm and is calibrated via Stark measurements of He-solvated HCN.[70] The tunable idler output from an IR continuous-wave, optical parametric oscillator (OPO) is used to vibrationally excite the molecules embedded in He droplets.[71] The IR radiation directed into the multipass cell intersects the droplet beam 20-30 times in an approximately perpendicular arrangement. The polarization of the OPO idler output is aligned parallel to the applied Stark field.

When in resonance with a rovibrational transition of the dopant, the vibrational excitation energy is quenched by the evaporation of He atoms from the droplet surface. One He atom is lost for every $\approx$5 cm^{-1} of vibrational energy. This laser-induced reduction in the droplet geometric cross-section leads to a reduction in the total ion signal produced upon electron-impact ionization in a downstream quadrupole mass spectrometer. The ion current from the mass spectrometer is processed with a lock-in amplifier as the OPO idler beam is amplitude modulated at 80 Hz and tuned continuously with $\approx$10 MHz resolution.[71] The resulting IR spectrum, reflected in this vibrational excitation induced cross section modulation, is normalized to the power of the OPO idler wave, as measured directly next to the window into the vacuum system. Wedged optical components and dry-N_2 purging are used to mitigate power modulations along the optical path leading from the OPO to the Stark/multipass cell. Stark spectra of molecules in He droplets reveal inertial components of the permanent electric dipole moment that have been shown, in most cases,[70] to be equivalent to their gas-phase values, within the error of the measurement.

6.3 Hydroxymethylene (HCOH)

A dried sample of glyoxylic acid was obtained using a similar procedure described by Schreiner and co-workers.[51] Briefly, a small amount (< 1 g) of glyoxylic acid monohydrate (SigmaAldrich) was placed in a glass bulb and heated (60-70°C) under vacuum for 24-48 hours. This sample was then attached to our custom pyrolysis source, consisting of a quartz tube (~15 cm) attached to water-cooled electrodes, with a tantalum wire wrapped at the exit of the tube (~1 cm length).[72] The quartz tube was seated into one end of a copper tube (~0.1 cm OD, ~50 cm length), with the other end fitted into a compression fitting making the air/vacuum interface. The temperature roughly at the middle of the copper tube was monitored with a K-type thermocouple. The sample was heated to ~60°C, and the external transfer lines from the sample to the vacuum interface were heated (70-90°C) using resistively heated heat tape. During the experiments the temperature of the copper tube was ~65°C via heat transfer from both the tantalum filament and the external heat tape. The source was positioned such that the He nanodroplet beam passed in front of the quartz tube, doping a fraction of the droplets with HCOH, FA, CO_2, H_2O, GA, or some combination. The doped droplet beam was then analyzed via electron impact mass spectrometry. The mass spectrum obtained when the pyrolysis source was operated near 100°C (Figure 6.2a) contains peaks assigned to H_2O^+ (18 u), HCO^+ or COH^+ (29 u), and CO_2H^+ (45 u), in addition to those assigned to ionized He clusters. When the temperature of the pyrolysis source was increased to ~1000° C the peak at m/z=44 u, assigned to CO_2^+, increased in intensity with a concomitant decrease in the intensity of the peaks at 29 and 45 u (Figure 6.2b). As was previously noted,[51] the pyrolysis of GA produces HCOH through the extrusion of CO_2, and these mass spectra therefore provided strong initial evidence that GA was

dissociating, at least to some extent, within our pyrolysis source. We synthesized the d_1-GA precursor using the procedure described by Schreiner and co-workers,[51] with the corresponding mass spectrum of the pyrolyzed precursor presented in Figure 6.2c. Peaks at both 45 and 46 u are observed in the mass spectrum, with the latter peak assigned to the CO_2D^+ ion, indicating that some isotope exchange was achieved.

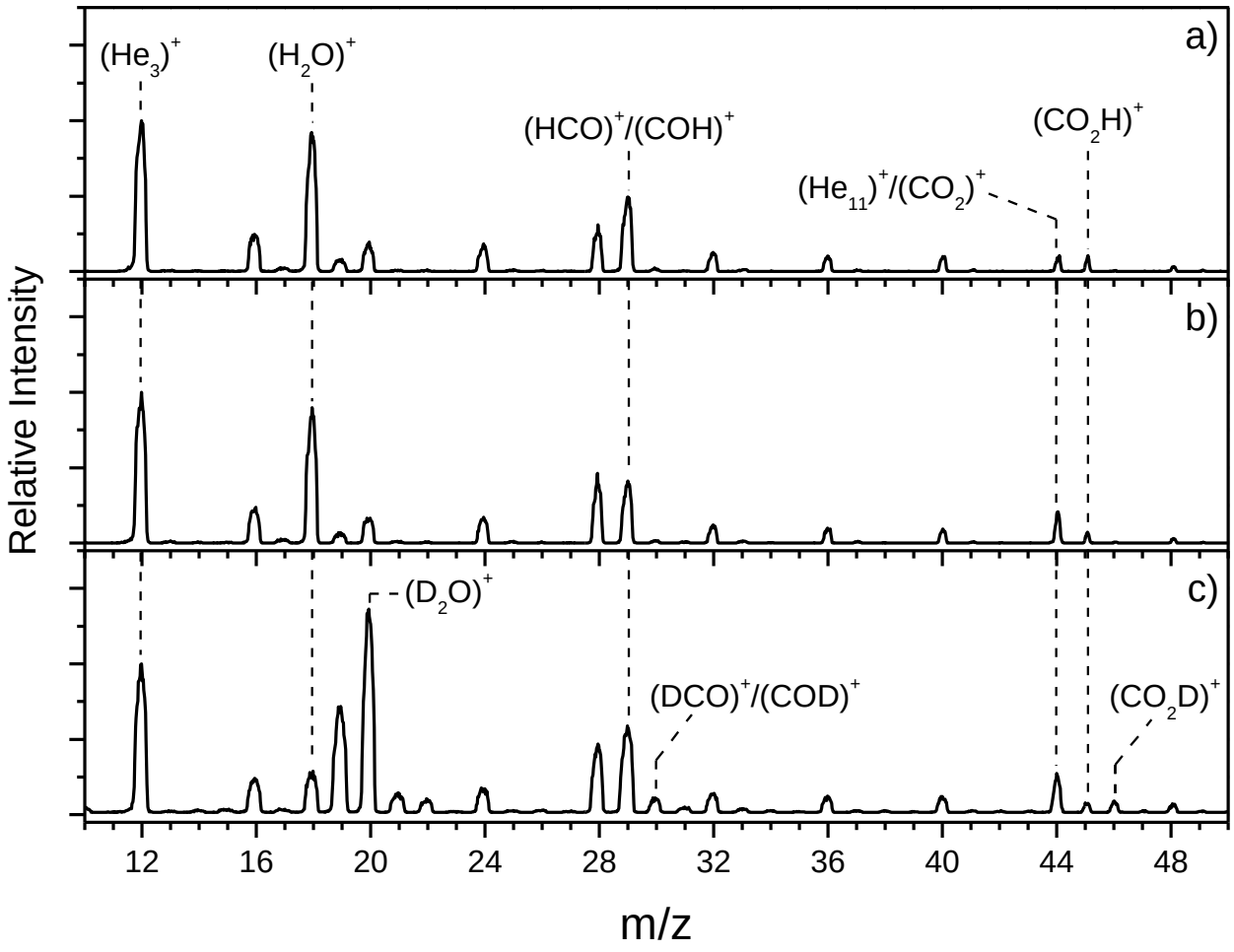

Figure 6.2: Mass spectra obtained from an effusive flow of glyoxylic acid when the temperature of the pyrolysis source was a) ~100° C and b) ~1000° C. Increased abundance of CO_2^+ in trace b) is indicative of the formation of HCOH. Trace c) presents the mass spectrum of the d_1-glyoxylic acid isotopologue with the pyrolysis source operated near 1000° C.

A survey vibrational spectrum through the CH and OH stretching regions are presented in Figure 6.3. The ν_1 band of formaldehyde (FA) is observed near 2785 cm^{-1},[73] and two intense bands centered at 3494.10 and 3580.36 cm^{-1} (FWHM ~0.6 cm^{-1}) are assigned to the OH stretches of the two *trans*-conformations of GA based on previous infrared studies.[74] The lower frequency band is assigned to the hydrogen bonded *cis*-configuration (*tc*-GA) of the OH group, while the higher frequency component is assigned to the "all-*trans*" structure (*tt*-GA). In addition, three sets of lines, split by ~5.82 cm^{-1} (indicated by * in Figure 6.3), are also present in the survey spectrum. The two lower frequency sets of lines at ~2700 and 2775 cm^{-1} are located near the previously measured vibrational band origins for *trans*-HCOH (*t*HCOH).[51] Based on the variational computations carried out by Schreiner, *et. al.*,[51] these two bands are assigned to a mixture of ν_2 (CH stretch) and the $\nu_3+\nu_4$ combination band (in-phase HCO and COH bend + CO stretch). A pair of lines is observed in the OH stretching region blue shifted by ~40 cm^{-1} compared to the Ar matrix FT-IR data.[51] Anharmonic frequencies obtained from both variational[51] and VCI[52] computations predict a similar blue shift with respect to the matrix value, and it was inferred[51] that the matrix imparted a non-negligible shift of the OH stretch. Based on these previous computations, as well as comparison with the experimental vibrational band origins,[51,52] we assign these sets of lines to *t*HCOH.

High resolution scans of the transitions derived from *t*HCOH are presented in Figure 6.4. At the 0.4 K droplet temperature, the entire *t*HCOH population collapses to the 0_{00} rovibrational ground state. Based on computed normal modes, the CH and OH stretches have transition dipole moment projections along the inertial *a*- and *b*-axes (Figure 6.4 inset), resulting in *a/b* hybrid bands split into *a*-type ($1_{01}\leftarrow 0_{00}$) and *b*-type ($1_{11}\leftarrow 0_{00}$) transitions separated by the difference in the A' and B' rotational constants. In general, the *b*-type component is broader than the *a*-type

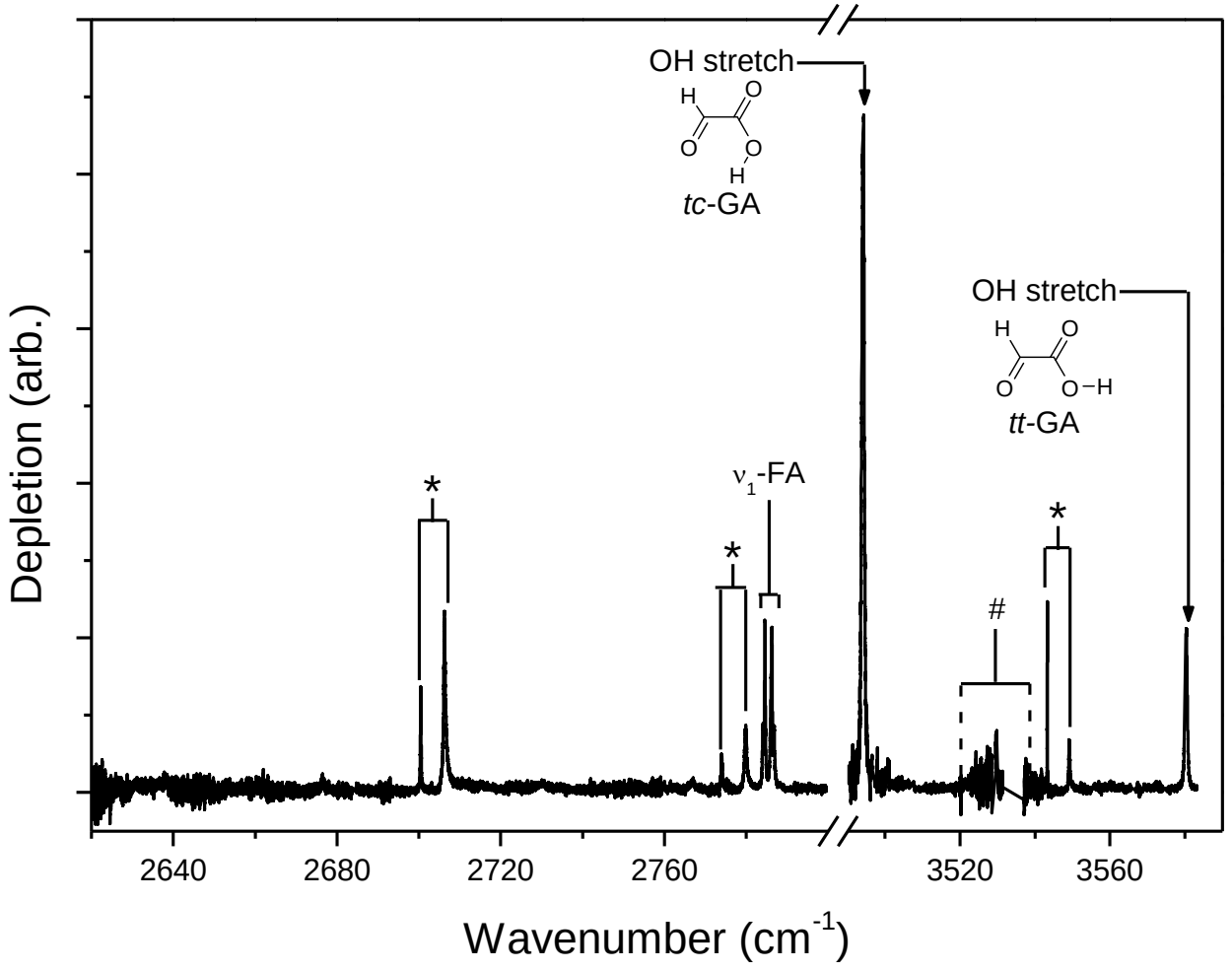

Figure 6.3: Survey scan of the pyrolysis of glyoxylic acid collected on mass channel 29 u. Two OH stretching bands are observed for two conformations (*tc*GA and *tt*GA) of the precursor, as well as the ν_1 band of formaldehyde. Three pairs of lines (indicated by *), split by ~5.82 cm^{-1}, are observed near the previously reported vibrational band origins of *trans*-HCOH. The poor coverage of the spectrum, indicated by #, is due to MgOH impurities in the PPLN crystal.

component, consistent with the larger droplet state density to which the rotor can couple upon excitation to the 1_{11} level.[72] The experimentally determined (A'–B') values are collected in Table 6.1, and compared to the computed (CCSD(T)/cc-pVTZ) ground state values, these are reduced by approximately 30%, which is typical for molecules isolated in superfluid He.[62,63] From these

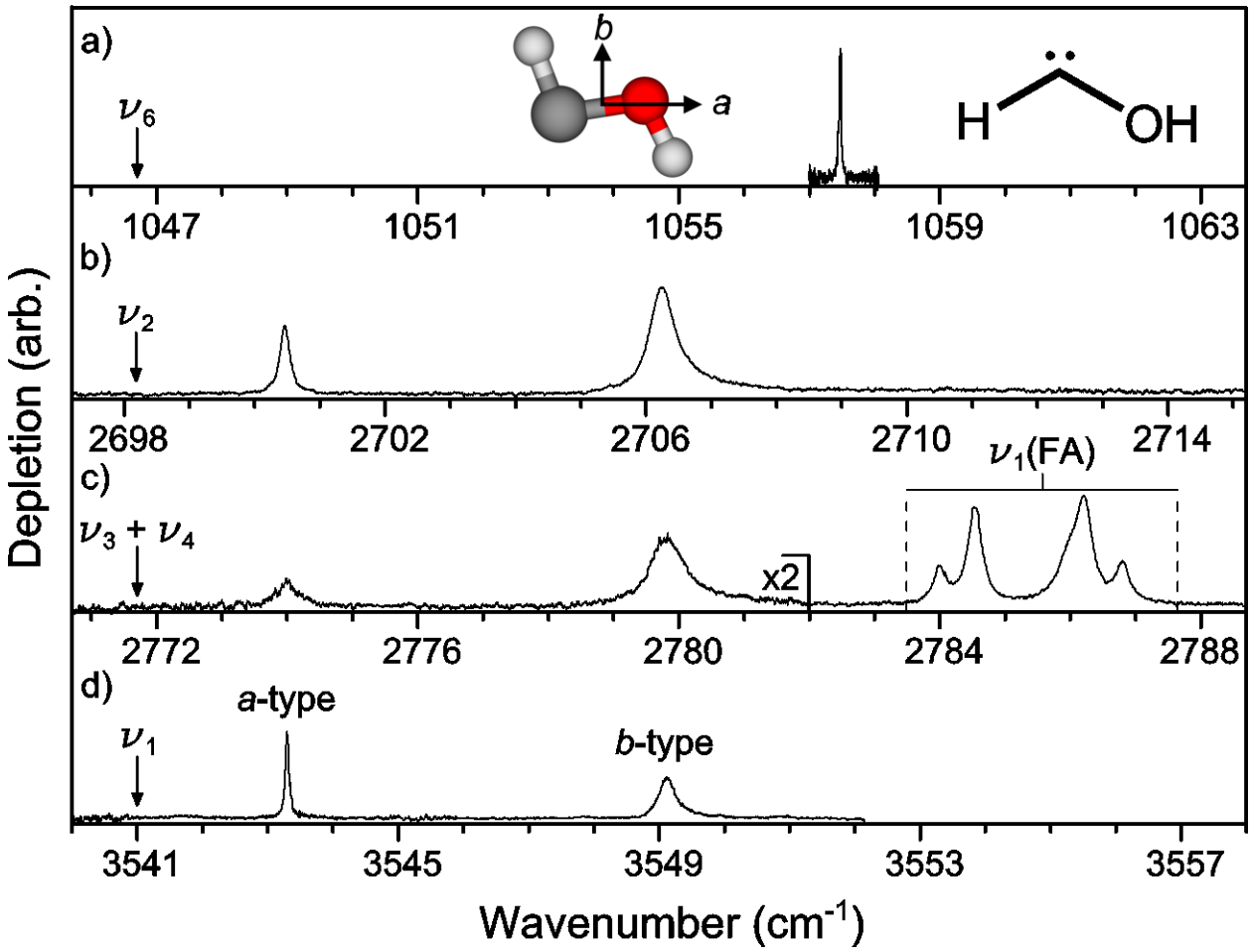

Figure 6.4: Infrared spectra highlighting the a) ν_6, b) ν_2, c) $\nu_3+\nu_4$ and d) ν_1 vibrational bands of *trans*-HCOH. Assignment of these bands was aided by anharmonic frequency computations.[51,52] Each band is split into *a*-type and *b*-type transitions, except ν_6, which consists of a single *c*-type transition. Lower estimates of the vibrational band origins, indicated by the black arrows, are obtained using the computed (CCSD(T)/cc-pVTZ) rotational constants.

computations, a lower limit to the vibrational band origin ($0_{00}\leftarrow 0_{00}$) can be estimated by subtracting the computed (*B*+*C*) value (CCSD(T)/cc-pVTZ) from the centroid of the *a*-type transition, and these are indicated by the arrows in Figure 6.4 and collected in Table 6.1. In addition to these three bands, we measured a single transition at 1057.48 cm^{-1}, falling near the computed and experimental Ar-matrix ν_6 band origin.[51,52] A single *c*-type transition is expected for this *a″* band, and we estimate a lower limit for the band origin to be 1046.69 cm^{-1} using the

Table 6.1: Experimental and computed vibrational band origins and rotational constants (cm^{-1}) for *trans*-HCOH and *trans*-HCOD. Relative intensities are given in parentheses.

Assignment[a]	Matrix[b]	Variational Computation[b]	VCI[c]	VPT2[d]	He droplet[e]	$(A'-B')^f$
trans-HCOH						
ν_6	1048.5(100)	1058.9	1060(100)	1051(100)	1046.69(41)[†]	
$\nu_3+\nu_5$	[g]		2622(19)		[g]	
ν_2	2703.3(42)(100[*])	2706.5	2691(97)(100[*])	2690(60)(100[*])	2698.18(100)	5.80
$\nu_3+\nu_4$	2776.2(18)(43[*])	2785.5	2776(20)(21[*])	2774(26)(43[*])	2771.72(42)	5.84
ν_1	3500.6(49)	3561.6	3553(43)	3553(56)	3541.01(29)	5.83
trans-HCOD						
ν_2	2588.1(100)	2626.8	2622(100)	2623(100)	2614.32(66)	4.12
ν_1	2675.9(34)	2682.8	2669(55)	2664(29)	2672.00(35)	4.15
$\nu_3+\nu_4$	2726.1(51)	2729.5	2713(33)	2722(73)	2720.55(100)	4.14
$2\nu_3$	2841.3(14)	2852.6	2851(17)	2853(34)	2838.75(35)	4.19

[a] Harmonic descriptions of the vibrational modes for *trans*-HCOH are ν_1: OH stretch, ν_2: CH stretch, ν_3: in-phase HOC/COH bending, ν_4: CO stretch, ν_5: out-of-phase HOC/COH bending, and ν_6: out-of-plane twist, and ν_1: CH stretch, ν_2: OD stretch, ν_3: HOC bend, ν_4: CO stretch, ν_5: COD bend, and ν_6: out-of-plane twist for *trans*-HCOD.

[b] The variational computations were obtained at the AE-CCSD(T)/cc-pCVQZ level of theory.[51]

[c] Vibrational configuration interaction (VCI) computation.[52]

[d] Vibrational perturbation theory computations at the CCSD(T)/cc-pVTZ level of theory. This work.

[e] Reported values are lower limits for the vibrational band origins, which assume $(B+C)$=2.284 cm^{-1} for HCOH or 2.107 cm^{-1} for HCOD obtained from CCSD(T)/cc-pVTZ computations. The He contribution to the effective moments of inertia about the inertial *b*- and *c*-axes is unknown for this system; therefore, we simply give lower limits but note that the band origins are likely to be centered ~0.5 cm^{-1} to the blue of those reported here.

[f] The computed $(A-B)$ value is 8.365 cm^{-1} for HCOH and 6.156 cm^{-1} for HCOD at the CCSD(T)/cc-pVTZ level of theory. The experimental 2σ error is less than 0.003 cm^{-1}.

[g] Not observed.

[†] Origin obtained using $(A+B)$=10.785 cm^{-1} from CCSD(T)/cc-pVTZ computation

[*] Relative intensities of the two components of the $\nu_2/(\nu_3+\nu_4)$ Fermi dyad.

computed A+B rotational constant. A comparison of the experimentally determined vibrational band origins from the He droplet spectra to those computed and obtained from the matrix FT-IR spectra are collected in Table 6.1. The band origins measured in this study are all within 20 cm^{-1} of the computed values. The satisfactory agreement between the computed and He droplet band origins is indicative of negligible solvent shifts, which is expected on the basis of a number of previously reported spectra of He-solvated hydrocarbon molecules.[63,64] Because the low temperature of the droplets results in a sparse number of rovibrational lines, it is not possible to extract the true band origin.

Figure 6.5 presents the infrared spectrum of the isotopically labeled, d_1-*trans*-hydroxymethylene (HCOD). Vibrational spectra were collected on mass channel 30 u to discriminate against the undeuterated species. Four pairs of transitions (Figure 6.5) are identified in the spectrum near the computed frequencies of *t*HCOD. The increased reduced mass upon deuteration decreases the rotational constants, with the computed (CCSD(T)/cc-pVTZ) value of (A–B) reduced by ~26% upon deuteration of the hydroxyl group. Assuming a similar droplet effect for both HCOH and HCOD, we predict a splitting of 4.28 cm^{-1} between the *a*- and *b*-type lines in the spectrum of *t*HCOD, based on the computed reduction in the rotational constants. The observed splitting is 4.15 cm^{-1} on average, and the band origins are in good agreement with anharmonic frequency computations. Therefore we assign these four bands to the ν_2, ν_1, ν_3+ν_4 and $2\nu_3$ transitions of *t*HCOD, with the lower estimate of the band origins and a zero-order description of the vibrational modes presented in Table 6.1. Overall, the computed frequencies obtained using both the variational and VCI methods are within 1% of the experimentally determined band origins for He-solvated *t*HCOH and *t*HCOD.

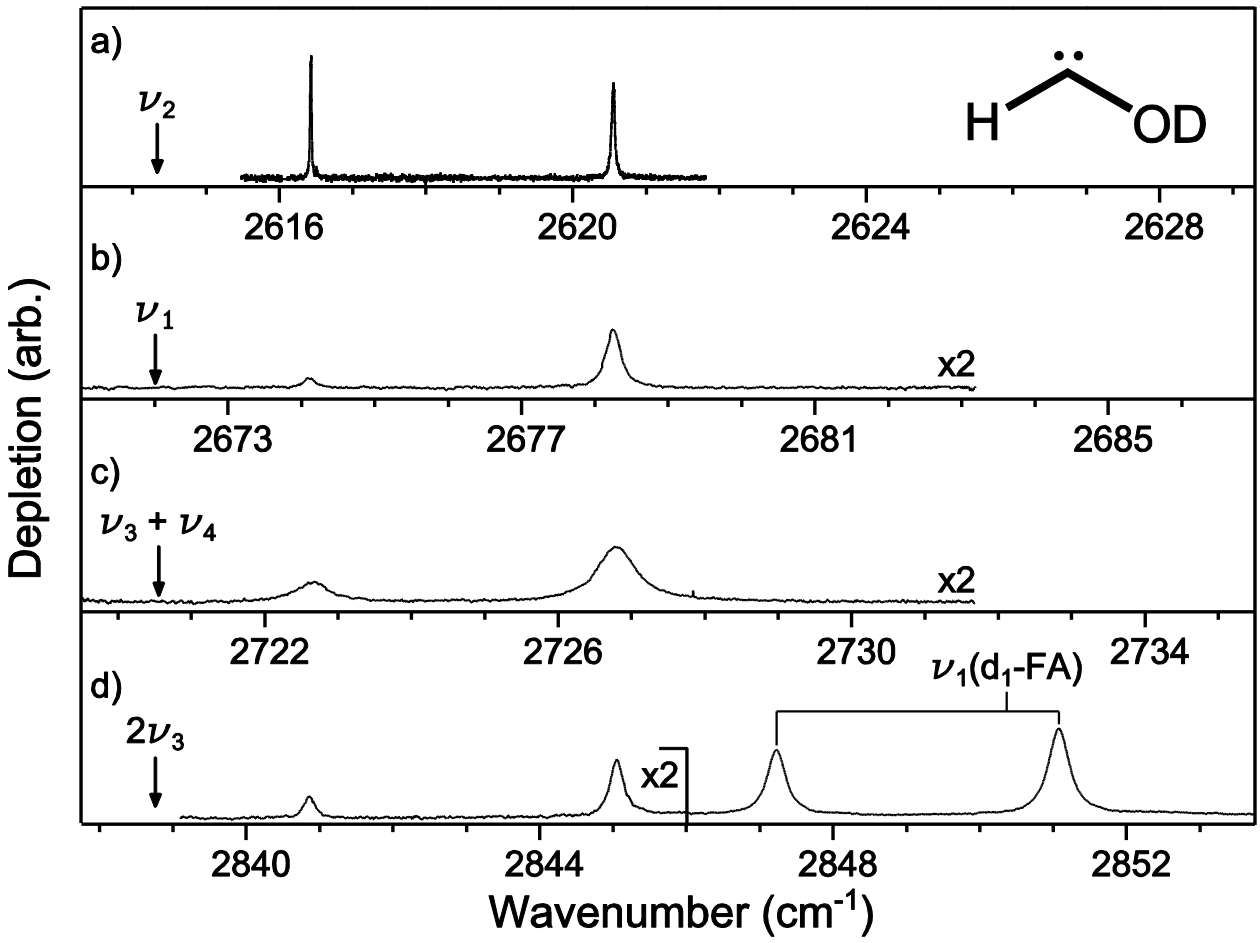

Figure 6.5: Infrared spectra highlighting the a) v_2, b) v_1, c) v_3+v_4 and d) $2v_3$ vibrational bands of *trans*-HCOD. Assignment of these bands was aided by anharmonic frequency computations.[51,52] Each band is split into *a*-type and *b*-type transitions. Lower estimates of the vibrational band origins, indicated by the black arrows, are obtained using the computed (CCSD(T)/cc-pVTZ) rotational constants.

From Lorentzian fits of the *a*- and *b*-type lines in the He droplet spectrum, we obtained the relative projection of the vibrational transition dipole moment for each transition. Using the CFOUR computational chemistry and spectroscopy package,[75] we computed anharmonic frequencies at the CCSD(T)/cc-pVTZ level with the ANO2 basis set,[76,77] making use of second-order vibrational perturbation theory (VPT2).[78] The results from these computations are summarized in Table 6.1, along with the previously reported computations. The predicted

frequencies for ν_1 and ν_6 are in good agreement (within 12 cm^{-1}) with the experimentally determined band origins; additionally these computations are also consistent with the other two sets of calculated anharmonic frequencies.[51,52] Previous variational computations indicated a large degree of mixing between ν_2 and $\nu_3+\nu_4$,[51] and the presence of an appreciable Fermi resonance was confirmed by the harmonic derivative analysis.[79] Standard deperturbation and diagonalization of an effective Hamiltonian yields frequencies within 8 cm^{-1} of the experimental band origins. Furthermore, the effective Hamiltonian matrix element that mixes the dressed ν_2 and $\nu_3+\nu_4$ states is 38 cm^{-1}, in pleasing agreement with the experimentally-inferred value of 34 cm^{-1}.[80] Similarly good agreement with the observed level positions is achieved for HCOD, and it is clear that the VPT2 computations do a serviceable job of predicting the relative intensities of the Fermi tetrad (again obtained by a deperturbation + diagonalization treatment) comprising ν_1, ν_2, $2\nu_3$, and $\nu_3 + \nu_4$. The relative intensities obtained with this approach are in vastly better agreement with experiment in comparison to previous computations. For the normal isotopic species, the projections of the transition dipole moment onto the *a*- and *b*-axes computed by the GUINEA module of CFOUR are [81:100], [52:100] and [48:100] for ν_1, $\nu_3+\nu_4$ and ν_2, respectively, compared to the experimental values of [67:100], [45:100] and [49:100]. For *t*HCOD the transition dipole moment projections onto the *a*- and *b*-axes are [77:100], [36:100], [55:100] and [56:100] for ν_2, ν_1, $\nu_3+\nu_4$ and $2\nu_3$, respectively, which compare favorably to the computed values of [84:100], [49:100], [64:100] and [56:100].

We are confident in the comparison of the ν_2 and $\nu_3+\nu_4$ band intensities in the *t*HCOH spectrum, given the similar experimental conditions with which these bands were recorded; however, the ν_1 and ν_6 intensities cannot be compared to the others directly. The ν_1 band falls near a problematic region of the laser, due to MgOH impurities in the PPLN crystal that result in

a dramatic reduction in the output power; ν_6 was collected with a quantum cascade laser (QCL), where the output power is ~20 times less than the idler output of the OPO. Additionally, vibrational relaxation of the ν_6 mode results in fewer evaporated He atoms, leading to a smaller laser induced depletion signal when compared to the higher frequency bands. The experimental relative intensities for *t*HCOD are far more reliable, given that all of the bands were recorded with similar laser conditions. Regardless of these caveats, the relative band intensities for He-solvated *t*HCOH and *t*HCOD are compared in Table 6.1 to the previously reported Ar matrix[51] and computed intensities from the VCI[52] and VPT2 computations. The relative intensities of ν_2 and $\nu_3+\nu_4$ (100:42) are approximately identical in both the He droplet and Ar-matrix studies when these two modes are considered independent of all other transitions. The $\nu_3+\nu_4$ combination band intensity relative to ν_2 is underestimated by a factor of two in the VCI computation, while a ratio of (100:43) is obtained from the VPT2 computation for these two modes (Table 6.1), which is nearly identical to the experimental value. One drastic difference between the VCI computation and both the matrix FT-IR and He spectra is the absence of the $\nu_3+\nu_5$ combination band predicted for *t*HCOH. This mode was found to be very sensitive to the computational method employed, with VMP2 predicting this mode 75 cm^{-1} higher in energy compared to the VCI value.[52]

From the matrix isolation spectra reported by Schreiner and co-workers,[51] it was determined that the ratio of HCOH to FA was 1:5.5, using the relative intensities of bands assigned to FA and HCOH scaled to the corresponding computed harmonic intensities. In a similar fashion, we estimate a ratio of 1:2.4. A combination of the rapid cooling inherent to He droplets,[81-83] and the millisecond timescale of the experiment could indeed yield the larger ratio of HCOH to FA observed in the He droplet experiment. The survey scan (Figure 6.3) did not

reveal any lines that could be assigned to the *cis*-conformation of hydroxymethylene (*c*HCOH), although the VCI computations[52] predict the $\nu_3+\nu_5$ combination band to be the only transition with significant intensity (>10 km/mol) in the surveyed region. The higher energy *c*HCOH was also not observed in the matrix spectrum, and this was rationalized as being due to the CO_2 extrusion process preferentially forming *t*HCOH.[51]

Lastly, we comment on the variable width associated with each vibrational band. For example, the *a*-type line widths for the ν_1 and $\nu_3+\nu_4$ bands of *t*HCOH are 0.065 and 0.37 cm^{-1}, respectively. This dramatic difference clearly cannot be attributed solely to the different state density of droplet phonon modes at the energy of the oscillator, as an opposite trend would be expected. Several previous reports of He-solvated hydrocarbon molecules, such as C_2H_2,[84] C_2H_4,[85] and C_2H_5,[86] have discussed vibrational state-dependent broadening in the high-frequency CH stretch region. Although a clear physical picture has yet to emerge, it is becoming increasingly evident that transitions to vibrational levels strongly mixed by mechanical anharmonicity are homogeneously broadened to an extent that is far greater than observed for more weakly coupled modes. Indeed, for *t*HCOH, the observed transitions within the $\nu_2/(\nu_3+\nu_4)$ Fermi dyad are broader than the analogous transitions within the ν_1 OH stretch, despite the latter mode lying ~800 cm^{-1} higher in energy. Invoking a simple model where a single bright state (i.e. CH stretch) is coupled to the bath of droplet states, through some series of doorway states (i.e. lower frequency vibrations and rotations), stronger coupling of the bright state to the doorway states could give rise to a more rapid decay of the vibrational resonance into the helium bath. Time resolved experiments are clearly needed in combination with theory to elucidate the rich vibrational dynamics operative in this dissipative superfluid environment.

6.4 Dihydroxycarbene (HOCOH)

6.4.1 Theoretical Methods

For comparison with experimental work, the singlet *trans,trans*-, *trans,cis*-, and *cis,cis*-HOCOH isomers were investigated with electronic structure theory, using the CFOUR quantum chemistry package.[75] Equilibrium geometries were obtained at two separate levels of theory: frozen core, coupled cluster singles and doubles with perturbative triples corrections (CCSD(T))[87]/ANO1[76] and all-electron CCSD(T)/cc-pCVQZ.[88] Ground state equilibrium rotational constants were determined at the CCSD(T)/cc-pCVQZ level of theory. Fundamental frequencies, corresponding infrared intensities as well as state-specific vibrationally averaged dipole moments and inertial components of the vibrational transition dipole moments were determined using second-order vibrational perturbation theory (VPT2)[78] at the frozen-core CCSD(T)/ANO1 level using the GUINEA module of CFOUR.[79] The optimized geometry of the lowest triplet *trans,trans*- isomer was also determined, revealing a zero-point corrected singlet-triplet energy gap of 61.7 kcal/mol at the frozen core CCSD(T)/ANO1 level of theory. Results from these calculations are presented in Table 6.2.

Table 6.2: Experimental and computed molecular properties of dihydroxycarbene rotamers. [a]

	***trans,trans-* (b_2)**		***trans,trans-* (a_1)**		***trans,cis-* (a')**		
	Helium	**Theory [b]**	**Helium**	**Theory [b]**	**Helium**	**Theory [b]**	**Gas [c]**
$\lvert\mu_a''\rvert$ (D)	–	0	0	0	1.63(3)	1.674	–
$\lvert\mu_b''\rvert$ (D)	–	0.661	0.68(6)	0.661	1.50(5)	1.705	–
$\lvert\mu_a'\rvert$ (D)	–	0	0	0	1.66(3)	1.709	–
$\lvert\mu_b'\rvert$ (D)	–	0.686	0.68(6)	0.687	1.50(5)	1.678	–
A''	1.45	2.86 [d]	1.45	2.86 [d]	1.55	2.4945 [d]	2.4853
A'	1.6	–	1.6	–	1.55	–	–
$\bar{B}''$	0.276	0.40 [d]	0.284	0.40 [d]	0.306	0.3878 [d]	0.3841
$\bar{B}'$	0.273	–	0.261	–	0.301	–	–
$(B-C)''$	0.12	0.05 [d]	0.12	0.05 [d]	0.15	0.0599 [d]	0.0597
$(B-C)'$	0.12	–	0.12	–	0.15	–	–
ν_0 [e]	3655.438	3660.3 (192.4)	3658.305	3664.1 (17.7)	3649.915	3656.1 (106.8)	–
$\dot{\mu}_a/\dot{\mu}_b$ [f]	*a*-type	*a*-type	*b*-type	*b*-type	2.63(6)	2.50	–

[a] Units in cm^{-1} unless otherwise specified.

[b] Equilibrium *ab initio* rotational constants at the CCSD(T)/cc-pCVQZ level of theory. VPT2-corrected *ab initio* dipole moments at the CCSD(T)/ANO1 level of theory.

[c] Ref. [57].

[d] The discrepancy between experimental He droplet and computed rotational constants is due to the well-known effect by which the He solvent contributes to the rotational moment of inertia of the molecule.[63-65]

[e] Uncertainties in He droplet band origins are ±0.001 cm^{-1}. Theoretical band origins, intensities (in parentheses) and transition dipole moment components are obtained via VPT2 at the CCSD(T)/ANO1 level of theory. The computed band origin for the lower frequency, unobserved a' band of the *trans,cis-* isomer is 3385.7 (6.2). Theoretical band origins and intensities for the *cis,cis-* isomer are (b_2) 3258.7 (42.5) and (a_1) 3308.6 (6.0). For comparison to the He droplet spectra, Argon matrix band origins of the *trans,trans-* (b_2), *trans,trans-* (a_1), and *trans,cis-* (a') vibrations are 3625.1, 3633.2/3628.6, and 3618.3 cm^{-1}, respectively.[53]

[f] Ratio of transition dipole moment components along the *a* and *b* inertial axes.

6.4.2. Results and Discussion

Electron impact ionization mass spectra (MS) of the neat and doped He droplet beam under various conditions are shown in Figure 6.6. Figure 6.6a shows the MS of the neat droplet beam, and the peaks separated by 4 u are assigned to a distribution of He cluster cations produced via the following mechanism (Equation 1), where m = 2, 3, ..., n.

$$\begin{aligned} (He)_n + e^- &\rightarrow He^+(He)_{n-1} + 2e^- \\ &\rightarrow (He)_2^+(He)_{n-2} + 2e^- \\ &\rightarrow (He)_m^+ + (n-m)\,(He) + 2e^- \end{aligned} \qquad \textbf{(Eq. 6.1)}$$

Upon heating the oxalic acid sample to 330 K, an intense peak at m/z = 45 u appears (Figure 6.6b), which is consistent with the primary product $(OCOH)^+$ observed upon electron-impact ionization of gas-phase oxalic acid.[89] The ionization and fragmentation of He-solvated oxalic acid occurs via the mechanism shown in Equation 6.2. Because of the large mismatch between the ionization potential of He and oxalic acid (≈14 eV), the dopant is ionized via charge transfer and readily fragments, producing $(OCOH)^+$.

$$\begin{aligned} (C_2H_2O_4)(He)_n + e^- &\rightarrow (C_2H_2O_4)He^+(He)_{n-1} + 2e^- \\ &\rightarrow (C_2H_2O_4)^+(He)_n + 2e^- \\ &\rightarrow (OCOH)^+ + (CHO_2)^* + n(He) + 2e^- \end{aligned} \qquad \textbf{(Eq. 6.2)}$$

The MS in Figures 6.6b to 6.6d are obtained with increasing pyrolysis filament current, with the top MS recorded under conditions that lead to the near complete decomposition of the oxalic acid precursor. The signature of this decomposition is both the dramatic reduction of m/z=45 u and the appearance of $(OCO)^+$ and $(HCO)^+$, the latter of which is the major ionization product of He-solvated HOCOH (*vide infra*).

The IR spectrum of oxalic acid in the OH stretch region was measured by monitoring the laser-induced depletion of ion signal in mass channel 45 u $(OCOH)^+$, and the results are shown in the bottom frame of Figure 6.7. Several bands are assigned to three separate conformers on the basis of comparisons to previous Ar matrix spectra of Fausto and co-workers.[90] The most intense band at 3475.40 cm^{-1} corresponds to the lower-frequency OH-stretching mode of the doubly intramolecular hydrogen bonded *cTc* (*cis*-*Trans*-cis) conformer (C_{2h} symmetry). The higher energy *cTt* and *tTt* conformers are also present, which give rise to three additional weak bands at 3520.66 cm^{-1}, 3576.84 cm^{-1}, and 3602.21 cm^{-1}. The structures of the three lowest energy oxalic acid conformers, *cTc*, *cTt*, and *tTt*, are shown as insets in Figure 6.7.

As was the case in the measurement of the IR spectrum of hydroxymethylene, we found $(HCO)^+$ to be a major ionization product of the HCOH doped He beam, and ion signal in this channel was substantially modulated by upstream laser-induced excitation of He-solvated HCOH. Our initial search for HOCOH under high-temperature pyrolysis conditions (≈1000 K) was therefore also carried out on mass channel 29 u. The top frame of Figure 6.7 shows the result of this survey scan, which consists of three distinct regions that contain OH stretch bands. The broad feature near 3470 cm^{-1} is due to residual signal from the unpyrolyzed *cTc* oxalic acid conformer. A series of sharp peaks centered around 3570 cm^{-1} are assigned to a Fermi triad involving the OH stretch of formic acid, and these bands have been observed and analyzed

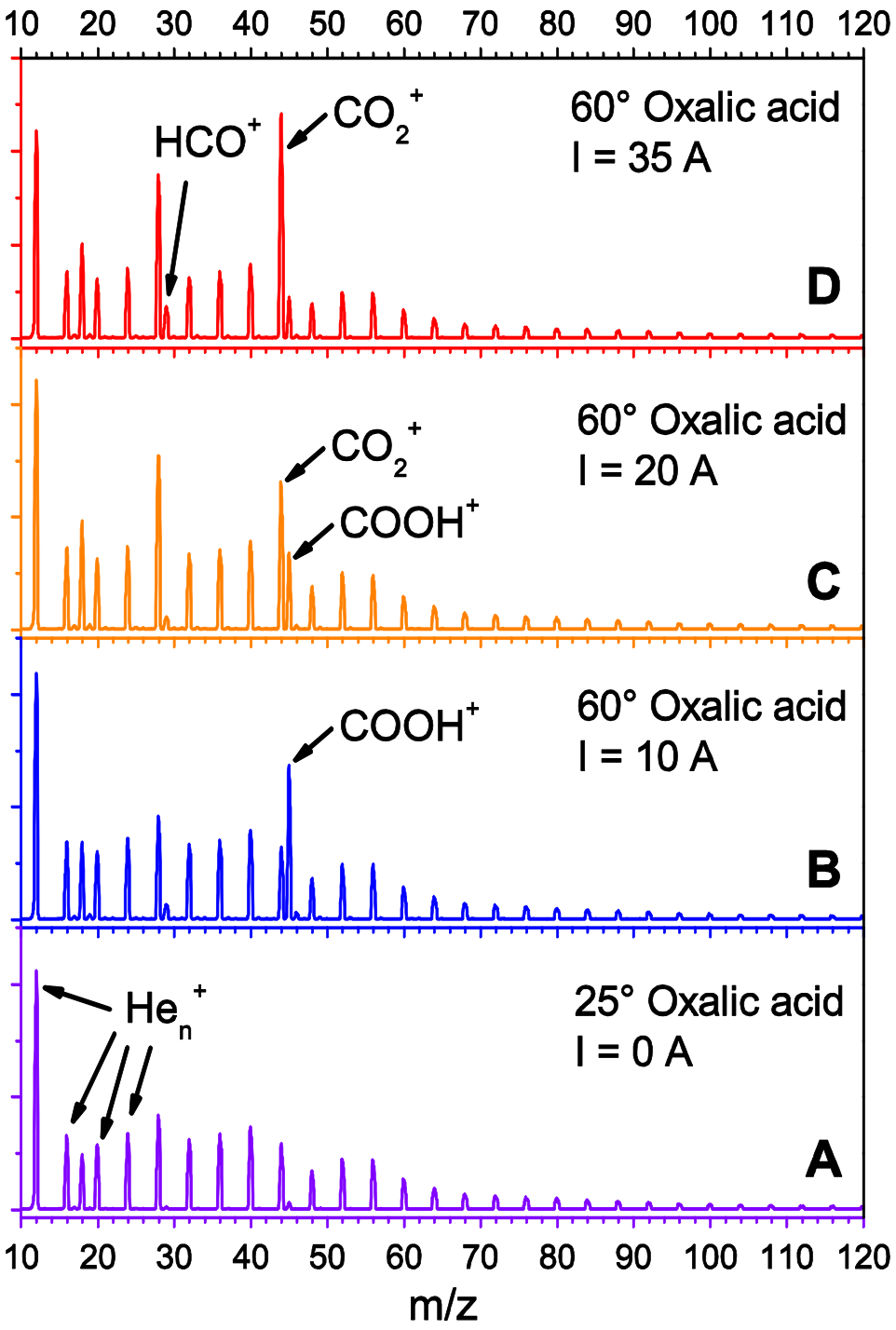

Figure 6.6: The mass spectrum of the neat helium droplet beam is shown in frame A. Frames B through D are mass spectra of the droplet beam after having passed through the heated oxalic acid source operated under various pyrolysis source conditions (filament current in Amps). Pyrolytic decomposition of oxalic acid is indicated by the rapid increase in m/z=44 u (assigned to OCO^+) with increasing filament current. Spectra of oxalic acid are obtained under condition B, whereas spectra of dihydroxycarbene are obtained under condition D.

previously.[90] Another set of sharp peaks centered near 3655 cm^{-1} are due to neither the precursor nor formic acid, yet they are approximately 30 cm^{-1} to the blue of the OH stretch bands assigned to HOCOH trapped in an Ar matrix (arrows in Figure 6.7). Computed anharmonic spectra are shown in the stick spectrum below the survey scan, where the red, blue and green lines are OH stretch band origins for the *trans,trans*-, *trans,cis*- and *cis,cis*-HOC̈OH rotamers, respectively. The computations for the *trans,trans*- (both OH stretch bands) and *trans,cis*- rotamers (highest frequency OH stretch band) are in good agreement with the set of sharp transitions observed near 3655 cm^{-1}. However, there is no evidence for the *cis,cis*-rotamer in the survey spectrum, and there is no obvious spectral feature near the computed band origin of the much weaker, lower frequency OH stretch band of the *trans,cis*- rotamer.

A higher resolution scan of the region centered around 3655 cm^{-1} is shown in Figure 6.8, revealing three rovibrational bands that can be assigned unambiguously to OH stretch bands of HOCOH rotamers. Line widths of individual features within each band are ≈0.07 cm^{-1}, allowing for an analysis of rotational fine-structure. The red simulation below the experimental spectrum is based on a summation of three separate asymmetric top spectra, each with a 0.35 K rotational temperature and rotational constants summarized in Table 6.2. The patterns associated with the bands centered near 3656 and 3660 cm^{-1} are consistent with *a*- and *b*-type selection rules, respectively. Moreover, to satisfactorily simulate the relative intensities within each band, a 1:3 nuclear spin weight ratio must be imposed for even:odd (K_a+K_c) rotational levels, consistent with a C_{2v} symmetry species having equivalent hydrogen atoms. Given these spectral features, we assign these two bands to the a_1 symmetric (*b*-type) and b_2 antisymmetric (*a*-type) OH stretching bands of *trans,trans*-HOCOH. The band origins for these modes are 3658.305 and 3655.438 cm^{-1}, respectively. The lowest frequency rovibrational band in Figure 4 is an *a,b*-

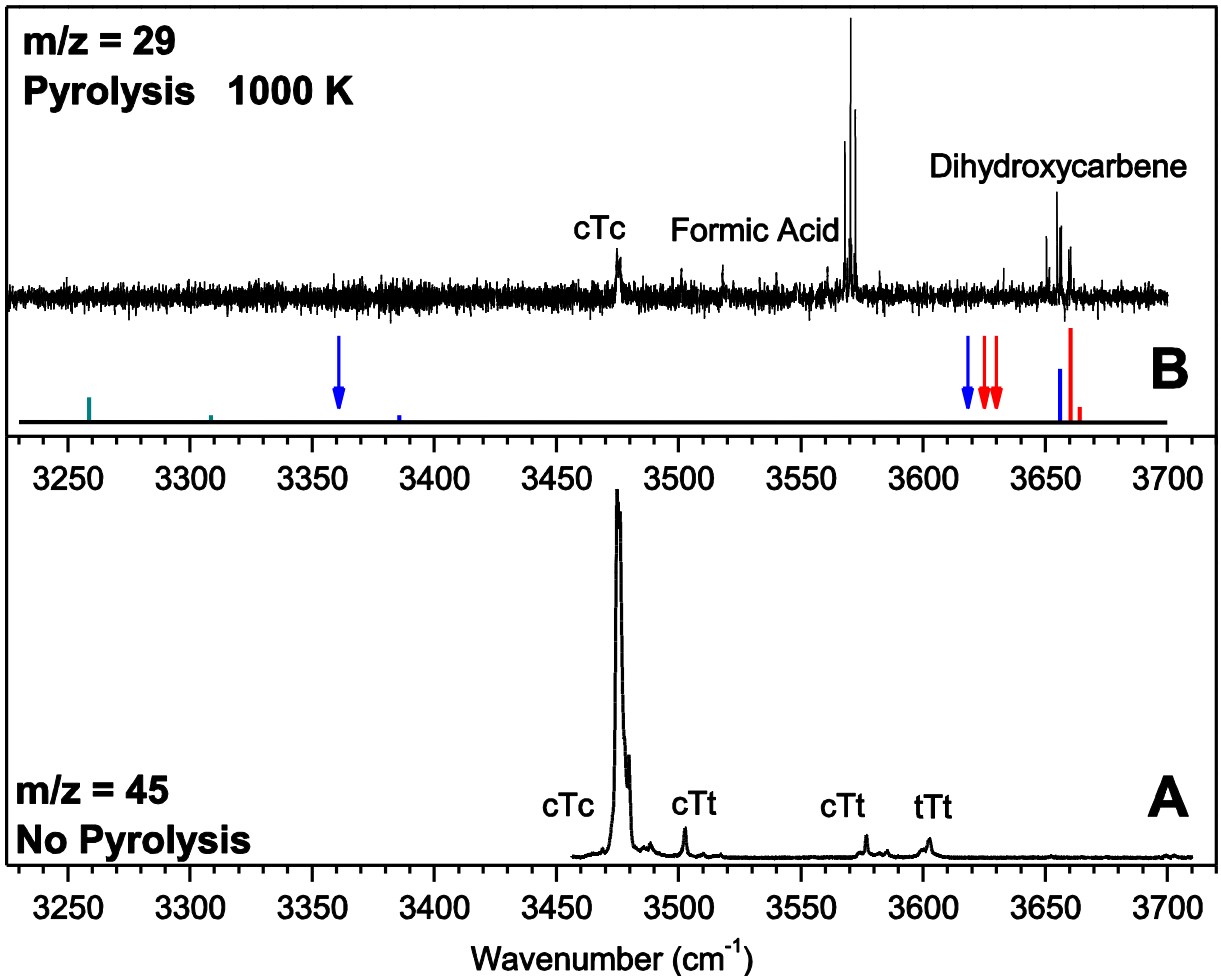

Figure 6.7: Survey spectra of the oxalic acid precursor (frame A) and the products of pyrolysis (frame B). Mass channels correspond to either 45 ($OCOH^+$) or 29 (HCO^+) for the precursor and pyrolysis spectra, respectively. Near complete decomposition of the oxalic acid precursor is achieved with a pyrolysis temperature near 1000 K, and a series of sharp bands are observed that can be assigned to either formic acid or dihydroxycarbene (top spectrum). The stick spectrum corresponds to computed band origins of *trans*,*trans*- (red), *trans*,*cis*- (blue), and *cis*,*cis*-HOCOH (green), and stick heights reflect the computed IR intensities. The arrows indicate the band origins reported for *trans*,*trans*- (red) and *trans*,*cis*-HOCOH (blue) isolated in an Ar matrix.

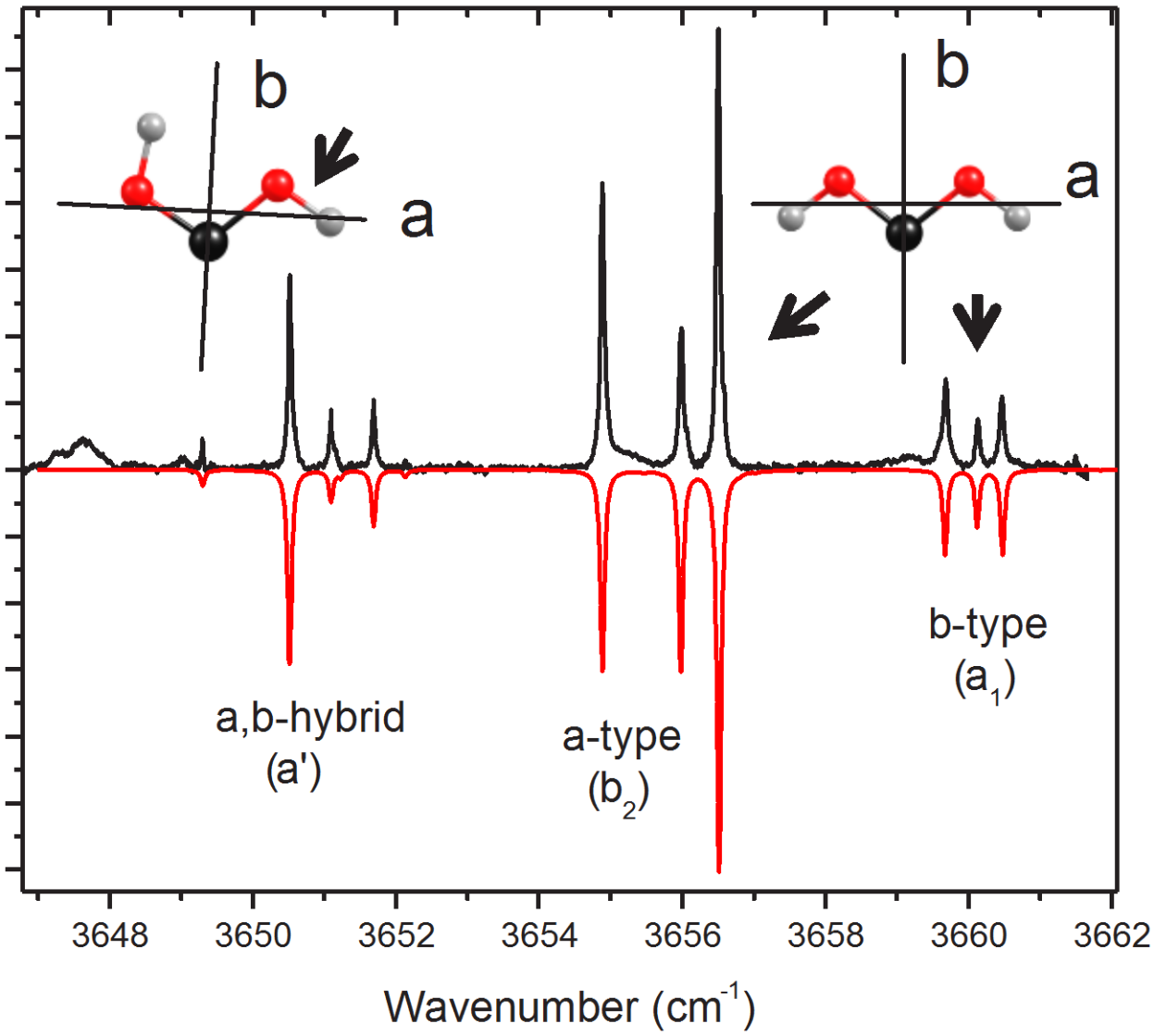

Figure 6.8: Rovibrational spectrum of *trans,trans*- and *trans,cis*-HOCOH rotamers in the OH stretch region. A simulation (red) derived from an asymmetric top Hamiltonian is shown below the experimental (black) spectrum. Assignments are based on band-types and nuclear spin statistical weights. Pure *b*- and *a*-type bands are observed for the symmetric and antisymmetric OH stretching vibrations of the C_{2v} *trans,trans* rotamer, respectively. The *a,b*-hybrid band corresponds to the higher frequency OH stretch of the C_s symmetry *trans,cis*- rotamer. The spectrum was measured under relatively low laser power conditions, so as to minimize saturation effects.

hybrid band, which has relative transition intensities consistent with a nuclear spin statistical weight ratio equal to 1:1. This hybrid band (a:b = 2.6), centered at 3649.915 cm^{-1}, must therefore be associated with a C_s symmetry species having non-equivalent hydrogen atoms. Because of these characteristic signatures, we assign this band to the higher frequency OH stretch (a') of the *trans*,*cis*-HOCOH rotamer. The structures and inertial axes of these two rotamers are shown as insets to Figure 6.8. The assignments are further justified by the comparison of experimental band origins and relative transition moment projections to those computed with VPT2. Each of the three bands are 5 to 6 cm^{-1} to the red of the computed values, given the above assignments. In several previous studies of He-solvated molecules, it was found that the band origins of higher-frequency X−H stretching modes were shifted by less than 1 cm^{-1} from their gas-phase values. Therefore, the excellent agreement between theory and experiment provides strong confidence in the above assignments.[72,73,86,91-93] These assignments imply rather large Ar matrix shifts of the high-frequency OH stretch bands of dihydroxycarbene,[36] which are ≈30 cm^{-1} to the red of the band origins of the He-solvated species.

Stark spectra at several field strengths were recorded for the *a*,*b*-hybrid and pure *b*-type rovibrational bands. A selection of Stark spectra for the hybrid band is shown in Figure 6.9, along with the zero-field spectrum for comparison. The electric field lifts the 2J+1 rotational state M-degeneracy, which leads to shifts and splitting of individual rovibrational lines and the appearance of a peak near the band origin that gains intensity with increasing field strength. A satisfactory simulation of these effects requires ground state inertial dipole components μ_a = 1.63(3) and μ_b = 1.50(5) D, where the error bars are derived from both the uncertainty in the field strength and the sensitivity of spectral changes to small changes in dipole components. Moreover, to obtain the best agreement between experiment and simulation, a slight increase in

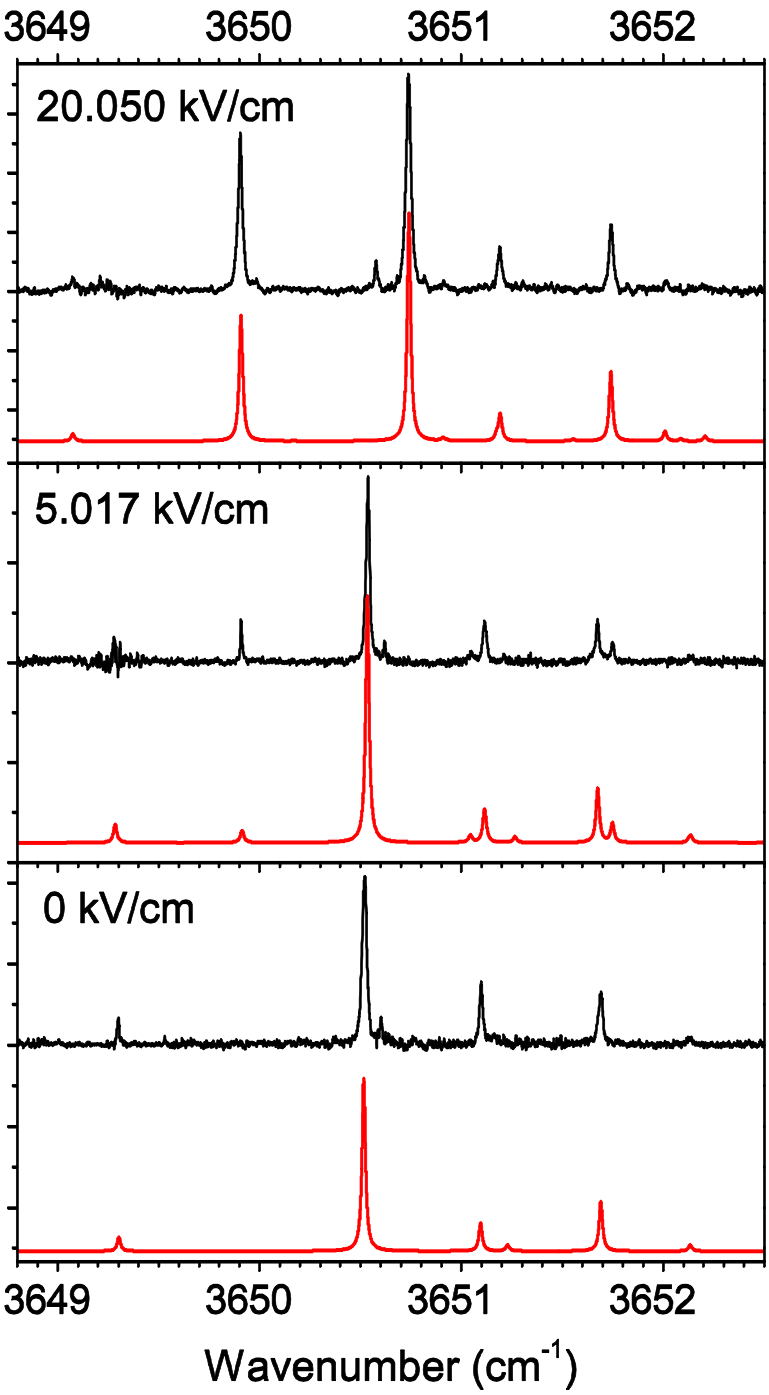

Figure 6.9: Zero-field (bottom) and Stark spectra of the highest frequency OH stretch *a*,*b*-hybrid band of *trans*,*cis*-HOCOH. The laser electric field is aligned parallel to the static, dc, Stark field, the strength of which is noted in each frame. Simulations are generated assuming a semi-rigid asymmetric top in a Stark field, and the constants that parameterize these simulations are given in Table 6.2.

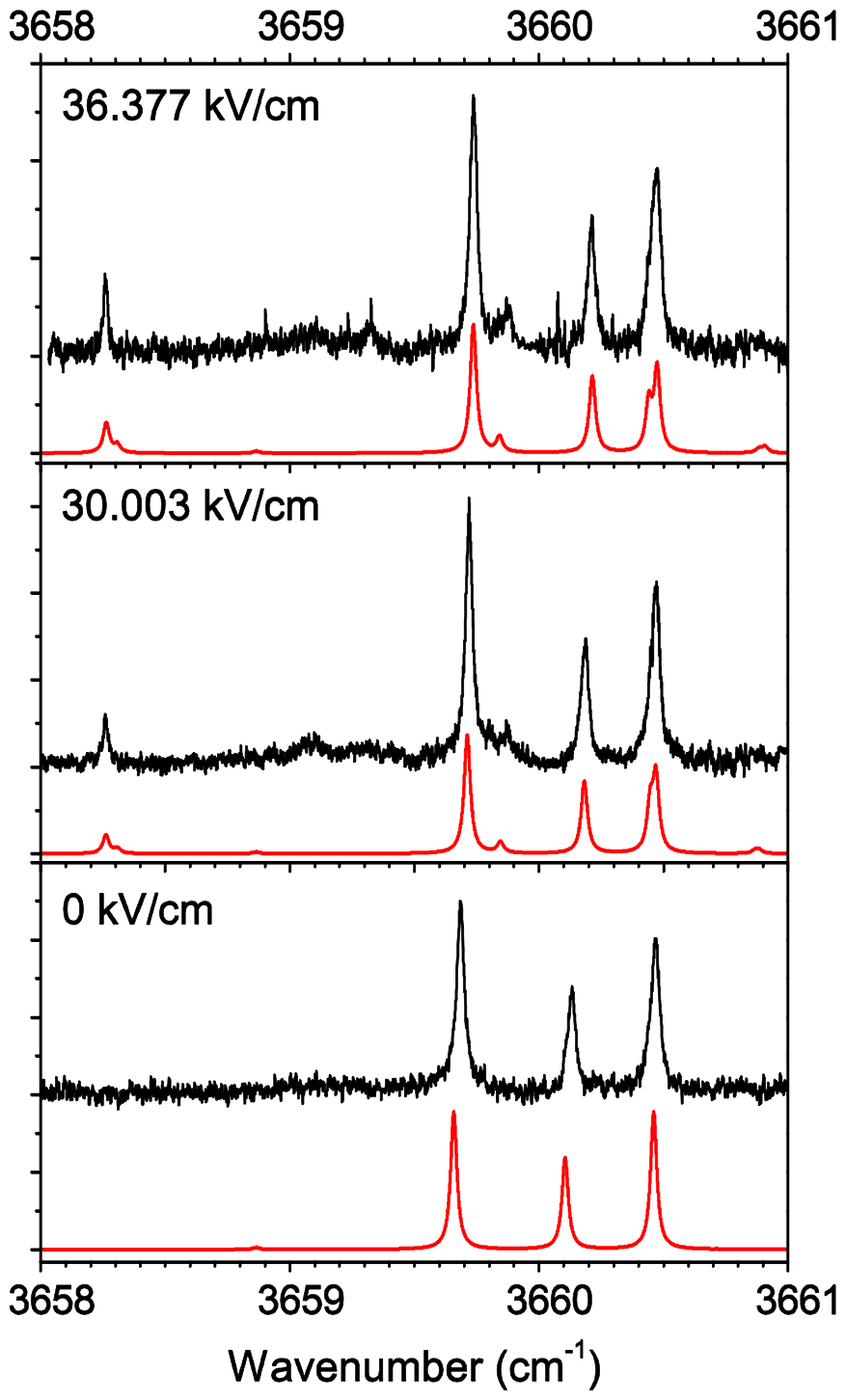

Figure 6.10: Zero-field (bottom) and Stark spectra of the OH stretch *b*-type band of *trans*,*trans*-HOCOH. The laser electric field is aligned parallel to the static, dc, Stark field, the strength of which is noted in each frame. Simulations are generated assuming a semi-rigid asymmetric top in a Stark field, and the constants that parameterize these simulations are given in Table 6.2.

μ_a is required upon vibrational excitation, the sign and magnitude of which is also found by the VPT2 calculations. Stark spectra of the pure *b*-type band are shown along with simulations in Figure 6.10. Constraining the *a* component of the dipole moment to zero (C_{2v} symmetry), the shifts and splitting of *b*-type lines and the rate at which the normally forbidden transition near the band origin grows are best simulated with μ_b = 0.68(6) D. Here, the uncertainty is somewhat higher because the spectral shifts are less sensitive to changes in electric field strength, in comparison to the *trans,cis*- Stark spectra. These experimental inertial dipole components are compared to the vibrationally averaged values from VPT2 in Table 6.2. The rather good agreement between experiment and theory observed here provides additional support to the above assignments.

The abundance of individual carbene rotamers can be determined by normalizing the integrated band areas to computed intensities, giving a 2:1 *trans,trans*- to *trans,cis*- ratio. Again, there is no evidence for the *cis,cis*- rotamer in He droplets, and there was also no evidence for it in the Ar matrix.[53] These observations are consistent with a unimolecular decomposition mechanism of oxalic acid,[94-98] in which a concerted hydrogen migration and C−C bond cleavage produces dihydroxycarbene and CO_2. Assuming this mechanism, it is expected that the thermal extrusion of CO_2 from the *cTc* oxalic acid isomer produces *trans,trans*-HOCOH, whereas the *cTt* isomer decomposes to *trans,cis*- (see Figure 6.1). Indeed, computations of Huang and co-workers predict barrier heights for these concerted processes to be 31.1 and 32.4 kcal/mol, respectively. The reverse barrier heights are both less than 10 kcal/mol, implying a rather low internal energy content for the carbene produced via this gas-phase unimolecular decomposition. Given the large torsional interconversion barriers (≈ 17 kcal/mol) and the rapid cooling provided by He atom evaporation, we expect the relative rotamer populations in He droplets to reflect the

gas-phase populations, which are dictated by the abundance of gas-phase oxalic acid conformers at the pyrolysis source temperature. Using the energetics reported by Fausto and co-workers (B3LYP/6-31G**/ZPE corrected)[90] and taking into account structural degeneracies, we find that a Boltzmann distribution over conformers at 1000 K leads to a *cTc*:*cTt* ratio of 1.7:1, which is certainly qualitatively consistent with the 2:1 *trans,trans*- to *trans,cis*-HOCOH ratio reported here. The absence of the *cis,cis*- rotamer is apparently due to the low internal energy content of gas-phase *trans,cis*-HOCOH, which cannot rotationally interconvert prior to being captured by a He droplet. These results strongly support the oxalic acid decomposition mechanism proposed by Lapidus *et al*.[94-97]

It is more difficult to rationalize the extent to which formic acid is produced in these experiments. In the Ar matrix study, Schreiner *et al.* reported a 1:5 ratio of dihydroxycarbene to formic acid upon pyrolysis of oxalic acid.[53] Using the computed transition intensities to normalize the experimental spectra, we find an almost identical ratio here. Bands due to formic acid are absent with the pyrolysis source operated under Figure 6.6b conditions, in which the pyrolysis zone and the sample region of the quartz tube are both at ≈330 K. We observe these bands to rise sharply as the pyrolysis zone is heated above ≈700 K, while at the same time the oxalic acid sample region is kept close to 330 K. Therefore, we can rule out the possibility of formic acid being produced directly from the 330 K oxalic acid sample. In the hot pyrolysis zone, formic acid and CO_2 can, in principle, be produced via the gas-phase unimolecular decomposition of oxalic acid. However, computations by Huang and co-workers predict an approximately 70 kcal/mol barrier for the lowest energy unimolecular pathway,[98] which makes gas-phase unimolecular dissociation of oxalic acid an unlikely source of formic acid at 1000 K and on the timescale of the experiment (≈15 μs transit time through pyrolysis zone). Indeed, the

absence of the *cis,cis*-HOCOH rotamer implies, as discussed above, an oxalic acid average internal energy that is too low to overcome the barriers leading to formic acid. Huang and co-workers also discovered a bimolecular path, in which oxalic acid collides with *trans,trans*-HOCOH and catalyzes its interconversion to formic acid via a doubly intramolecular hydrogen bonded transition state.[98] The barrier for this process is 13 kcal/mol above the carbene on the potential surface. Nevertheless, using rate constants from transition state theory,[98] we estimate that the concentration of precursor molecules is simply too low in the pyrolysis zone, by several orders of magnitude, for this bimolecular path to account for the formic acid observed in the spectra. We note that the pyrolysis sources used in the He droplet and Ar matrix studies were rather similar implementations of a quartz tube furnace. Given the experimental evidence and available theory for the above mentioned gas-phase processes, it is quite possible that the formic acid derives instead from a surface catalyzed process, which facilitates the direct decomposition of oxalic acid to formic acid prior to its desorption from the quartz surface. Future work in this area may benefit from a systematic examination of alternative pyrolysis sources, such as SiC furnaces, to maximize the production of carbenes from the decomposition of α-keto carboxylic acid precursors.

6.5 Summary

Rotationally resolved spectra are obtained for *t*HCOH and *t*HCOD solvated in He nanodroplets, and the experimentally determined band origins agree with anharmonic frequency computations, and these should be only slightly perturbed from the true gas-phase values.[62,63] The isolation of this transient species in He droplets should lead to future studies probing the

reactivity of HCOH, for example with formaldehyde, providing valuable insight into the role of HCOH in the formation of simple sugars and other prebiotic chemical species.[40,44,46]

Pyrolysis of gas-phase oxalic acid produces formic acid and two of three possible rotamers of singlet dihydroxycarbene. The products of this pyrolytic decomposition are captured by helium droplets and cooled to 0.35 K. In addition to bands previously observed for formic acid, IR spectra in the OH stretch region reveal three bands exhibiting rotational fine structure. These rotationally resolved bands are assigned to the C_{2v} *trans,trans*- and C_s *trans,cis*-HOCOH rotamers on the basis of relative transition intensities within each band (revealing the vibrational symmetry and nuclear spin statistical weight ratios) and the comparison of experimental band origins to VPT2 estimates. Stark spectroscopy reveals inertial components of the permanent electric dipole moment for each of the two rotamers. Experimental inertial components of the permanent electric dipole moment compare favorably to the vibrationally averaged predictions from VPT2 calculations. The observed 5:1 formic acid to dihydroxycarbene ratio cannot be rationalized on the basis of the energetics for gas-phase oxalic acid unimolecular decomposition or other proposed gas-phase bimolecular processes. These results seem instead to imply a surface catalyzed oxalic acid decomposition mechanism.

References

(1) Raubenheimer, H. G. *Dalton Trans.* **2014**, *43*, 16959-16973.

(2) Doetz, K. H.; Stendel Jr, J. *Chem. Rev.* **2009**, *109*, 3227-3274.

(3) Wang, Y.; Xie, Y.; Wei, P.; King, R. B.; Schaefer, H. F.; von R. Schleyer, P.; Robinson, G. H. *Science* **2008**, *321*, 1069-1071.

(4) de Frémont, P.; Marion, N.; Nolan, S. P. *Coord. Chem. Rev.* **2009**, *253*, 862-892.

(5) Namitharan, K.; Zhu, T. S.; Cheng, J. J.; Zheng, P. C.; Li, X. Y.; Yang, S.; Song, B. A.; Chi, Y. R. *Nat. Commun.* **2014**, *5*, 7.

(6) Check, C. T.; Jang, K. P.; Schwamb, C. B.; Wong, A. S.; Wang, M. H. S., K. A. *Angew. Chem., Int. Ed.* **2015**, *54*.

(7) Wanzlick, H. *Angew. Chem., Int. Ed.* **1962**, *1*, 75-80.

(8) *Kinetics and Spectroscopy of Carbenes and Biradicals*; Platz, M. S., Ed.; Plenum: New York, 1990.

(9) *Reactive Intermediate Chemistry*; Moss, R. A.; Platz, M. S.; Jones, M., Jr., Eds.; Wiley: Hoboken, NJ, 2004.

(10) Kable, S. H.; Reid, S. A.; Sears, T. J. *Int. Rev. Phys. Chem.* **2009**, *28*, 435-480.

(11) Tao, C.; Ebben, C.; Ko, H.-T.; Reid, S. A. *Phys. Chem. Chem. Phys.* **2008**, *10*, 6090-6092.

(12) Taatjes, C. A.; Klippenstein, S. J.; Hansen, N.; Miller, J. A.; Cool, T. A.; Wang, J.; Law, M. E.; Westmoreland, P. R. *Phys. Chem. Chem. Phys.* **2005**, *7*, 806-813.

(13) Maksyutenko, P.; Zhang, F. T.; Gu, X. B.; Kaiser, R. I. *Phys. Chem. Chem. Phys.* **2011**, *13*, 240-252.

(14) Thaddeus, P.; Gottlieb, C. A.; Mollaaghababa, R.; Vrtilek, J. M. *J. Chem. Soc. Faraday Trans.* **1993**, *89*, 2125-2129.

(15) McCarthy, M. C.; Travers, M. J.; Kovacs, A.; Chen, W.; Novick, S. E.; Gottlieb, C. A.; Thaddeus, P. *Science* **1997**, *275*, 518-520.

(16) Fulara, J.; Freivogel, P.; Forney, D.; Maier, J. P. *J. Chem. Phys.* **1995**, *103*, 8805-8810.

(17) Ding, H.; Schmidt, T. W.; Pino, T.; Boguslavskiy, A. E.; Guthe, F.; Maier, J. P. *J. Chem. Phys.* **2003**, *119*, 814-819.

(18) Bourissou, D.; Guerret, O.; Gabbai, F. P.; Bertrand, G. *Chem. Rev.* **2000**, *100*, 39-92.

(19) Herzberg, G.; Johns, J. W. C. *Proc. R. Soc. London, Ser. A* **1966**, *295*, 107-128.

(20) Herzberg, G.; Johns, J. W. C. *J. Chem. Phys.* **1971**, *54*, 2276-2278.

(21) Zittel, P. F.; Ellison, G. B.; Oneil, S. V.; Herbst, E.; Lineberger, W. C.; Reinhardt, W. P. *J. Am. Chem. Soc.* **1976**, *98*, 3731-3732.

(22) Engelking, P. C.; Corderman, R. R.; Wendoloski, J. J.; Ellison, G. B.; Oneil, S. V.; Lineberger, W. C. *J. Chem. Phys.* **1981**, *74*, 5460-5473.

(23) Murray, K. K.; Leopold, D. G.; Miller, T. M.; Lineberger, W. C. *J. Chem. Phys.* **1988**, *89*, 5442-5453.

(24) Clifford, E. P.; Wenthold, P. G.; Lineberger, W. C.; Petersson, G. A.; Broadus, K. M.; Kass, S. R.; Kato, S.; DePuy, C. H.; Bierbaum, V. M.; Ellison, G. B. *J. Phys. Chem. A* **1998**, *102*, 7100-7112.

(25) Schwartz, R. L.; Davico, G. E.; Ramond, T. M.; Lineberger, W. C. *J. Phys. Chem. A* **1999**, *103*, 8213-8221.

(26) Sander, W.; Bucher, G.; Wierlacher, S. *Chem. Rev.* **1993**, *93*, 1583-1621.

(27) Milligan, D. E.; Pimentel, G. C. *J. Chem. Phys.* **1958**, *29*, 1405.

(28) Zuev, P. S.; Sheridan, R. S.; Albu, T. V.; Truhlar, D. G.; Hrovat, D. A.; Borden, W. T. *Science* **2003**, *299*, 867-870.

(29) Zuev, P. S.; Sheridan, R. S. *J. Am. Chem. Soc.* **2004**, *126*, 12220-12221.

(30) Moss, R. A.; Sauers, R. R.; Sheridan, R. S.; Tian, J. Z.; Zuev, P. S. *J. Am. Chem. Soc.* **2004**, *126*, 10196-10197.

(31) Nicolaides, A.; Matsushita, T.; Yonezawa, K.; Sawai, S.; Tomioka, H.; Stracener, L. L.; Hodges, J. A.; McMahon, R. J. *J. Am. Chem. Soc.* **2001**, *123*, 2870-2876.

(32) Bowling, N. P.; Halter, R. J.; Hodges, J. A.; Seburg, R. A.; Thomas, P. S.; Simmons, C. S.; Stanton, J. F.; McMahon, R. J. *J. Am. Chem. Soc.* **2006**, *128*, 3291-3302.

(33) Seburg, R. A.; Patterson, E. V.; McMahon, R. J. *J. Am. Chem. Soc.* **2009**, *131*, 9442-9455.

(34) Lucchese, R. R.; Schaefer, H. F. *J. Am. Chem. Soc.* **1978**, *100*, 298-299.

(35) Shepler, B. C.; Epifanovsky, E.; Zhang, P.; Bowman, J. M.; Krylov, A. I.; Morokuma, K. *J. Phys. Chem. A* **2008**, *112*, 13267-13270.

(36) Townsend, D.; Lahankar, S. A.; Lee, S. K.; Chambreau, S. D.; Suits, A. G.; Zhang, X.; Rheinecker, J.; Harding, L. B.; Bowman, J. M. *Science* **2004**, *306*, 1158-1161.

(37) Fu, B. N.; Shepler, B. C.; Bowman, J. M. *J. Am. Chem. Soc.* **2011**, *133*, 7957-7968.

(38) Zhang, P.; Maeda, S.; Morokuma, K.; Braams, B. J. *J. Chem. Phys.* **2009**, *130*, 114304.

(39) Hoffmann, M. R.; Schaefer, H. F. *Astrophys. J.* **1981**, *249*, 563-565.

(40) Ley, D.; Gerbig, D.; Schreiner, P. R. *Org. Biomol. Chem.* **2012**, *10*, 3781-3790.

(41) Osamura, Y.; Goddard, J. D.; Schaefer, H. F.; Kim, K. S. *J. Chem. Phys.* **1981**, *74*, 617-621.

(42) Leon, S. *Chem. Phys. Lett.* **1998**, *296*, 292-298.

(43) Peters, P. S.; Duflot, D.; Faure, A.; Kahane, C.; Ceccarelli, C.; Wiesenfeld, L.; Toubin, C. *J. Phys. Chem. A* **2011**, *115*, 8983-8989.

(44) Kiselev, V. G.; Swinnen, S.; Nguyen, V. S.; Gritsan, N. P.; Nguyen, M. T. *J. Phys. Chem. A* **2010**, *114*, 5573-5579.

(45) Koziol, L.; Mozhayskiy, V. A.; Braams, B. J.; Bowman, J. M.; Krylov, A. I. *J. Phys. Chem. A* **2009**, *113*, 7802-7809.

(46) Buck, H. M. *Int. J. Quant. Chem.* **2012**, *112*, 3711-3719.

(47) Sodeau, J. R.; Lee, E. K. C. *Chem. Phys. Lett.* **1978**, *57*, 71-74.

(48) Feng, L.; Demyanenko, A. V.; Reisler, H. *J. Chem. Phys.* **2004**, *120*, 6524-6530.

(49) Feng, L.; Reisler, H. *J. Phys. Chem. A* **2004**, *108*, 9847-9852.

(50) Rodrigo, C. P.; Zhou, C.; Reisler, H. *J. Phys. Chem. A* **2013**, *117*, 12049-12059.

(51) Schreiner, P. R.; Reisenauer, H. P.; Pickard IV, F. C.; Simmonett, A. C.; Allen, W. D.; Mátyus, E.; Császár, A. G. *Nature* **2008**, *453*, 906-909.

(52) Koziol, L.; Wang, Y. M.; Braams, B. J.; Bowman, J. M.; Krylov, A. I. *J. Chem. Phys.* **2008**, *128*, 204310.

(53) Schreiner, P. R.; Reisenauer, H. P. *Angew. Chem., Int. Ed.* **2008**, *47*, 7071-7074.

(54) Burgers, P. C.; McGibbon, G. A.; Terlouw, J. K. *Chem. Phys. Lett.* **1994**, *224*, 539-543.

(55) Wiedmann, F. A.; Cai, J. N.; Wesdemiotis, C. *Rapid Commun. in Mass Spectrom.* **1994**, *8*, 804-807.

(56) Feller, D.; Borden, W. T.; Davidson, E. R. *J. Chem. Phys.* **1979**, *71*, 4987-4992.

(57) Womack, C. C.; Crabtree, K. N.; McCaslin, L.; Martinez, O., Jr.; Field, R. W.; Stanton, J. F.; McCarthy, M. C. *Angew. Chem., Int. Ed.* **2014**, *53*, 4089-4092.

(58) Welz, O.; Savee, J. D.; Osborn, D. L.; Vasu, S. S.; Percival, C. J.; Shallcross, D. E.; Taatjes, C. A. *Science* **2012**, *335*, 204-207.

(59) Beames, J. M.; Liu, F.; Lu, L.; Lester, M. I. *J. Am. Chem. Soc.* **2012**, *134*, 20045-20048.

(60) Lehman, J. H.; Li, H. W.; Beames, J. M.; Lester, M. I. *J. Chem. Phys.* **2013**, *139*.

(61) Samanta, K.; Beames, J. M.; Lester, M. I.; Subotnik, J. E. *J. Chem. Phys.* **2014**, *141*, 134303.

(62) Callegari, C.; Lehmann, K. K.; Schmied, R.; Scoles, G. *J. Chem. Phys.* **2001**, *115*, 10090-10110.

(63) Toennies, J. P.; Vilesov, A. F. *Angew. Chem., Int. Ed.* **2004**, *43*, 2622-2648.

(64) Choi, M. Y.; Douberly, G. E.; Falconer, T. M.; Lewis, W. K.; Lindsay, C. M.; Merritt, J. M.; Stiles, P. L.; Miller, R. E. *Int. Rev. Phys. Chem.* **2006**, *25*, 15-75.

(65) Stienkemeier, F.; Lehmann, K. K. *J. Phys. B* **2006**, *39*, R127-R166.

(66) Lewerenz, M.; Schilling, B.; Toennies, J. P. *Chem. Phys. Lett.* **1993**, *206*, 381-387.

(67) Knuth, E.; Schilling, B.; Toennies, J. P. *Proceedings of the 19th International Symposium on Rarefied Gas Dynamics*; Oxford University Press: London, 1995.

(68) Hartmann, M.; Miller, R. E.; Toennies, J. P.; Vilesov, A. *Phys. Rev. Lett.* **1995**, *75*, 1566-1569.

(69) Leavitt, C. M.; Moradi, C. P.; Stanton, J. F.; Douberly, G. E. *J. Chem. Phys.* **2014**, *140*, 171102.

(70) Stiles, P. L.; Nauta, K.; Miller, R. E. *Phys. Rev. Lett.* **2003**, *90*, 135301.

(71) Morrison, A. M.; Liang, T.; Douberly, G. E. *Rev. Sci. Instrum.* **2013**, *84*, 013102.

(72) Morrison, A. M.; Raston, P. L.; Douberly, G. E. *J. Phys. Chem. A* **2012**, *117*, 11640-11647.

(73) Raston, P. L.; Douberly, G. E. *J. Mol. Spec.* **2013**, *292*, 15-19.

(74) Plath, K. L.; Axson, J. L.; Nelson, G. C.; Takahashi, K.; Skodje, R. T.; Vaida, V. *React. Kinet. Catal. Lett.* **2009**, *96*, 209-224.

(75) CFOUR, a quantum-chemical program package by J. F. Stanton, J. Gauss, M. E. Harding, P. G. Szalay, et al. For the complete citation and current version, see http://www.cfour.de.

(76) Almlöf, J.; Taylor, P. R. *J. Chem. Phys.* **1987**, *86*, 4070-4077.

(77) McCaslin, L.; Stanton, J. *Mol. Phys.* **2013**, *111*, 1492-1496.

(78) Mills, I. M. *Molecular Spectroscopy: Modern Research*; Academic Press: New York, 1972.

(79) Matthews, D. A.; Stanton, J. F. *Mol. Phys.* **2009**, *107*, 213-222.

(80) Herzberg, G. *Molecular Spectra and Molecular Structure*; Van Nostrand Reinhold Company, Inc.: New York, 1945; Vol. II: Infared and Raman Spectra of Polyatomic Molecules.

(81) Skvortsov, D. S.; Vilesov, A. F. *J. Chem. Phys.* **2009**, *130*, 151101.

(82) Lindinger, A.; Toennies, J. P.; Vilesov, A. F. *J. Chem. Phys.* **1999**, *110*, 1429-1436.

(83) Choi, M. Y.; Miller, R. E. *J. Am. Chem. Soc.* **2006**, *128*, 7320-7328.

(84) Nauta, K.; Miller, R. E. *J. Chem. Phys.* **2001**, *115*, 8384-8392.

(85) Lindsay, C. M.; Miller, R. E. *J. Chem. Phys.* **2005**, *122*, 104306.

(86) Raston, P. L.; Agarwal, J.; Turney, J. M.; Schaefer, H. F.; Douberly, G. E. *J. Chem. Phys.* **2013**, *138*, 194303.

(87) Raghavachari, K.; Trucks, G. W.; Pople, J. A.; Head-Gordon, M. *Chem. Phys. Lett.* **1989**, *157*, 479-483.

(88) Woon, D. E.; Dunning Jr, T. H. *J. Chem. Phys.* **1995**, *103*, 4572-4585.

(89) "Mass Spectra" by NIST Mass Spec Data Center, S. E. Stein, director, in *NIST Chemistry WebBook*, NIST Standard Reference Database Number 69, edited by P. J. Linstrom and W. G. Mallard (National Institute of Standards and Technology, Gaithersburg, MD 20899), http://webbook.nist.gov (retrieved January 9, 2015).

(90) Maçôas, E. M. S.; Fausto, R.; Pettersson, M.; Khriachtchev, L.; Räsänen, M. *J. Phys. Chem. A* **2000**, *104*, 6956-6961.

(91) Callegari, C.; Conjusteau, A.; Reinhard, I.; Lehmann, K. K.; Scoles, G. *J. Chem. Phys.* **2000**, *113*, 10535-10550.

(92) Wiedmann, F. A.; Cai, J. N.; Wesdemiotis, C. *Rapid Commun. Mass Spectrom.* **1994**, *8*, 804.

(93) Leavitt, C. M.; Moradi, C. P.; Acrey, B. W.; Douberly, G. E. *J. Chem. Phys.* **2013**, *139*, 234301.

(94) Lapidus, G.; Barton, D.; Yankwich, P. E. *J. Phys. Chem.* **1966**, *70*, 407.

(95) Lapidus, G.; Barton, D.; Yankwich, P. E. *J. Phys. Chem.* **1966**, *70*, 1575.

(96) Lapidus, G.; Barton, D.; Yankwich, P. E. *J. Phys. Chem.* **1966**, *70*, 3135.

(97) Lapidus, G.; Yankwich, P. E.; Barton, D. *J. Phys. Chem.* **1964**, *68*, 1863.

(98) Higgins, J.; Zhou, X. F.; Liu, R. F.; Huang, T. T. S. *J. Phys. Chem. A* **1997**, *101*, 2702-2708.

CHAPTER 7

INFRARED LASER SPECTROSCOPY OF THE L-SHAPED CL–HCL COMPLEX FORMED IN SUPERFLUID ^{4}HE DROPLETS

Chlorine atoms, generated through the thermal decomposition of Cl_2, are solvated in superfluid helium nanodroplets and clustered with HCl molecules. The H–Cl stretching modes of these clusters are probed via infrared laser spectroscopy. A band centered at ≈2880.8 cm^{-1} is assigned to the binary Cl–HCl complex on the basis of HCl pressure dependence and difference mass spectra. The band lies in the "free" HCl stretching region, implying that the complex is not hydrogen bound. Furthermore, the breadth of the band (≈2 cm^{-1} FWHM) is consistent with an assignment to a predominantly *b*-type component of the H–Cl stretch, as the dominant *b*-type selection rules and *A* rotational constant allow for high energy rotational excitations that efficiently couple to droplet excitations, resulting in fast rotational deactivation. Despite the lack of rotational fine structure, which would verify the assignment, the observed band is consistent with the stabilization of a weakly-bound complex having an approximately L-shaped geometry. Frequency computations for a rigid, L-shaped complex reveal that the transition dipole moment vector points almost entirely along the *b* inertial axis; indeed, the signal-to-noise ratio in our experiment precluded the observation of an *a*-type component of the HCl stretching band for the complex. No bands were observed that could be assigned to a linear H-bonded Cl–HCl complex. Additionally, we located bands that are consistent with the formation of Cl_2–HCl, Cl_2–$(HCl)_2$,

and Cl–$(HCl)_2$. Two vibrations of the Cl–$(HCl)_2$ complex were found, and harmonic frequencies and intensities computed for a cyclic structure are consistent with the observations.

7.1 Introduction

The Cl + HCl → HCl + Cl reaction has been extensively studied both experimentally and theoretically due to its importance as a prototypical hydrogen-exchange reaction between two heavy atoms. A variety of techniques have been employed to elucidate the dynamics of this important reaction, such as anion photodetachment,[1] transient infrared (IR) absorption,[2] and bond-specific photodissociation of the HCl dimer.[3] Much of the available experimental work, however, focuses on the transition state region of the potential energy surface (PES). Although an important region of the PES worthy of rigorous study, it provides only an incomplete picture of the associated dynamics. Indeed, product branching ratios can be observably sensitive to the long-range van der Waals forces in the entrance-channel to the reaction, which steer the reactants into product channels.[4] These forces are quite strong for the Cl–HCl van der Waals complex due to interaction of the rather large quadrupole moment of the Cl atom ($^2P_{3/2}$) with the multipoles of the HCl molecule,[5] motivating the study of the long-range region of the PES.

Computations of the PES in the vicinity of the weakly bound Cl–HCl complex are challenging for several reasons. The Cl atom has a half-filled *p*-orbital that is triply degenerate in the absence of external effects. This degeneracy is lifted, however, as the Cl and HCl moieties interact. There exist three low-lying electronic states that can be thought of qualitatively as being related to the orientation of the half-filled *p*-orbital with respect to the vector connecting the two centers of mass. These three PESs support geometries corresponding to linear hydrogen-

bonded, L-shaped, and linear chlorine-bonded complexes.[5-7] In the linear configuration, the electronic states of the complex are $^2\Sigma^+$ and $^2\Pi$ when the half-filled *p*-orbital lies along the vector connecting the two centers of mass or perpendicular to it, respectively. When the complex is bent from linearity, the $^2\Pi$ state, with the half-filled *p*-orbital perpendicular to the molecular axis, splits into states of $^2A'$ and $^2A''$ symmetry, and the $^2\Sigma^+$ state becomes a $^2A'$ state. The adiabatic PESs of A′ symmetry are coupled due to mixing of the in-plane p_x and p_z Cl orbitals, however, and adiabatic-to-diabatic transformations yield drastically different PESs with stationary points that appear and disappear altogether.[5,7] The inclusion of the chlorine spin-orbit coupling further reshapes these PESs, resulting in even more theoretical difficulties.[5,6] These early calculations predicted a linear H-bonded global minimum structure. More recent van der Waals, bound state calculations predict both the linear H-bonded complex as well as the L-shaped complex with very similar binding energies, D_0, of 290.8 cm^{-1} and 291.1 cm^{-1}, respectively.[8,9] Nevertheless, the wavefunctions associated with these lowest energy bound states are significantly delocalized over bending and intermolecular stretching degrees of freedom.[8,9]

The low barrier to reaction and weak binding typical of the class of symmetric X–HX (X = F, Cl, Br) van der Waals complexes makes them somewhat difficult to stabilize and probe in the gas phase. Matrix isolation techniques have therefore been employed for quite some time in order to study these and other entrance-channel complexes. The related Br–HBr and Br–DBr complexes were studied in solid parahydrogen where large monomer-to-complex vibrational frequency shifts suggest formation of a linear H-bonded complex.[10] The HF vibrations of the X–HF (X = Cl, Br, I) complexes were studied in helium nanodroplets where it was again found that each complex had a linear H-bonded structure.[11] Most relevant to the current work is the Ar matrix experiment performed by Andrews and Hunt, in which they codeposited Cl atoms

generated in a microwave discharge with HCl and reported a pair of peaks redshifted by roughly 50 cm^{-1} from the HCl *R*(0) transition, which they assigned to the linear H-bonded Cl–HCl complex.[12] Their assignment is in agreement with the predictions of theory,[5,6] although they found no evidence for an L-shaped structure, which again, is nearly isoenergetic with the linear species.[8,9] In the current work, we form the Cl–HCl complex in helium nanodroplets and use IR laser spectroscopy to probe the structure of the He-solvated complex.

7.2 Experimental Methods

The helium nanodroplet methodology has been discussed in detail previously.[13-16] Superfluid helium nanodroplets are generated in the high-pressure region of a continuous expansion of helium gas (30 bars backing pressure) through a nozzle with a 5 ± 1 μm aperture that has been cooled to ≈17 K. Under these conditions, the mean droplet size is 4500 He atoms per droplet.[13] Nascent droplets evaporatively cool to ≈0.4 K before being collimated into a beam by a 0.4 mm skimmer.[14] The droplet beam passes into a pickup chamber where droplets collide with and solvate gas-phase Cl_2 molecules, Cl atoms, and HCl molecules and cool their internal degrees of freedom to 0.4 K.[17] The gaseous HCl was generated by the reaction of PCl_3 with water, collected in a condenser cooled by liquid nitrogen, and trap-to-trap distilled. The Cl atoms are generated through the thermal decomposition of ≥99.5% purity Cl_2 (Sigma-Aldrich) as it passes through a resistively heated SiC tube (ID = 1mm).[18] With 3.5 A of current flowing through a 19 mm length of SiC tube, spectroscopic signals assigned to complexes of Cl_2 with HCl were nearly completely eliminated. The pyrolysis source is positioned adjacent to the droplet beam with the SiC tube exit just to the side of the beam, such that Cl atoms exiting the

tube effuse into the droplet path and are picked up by the droplets. The partially doped droplet beam then passes through a stainless steel tube containing ≈10^{-6} Torr of gaseous HCl before entering the ionization region of a quadrupole mass spectrometer.

The tunable, mid-IR (2600-3150 cm^{-1}) idler beam from a continuous wave optical parametric oscillator (OPO) counter-propagates the droplet beam. Upon resonance, rovibrational excitation of the dopant is quickly quenched by the evaporative loss of many He atoms, with an individual He atom removing ≈5 cm^{-1} of energy.[19] The reduction in the geometric cross-section of the droplet upon dopant excitation/relaxation reduces the efficiency by which the droplets are ionized by electron impact. Therefore, a depletion of ion signal is observed in mass channels associated with ionization-induced dopant fragmentation. In most of this work, the quadrupole is set to pass only $H^{35}Cl^+$ ions with m/z = 36 u, which discriminates somewhat against complexes containing the ^{37}Cl isotope. The laser-induced depletion in this mass channel is recorded as the IR radiation is continuously tuned from 2700 – 2920 cm^{-1} with ≈10 MHz resolution.[20] The OPO beam is mechanically chopped at 80 Hz enabling background-free measurement of the laser-induced depletion signal. The modulated MS ion current is converted into a voltage, processed with a lock-in amplifier, and recorded by a Labview data collection program.

7.3 Results and Discussion

7.3.1 Cl_2 + HCl

A survey scan of the HCl stretching region on m/z = 36 u is shown in the bottom of Figure 7.1, and the previously reported HCl monomer *R*(0) transition and $(HCl)_n$ (n=2–4+)

cluster bands are observed along with the binary HCl–H_2O complex. Upon the addition of Cl_2 gas to the pickup chamber, three bands are observed to grow in (marked by * in the middle spectrum in Figure 7.1). Significant redshift of these bands relative to the HCl monomer band origin (≈2886 cm^{-1}) indicates the stabilization of hydrogen bonded complexes in the droplets. Because the probability of a droplet picking up a specified number of molecules obeys Poisson statistics,[15] the number of HCl molecules that make up the complex giving rise to the particular band can be determined. This is done by monitoring the laser-induced depletion of the ion signal at a specific IR frequency (which here is the most intense feature of each band) as a function of pickup cell pressure. The HCl pressure, measured via an uncorrected ion gauge reading, is allowed to vary while the Cl_2 pressure is kept fixed and low, such that the probability of picking up two Cl_2 molecules is essentially set to zero. The Poisson curves are shown in Figure 7.2 for each of the three newly observed bands as well as those associated with the HCl monomer and HCl dimer, for comparison. These Poisson curves clearly indicate that the band at 2850.4 cm^{-1} arises from a complex containing a single HCl molecule, whereas the two bands at 2821.4 cm^{-1} and 2836.5 cm^{-1} predominantly arise from clusters involving two HCl molecules. Given the low pressure of Cl_2 in the pickup chamber, we conclude that the 2850.4 cm^{-1} band is due to the hydrogen bonded Cl_2–HCl complex, and the 2821.4 cm^{-1} and 2836.5 cm^{-1} bands arise mainly from the Cl_2–$(HCl)_2$ complex. Difference mass spectra (DMS) were also recorded for these three bands by tuning the OPO frequency to the most intense feature of each band and measuring the laser-induced depletion of the ion signal on mass channels from 10 u to 82 u. These DMS, shown in Figure 7.3, corroborate the cluster assignments above; the band at 2850.4 cm^{-1} predominantly shows depletion of m/z = 36 and 70 u, indicating this complex is most efficiently ionized to form ions of its constituent molecules $(H^{35}Cl)^+$ and $(^{35}Cl_2)^+$. This is in contrast to the

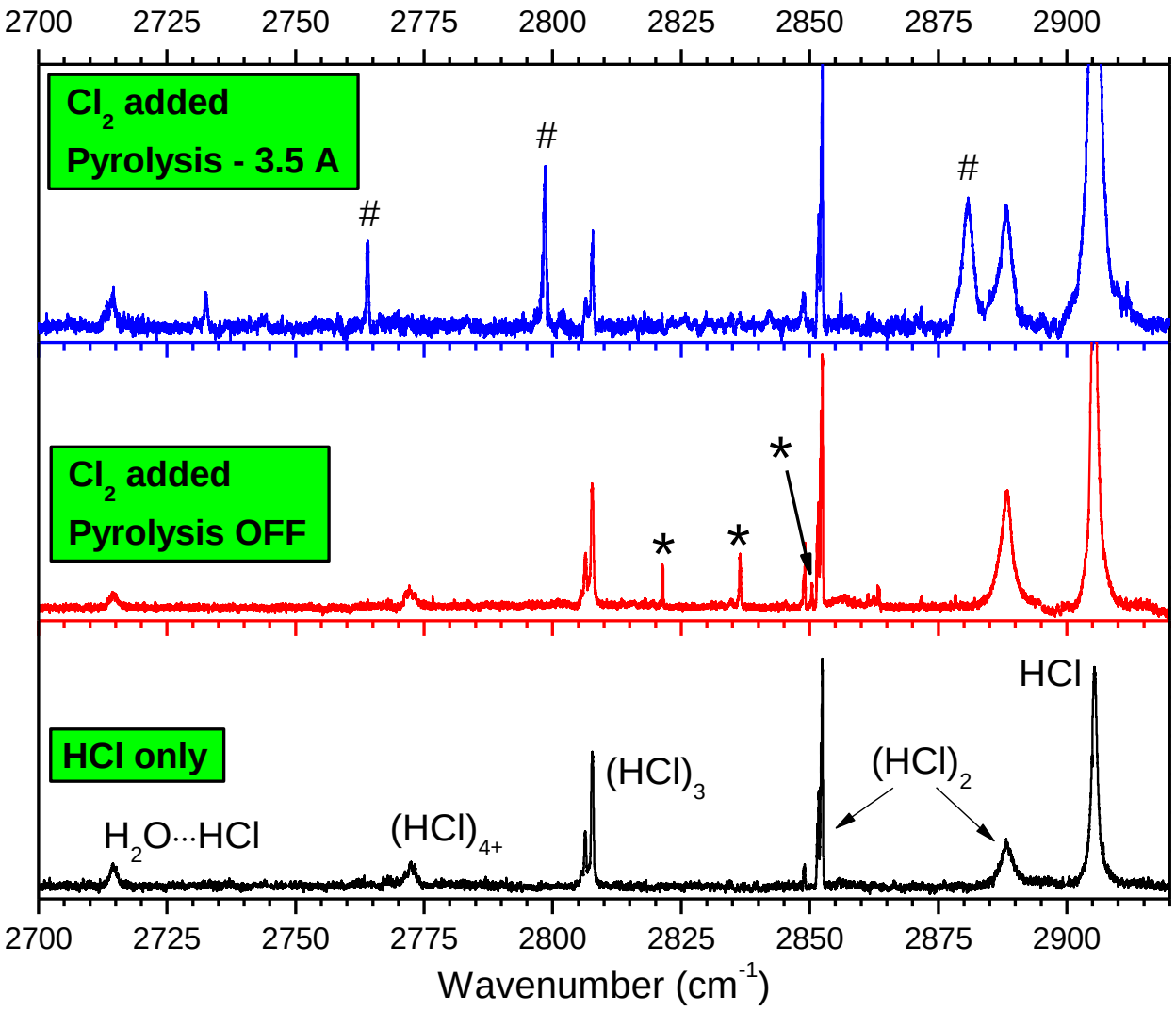

Figure 7.1: Survey spectra measured as depletion in mass channel m/z =36 u but under different pickup/pyrolysis conditions. The bottom (black) spectrum was measured with only HCl present in the pickup chamber. The middle (red) spectrum was measured with HCl present and Cl_2 flowing through the room temperature pyrolysis source. The top (blue) spectrum was measured with HCl present and Cl_2 flowing through the SiC pyrolysis source being operated with 3.5 A of current. Bands marked by * are due to complexes containing Cl_2 and one or two HCl molecules. Bands marked by # are due to complexes containing a Cl atom and one or two HCl molecules. The unlabeled weak features in the spectra were investigated, and they have been ruled out as being relevant to the current study on the basis of reproducibility.

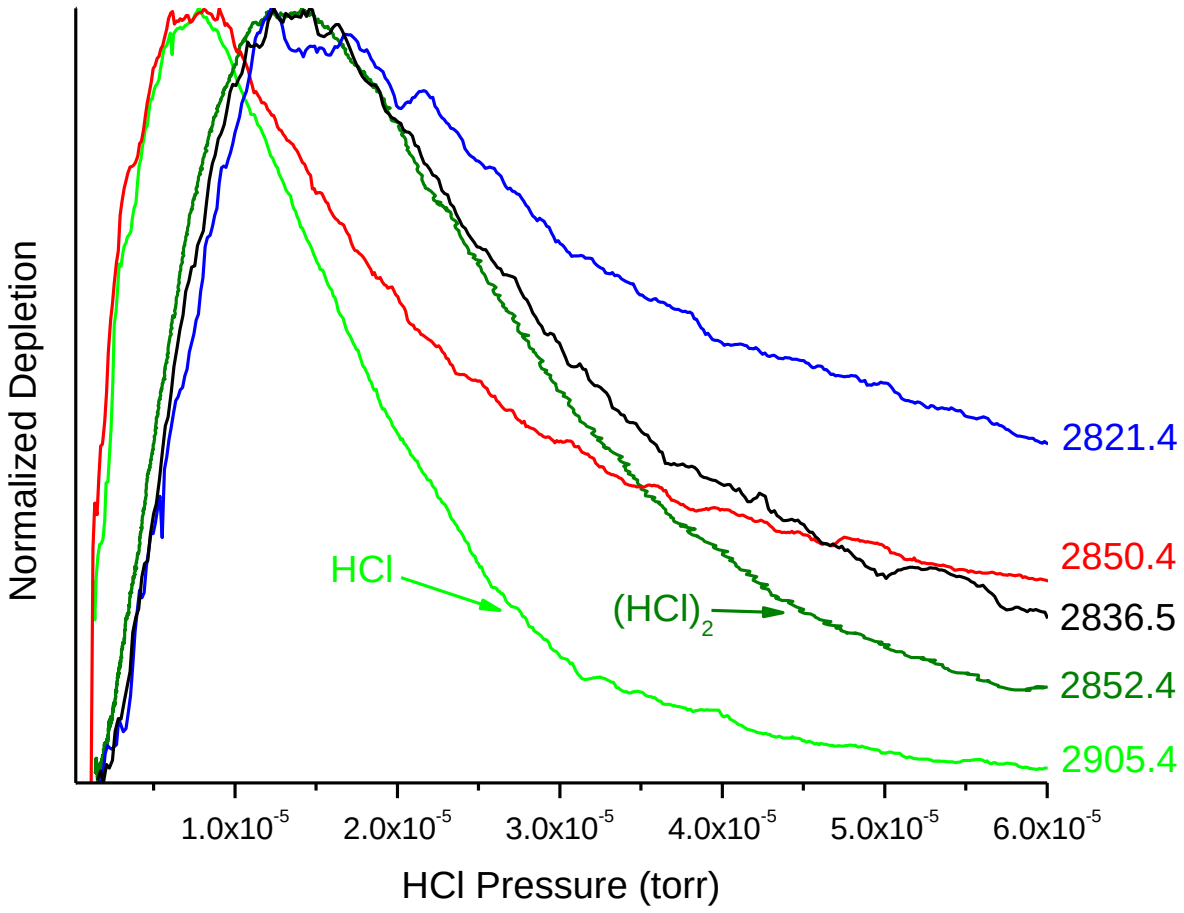

Figure 7.2: Pickup cell pressure curves associated with bands assigned to the Cl_2–$(HCl)_n$ clusters. The light green curve corresponds to depletion signal on the HCl monomer R(0) transition. The dark green curve corresponds to the depletion signal on the $(HCl)_2$ ν_2 "bound" stretch. The three remaining curves (red, blue, black) are the depletion signals for the bands observed when Cl_2 and HCl are both present in the pickup chamber. Only the HCl pressure was allowed to vary as the depletion signal was recorded. The IR frequency (cm^{-1}) at which the curves were measured is given on the right.

2821.4 cm^{-1} and 2836.5 cm^{-1} bands, which are both depleted primarily on m/z = 37 and 71 u implying that ionization of Cl_2–$(HCl)_2$ prefers hydrogen transfer from one or both HCl molecules to yield $(H_2{}^{35}Cl)^+$ and $({}^{35}Cl_2H)^+$. Depletion on other mass channels corresponding to complexes involving the ^{37}Cl isotope, e.g. m/z = 72 $({}^{35}Cl{}^{37}Cl)^+$, is expected on the basis of a natural abundance of ^{35}Cl:$^{37}Cl \approx 3$:1.

Expanded views of the three bands attributed to Cl_2–HCl and Cl_2–$(HCl)_2$ are shown in Figures 7.4 and 7.5, respectively, along with equilibrium geometries computed at the MP2/aug-cc-pVTZ level with a C_s symmetry constraint. Harmonic frequency calculations were performed at the same level of theory using these geometries, and no imaginary frequencies were obtained. Two equilibrium geometries were located for the Cl_2–HCl complex: a hydrogen bonded L-shaped complex and a Cl-bonded complex (with a "free" HCl stretch). However, only the L-shaped Cl_2–HCl geometry is consistent with the observed frequency of the only band in the spectrum that can be attributed to the binary complex. This Cl_2–$H^{35}Cl$ band is observed at 2850.4 cm^{-1} and is only redshifted from the ν_2 "bound" stretch of the similarly L-shaped $(HCl)_2$ by ≈2 cm^{-1}. This is indicative of a similar interaction strength between the constituent molecules of the two complexes and implies that the geometries of both Cl_2–HCl and $(HCl)_2$ are dictated mainly by dipole-quadrupole and quadrupole-quadrupole forces.

Figure 7.5 shows the expanded view of the two bands assigned to Cl_2–$(HCl)_2$ on the basis of pickup cell curves and DMS. The harmonic frequency difference between the in-phase and out-of-phase HCl stretching modes of Cl_2–$(HCl)_2$ is predicted to be 21.3 cm^{-1}, which is in good agreement with the observed difference of roughly 15 cm^{-1}. However, as seen in Table 7.1, the monomer-to-complex frequency shifts are over-predicted by the calculation, likely due to the rather low level of theory employed. These two computed vibrations are predicted to have quite

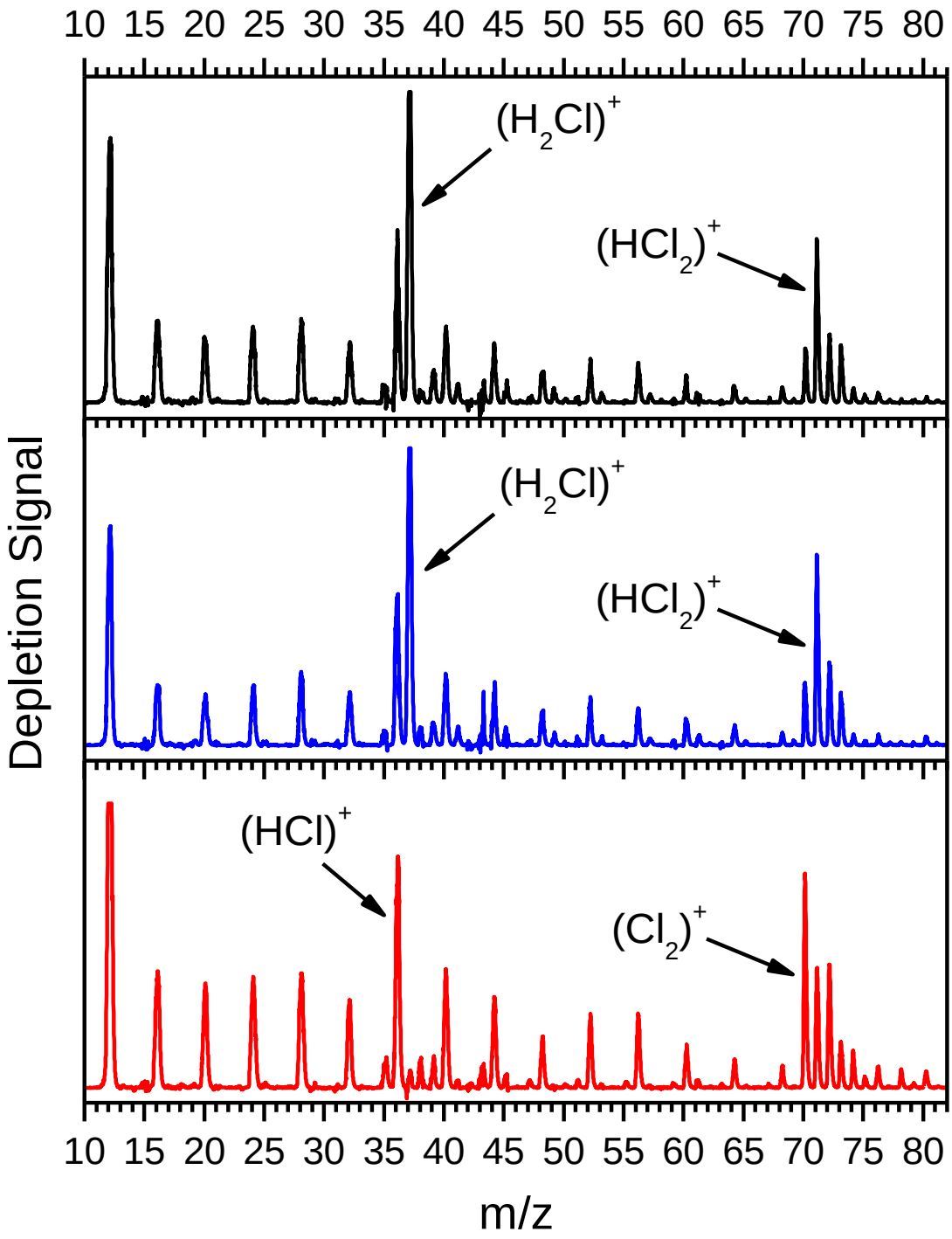

Figure 7.3: Difference mass spectra (laser OFF – laser ON) obtained for the three bands observed when Cl_2 and HCl are both present in the pickup chamber. The bottom DMS (red) was measured with the laser frequency fixed to 2850.4 cm^{-1}, middle DMS (blue) – 2821.4 cm^{-1}, top DMS (black) – 2836.5 cm^{-1}.

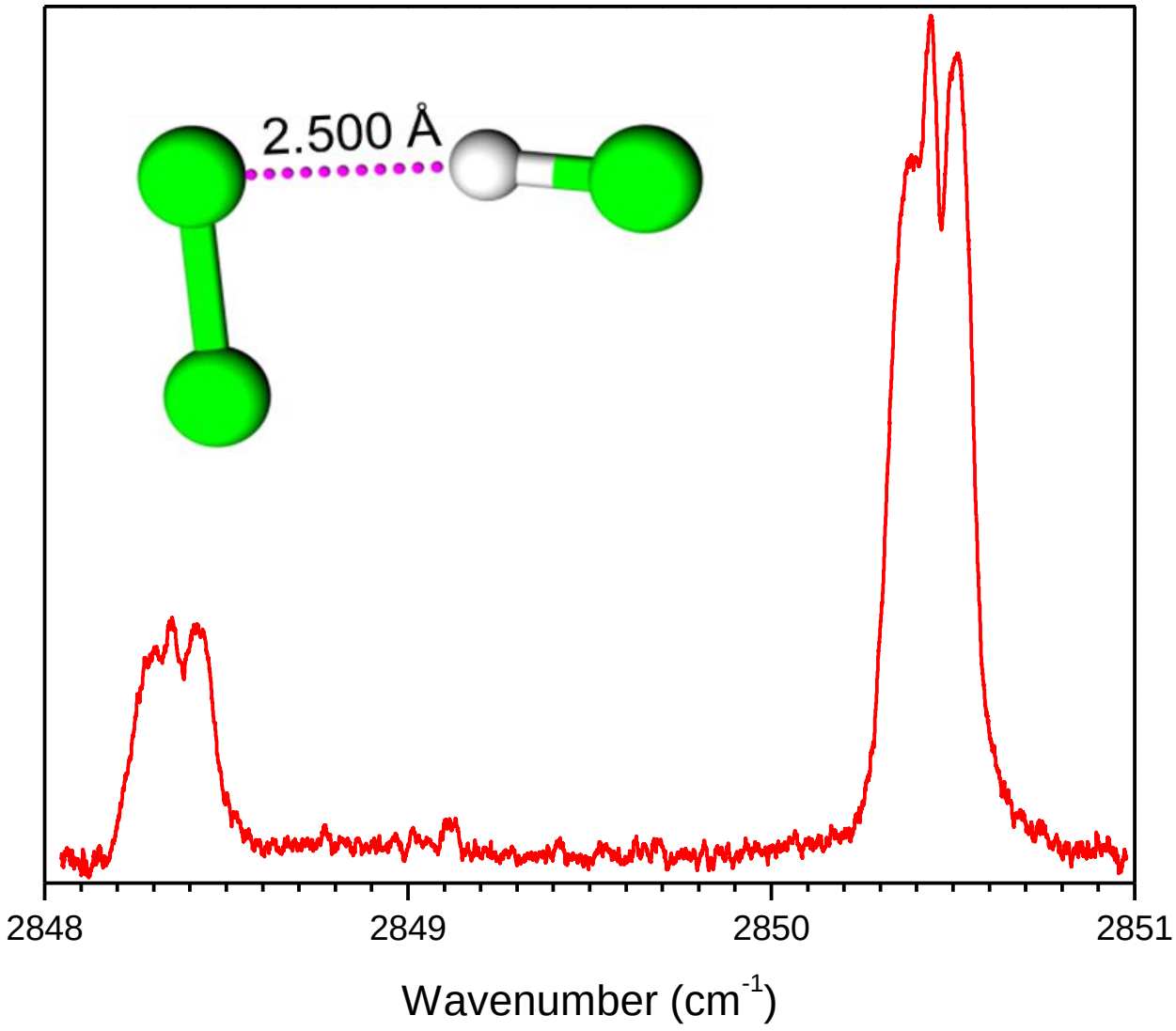

Figure 7.4: Expanded view of the bands assigned to binary complexes consisting of one Cl_2 molecule and one HCl molecule. The band at 2850.4 cm^{-1} is due to complexes containing $H^{35}Cl$ whereas the band at 2848.3 cm^{-1} is due to complexes containing $H^{37}Cl$.

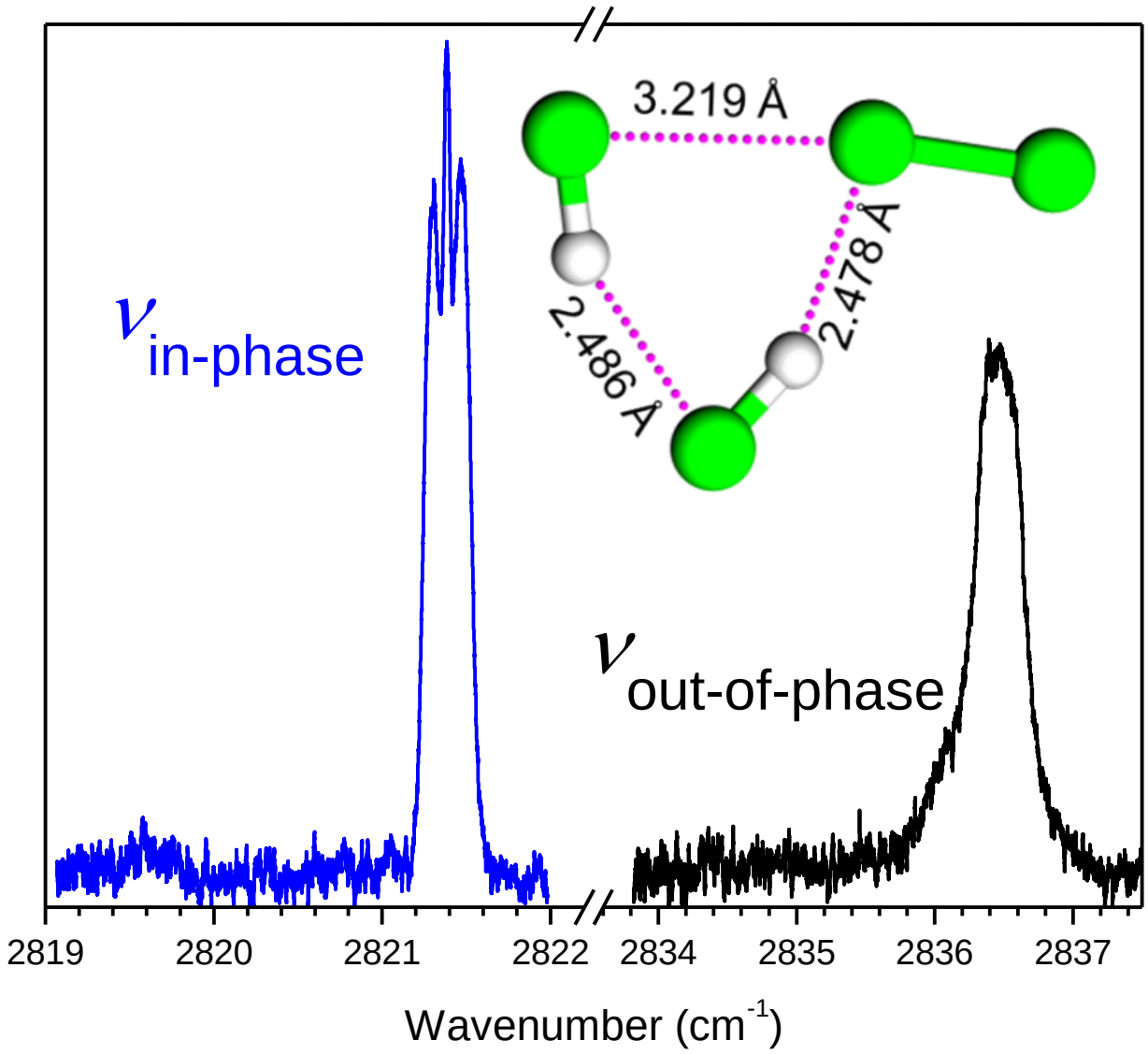

Figure 7.5: Expanded view of the two bands which arise from clusters containing a Cl_2 molecule and two HCl molecules. The Cl_2–$(HCl)_2$ geometry was computed at the MP2/aug-cc-pVTZ level. The two modes are labeled as in-phase, where the two HCl bond distances increase and decrease together, or as out-of-phase, where one bond lengthens as the other shortens. The computed frequency difference for these two bands at this level is 21 cm^{-1}.

different transition dipole moment projections. The in-phase stretch is predicted to be mostly *a*-type with $\dot{\mu}_a : \dot{\mu}_b \approx 2.75$.

Indeed, this *a*-type band contour can be satisfactorily simulated using an asymmetric top rigid rotor Hamiltonian. The rotational constants used in the simulation are reduced by a factor of ≈3 from the *ab initio* rotational constants computed for the complex. This reduction accounts for the contribution of the He solvent to the rotor's effective moment of inertia. A 0.05 cm^{-1} Lorentzian line shape is convoluted on each transition. The out-of-phase stretch, however, is predicted to be mostly *b*-type with $\dot{\mu}_a : \dot{\mu}_b \approx 0.39$, but this band cannot be simulated simply by keeping the same rotational constants and only adjusting the transition dipole moment projections. Interestingly, there is a broadening mechanism that washes out the rotational contour expected for the out-of-phase vibration. Indeed, the simulation requires a linewidth equal to 0.2 cm^{-1} to reproduce the width of the observed band, although the mechanism of this broadening is not clear.

7.3.2 Cl + HCl

The top survey spectrum in Figure 7.1 was recorded on m/z = 36 u with 3.5 A of current passing through the SiC pyrolysis source. The flow of Cl_2 through the source was low in order to minimize the probability of pickup of multiple Cl atoms by a single droplet. Under these conditions, vibrational bands assigned to Cl_2-containing clusters are nearly completely eliminated, and three new bands appear in the spectrum (marked by #). These bands are assigned to complexes composed of a chlorine atom with either one or two HCl molecules by analyzing Poisson curves and DMS (Figures 7.6 and 7.7, respectively) for each of the three

Table 7.1: Unscaled harmonic frequencies computed at the MP2/aug-cc-pVTZ level for the various complexes for comparison with observed frequencies in helium droplets. All units are wavenumbers and all chlorine atoms correspond to the ^{35}Cl isotope.

	Computed				**Helium Droplets**			
	ν_{HCl}	$\nu_{in\text{-}phase}$	$\nu_{out\text{-}of\text{-}phase}$	$\Delta\nu$ [a]	ν_{HCl}	$\nu_{in\text{-}phase}$	$\nu_{out\text{-}of\text{-}phase}$	$\Delta\nu$ [a]
HCl	3049.0	--	--	0.0	2905.4 [b]	--	--	0.0
Cl_2–HCl (H-bonded)	2994.5	--	--	54.5	2850.4	--	--	36.4
Cl_2–HCl (Cl-bonded)	3039.9	--	--	10.1	--	--	--	--
$(HCl)_2$ (bound stretch)	2976.5	--	--	72.5	2852.246(2) [c]	--	--	33.8 [c]
$(HCl)_2$ (free stretch)	3033.8	--	--	15.2	2888.2 [d]	--	--	5.8 [d]
Cl–HCl (L-shaped)	3031.6	--	--	17.4	2880.8 [e]	--	--	16 [e]
Cl–HCl (linear)	2998.7	--	--	50.3	--	--	--	--
Cl–$(HCl)_2$	--	2924.2	2954.3	30.1	--	2764.0	2798.4	34.4
Cl_2–$(HCl)_2$	--	2943.4	2964.7	21.3	--	2821.7	2736.4	14.7

[a] The quantity $\Delta\nu$ in the top portion of the table is the (computed or observed) frequency for the complexes subtracted from the HCl band origin. In the bottom portion of the Table, $\Delta\nu$ corresponds to $\nu_{in\text{-}phase} - \nu_{out\text{-}of\text{-}phase}$.

[b] The frequency corresponds to the R(0) transition of the HCl monomer. The band origin is approximately 2886 cm^{-1}, and it is this value used to determine the quantity $\Delta\nu$.

[c] Ref. [23]

[d] Frequency of the *b*-type band observed in helium droplets. The gas-phase band origin is 2880.2495(2) cm^{-1} as measured by Schuder, et. al.[21] Ignoring helium solvent effects on the vibrational frequency, this yields $\Delta\nu \approx 5.1$ cm^{-1}.

bands, as described in the previous section. Each of the Poisson curves were recorded on m/z = 36 u, and the Cl_2 flow and pyrolysis current were constant while the HCl pressure was varied. The Poisson curves clearly indicate that the 2880.8 cm^{-1} band is due to a cluster containing a single HCl molecule, and the 2764.0 and 2798.4 cm^{-1} bands are due to clusters (or a single cluster) having two HCl molecules. The high-pressure tails of these curves indicate the presence of higher order clusters at higher HCl pressures. Indeed, the ≈2740 – 2820 cm^{-1} region reported

by Skvortsov, et. al. corresponds to vibrations of He-solvated $(HCl)_n$ clusters with $n \geq 4$, and this frequency region quickly becomes a broad absorption band at HCl pressures higher than $\approx 10^{-5}$ Torr.[22] Nonetheless, under the low HCl pressure conditions used to measure the survey scans in Figure 7.1, these two low-frequency bands must arise predominantly from clusters containing two HCl molecules. We note that there is a persistent background of HCl when Cl_2 is flowing through the hot pyrolysis source, likely due to reaction of gas-phase Cl atoms with molecules on the surfaces of the vacuum chamber. This background manifests itself in the Poisson curves for droplets containing a single HCl, as the HCl partial pressure cannot be completely eliminated. However, this effect is less problematic for the Poisson curves for bands associated with clusters containing more than one HCl.

The 2764.0 and 2798.4 cm^{-1} bands shown in Figure 7.8 are consistent with hydrogen bonded complexes containing a Cl atom with two HCl molecules. Again, geometry optimizations and harmonic frequency calculations at the MP2 level predict a difference of 30 cm^{-1} between the in-phase and out-of-phase HCl stretching modes; the difference observed in helium droplets is 34.4 cm^{-1}. Both of these bands are broadened beyond the expected rotational contour on the basis of spectral simulations utilizing the (renormalized) *ab initio* rotational constants and dipole derivatives. This is surprising because the analogous in-phase vibration of Cl_2–$(HCl)_2$ discussed above does have the expected rotational contour. Furthermore, the out-of-phase vibration of Cl_2–$(HCl)_2$ discussed above does have the expected rotational contour. Furthermore, the out-of-phase vibration of Cl–$(HCl)_2$ is approximately twice as broad (FWHM) as the in-phase vibration. The source of this broadening is likely due to vibrational dephasing, which is consistent with the observed mode specificity. Because these systems have not been

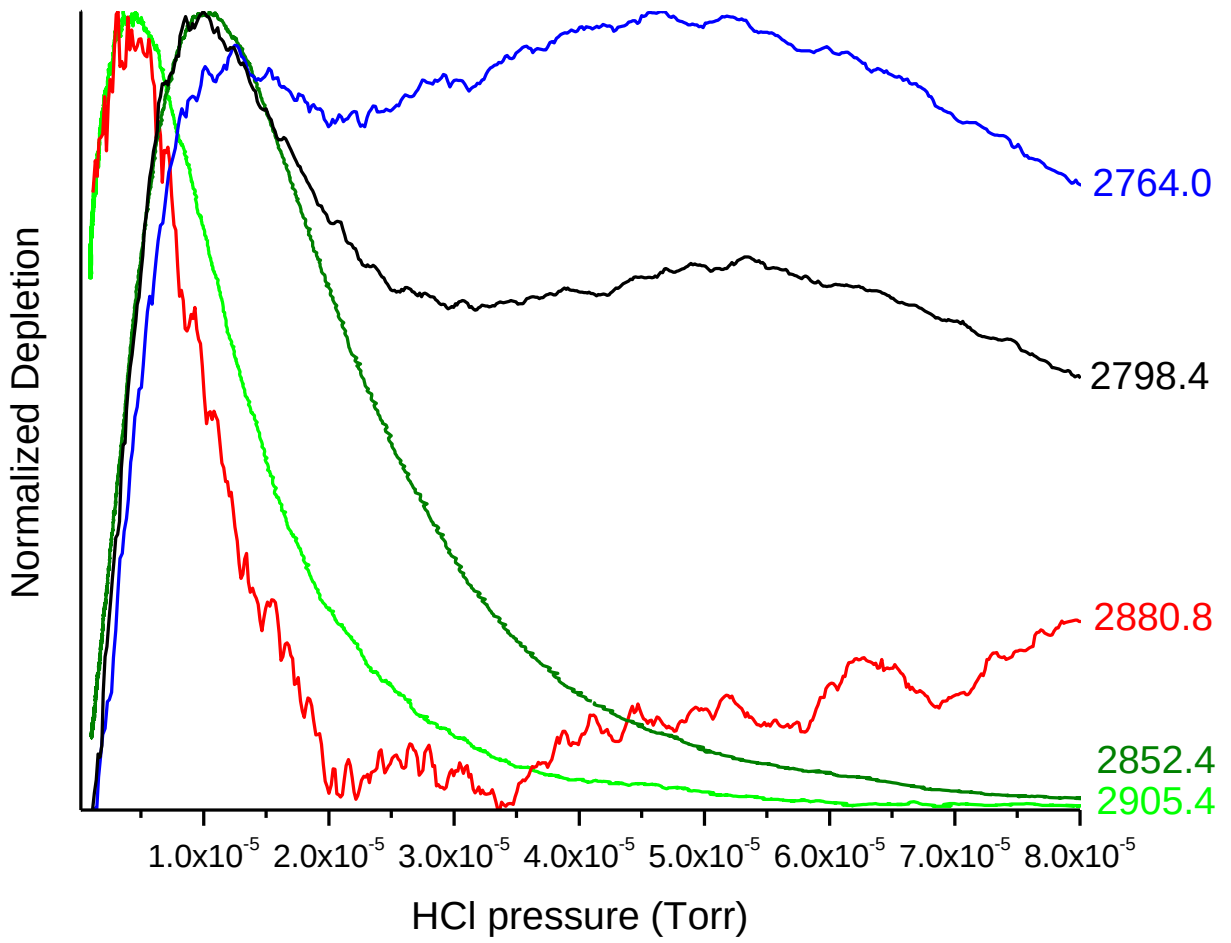

Figure 7.6: Pickup cell pressure curves associated with bands assigned to the Cl–$(HCl)_n$ clusters. The light green curve corresponds to depletion signal on the HCl monomer R(0) transition. The dark green curve corresponds to the depletion signal on the $(HCl)_2$ ν_2 "bound" stretch. The three remaining curves (red, blue, black) are the depletion signals for the bands observed when Cl_2 is flowing through the hot pyrolysis source (3.5 A) and HCl is present in the pickup chamber. Only the HCl pressure was allowed to vary as the depletion signal was recorded. The IR frequency (cm^{-1}) at which the curves were measured is given on the right. At high HCl pressures, these Poisson curves indicate formation of clusters with more than two HCl molecules.

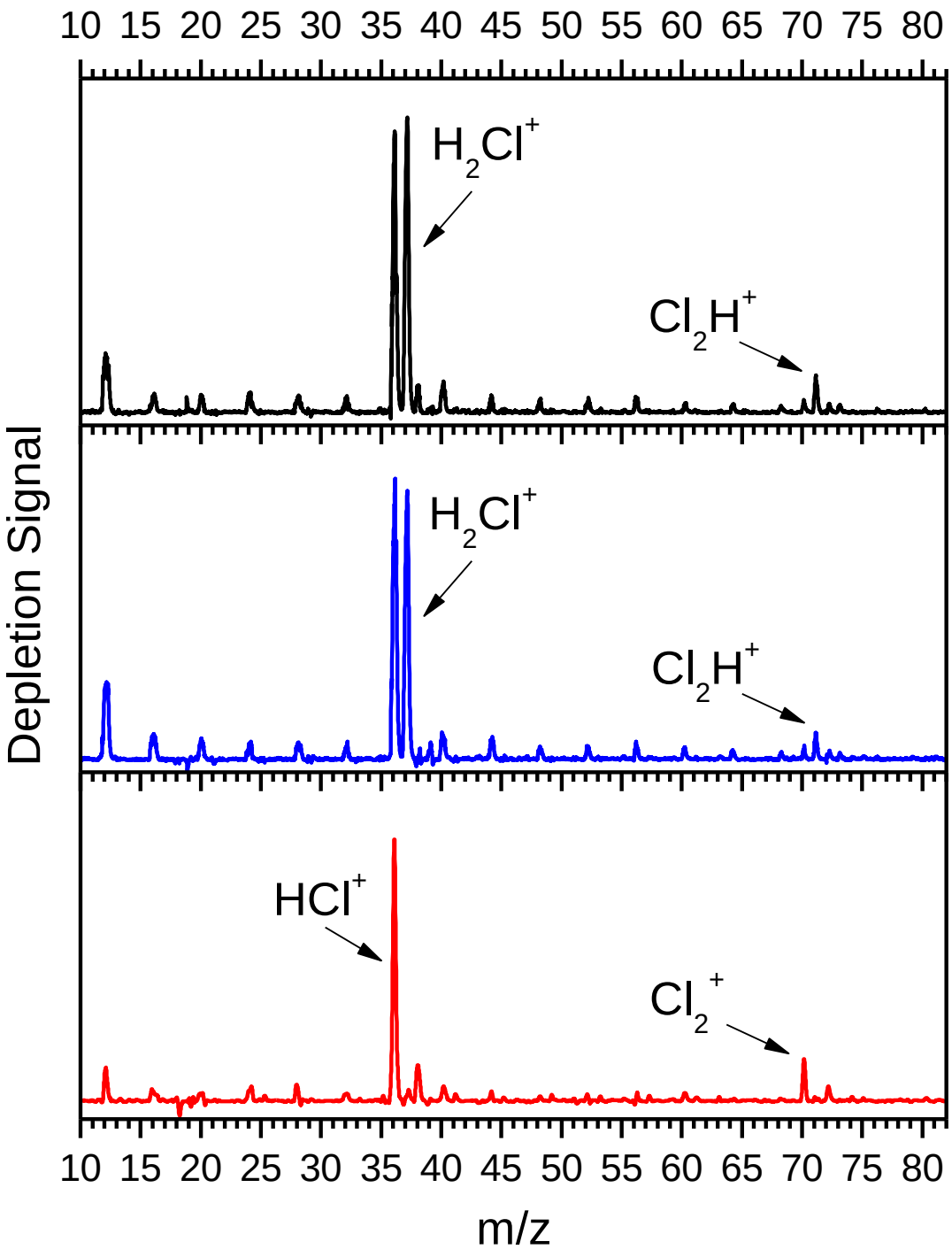

Figure 7.7: Difference mass spectra (laser OFF – laser ON) obtained for the three bands observed when HCl is present in the pickup chamber and Cl_2 is flowing through the hot pyrolysis source. The bottom DMS (red) was measured with the laser frequency fixed to 2880.8 cm^{-1}, middle DMS (blue) – 2764.0 cm^{-1}, top DMS (black) – 2798.4 cm^{-1}. The appearance of m/z = 37 and 71 u is due to the pickup of multiple HCl molecules and subsequent hydrogen transfer upon ionization of the complex.

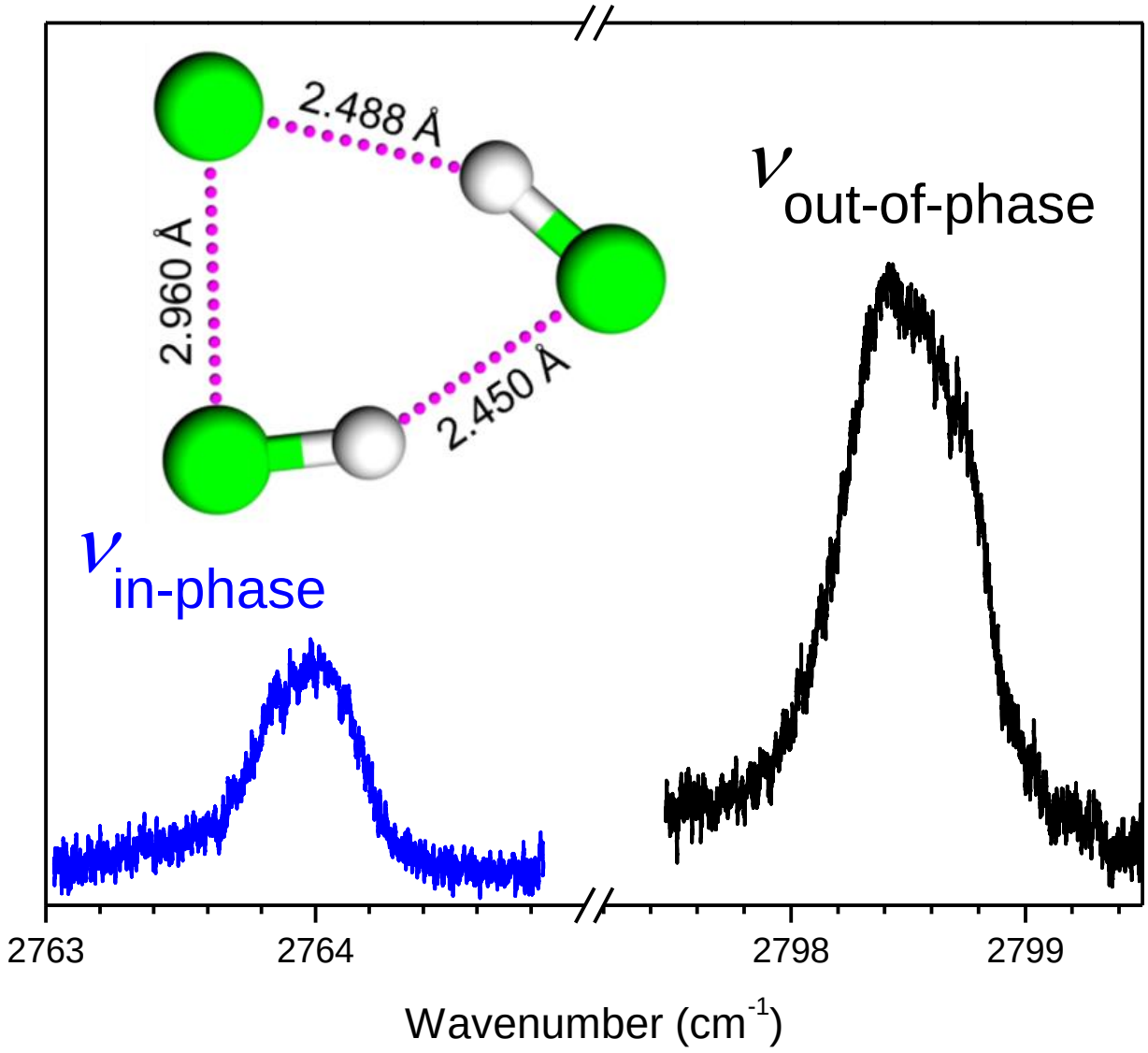

Figure 7.8: Expanded view of the two bands which arise from clusters containing a Cl atom and two HCl molecules. The Cl–$(HCl)_2$ geometry was computed at the MP2/aug-cc-pVTZ level, and the computed frequency difference between the in-phase and out-of-phase stretches is 30 cm^{-1}.

observed previously in the gas phase, it is unclear whether the dynamical timescale associated with the decay of the bright state is modified by the presence of the solvent.

Again, the Poisson curves and DMS (Figures 7.6 and 7.7, red) for the 2880.8 cm^{-1} feature are consistent with a Cl–HCl complex. This Cl–HCl band, shown in red in Figure 7.9, has a FWHM linewidth of 2 cm^{-1} and is only slightly less broad than that observed previously for the ν_1 free stretch of the L-shaped $(HCl)_2$ complex (3.43 cm^{-1} FWHM) in helium droplets.[23] The broadening observed for the 2880.8 cm^{-1} band is completely consistent with an assignment to an L-shaped Cl–HCl complex, and the broadening can be similarly rationalized as discussed previously for the $(HCl)_2$ ν_1 band. A similar magnitude 2.2 cm^{-1} linewidth was first reported by Nauta and Miller for the free stretch of He-solvated $(HF)_2$, with the liquid He environment leading to a preferentially broadening of the free stretch over the bound stretch,[24] and we follow their line of reasoning to assign an L-shaped geometry to the Cl–HCl complex isolated in helium droplets (see inset of Figure 7.9). To summarize their discussion, the elementary excitations of the helium droplet facilitate fast quenching of the dimer's rotational energy upon excitation of the ν_1 free stretch, leading to a broadened $K_a = 0 \rightarrow K_a = 1$ sub-band that lacks additional structure. In contrast, the ν_2 bound stretch exhibits rotational fine-structure indicative of a much longer timescale for rotational deactivation.

This difference between the two excited state lifetimes can be traced to the dominant selection rules and the rotational energies accessed by infrared excitation. The vibrational transition dipole moment for $(HF)_2$ is projected almost entirely along the inertial *a*-axis for the ν_2 bound stretch, whereas it lies almost entirely along the inertial *b*-axis for the ν_1 free stretch. This leads to *a*-type ($\Delta K_a = 0$ and $\Delta K_c = \pm 1$) and *b*-type ($\Delta K_a = \pm 1$ and $\Delta K_c = \pm 1$) selection rules for ν_1 and ν_2 bands, respectively. In the near-prolate limit ($(HF)_2$ is a near-prolate asymmetric top), *b*-

type transitions from $K_a = 0 \rightarrow K_a = 1$ populate final states with significantly greater rotational energy than do *a*-type transitions, in which $\Delta K_a = 0$. As depicted in Figure 7.10, the greater rotational energies accessed by *b*-type transitions can resonantly couple to a rather large density of droplet excitations, resulting in a reduction in the rotational lifetime and a concomitant broadening of the rovibrational sub-band beyond the linewidth expected due to the rotational contour. The rotational energies accessed by *a*-type transitions, however, lie within the "phonon gap" of the helium droplet dispersion curve.[23] The density of droplet states to which the excited rotor can couple is therefore significantly less in this case; therefore, the associated spectrum of the ν_2 bound stretch of $(HF)_2$ is rotationally resolved. Harmonic frequency calculations done at the MP2/aug-cc-pVTZ level for the L-shaped Cl–HCl complex predict the ratio of transition dipole moment projections for the HCl stretching mode to be $\dot{\mu}_b : \dot{\mu}_a = 26.7$. With the caveat that the computation is for a rigid complex, this transition moment ratio implies that the *b*-type component will be >700 times more intense than the *a*-type component. Because of the large computed *A* rotational constant for Cl–HCl (10.59 cm^{-1}), we expect the *b*-type component of the HCl stretch band to be homogeneously broadened, as observed for the $(HF)_2$ and $(HCl)_2$ ν_1 bands, and via a similar mechanism. Indeed, this expectation is completely consistent with the observed feature at 2880.8 cm^{-1}. Moreover, a rotationally resolved *a*-type band was not found, despite careful searching to the red of the *b*-type component at 2880.8 cm^{-1}. Further support for the assignment of the 2880.8 cm^{-1} band to an approximately L-shaped complex comes from the band origin. Because the 2880.8 cm^{-1} band lies in the free HCl stretching region, this band must arise from a Cl–HCl complex with minimal hydrogen bonding. Indeed, the L-shaped complex contains a "free" HCl stretch; the band origin of this complex is predicted to be redshifted from the HCl monomer stretch by only ≈17 cm^{-1}. On the basis of the computed *A* rotational constant

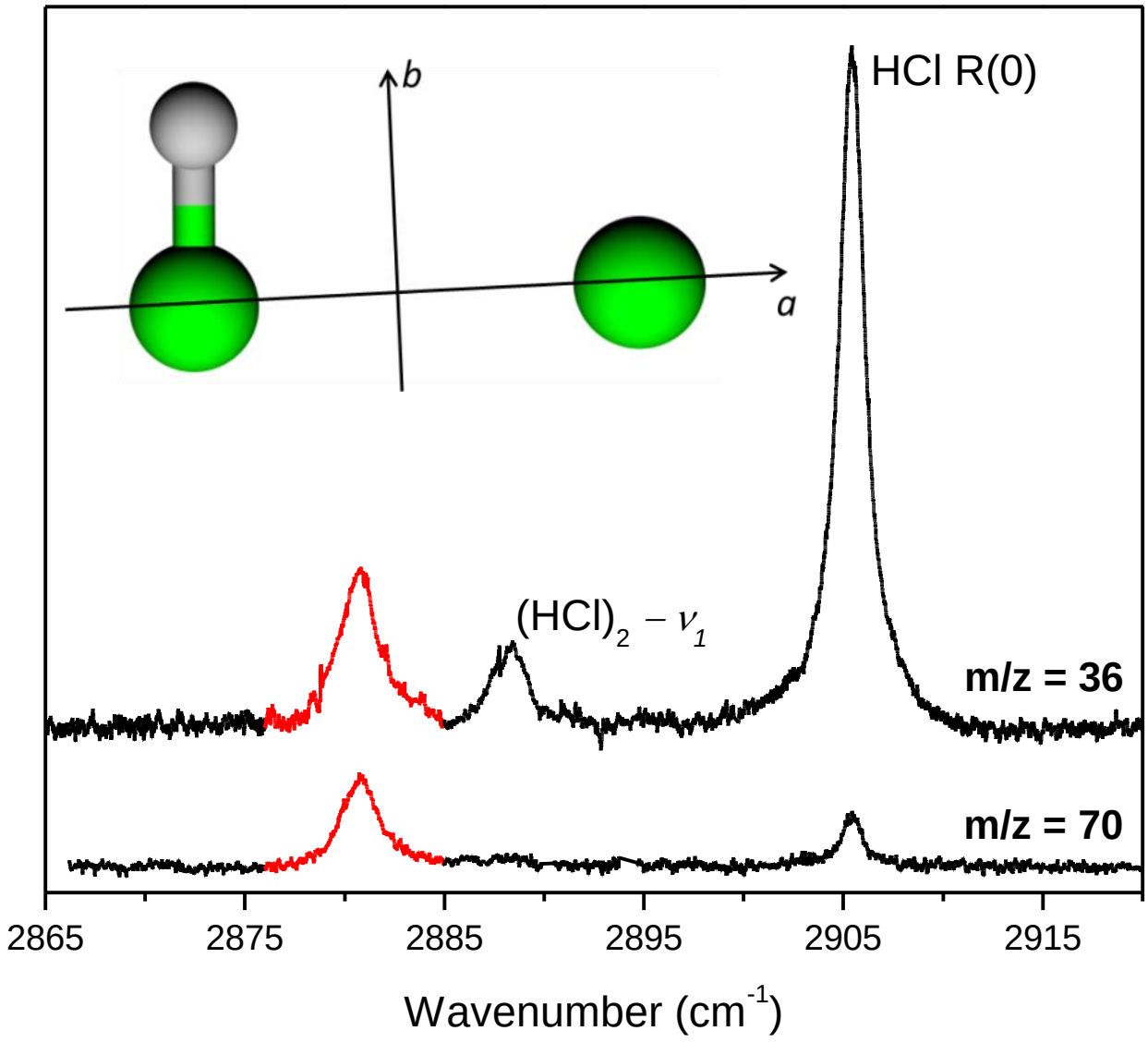

Figure 7.9: Expanded view of the "free" HCl stretching region measured on the mass channels indicated. The Cl–HCl geometry was optimized at the MP2/aug-cc-pVTZ level, and the inertial axes are drawn approximately. The broad band in red is assigned to the HCl stretch of this complex based on the band frequency and linewidth (see text for discussion). Additionally, scanning on m/z = 70 u discriminates against droplets containing HCl clusters that do not also contain a Cl atom. Signal due to $(HCl)_2$ is completely eliminated and the HCl monomer intensity is greatly reduced; the source of monomer signal likely results from droplets which first pickup a single HCl, are vibrationally excited, and then pick up a Cl atom.

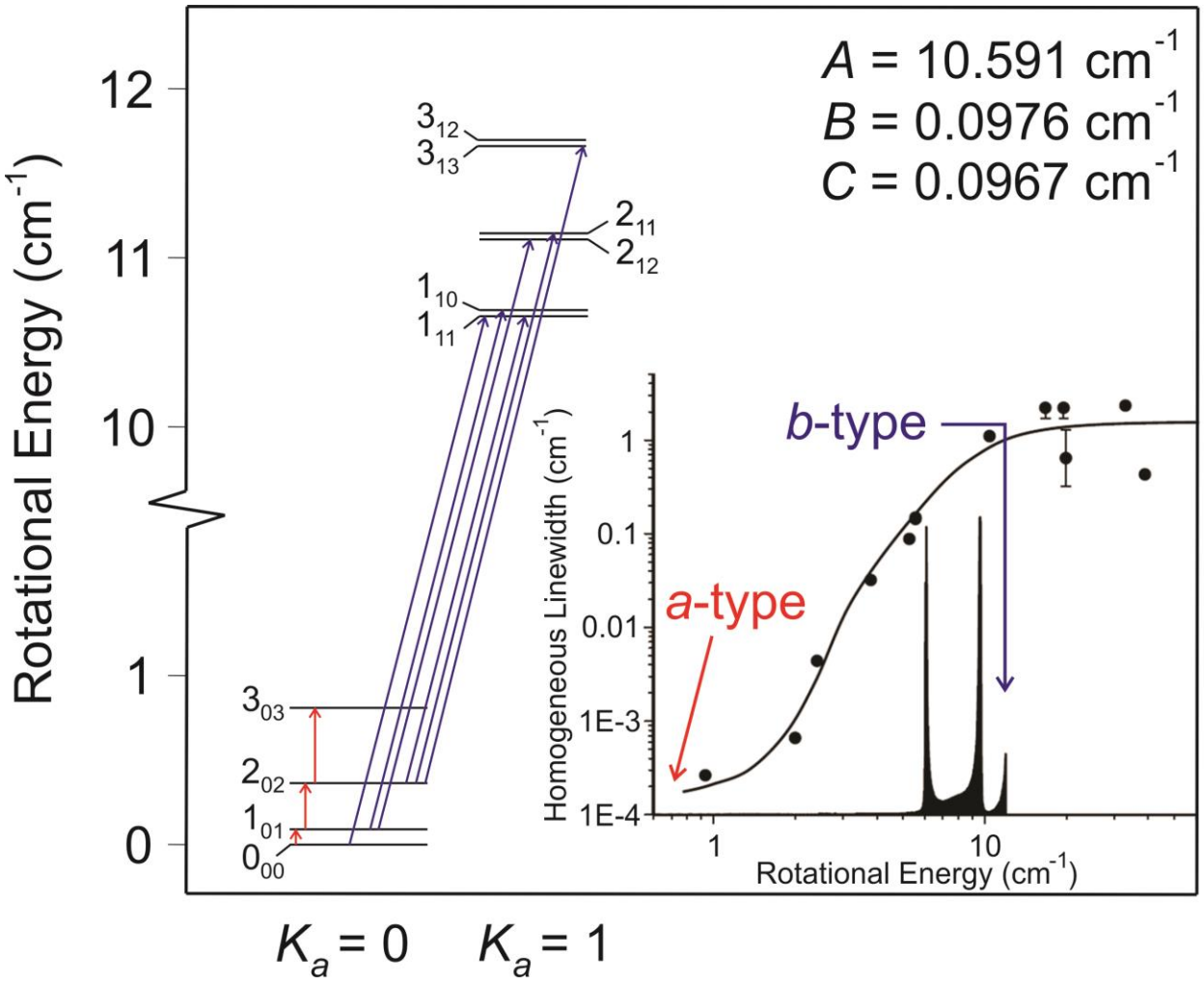

Figure 7.10: On the left is an energy diagram showing the allowed *a*-type (red, vertical arrows) and *b*-type (blue, diagonal arrows) transitions out of the three lowest rotational levels. The asymmetric top rotational levels were computed using *ab initio* rotational constants for Cl–HCl and are drawn somewhat exaggerated for clarity. The right inset shows the density of states for bulk, superfluid ^{4}He with the peaks near 6 and 10 cm^{-1} corresponding to the roton and maxon elementary excitations, respectively. The data points and trend line correspond to observed linewidths for various molecular rotors in ^{4}He nanodroplets.[15] Fast rotors tend to couple more efficiently to the He droplet environment leading to more efficient rotational deactivation.

(10.59 cm^{-1}), which is expected to be only slightly affected by the helium environment, the experimental band origin is estimated to be ≈2870 cm^{-1}. This gives an experimental monomer-to-complex redshift of 16 cm^{-1}, in good agreement with the *ab initio* prediction. Again, this approximate band origin is determined with the caveat that the *A* constant is set equal to the equilibrium *ab initio* value. However, the system exhibits wide-amplitude bending and stretching motions in the ground rovibrational state. Indeed, the eigenvalue of the lowest energy bound state is above the barrier to interconversion between linear and L-shaped wells on the lowest adiabatic potential surface.[8] It is interesting to note that the "*A*" constant from bound state calculations[9] is approximately 12.4 cm^{-1}, which indicates that vibrational averaging brings the complex somewhat closer to linearity. The MP2 calculations in Table 7.1 predict similar vibrational frequencies for a strictly linear Cl–HCl complex and the L-shaped Cl_2–HCl complex, both of which are redshifted from the HCl monomer ν_0 by ≈50 cm^{-1}. This value agrees well with the 2836.4 and 2834.5 cm^{-1} bands in the Ar matrix, reported by Andrews and Hunt.[12] They assigned these bands to Cl–H^{35}Cl and Cl–H^{37}Cl, respectively. While it is possible that these bands in the Ar matrix instead correspond to the Cl_2–HCl type clusters discussed in this report, it may also be the case that either solvent effects or the higher temperature of the Ar matrix leads to the population of Cl–HCl bound states that are more localized in the linear well, leading to an expectation value for the HCl stretch frequency that is significantly red-shifted in comparison to the equilibrium value computed for the L-shaped complex.

7.4 Summary

Complexes consisting of one chlorine molecule with one or two HCl molecules were formed in He nanodroplets via sequential pickup of the monomers, and their HCl stretching

modes were probed with infrared laser spectroscopy. The number of HCl molecules in the complexes was determined by comparing the depletion signal of each band as a function of HCl pressure with the pure HCl monomer and dimer Poisson curves. The band assigned to the Cl_2–HCl complex is consistent with a hydrogen-bonded, L-shaped geometry based on its proximity to the band origin for the bound (ν_2) stretch of $(HCl)_2$. Two bands assigned to the Cl_2–$(HCl)_2$ complex are even more strongly hydrogen bound with vibrational frequencies lying between the HCl dimer and trimer bands. Harmonic frequency computations were performed on a C_s symmetry Cl_2–$(HCl)_2$ geometry optimized at the MP2/aug-cc-pVTZ level of theory, and the predicted frequency differences agree with those observed in helium droplets.

Complexes containing a Cl atom and one to two HCl molecules were also stabilized in helium droplets. The Cl atoms were produced by allowing Cl_2 to effuse through a SiC furnace operated near 2000 K.[18] Two bands are tentatively assigned to the cyclic Cl–$(HCl)_2$ complex on the basis of harmonic frequency calculations at the same level as above. In-phase and out-of-phase HCl stretches of this complex are predicted to have a frequency difference of 30 cm^{-1}, in agreement with the observed difference of 34.4 cm^{-1}. Additionally, a broad vibrational band centered at 2880.8 cm^{-1} (2 cm^{-1} FWHM) is consistent with an assignment to an approximately L-shaped Cl–HCl complex. It is shifted from the monomer frequency and broadened to a similar extent as the previously studied free stretches of $(HF)_2$ and $(HCl)_2$.[23,24] The broad line shape in those cases was attributed to the transition dipole moment lying nearly entirely along the *b*-axis: the associated *b*-type selection rules access highly excited rotational states with $K_a = 1$, and these rotational levels can couple to a large density of droplet excitations, which results in efficient resonant energy transfer from the complex to the droplet and a reduced excited state lifetime. The estimated band origin of 2870 cm^{-1} yields only a ≈16 cm^{-1} monomer-to-complex redshift,

indicating a lack of strong H-bonding. Previous Ar matrix measurements assign two bands near 2835 cm^{-1} to a linear, hydrogen-bonded Cl–HCl complex.[12] We, however, find no evidence for any other Cl–HCl complex in helium droplets, and our observations agree with the results of recent bound state calculations that predict a ground state L-shaped complex.[8]

References

(1) Metz, R. B.; Kitsopoulos, T.; Weaver, A.; Neumark, D. M. *J. Chem. Phys.* **1988**, *88*, 1463-1465.

(2) Zhao, Z. Q.; Chapman, W. B.; Nesbitt, D. J. *J. Chem. Phys.* **1995**, *102*, 7046-7058.

(3) Liu, K.; Kolessov, A.; Partin, J. W.; Bezel, I.; Wittig, C. *Chem. Phys. Lett.* **1999**, *299*, 374-380.

(4) Skouteris, D.; Manolopoulos, D. E.; Bian, W. S.; Werner, H. J.; Lai, L. H.; Liu, K. P. *Science* **1999**, *286*, 1713-1716.

(5) Dubernet, M. L.; Hutson, J. M. *J. Phys. Chem.* **1994**, *98*, 5844-5854.

(6) Zdanska, P.; Nachtigallova, D.; Nachtigall, P.; Jungwirth, P. *J. Chem. Phys.* **2001**, *115*, 5974-5983.

(7) Klos, J. A.; Chalasinski, G.; Szczsniak, M. M.; Werner, H. J. *J. Chem. Phys.* **2001**, *115*, 3085-3098.

(8) Zeimen, W. B.; Klos, J.; Groenenboom, G. C.; van der Avoird, A. *J. Phys. Chem. A* **2003**, *107*, 5110-5121.

(9) Zeimen, W. B.; Klos, J.; Groenenboom, G. C.; van der Avoird, A. *J. Phys. Chem. A* **2004**, *108*, 9319-9322.

(10) Kettwich, S. C.; Pinelo, L. F.; Anderson, D. T. *Phys. Chem. Chem. Phys.* **2008**, *10*, 5564-5573.

(11) Merritt, J. M.; Kupper, J.; Miller, R. E. *Phys. Chem. Chem. Phys.* **2005**, *7*, 67-78.

(12) Andrews, L.; Hunt, R. D. *J. Chem. Phys.* **1988**, *89*, 3502-3504.

(13) Callegari, C.; Lehmann, K. K.; Schmied, R.; Scoles, G. *J. Chem. Phys.* **2001**, *115*, 10090-10110.

(14) Toennies, J. P.; Vilesov, A. F. *Angew. Chem., Int. Ed.* **2004**, *43*, 2622-2648.

(15) Choi, M. Y.; Douberly, G. E.; Falconer, T. M.; Lewis, W. K.; Lindsay, C. M.; Merritt, J. M.; Stiles, P. L.; Miller, R. E. *Int. Rev. Phys. Chem.* **2006**, *25*, 15-75.

(16) Stienkemeier, F.; Lehmann, K. K. *J. Phys. B: At., Mol. Opt. Phys.* **2006**, *39*, R127-R166.

(17) Hartmann, M.; Miller, R. E.; Toennies, J. P.; Vilesov, A. *Phys. Rev. Lett.* **1995**, *75*, 1566-1569.

(18) Kohn, D. W.; Clauberg, H.; Chen, P. *Rev. Sci. Instrum.* **1992**, *63*, 4003-4005.

(19) Brink, D. M.; Stringari, S. *Z. Phys. D: At., Mol. Clusters* **1990**, *15*, 257-263.

(20) Morrison, A. M.; Liang, T.; Douberly, G. E. *Rev. Sci. Instrum.* **2013**, *84*, 013102.

(21) Schuder, M. D.; Lovejoy, C. M.; Lascola, R.; Nesbitt, D. J. *J. Chem. Phys.* **1993**, *99*, 4346-4362.

(22) Skvortsov, D.; Choi, M. Y.; Vilesov, A. F. *J. Phys. Chem. A* **2007**, *111*, 12711-12716.

(23) Ortlieb, M.; Birer, O.; Letzner, M.; Schwaab, G. W.; Havenith, M. *J. Phys. Chem. A* **2007**, *111*, 12192-12199.

(24) Nauta, K.; Miller, R. E. *J. Chem. Phys.* **2000**, *113*, 10158-10168.

CHAPTER 8

TWO-CENTER THREE-ELECTRON BONDING IN $CLNH_3$ REVEALED VIA HELIUM DROPLET INFRARED LASER STARK SPECTROSCOPY: ENTRANCE CHANNEL COMPLEX ALONG THE $CL + NH_3 \rightarrow CLNH_2 + H$ REACTION

Pyrolytic dissociation of Cl_2 is employed to dope helium droplets with single Cl atoms. Sequential addition of NH_3 to Cl-doped droplets leads to the formation of a complex residing in the entry valley to the substitution reaction, $Cl + NH_3 \rightarrow ClNH_2 + H$. Infrared Stark spectroscopy in the NH stretching region reveals symmetric and antisymmetric vibrations of a C_{3v} symmetric top. Frequency shifts from NH_3 and dipole moment measurements are consistent with a $ClNH_3$ complex containing a relatively strong two-center three-electron (2c-3e) bond. The nature of the 2c-3e bonding in $ClNH_3$ is explored computationally and found to be consistent with the complexation-induced blue shifts observed experimentally. Computations of interconversion pathways reveal nearly barrierless routes to the formation of this complex, consistent with the absence in experimental spectra of two other complexes, NH_3Cl and $Cl–HNH_2$, which are predicted in the entry valley to the hydrogen abstraction reaction, $Cl + NH_3 \rightarrow HCl + NH_2$.

8.1 Introduction

The two-center three-electron (2c-3e) bonding concept was first introduced by Pauling in the early 1930s,[1] and it is commonly invoked to describe the chemistry and molecular orbital theory of free-radicals.[2-5] Nearly resonant interaction between a doubly-occupied orbital on one atomic center with a singly-occupied orbital on another generates bonding and anti-bonding molecular orbitals, the latter of which is singly-occupied (SOMO). Although longer and weaker in comparison to a typical two-electron bond, 2c-3e hemi-bonds have nevertheless been shown to be significantly stronger than the electrostatic or dispersion binding associated with closed-shell molecular complexes.[6,7] We present a combined experimental and theoretical study of the $ClNH_3$ complex, which exhibits a strong 2c-3e hemi-bonding interaction that is revealed in the analysis of the NH stretch vibrations measured via helium nanodroplet isolation spectroscopy.

One of the simplest examples of a molecule containing a 2c-3e bond is the helium dimer cation (He^+ ($1s^1$) + He ($1s^2$) → He_2^+ $(\sigma)^2(\sigma^*)^1$), which has a dissociation energy equal to 2.47 eV.[8] By contrast, neutral He_2 is characterized by a largely repulsive potential with a 1.3 meV equilibrium well-depth.[9] As another example, Pauling described the bonding in nitric oxide (NO) as consisting of a double bond and a three-electron bond. Pauling postulated that the presence of the three-electron bond precludes NO dimerization at room temperature.[1] In a theoretical study of Cl atom addition to nitrogen bases, Radom and co-workers found several examples of 2c-3e bond formation; in general, the strength of the 2c-3e bond was found to be inversely proportional to the difference between the ionization potential of the nitrogen base and the Cl electron affinity (3.62 eV).[4] 2c-3e hemi-bonding was also explored in computational work by Guo and co-workers, in which the interactions between halogen atoms (F, Cl, and Br)

and water were discussed in terms of the aforementioned molecular orbital picture. Rather than electrostatic or dispersive, the interaction between monomers was shown to be electronic in character due to the near resonant mixing of the half-filled p-orbital on the halogen atom with the highest occupied molecular orbital (HOMO) on water.[7]

Careful consideration of the long-range interaction potential between halogen atoms and closed shell molecules is essential for an accurate description of the associated chemical reaction dynamics, especially at low temperature.[10] As they approach one another, long-range stereodynamic forces can steer reactants toward or away from the transition state geometry, affecting the reaction rate and/or the branching ratio of the products.[10-13] Electronic structure theory predicts a stable van der Waals complex (**CR1**; Figure 8.1) in the entrance channel of the $Cl + NH_3$ reaction.[6] In addition to the van der Waals complex, two minima are predicted that correspond to more strongly bound 2c-3e complexes (**CR2** and **CR3**; Figure 8.1).[6,14] **CR1** and **CR3** are entrance channel complexes along the hydrogen abstraction path $Cl + NH_3 \rightarrow NH_2 + HCl$, whereas **CR2** lies in the entry valley to the substitution reaction $Cl + NH_3 \rightarrow NH_2Cl + H$.[14] **CR2** is the most strongly bound adduct of the three, and the barrier to substitution is ten times larger than for hydrogen abstraction, as shown in Figure 8.2.[6,14]

$Cl\text{-}NH_3$ complexes were investigated theoretically by Monge-Palacios and Espinosa-Garcia in an attempt to rationalize the disagreement between computed hydrogen abstraction barrier heights[6,14] and experimental determinations of rate coefficients near room temperature.[15-17] They concluded that **CR1** and **CR3** indirectly influence the kinetics by increasing the tunneling contribution to reaction. However, the authors noted that **CR1** and **CR3** complexes were elusive even at the CCSD(T)/cc-pVTZ level, and in fact, the **CR3** complex could not be located at the MP2 level. Harmonic frequency computations for **CR1** at the CCSD(T)/cc-pVTZ

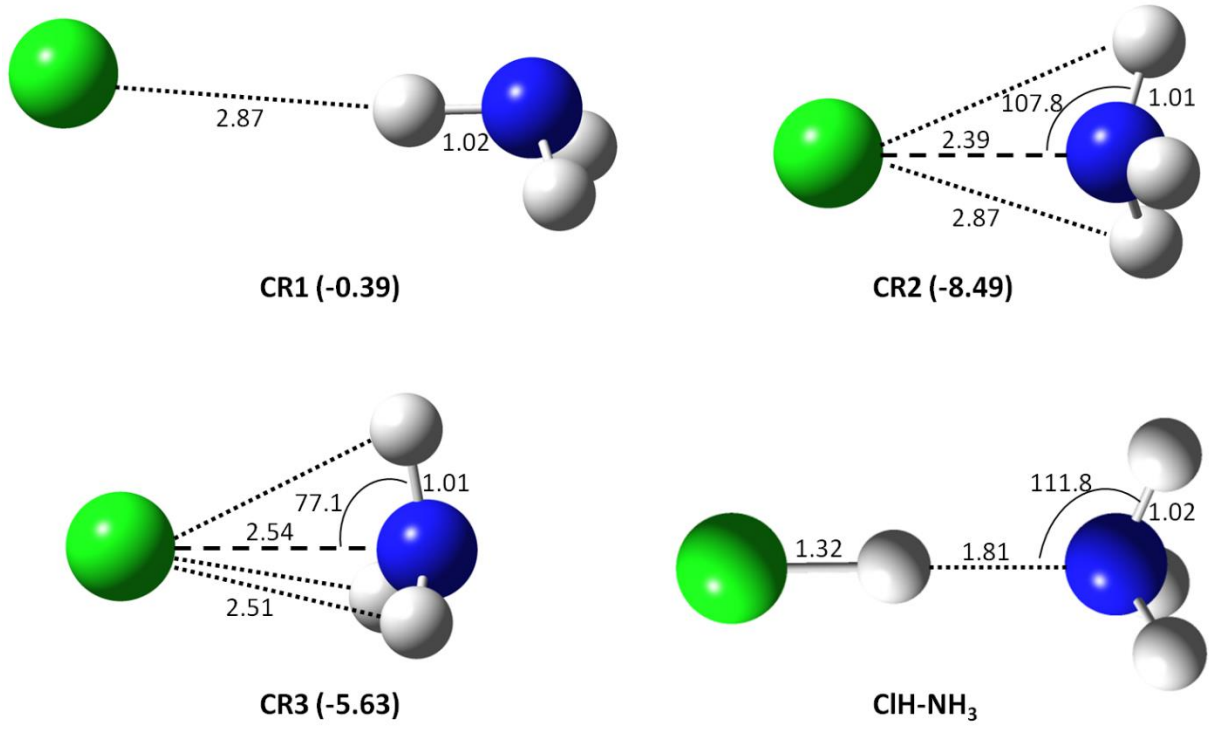

Figure 8.1: The geometries of the CR1, CR2, CR3 and ClH–NH_3 complexes. The numbers in parenthesis for CR1, CR2 and CR3 are the relative energies (in kcal/mol) including ZPE corrections with respective to the Cl + NH_3 channel. The distances and angles are given in Å and degrees, respectively.

level yield three vibrations with frequencies < 90 cm^{-1}, indicative of a very flat potential energy surface in the vicinity of the van der Waals complex.

Experimental investigation of the Cl + NH_3 reaction system is limited to two gas-phase kinetics studies of the hydrogen abstraction reaction near room temperature.[15,16] Related 2c-3e Cl-NR_3 systems were postulated in the analysis of ESR spectra obtained following the radiolysis of alkylammonium salts at 77 K.[18] To the best of our knowledge, however, there are no spectroscopic reports for the isolated entrance or exit channel complexes of the Cl + NH_3 reaction. Helium droplets are advantageous in the study of pre-reactive complexes because of their ability to capture and quickly cool individual "reactants" and quench the associated kinetic

energy generated upon molecular complexation. Due to this rapid cooling, He droplets are capable of stabilizing entrance channel complexes involving open-shell reactants.[19-21] In this work, we sequentially add Cl and NH_3 to He droplets and probe with infrared (IR) laser Stark spectroscopy the outcome of the low temperature reaction between these species. The results are rationalized with high-level electronic structure computations of the Cl + NH_3 potential energy surface, revealing facile rearrangement pathways favoring the formation of the 2c-3e **CR2** complex. The nature of the bonding in this system and its impact on the infrared spectrum is discussed.

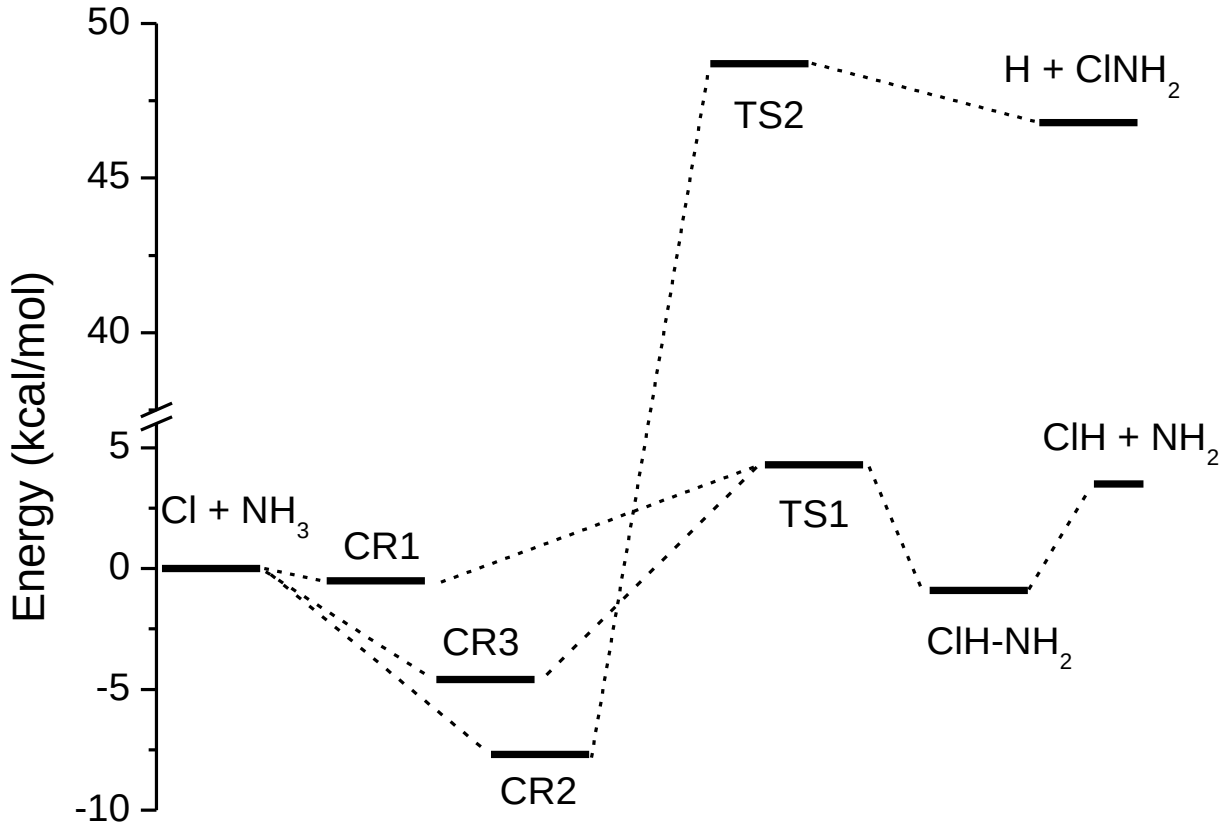

Figure 8.2: Potential energy surface for the Cl + NH_3 reaction. The energies of TS2 and H + $ClNH_2$ are taken from Xu and Lin,[14] whereas the energetics of the remaining species are from Monge-Palacios and Espinosa-Garcia.[6]

8.2 Experimental Methods

A brief description of the helium nanodroplet methodology follows, although it has been discussed in detail previously.[22-25] Superfluid helium nanodroplets are generated in the high-pressure region of a continuous expansion of He gas (30 bar backing pressure) through a cold nozzle with a 5 ± 1 μm diameter aperture. With the nozzle temperature at 17 K, droplets are produced with an average size of 4500 He atoms.[22,26-28] Nascent droplets evaporatively cool to ≈0.4 K and are collimated into a beam by a skimmer having a 0.4 mm aperture.[23,29] The droplet beam passes into a pickup chamber where droplets collide with and solvate gas-phase Cl atoms and NH_3 molecules and subsequently cool their internal degrees of freedom to 0.4 K.[30] Atomic Cl is generated through the thermal decomposition of Cl_2 (Sigma-Aldrich, ≥99.5% purity) as it collides with the walls of a resistively heated SiC tube (ID = 1 mm; T≈1600 K).[20,31] This SiC pyrolysis source is oriented perpendicular to the droplet beam path with the SiC tube adjacent to the droplet beam such that Cl atoms exiting the SiC tube effuse into the droplet path and are picked up. The effusive flow of Cl_2 through the SiC source is adjusted to optimize for the pick-up of single Cl atoms. The Cl-doped droplet beam subsequently passes through a 2 cm long, differentially pumped, stainless steel tube containing $\approx 10^{-6}$ Torr of anhydrous NH_3 (99.99% purity), metered directly from a lecture bottle.

Following dopant pickup, the droplet beam enters a Stark cell consisting of two Au-coated multipass mirrors and two parallel, stainless steel electrodes mounted orthogonal to the mirrors.[32-35] A homogeneous electric field up to tens of kV/cm can be applied to a ≈20 cm portion of the droplet beam, and the interaction of the electric dipole moment of the He-solvated molecule with the applied field lifts the *M* degeneracy of the rotational energy levels. Droplets

subsequently pass into a mass spectrometer where they are ionized by electron impact.[23] The $He^+ + M \rightarrow He + M^+$ charge transfer reaction ionizes the He-solvated molecular complex, which typically results in molecular fragmentation and the complete evaporation of the droplet.[36,37] Gas-phase ions subsequently enter the quadrupole mass spectrometer (QMS) and are detected by an electron multiplier. The current from the electron multiplier is converted into a voltage, processed by a lock-in amplifier, and recorded by a custom Labview data collection program.

The tunable, mid-IR (3150-4100 cm^{-1}) idler beam from a continuous-wave optical parametric oscillator (cw-OPO) counter-propagates the droplet beam or intersects the droplet beam at nearly right angles in the Stark/multipass cell. Upon rovibrational excitation, the internal energy of the dopant is quickly quenched by the evaporative loss of many He atoms, with an individual He atom carrying away ≈5 cm^{-1} of internal energy.[38] This geometric cross-section change reduces the probability for ionization by electron impact. Ion-signal depletion is therefore observed in mass channels associated with ionization-induced dopant/droplet fragmentation. The IR radiation is mechanically chopped at 80 Hz and continuously tuned from 3150 – 3530 cm^{-1} with ≈10 MHz resolution,[39] enabling background-free measurement of the laser-induced depletion signal. In most of the current work, the quadrupole is set to pass only ions with m/z = 51 u. The relevant ions of this mass correspond to the $^{35}ClNH_2^+$ species, however droplets containing $(NH_3)_{n\geq3}$ clusters may be ionized (and fragment), producing laser-induced depletion in the 51 u mass channel ($N_3H_9^+$). Nevertheless, the experimental conditions minimize the production of ammonia clusters larger than the dimer. Moreover, the 51 u mass channel largely discriminates against complexes containing the ^{37}Cl isotope. Spectral simulations of experimental rovibrational bands were carried out with PGOPHER software.[40]

8.3 Theoretical Methods

Following our recent work on hemi-bond complexes,[7,41] structures of NH_3, NH_3Cl, and the NH_4Cl complex were optimized using the coupled-cluster method (unrestricted coupled-cluster method for the open shell molecule NH_3Cl) with singles, doubles, and perturbative triples excitations (CCSD(T)/UCCSD(T)),[42,43] with the augmented correlation consistent polarized valence triple zeta (aug-cc-pVTZ or AVTZ) basis.[44] The harmonic frequencies of the molecules were further calculated at the same CCSD(T)/AVTZ level of theory. These calculations have been carried out using MOLPRO 2010.1.[45] For the infrared intensity calculations, the CCSD method[46] with AVTZ basis was employed in GAUSSIAN 09.[47]

8.4 Results

Figure 8.3 is a survey spectrum covering the relevant N–H stretching region. The survey scan was carried out with Cl_2 flowing through the hot pyrolysis source, 10^{-6} Torr of NH_3 in the pickup cell, and the QMS set to pass ions having m/z = 51 u. As described above, the spectrum corresponds to the laser-induced cross-section reduction for droplets producing m/z=51 u upon ionization in the mass spectrometer. Spectral signatures of NH_3 monomer and dimer do not appear in this mass channel. Several broad, weak features in the survey spectrum are assigned to $(NH_3)_{n\geq3}$ clusters via comparison to previous work by Vilesov and co-workers.[48] Three distinct regions near 3350, 3450, and 3500 cm^{-1} contain intense laser-induced depletion signals. To determine the origin of these features, these regions were re-measured with Cl_2 flowing through the pyrolysis source at room temperature. Only the features straddling 3450 cm^{-1} are present

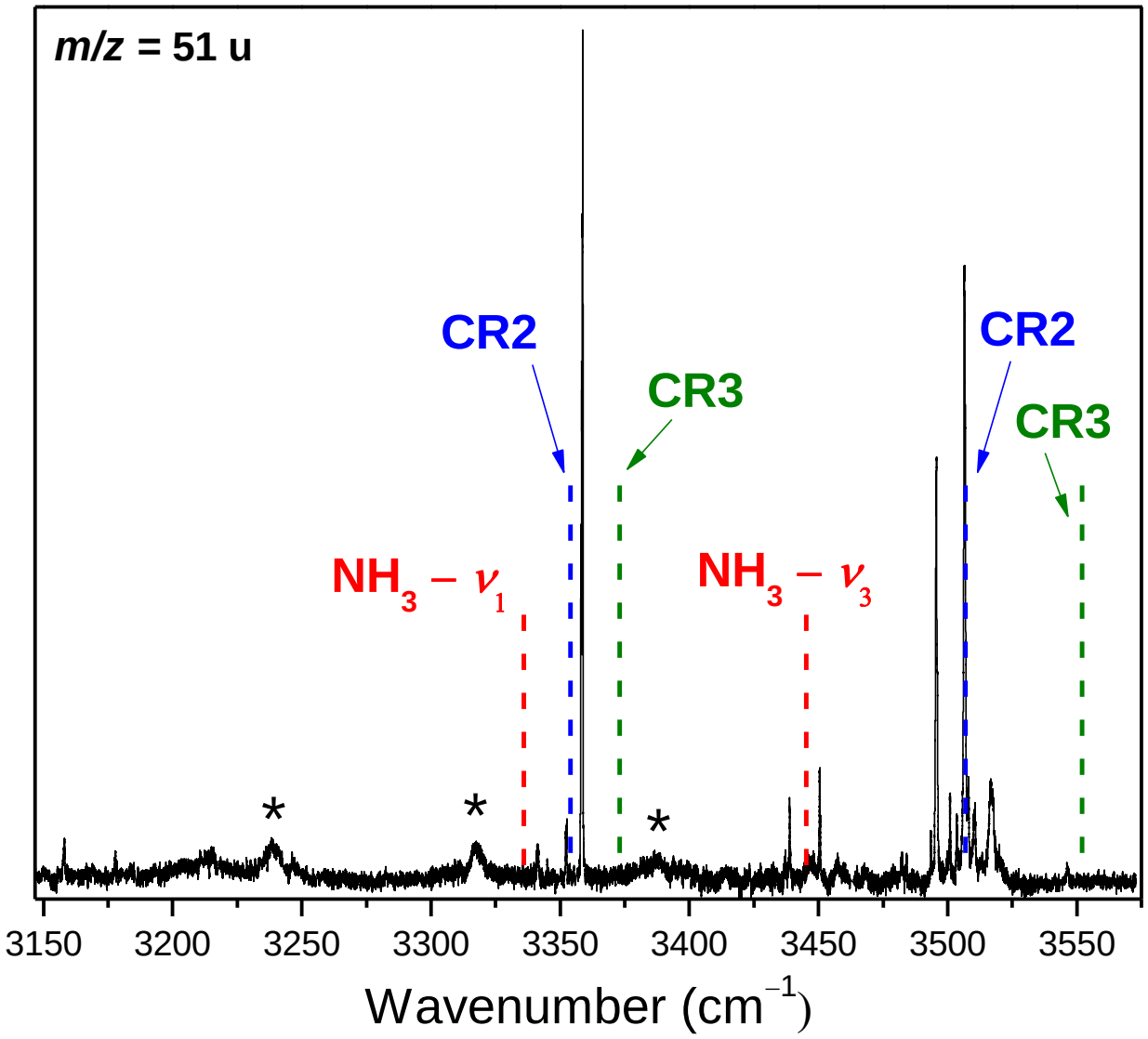

Figure 8.3: "Hot-pyrolysis" survey scan of the NH stretching region measuring the laser-induced depletion signal on *m/z* = 51 u $(ClNH_3)^+$. Several broad features marked by * are likely due to the formation of larger NH_3 clusters ($n \geq 3$). The approximate band origins for the symmetric and antisymmetric vibrations of NH_3 are shown in red (short dashed lines). Scaled harmonic frequencies for both the $ClNH_3$ (CR2) and NH_3Cl (CR3) isomers are shown in blue and green, respectively (longer dashed lines).

under these "cold-pyrolysis" source conditions, and because these bands cannot be ascribed to NH_3 or NH_3 clusters alone, they must arise from complexes consisting of at least one Cl_2 molecule and one NH_3 molecule. Spectral features in the 3350 and 3500 cm^{-1} regions, however, are only present upon heating the SiC pyrolysis furnace (T≈1600 K). These bands likely arise from species produced via the Cl + NH_3 reaction carried out within He droplets. The analysis of partially resolved rotational fine-structure exhibited by bands near 3350 and 3500 cm^{-1} provides strong evidence for an assignment to symmetric and antisymmetric NH_3 stretches of a $ClNH_3$ molecular complex (either **CR2** or **CR3**). As described below, Stark spectroscopy reveals the structural identity of this $ClNH_3$ species.

8.4.1 ClH−NH_3

The generation of gas-phase Cl atoms yields a low background of HCl within the pickup chamber. To rule out the possibility that the observed bands in Figure 8.3 are due to formation of ClH−NH_3 complexes, the 3350 and 3500 cm^{-1} regions were measured on m/z = 51, 52, and 53 u with the pyrolysis source turned off and both HCl and NH_3 (taken from lecture bottles) present in the pickup cell. The $(^{35}ClNH_3)^+$ species may contribute to the 52 u mass channel. (Throughout the remainder of this article, references to Cl correspond to the more abundant ^{35}Cl isotope unless otherwise indicated.) There are no observed vibrations of an ClH−NH_3 complex in either the 3350 or 3500 cm^{-1} regions; however, measurements in the 52 u channel reveal *K* sub-bands between 3430 and 3460 cm^{-1} (Figure 8.4) consistent with the antisymmetric stretch of the ClH−NH_3 binary complex. This signature of the ClH−NH_3 complex is not observed in the "hot-pyrolysis" survey spectrum (Figure 8.3), indicating that the subset of droplets containing

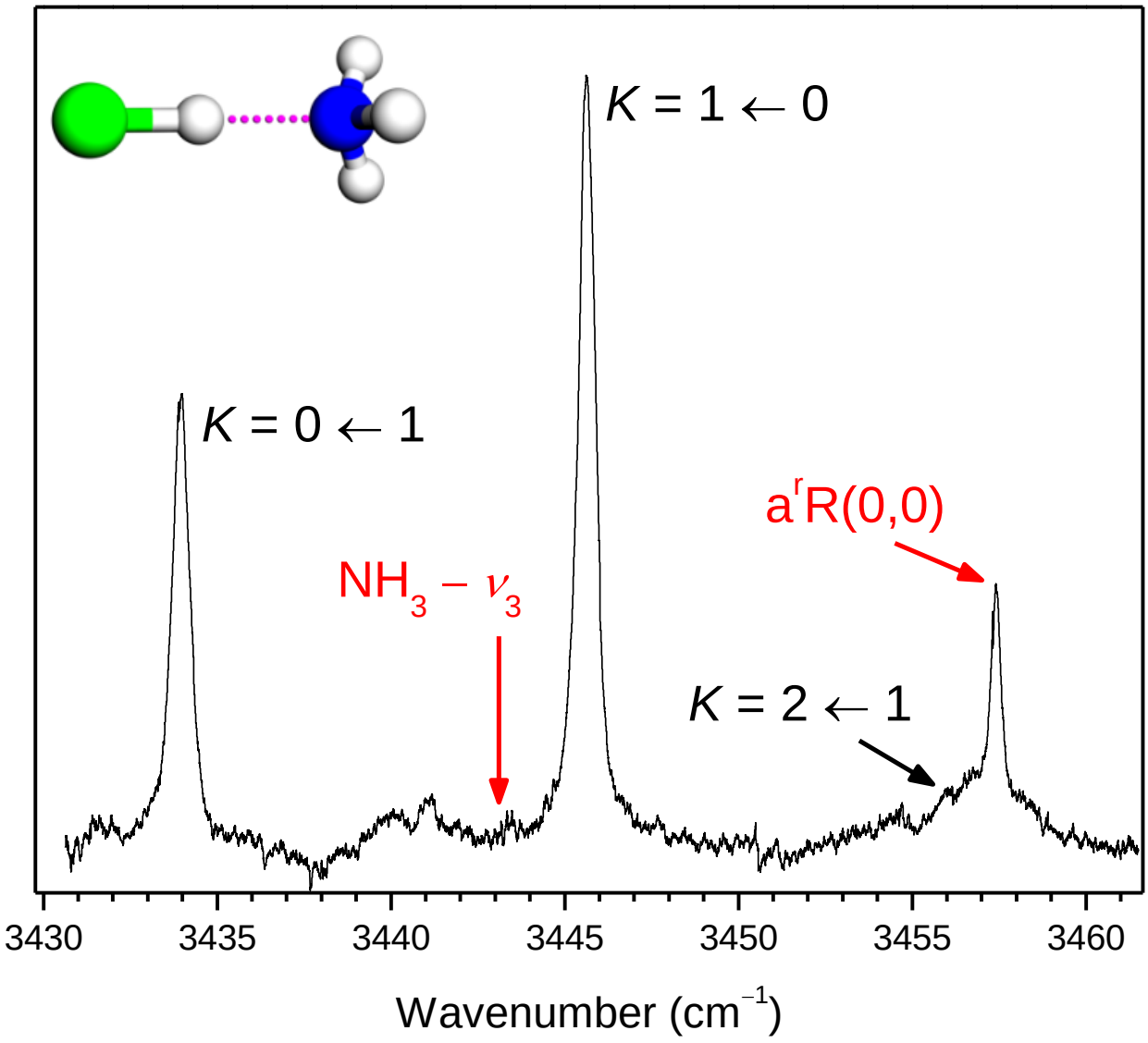

Figure 8.4: Rovibrational bands assigned to the antisymmetric NH stretching vibration of the ClH–NH_3 complex. Shown in red is the location of the band origin for the antisymmetric stretch of NH_3 and one of its observed transitions. The broad feature underlying the NH_3 $a^rR(0,0)$ transition is assigned to ClH–NH_3 rovibrational transitions from $K = 1$ to $K = 2$, and a discussion of the observed broadening is given in the text. We note that NH_3 monomers can be observed on $m/z = 51$ if the following events happen in order: a) some fraction of droplets pickup an NH_3 molecule ($m/z = 17$), b) IR excitation of He-solvated NH_3 leads to droplet beam depletion, c) the depleted droplet containing NH_3 then picks up a Cl atom ($m/z = 35$) to form $ClNH_3$, d) the He-solvated $ClNH_3$ is ionized to form m/z = 51.

ClH−NH_3 are discriminated against when measuring depletion in the 51 u channel. The ClH−NH_3 band origin (3439.75 cm^{-1}) lies very close to the ν_3 band origin of He-solvated NH_3 at 3443.1 cm^{-1}.[29] Consistent with this, harmonic frequency calculations at the CCSD(T)/AVTZ level predict small complexation-induced shifts of the NH_3 stretching vibrations (Table 8.1). No symmetric NH_3 vibration was located for this complex, which is consistent with the small intensity (0.0042 km/mol at the CCSD/AVTZ level) computed for this mode.

The ClH−NH_3 antisymmetric stretch, perpendicular band (*e* symmetry) is satisfactorily simulated using a symmetric top Hamiltonian. The observation of three *K* sub-bands is consistent with the expected nuclear spin statistics associated with this C_{3v} complex, which contains three equivalent H atoms.[49] The *B* rotational constant was set in the simulation to three times less than the *ab initio* equilibrium value (Table 1) to account for coupling of the He environment to *b*-axis rotation.[22-24,50] In comparison, the coupling of the He solvent to the faster rotational motion about the *a*-axis is expected to be less efficient.[51] The *A* rotational constant and the band origin were adjusted to satisfactorily simulate the observed band, revealing an *A* constant (5.89 cm^{-1}) in qualitative agreement with the *ab initio* equilibrium value (6.27 cm^{-1}). Indeed, the contribution of the He solvent (ΔI_a = 0.17 amu-$Å^2$) to the effective moment of inertia for rotation about the *a*-axis is small in comparison to *b*-axis rotation ($\Delta I_b \sim$ 240 amu-$Å^2$). The $K = 2 \leftarrow 1$ sub-band is significantly broadened in comparison to the others, an effect observed previously for other He-solvated symmetric tops, such as NH_3[29] and CH_3.[52] The origin of this broadening is related to the three-fold symmetry of the molecule-He interaction potential, which leads to a strong propensity for changes in the *K* quantum number by ±3.[53] As a result, rotational dephasing/relaxation via the $|K| = 2 \rightarrow |K| = 1$ pathway is expected to be efficient, consistent with the observed homogeneous broadening of the $K = 2 \leftarrow 1$ sub-band.[52]

Table 8.1: Comparison of computed and experimental parameters (frequencies and rotational constants in cm^{-1}).

	NH_3[a]	Expt.[b]	CR1[a]	CR2[a]	CR3[a]	Expt.[c]		$HCl–NH_3$[a]	Expt.[c]
a_1	3464	3335.8	3464	3491 (17)	3511 (145)	3358.42		3465 (0.004)	
e	3592	3443.1	3592	3650 (32)	3697 (53)	3501.05		3594 (13)	3439.75
A			9.512	6.009	5.771	5.45 (8)		6.274	5.89
B			0.0976	0.239	0.230	0.075 (6)		0.142	0.0474[d]
$D_J \times 10^{-4}$						3.2 (7)			
μ (D)			1.54	4.08	2.21	4.0(3)		4.27	

[a] Harmonic frequencies were computed at the CCSD(T)/AVTZ level. Intensities in parenthesis are obtained at the CCSD/AVTZ level (km/mol). CR1 is not stable at the CCSD/AVTZ level; therefore, no intensities are given.

[b] Ref. [29]

[c] This work. Uncertainties in band origins are ±0.001 cm^{-1}.

[d] $\frac{0.142}{3}$ (*B* constant reduced by a factor of three to account for He droplet effects)

8.4.2 $ClNH_3$ Parallel Band (Symmetric Stretch)

An expanded view of the intense vibrational band near 3359 cm^{-1} observed in the "hot-pyrolysis" survey scan is shown in Figure 8.5. This band is well simulated using a symmetric top Hamiltonian and a_1 vibrational symmetry (bottom of Figure 8.5). The simulation requires equal nuclear spin statistical weights for A_1/A_2 and E rotational levels. These weights are expected for a system like $ClNH_3$, which belongs to the C_{3v}(M) molecular symmetry group and has three equivalent H atoms.[49] Upon capture by He droplets, the $ClNH_3$ population cools into levels with $K = 0$ (A_1 or A_2 rotational symmetry) and $K = 1$ (E rotational symmetry). Because nuclear spin conversion is slow on the timescale of the measurement,[54] the observed spectrum is comprised of two sub-bands obeying the symmetric top, parallel band (a_1 symmetry), $\Delta K = 0$ selection rule.[49]

The band origin and rotational constants used for the simulated spectrum are given in Table 1 alongside values computed for both isomers at the CCSD(T)/AVTZ level of theory. Although the rotational constants for the **CR2** and **CR3** isomers are too similar to settle on a definitive assignment on the basis of the zero-field rotational fine structure, the constants used in the simulation are in agreement with the computed values for both, given the above discussion of expected He contributions to effective moments of inertia. The rotational line positions are not sensitive to the absolute magnitude of the A' or A'' rotational constants, but they are rather sensitive to the difference between the two. The best agreement is obtained when ΔA ($A' - A''$) = –0.045 cm^{-1}, indicating an increase in I_a, consistent with the expectation of elongated NH bonds upon vibrational excitation. The experimental B constant (0.075 cm^{-1}) is reduced by a factor of ≈3 relative to the computed B constant (0.24 cm^{-1}) due to the aforementioned contribution of the

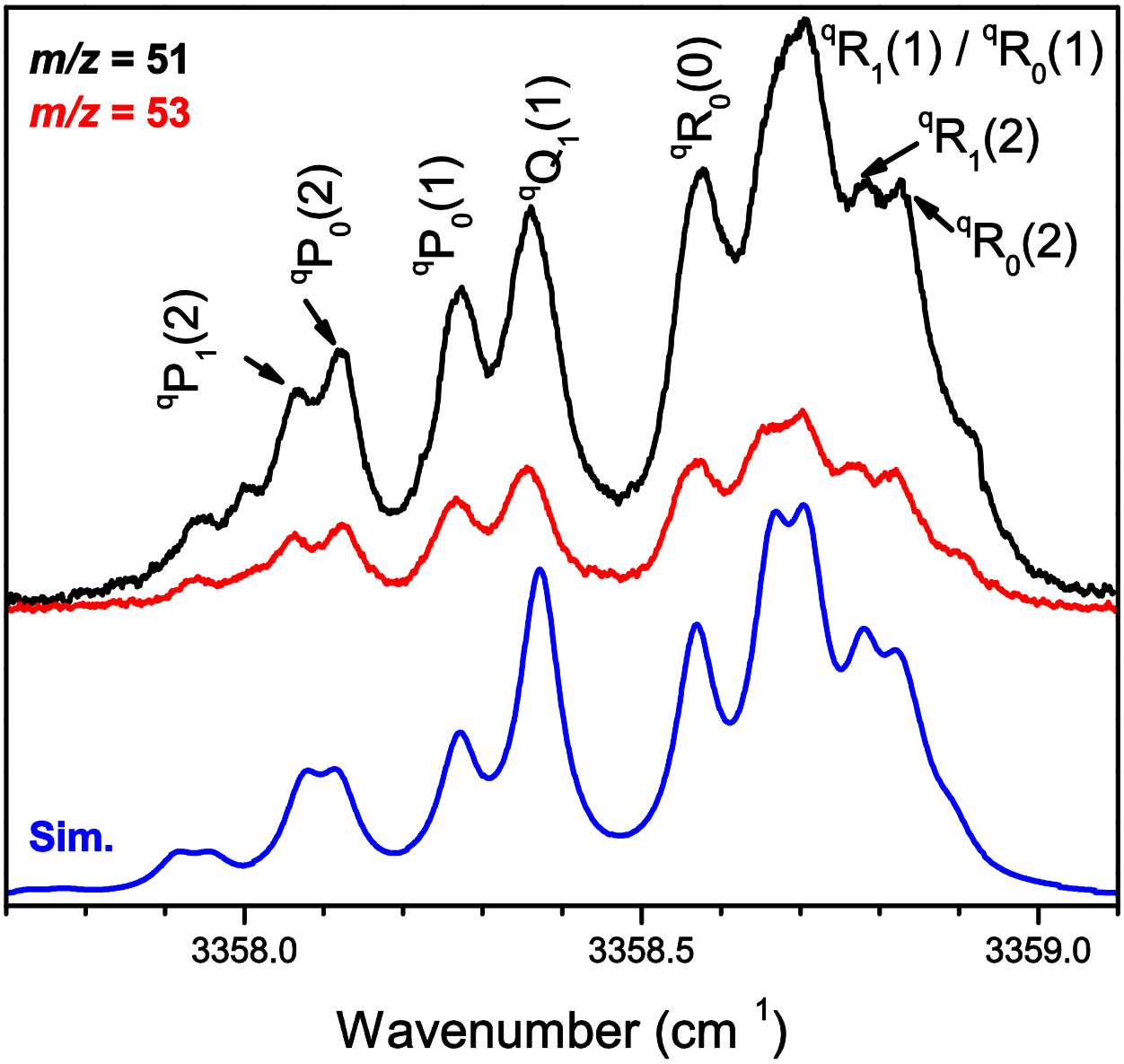

Figure 8.5: The black (top) and red (middle) spectra are the symmetric NH_3 stretches of $^{35}ClNH_3$ and $^{37}ClNH_3$, respectively. The spectra were obtained under the same pickup conditions with only a change of mass channel to select between the two isotopologues. The intensity ratio between the two bands is clearly indicative of the 3:1 natural abundance of ^{35}Cl:^{37}Cl. The simulation in blue (bottom) is obtained using a symmetric top Hamiltonian and the constants given in Table 1. Rotational transitions are labeled using ${}^{\Delta K}\Delta J_{K''}(J'')$ notation.

He solvent to the moment inertia about the *b*-axis. The observed band origin is blue-shifted by ≈22 cm^{-1} relative to the NH_3 ν_1 band origin, and this is consistent with a shortening of the N–H bond distances, as predicted for the geometries of the **CR2** and **CR3** isomers. Using an average scale factor of 0.96, derived from comparing the experimental and computed harmonic ν_1 and ν_3 vibrations of NH_3, the experimental bands best agree with the scaled harmonic frequencies of the **CR2** isomer (hydrogen atoms pointing away from the Cl atom).

This partially rotationally-resolved band was measured in both 51 and 53 u mass channels to verify the formation of both $^{35}ClNH_3$ and $^{37}ClNH_3$ complexes. Although the fine structure between the two spectra remains essentially unchanged at our resolution, the reduced depletion signal observed on *m/z* = 53 u is qualitatively consistent with the ^{35}Cl: $^{37}Cl \approx 3:1$ ratio associated with the natural abundance of Cl isotopes.

8.4.3 $ClNH_3$ Perpendicular Band (Antisymmetric Stretch)

Several features are observed in the survey spectrum near 3500 cm^{-1}, which is expanded in Figure 8.6. Three of these are assigned to $\Delta K = \pm 1$ rotational sub-bands of a perpendicular vibrational excitation (*e* symmetry), in accordance with the symmetric top rotational selection rule.[49] This perpendicular band allows for the determination of a vibrationally averaged *A* rotational constant, in addition to the band origin (3501.05 cm^{-1}). Assuming this band is derived from the same carrier associated with the parallel band at 3358 cm^{-1}, it is reasonable to use the *B* and D_J extracted from the parallel band in a simulation of the perpendicular band. With these constants fixed in the simulation, best agreement is obtained when the A'' and A' constants are set

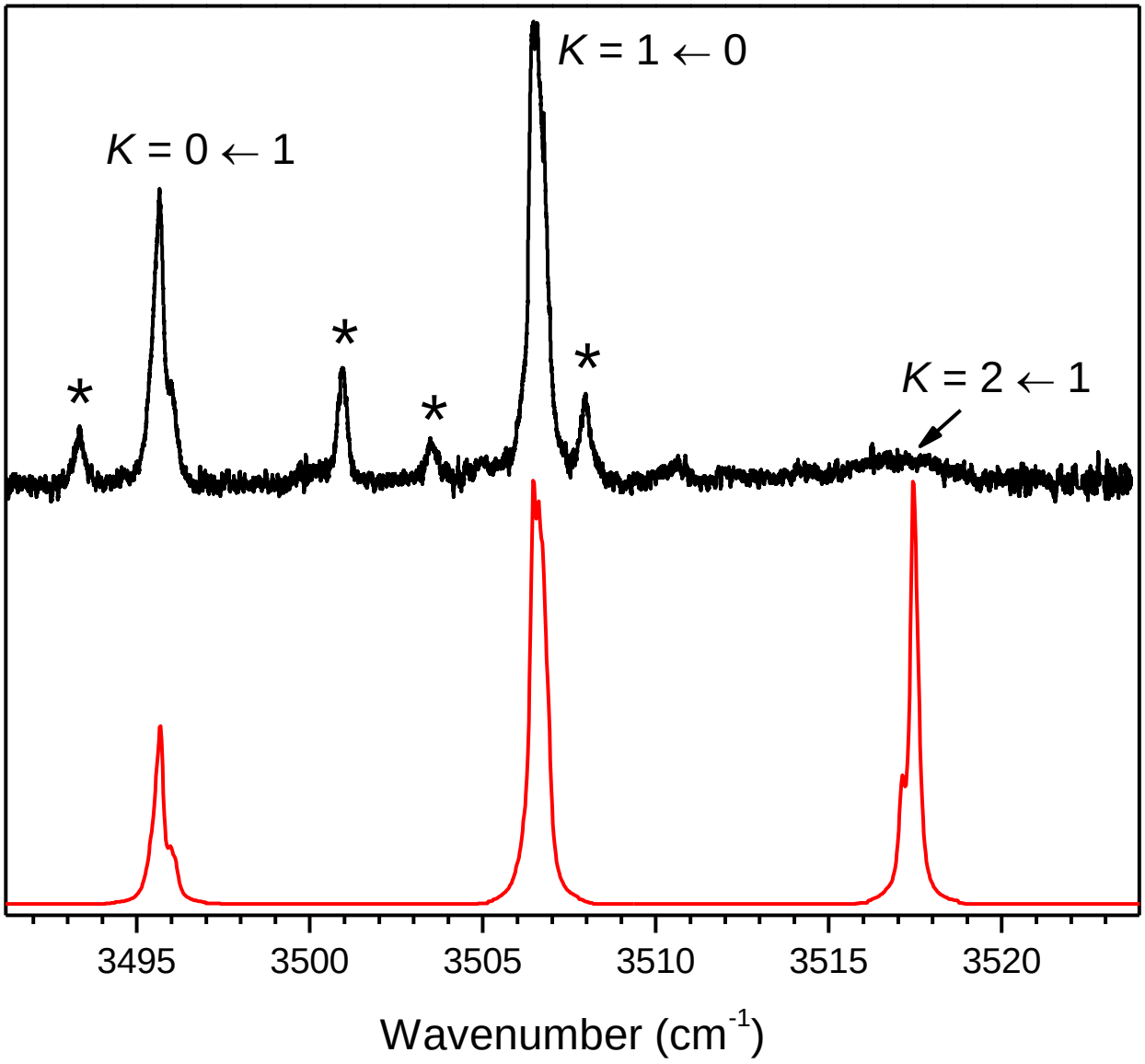

Figure 8.6: The top spectrum shows the antisymmetric NH_3 stretching band of $^{35}ClNH_3$. Sub-bands are labeled with their change in the *K* quantum number upon rovibrational excitation. Bands marked by * were found to be preferentially formed at higher fluxes of Cl_2 through the pyrolysis source and are thought to originate from complexes of the type $(Cl_2)_n{-}ClNH_3$ with $n \geq 1$. The simulation (red, bottom) is obtained using the rotational constants and band origins given in Table 1.

to 5.45 cm^{-1}. This is in good agreement with the computed *A* constants for both the **CR2** and **CR3** isomers, where only a small renormalization is induced by the He environment (ΔI_a = 0.24 amu-$Å^2$). As observed and described above for the perpendicular band of the $ClH{-}NH_3$ complex, the $K = 2 \leftarrow 1$ sub-band is significantly broadened beyond the rotational contour of the $K = 0 \leftarrow 1$ and $K = 1 \leftarrow 0$ sub-bands.[52] The line width of this homogenously broadened transition implies an upper state lifetime of ~1.6 ps. The remaining bands observed in this region, marked by * in Figure 8.6, were optimized at higher background pressures and are likely due to unpyrolyzed Cl_2 effusing through the pyrolysis source at higher flow rates. Given the droplet pickup process obeys Poisson statistics,[22-24,55] these bands are likely due to the antisymmetric NH_3 vibrations of $(Cl_2)_n$–$ClNH_3$ isomers, although no effort to further characterize their origin was undertaken.

The features in the spectrum near 3500 cm^{-1} (Figure 8.6) are consistent with the large blue-shifts predicted for the antisymmetric NH_3 vibrations (relative to the NH_3 monomer) of the **CR2** and **CR3** isomers. The aforementioned scale factor of 0.96 applied to the frequency predictions for the antisymmetric NH_3 vibrations again yields slightly better agreement between the observed band origin and that predicted for **CR2**. Comparisons to computations strongly suggest that the 3358 and 3501 cm^{-1} bands should be assigned to the symmetric (a_1) and antisymmetric (*e*) stretches of the **CR2** $ClNH_3$ complex formed via the He-mediated Cl + NH_3 reaction.

8.4.4 Stark Spectroscopy

Because the **CR2** and **CR3** isomers are both symmetric top molecules having similar computed rotational constants, it is not possible to arrive at a definitive assignment of the observed bands on the basis of rotational fine structure analysis alone. Again, the comparison between computed band origins is strongly suggestive of the aforementioned assignment to **CR2**. We employ Stark spectroscopy to measure the permanent electric dipole moment, which is predicted to be quite different for the two isomers in question. Indeed, the dipole moments for **CR2** and **CR3** are 4.08 D and 2.21 D, respectively, at the CCSD(T)/AVTZ level (Table 1). Given this large difference and the relatively good rotational resolution of the parallel band at 3358 cm^{-1}, the Stark effect can be used to determine which of the two isomers is formed following sequential addition of Cl and NH_3 to He droplets. When comparisons are available, the dipole moments of He-solvated molecules are close to their gas-phase values (within a few percent) as a result of the small net polarization of the He solvent.[32] The spectra shown on the left of Figure 8.7 were obtained at the indicated electric field strengths with the polarization of the laser beam oriented perpendicular to the applied electric field, resulting in $\Delta M = \pm 1$ selection rules. The excellent agreement between the simulations (μ = 4 D) and the experimental spectra confirms the assignment of the 3358 cm^{-1} band to the symmetric NH_3 stretch of the **CR2** complex. Indeed, simulations with μ = 2.2 D yield Stark spectra that qualitatively disagree with the observed spectra at all field strengths, ruling out the possibility that the band arises from the **CR3** isomer. Because the presence of an intense **CR2** symmetric stretch band implies the presence of an intense antisymmetric stretch band (on the basis of intensity calculations at the

CCSD/AVTZ level), we also take the Stark measurement as confirmation of the 3501 cm^{-1} band assignment to the antisymmetric NH_3 stretch of the **CR2** complex.

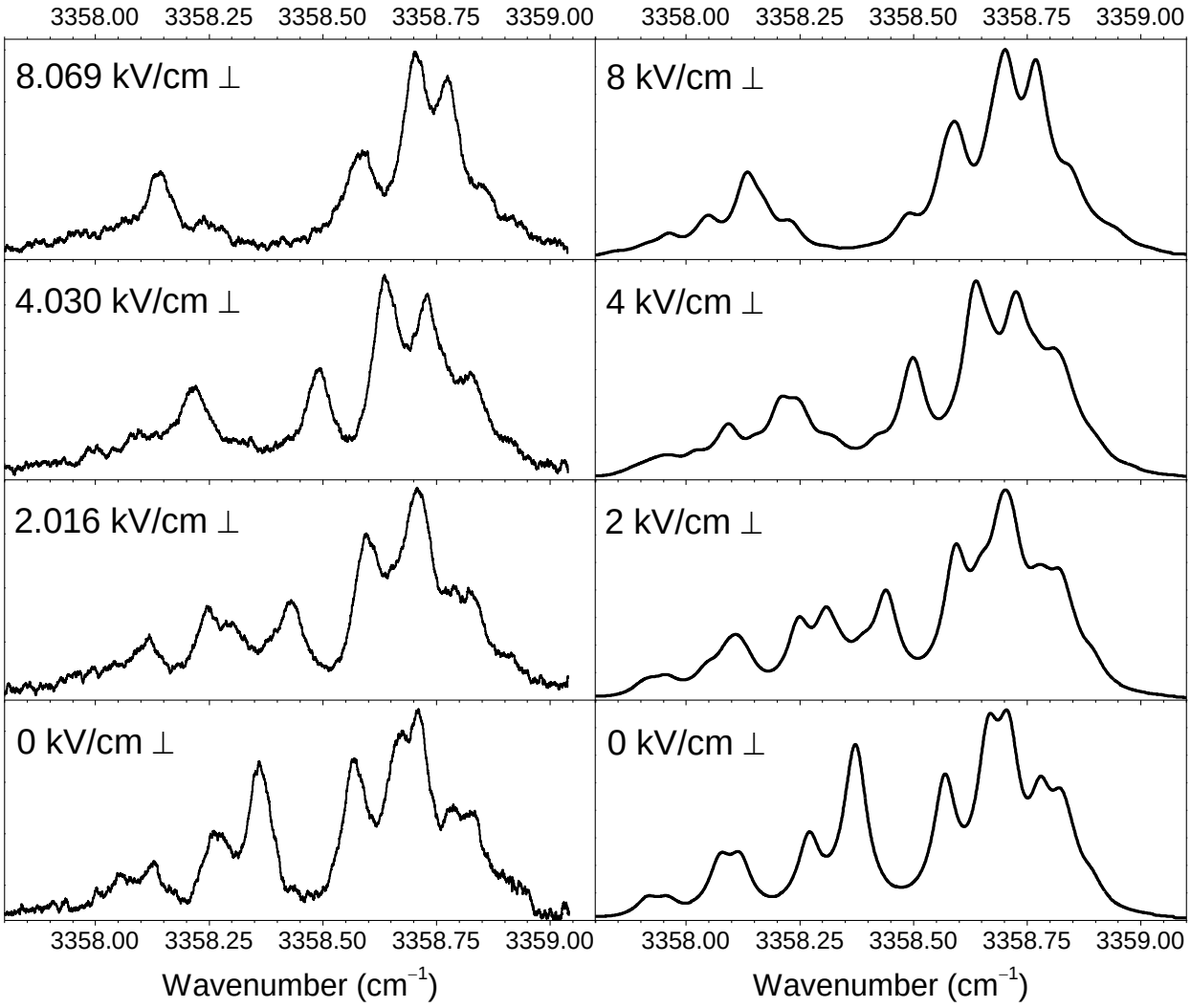

Figure 8.7: Stark spectroscopy of the symmetric NH_3 stretch of $^{35}ClNH_3$ at the indicated electric field strengths (left) and corresponding simulations (right). The experimental spectra were obtained with the laser polarization perpendicular to the Stark field. For the simulations, rotational constants were fixed to the zero-field values for each field strength (Table 1), and the ground and excited state permanent electric dipole moments were fixed to 4 D.

8.5 Discussion

All spectroscopic evidence points to the exclusive formation of the **CR2** complex upon Cl + NH_3 association within He droplets. The formation and stabilization of entrance channel complexes is expected due to the dissipative nature of He droplets. Indeed, the computed barrier heights to hydrogen abstraction and Cl substitution are both well above the asymptotic reactant energy (Figure 8.2).[6,14] It is interesting, however, that while CCSD(T) computations predict three stable isomers for $ClNH_3$, there is no spectroscopic evidence for either the C_{3v} "hydrogen-bound" complex (**CR3**) or the C_s van der Waals complex (**CR1**). Although it was noted in earlier work that **CR1** and **CR3** are entrance complexes along the hydrogen abstraction path, whereas **CR2** lies in the entry valley to the substitution reaction path,[6,14] interconversion barriers between these complexes were not considered. **CR3** lies ~1000 cm^{-1} higher in energy than **CR2**.[6] Because the He atom evaporation process is expected to preclude the uphill **CR2** → **CR3** isomerization upon *direct* formation of **CR2**, a facile interconversion path leading from **CR3** to **CR2** could explain the lack of the former. With CCSD(T) computations, we find the interconversion pathway to be largely composed of NH_3 inversion and Cl–NH_3 intermolecular stretching. Despite many attempts, however, it was not possible to locate a transition state between **CR3** and **CR2**, apparently due to the potential being rather flat in the vicinity of the **CR3** minimum. We estimate the interconversion barrier by computing a one-dimensional potential curve along a distinguished reaction path. The potential shown in Figure 8.8 is obtained as the Cl–N–H angle is scanned between the **CR3** to **CR2** geometries with other coordinates fixed at the geometry of CR3 while maintaining C_{3v} symmetry. Along this distinguished reaction path, the computed NH_3 inversion barrier is estimated to be <53.5 cm^{-1},

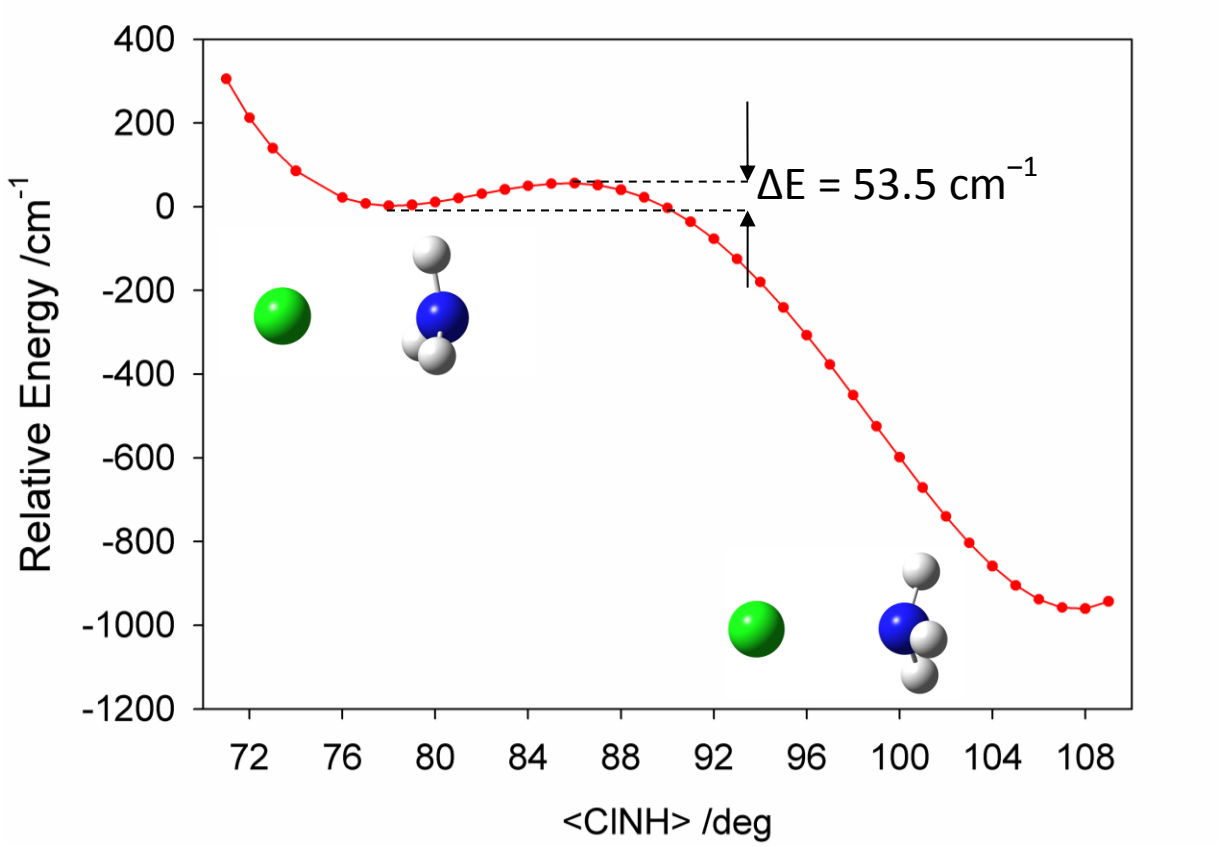

Figure 8.8: Potential profile connecting CR2 and CR3 as a function of the Cl-N-H angle in C_{3v} symmetry with other coordinates fixed at the CR3 equilibrium geometry at the CCSD(T)/AVTZ level of theory.

revealing the facile interconversion pathway necessary for exclusive formation of **CR2**. The interconversion path is found to be barrierless at the MP2/AVTZ level, and we estimate on the basis of frequency calculations that the CCSD(T)/AVTZ barrier is somewhat smaller upon zero-point correction. Provided the He evaporative cooling is insufficiently rapid to trap the **CR3** species, the **CR2** minimum can be accessed *indirectly* via interconversion of **CR3**. Moreover, we also note that Cl + NH_3 approach trajectories should favor the *direct* formation of **CR2** in He droplets, because the long-range intermolecular interaction for Cl–NH_3 approach is somewhat

stronger (e.g. larger dipole moment) in comparison to NH_3–Cl approach. Similar arguments can be invoked to explain the absence of the van der Waals complex, **CR1**. Despite many attempts, the barrier to **CR1** → **CR3** interconversion was not found, again due to the floppy nature of the system in the vicinity of the **CR1** minimum.

The molecular orbital (MO) diagram and wavefunctions obtained at the B3LYP/AVTZ level for the $ClNH_3$ complex (**CR2**) and its constituents are shown in Figure 8.9. Because the Cl half-filled p-orbital and the NH_3 highest occupied MO (HOMO) are similar in energy, orbital mixing is efficient and leads to the bonding and antibonding MOs shown in the center of the figure. The bonding MO is more stabilizing than the anti-bonding MO is destabilizing, revealing a partial covalent character to the bonding consistent with the ~8 kcal/mol binding energy predicted at the CCSD(T)/AVTZ level. Covalent mixing of the NH_3 lone-pair orbital with the singly-occupied p-orbital on Cl can be viewed as affecting a rehybridization of the NH_3 moiety, as the p-orbital contribution to the three NH bonds is diminished in favor of its contribution to N–Cl bonding. This effect leads to an opening of the ∠HNH angle (~4°) and a shortening of the N–H bond lengths (0.005 Å). Indeed, this prediction is completely consistent with the complexation-induced blue shifts observed for both the symmetric (+22.6 cm^{-1}) and antisymmetric (+58.0 cm^{-1}) NH_3 stretching vibrations. Furthermore, this rehybridization makes the NH_3 moiety in the $ClNH_3$ complex more "D_{3h} – like", consistent with the small **CR3** to **CR2** interconversion barrier discussed above, which in comparison to NH_3 inversion (~1770 cm^{-1}),[56-58] represents a rather significant change.

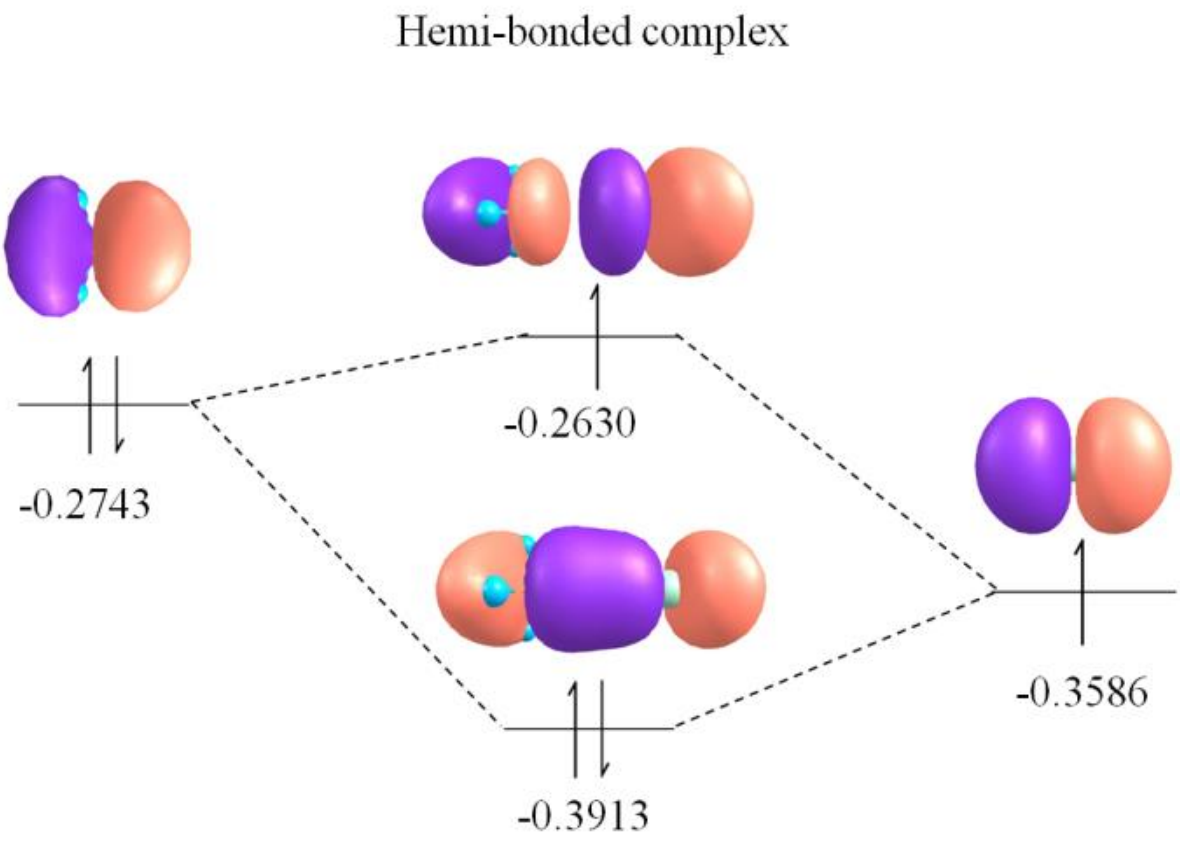

Figure 8.9: Molecular orbital energy levels and wavefunctions for NH_3, $ClNH_3$, and Cl (energies given in Hartrees). Mixing of the SOMO of Cl with the nonbonding HOMO orbital of NH_3 leads to net stabilization of the adduct.

8.6 Summary

Sequential addition of a Cl atom and NH_3 to a helium droplet leads to the formation of a C_{3v} complex, $ClNH_3$ (**CR2**), which exhibits a strong two-center three-electron (2c-3e) Cl–N hemi-bond. This $ClNH_3$ species is an entrance channel complex leading into the substitution reaction ($Cl + NH_3 \rightarrow ClNH_2 + H$). Assignment of the infrared spectrum in the NH stretch region to this entrance complex is confirmed via comparisons to high-level electronic structure

theory vibrational band origin computations, the analysis of rotational fine structure that reveals the presence of both parallel (a_1 symmetry) and perpendicular NH_3 stretching bands (e symmetry), and Stark measurements of the complexes' permanent electric dipole moment (4 D). Another C_{3v} complex, NH_3Cl (**CR3**), and a weakly interacting $Cl–HNH_2$ complex (**CR1**) are predicted as stable minima in the entry valley to the hydrogen abstraction reaction ($Cl + NH_3 \rightarrow HCl + NH_2$). Neither of these species are observed upon cluster formation in helium droplets. This observation is rationalized via computations of the interconversion pathways between the three entrance channel complexes. Orbital mixing between the Cl atom's half-filled p-orbital and the NH_3 HOMO leads to the 2c-3e bond and a rehybridization of the NH bonds (loss of p-character). This rehybridization results in a more planar NH_3 moiety, which affects the inversion barrier and therefore the **CR3** → **CR2** interconversion barrier. The interconversion between these entrance channel complexes is predicted to be both downhill and almost barrierless (~50 cm^{-1}), consistent with the absence of **CR3** upon cluster formation in helium droplets.

References

(1) Pauling, L. *J. Am. Chem. Soc.* **1931**, *53*, 3225-3237.

(2) Baird, N. C. *J. Chem. Ed.* **1977**, *54*, 291-293.

(3) Gill, P. M. W.; Radom, L. *J. Am. Chem. Soc.* **1988**, *110*, 4931-4941.

(4) McKee, M. L.; Nicolaides, A.; Radom, L. *J. Am. Chem. Soc.* **1996**, *118*, 10571-10576.

(5) Fourré, I.; Silvi, B. *Heteroat. Chem.* **2007**, *18*, 135-160.

(6) Monge-Palacios, M.; Espinosa-Garcia, J. *J. Phys. Chem. A* **2010**, *114*, 4418-4426.

(7) Li, J.; Li, Y.; Guo, H. *J. Chem. Phys.* **2013**, *138*, 141102.

(8) Liu, B. *Phys. Rev. Lett.* **1971**, *27*, 1251-1253.

(9) Tang, K. T.; Toennies, J. P.; Yiu, C. L. *Phys. Rev. Lett.* **1995**, *74*, 1546-1549.

(10) Skouteris, D.; Manolopoulos, D. E.; Bian, W. S.; Werner, H. J.; Lai, L. H.; Liu, K. P. *Science* **1999**, *286*, 1713-1716.

(11) Czakó, G.; Bowman, J. M. *J. Am. Chem. Soc.* **2009**, *131*, 17534-17535.

(12) Zhang, W.; Kawamata, H.; Liu, K. *Science* **2009**, *325*, 303-306.

(13) Li, J.; Jiang, B.; Guo, H. *Chem. Sci.* **2013**, *4*, 629-632.

(14) Xu, Z. F.; Lin, M. C. *J. Phys. Chem. A* **2007**, *111*, 584-590.

(15) Westenberg, A. A.; deHaas, N. *J. Chem. Phys.* **1977**, *67*, 2388-2390.

(16) Gao, Y.; Alecu, I. M.; Hsieh, P. C.; Morgan, B. P.; Marshall, P.; Krasnoperov, L. N. *J. Phys. Chem. A* **2006**, *110*, 6844-6850.

(17) Kondo, S.; Tokuhashi, K.; Takahashi, A.; Kaise, M. *J. Hazard Mater.* **2000**, *79*, 77-86.

(18) Raynor, J. B.; Rowland, I. J.; Symons, M. C. R. *J. Chem. Soc., Faraday Trans.* **1991**, *87*, 571-577.

(19) Merritt, J. M.; Kupper, J.; Miller, R. E. *Phys. Chem. Chem. Phys.* **2005**, *7*, 67-78.

(20) Moradi, C. P.; Douberly, G. E. *J. Phys. Chem. A* **2015**, *119*, 12028-12035.

(21) Douberly, G. E.; Raston, P. L.; Liang, T.; Marshall, M. D. *J. Chem. Phys.* **2015**, *142*, 134306.

(22) Callegari, C.; Lehmann, K. K.; Schmied, R.; Scoles, G. *J. Chem. Phys.* **2001**, *115*, 10090-10110.

(23) Toennies, J. P.; Vilesov, A. F. *Angew. Chem., Int. Ed.* **2004**, *43*, 2622-2648.

(24) Choi, M. Y.; Douberly, G. E.; Falconer, T. M.; Lewis, W. K.; Lindsay, C. M.; Merritt, J. M.; Stiles, P. L.; Miller, R. E. *Int. Rev. Phys. Chem.* **2006**, *25*, 15-75.

(25) Stienkemeier, F.; Lehmann, K. K. *J. Phys. B: At., Mol. Opt. Phys.* **2006**, *39*, R127-R166.

(26) Lewerenz, M.; Schilling, B.; Toennies, J. P. *Chem. Phys. Lett.* **1993**, *206*, 381-387.

(27) Knuth, E.; Schilling, B.; Toennies, J. P. *Proceedings of the 19th International Symposium on Rarefied Gas Dynamics*; Oxford University Press: London, 1995; Vol. 19.

(28) Harms, J.; Toennies, J. P.; Dalfovo, F. *Phys. Rev. B* **1998**, *58*, 3341-3350.

(29) Slipchenko, M. N.; Vilesov, A. F. *Chem. Phys. Lett.* **2005**, *412*, 176-183.

(30) Hartmann, M.; Miller, R. E.; Toennies, J. P.; Vilesov, A. *Phys. Rev. Lett.* **1995**, *75*, 1566-1569.

(31) Kohn, D. W.; Clauberg, H.; Chen, P. *Rev. Sci. Instrum.* **1992**, *63*, 4003-4005.

(32) Stiles, P. L.; Nauta, K.; Miller, R. E. *Phys. Rev. Lett.* **2003**, *90*, 135301.

(33) Nauta, K.; Miller, R. E. *Phys. Rev. Lett.* **1999**, *82*, 4480-4483.

(34) Nauta, K.; Moore, D. T.; Miller, R. E. *Faraday Discuss.* **1999**, *113*, 261-278.

(35) Liang, T.; Magers, D. B.; Raston, P. L.; Allen, W. D.; Douberly, G. E. *J. Phys. Chem. Lett.* **2013**, *4*, 3584-3589.

(36) Scheidemann, A.; Schilling, B.; Toennies, J. P. *J. Phys. Chem.* **1993**, *97*, 2128-2138.

(37) Callicoatt, B. E.; Mar, D. D.; Apkarian, V. A.; Janda, K. C. *J. Chem. Phys.* **1996**, *105*, 7872-7875.

(38) Chin, S. A.; Krotscheck, E. *Phys. Rev. B* **1995**, *52*, 10405-10428.

(39) Morrison, A. M.; Liang, T.; Douberly, G. E. *Rev. Sci. Instrum.* **2013**, *84*, 013102.

(40) PGOPHER, a Program for Simulating Rotational Structure, C. M. Western, University of Bristol, http://pgopher.chm.bris.ac.uk.

(41) Alday, B.; Johnson, R.; Li, J.; Guo, H. *Theor. Chem. Acc.* **2014**, *133*, 1540.

(42) Deegan, M. J. O.; Knowles, P. J. *Chem. Phys. Lett.* **1994**, *227*, 321-326.

(43) Knowles, P. J.; Hampel, C.; Werner, H.-J. *J. Chem. Phys.* **1993**, *99*, 5219-5227.

(44) Kendall, R. A.; Dunning, T. H.; Harrison, R. J. *J. Chem. Phys.* **1992**, *96*, 6796-6806.

(45) Werner, H. J.; Knowles, P. J.; Knizia, G.; Manby, F. R.; Schütz, M. *WIREs Comput. Mol. Sci.* **2012**, *2*, 242-253.

(46) Scuseria, G. E.; Janssen, C. L.; Schaefer, H. F. *J. Chem. Phys.* **1988**, *89*, 7382-7387.

(47) Frisch, M. J.; Trucks, G. W.; Schlegel, H. B.; Scuseria, G. E.; Robb, M. A.; Cheeseman, J. R.; Scalmani, G.; Barone, V.; Mennucci, B.; Petersson, G. A.; Nakatsuji, H.; Caricato, M.; Li, X.; Hratchian, H. P.; Izmaylov, A. F.; Bloino, J.; Zheng, G.; Sonnenberg, J. L.; Hada, M.; Ehara, M.; Toyota, K.; Fukuda, R.; Hasegawa, J.; Ishida, M.; Nakajima, T.; Honda, Y.; Kitao, O.; Nakai, H.; Vreven, T.; Montgomery, J., J. A.; Peralta, J. E.; Ogliaro, F.; Bearpark, M.; Heyd, J. J.; Brothers, E.; Kudin, K. N.; Staroverov, V. N.; Kobayashi, R.; Normand, J.; Raghavachari, K.; Rendell, A.; Burant, J. C.; Iyengar, S. S.; Tomasi, J.; Cossi, M.; Rega, N.; Millam, N. J.; Klene, M.; Knox, J. E.; Cross, J. B.; Bakken, V.; Adamo, C.; Jaramillo, J.; Gomperts, R.; Stratmann, R. E.; Yazyev, O.;

Austin, A. J.; Cammi, R.; Pomelli, C.; Ochterski, J. W.; Martin, R. L.; Morokuma, K.; Zakrzewski, V. G.; Voth, G. A.; Salvador, P.; Dannenberg, J. J.; Dapprich, S.; Daniels, A. D.; Farkas, Ö.; Foresman, J. B.; Ortiz, J. V.; Cioslowski, J.; Fox, D. J. Gaussian09; Gaussian Inc. : Wallingford CT, 2009; Vol. C.01.

(48) Slipchenko, M. N.; Sartakov, B. G.; Vilesov, A. F.; Xantheas, S. S. *J. Phys. Chem. A* **2007**, *111*, 7460-7471.

(49) Bunker, P. R.; Jensen, P. *Molecular Symmetry and Spectroscopy*; NRC Research: Ottawa, 1998.

(50) Kwon, Y.; Huang, P.; Patel, M. V.; Blume, D.; Whaley, K. B. *J. Chem. Phys.* **2000**, *113*, 6469-6501.

(51) Douberly, G. E.; Nauta, K.; Miller, R. E. *Chem. Phys. Lett.* **2003**, *377*, 384-390.

(52) Morrison, A. M.; Raston, P. L.; Douberly, G. E. *J. Phys. Chem. A* **2013**, *117*, 11640-11647.

(53) Dagdigian, P. J.; Alexander, M. H. *J. Chem. Phys.* **2011**, *135*, 064306.

(54) Gomez, L. F.; Sliter, R.; Skvortsov, D.; Hoshina, H.; Douberly, G. E.; Vilesov, A. F. *J. Phys. Chem. A* **2013**, *117*, 13648-13653.

(55) Lewerenz, M.; Schilling, B.; Toennies, J. P. *J. Chem. Phys.* **1995**, *102*, 8191-8207.

(56) Léonard, C.; Carter, S.; Handy, N. C. *Chem. Phys. Lett.* **2003**, *370*, 360-365.

(57) Lin, H.; Thiel, W.; Yurchenko, S. N.; Carvajal, M.; Jensen, P. *J. Chem. Phys.* **2002**, *117*, 11265-11276.

(58) Klopper, W.; Samson, C. C. M.; Tarczay, G.; Császár, A. G. *J. Comp. Chem.* **2001**, *22*, 1306-1314.

CHAPTER 9

CONCLUSIONS AND OUTLOOK

As demonstrated in this dissertation, helium nanodroplets are an excellent medium in which reactive radicals, carbenes, and open-shell, weakly-bound complexes may be investigated. The alkyl radicals discussed in Chapters 3-5 each consist of a chain of three C atoms and three, five, or seven H atoms corresponding to the propargyl, allyl, and *n*,*i*-propyl radicals, respectively. It was shown that the vibrational spectra in the C–H stretch region became significantly more complicated as the degree of unsaturation in the alkyl radical was reduced. Five vibrational bands are expected for the allyl radical (CH_2CHCH_2) in the CH stretching region, but nine vibrational bands are observed in this region and assigned to allyl. The scissor vibrations of the CH_2 groups (along with an overtone of the CH_2 wagging mode) in the allyl radical are predicted by DFT computations to possibly lead to Fermi resonances, involving four or more quanta of vibrational excitation, which may couple to the higher frequency C–H stretching vibrations and cause the complexity observed in both gas-phase and He droplet experiments. Fermi resonances between select normal mode vibrations, however, were shown to be insufficient in the modeling of vibrational spectra for the *n*-propyl radical.[1] However, transformation into an internal coordinate system where the C–H oscillators are local-mode vibrations, as well as including cubic terms that couple C–H stretches to overtones/combinations of scissor vibrations,[2] leads to good agreement with the spectra measured for both He-solvated *n*- and *i*-propyl radicals.

The addition of molecular oxygen to the propargyl and allyl radicals was shown to occur within He droplets, and the obtained spectra of the alkyl peroxy products indisputably correspond to the predicted minimum-energy structure for both species. However, given that there are four stable isomers/conformers of the propargyl peroxy radical and five stable conformers of the allyl peroxy radical (within 1 kcal/mol of each other) in the ground electronic state,[3,4] this is quite surprising. We hypothesize that for barrierless He-solvated alkyl + O_2 reactions, the exothermicity of the addition reaction results in a highly vibrationally excited C–O bond in which the CC–OO torsional potential, which is partially responsible for the orientation of the O_2 moiety relative to the carbon backbone, is relatively flat. As the molecule vibrationally relaxes, the wells along the torsional coordinate develop. The deepest well is likely to support bound states before the other wells, thereby funneling the alkyl peroxy population into a single geometry. This argument is entirely qualitative and is in need of both theoretical analysis and further experimental support.

The reactive HCOH, HCOD, and HOCOH carbenes investigated in Chapters 6 and 7 had previously only been observed in an Ar matrix,[5,6] with the exception of the *cis,trans*-HOCOH isomer, which was identified in gas-phase microwave spectroscopy experiments.[7] The carbenes were generated in the gas-phase for He droplet pickup via the thermal decomposition of α-keto carboxylic acid precursors (glyoxylic acid for HCOH/HCOD and oxalic acid for HOCOH).[5,6] The overall agreement is excellent between the estimated band origins for He-solvated *trans*-HCOH/D, *trans,trans*-HOCOH, and *trans,cis*-HOCOH and the results of high-level anharmonic frequency computations.[5,8] The OH/OD vibrational frequencies of each of these carbenes in the Ar matrix were shown to be significantly red-shifted as was inferred in the original analyses.[5,6] Furthermore, the permanent electric dipole moment of both *trans,trans*- and *trans,cis*-HOCOH

was able to be determined from Stark spectroscopy measurements and found to also be in good agreement with theoretical predictions.

Chlorine atoms were generated through the thermal decomposition of Cl_2 in a SiC pyrolysis source,[9] and they were picked up by droplets alongside a co-dopant molecule (HCl in Chapter 7 and NH_3 in Chapter 8) in order to study complex formation. The He-solvated Cl–HCl complex was determined to have an L-shaped geometry rather than a linear, H-bonded geometry observed for other similar systems.[10,11] A linear, H-bonded Cl–HCl structure was also reported in a previous Ar matrix experiment which is at odds with the results reported here.[12] Calculations of the wavefunction near the ground rovibronic state reveal that the "floppiness" of the Cl–HCl complex may play a large role in the disparity of the two results.[13] The $ClNH_3$ species formed in He droplets, however, is much more strongly bound (~8 kcal/mol) than Cl–HCl (< 1 kcal/mol).[14] The observed bands of $ClNH_3$ are strongly blueshifted from the vibrations of the NH_3 monomer indicating bonding that is more electronic than electrostatic in nature. Our results agree well with frequencies predicted for one of three isomers predicted to be entrance-channel minima on the reactive PES by theoretical computations.[14] There is no evidence for a NH_3Cl adduct, where the hydrogen atoms point "toward" the Cl atom, nor is there evidence for a weakly-bound Cl–HNH_2 complex. These experimental results test the ability of theory to predict accurate molecular structures and energies for pre-reactive complexes containing open-shell atoms.

Helium nanodroplets provide a unique environment in which chemical reactions can be studied. Although chemistry is usually greatly suppressed at the cold temperatures inherent to He droplets combined with the short, millisecond experimental times, this dissertation demonstrates that some reactions can occur at 0.4 K, allowing for the investigation of transient

intermediates. Nonetheless, the outcome of sequentially doping a He droplet with a radical and a closed-shell molecule is often a vdW complex. If the complex has a low barrier to reaction, however, it is reasonable to suggest that absorption of an IR photon might vibrationally excite a bond that lies along the reaction coordinate allowing for the reaction to occur before the He environment can dissipate the vibrational energy. This opens the door for IR-IR pump-probe experiments in which a vibration of a vdW complex is optically pumped, and the reaction products are probed using a second tunable IR laser. An experiment of this type might investigate the reaction between a methyl radical and hydrogen chloride: $CH_3 + HCl \rightarrow CH_4 + Cl$. As the diagram in Figure 9.1 shows, the CH_3–HCl complex is stabilized by ~820 cm^{-1} relative to the isolated reactants, and the transition state lies ~1400 cm^{-1} above the vdW complex.{, #18} Excitation of the HCl stretch should promote the reaction because the vibrational coordinate has a large projection on the reaction coordinate. The HCl stretching frequency of the He-solvated CH_3–HCl complex has been located at 2752 cm^{-1} (see Figure 9.2), and it is red-shifted by ~130 cm^{-1} relative to the approximate HCl band origin (~2886 cm^{-1}). The band is anomalously broadened, having a full-width at half-maximum linewidth of ~5 cm^{-1} and being even more broad than the strongly H-bonded H_2O–HCl vdW complex. It is possible that the band is broadened due to a reduction in the excited state lifetime due to reaction within the He droplet to form $Cl + CH_4$. An IR-IR pump-probe experiment could easily verify this and open the door for similar experiments. For instance, the carbenes discussed above could easily be re-introduced to the droplets alongside a co-reactant in order to search for reaction products. Although this may also lead to vdW complex formation, preliminary computations at the MP2/6-31++G(d,p) level of theory indicate that the acid-base type reaction between HOCOH and BH_3 to form the adduct may be barrierless (although the formation of the C–B bond is expected to be

~100 kcal/mol exothermic). Reactions between two radicals, such as between propargyl and allyl, are another possible avenue of exploration, and these are important because they are thought to be the initial reactions that ultimately lead to soot formation in combustion processes. The reactive intermediates along these reaction pathways are not well-characterized, and these types of experiments could, in principle, be easily accomplished using the He droplet technique.

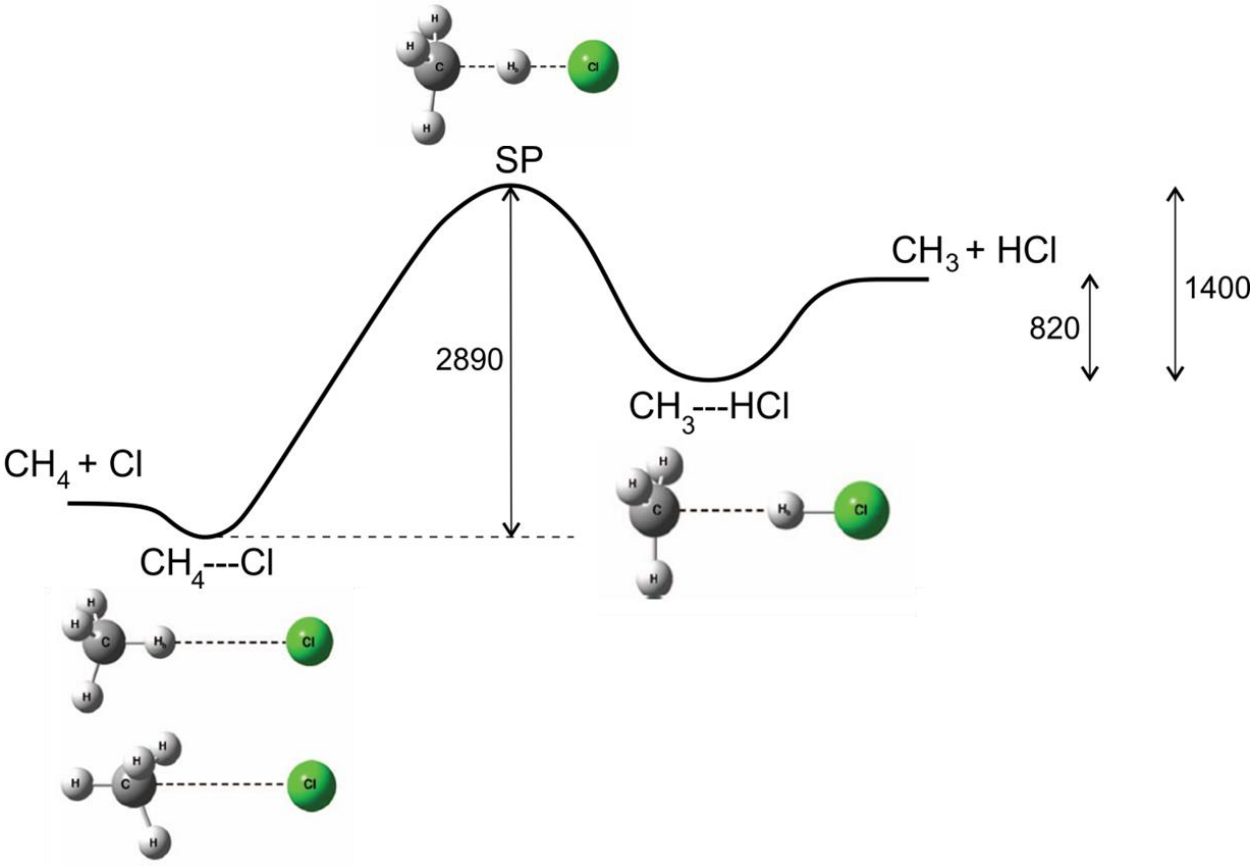

Figure 9.1: PES diagram for the $CH_3 + HCl \rightarrow CH_4 + Cl$ reaction.[15] Energies are given in units of wavenumber.

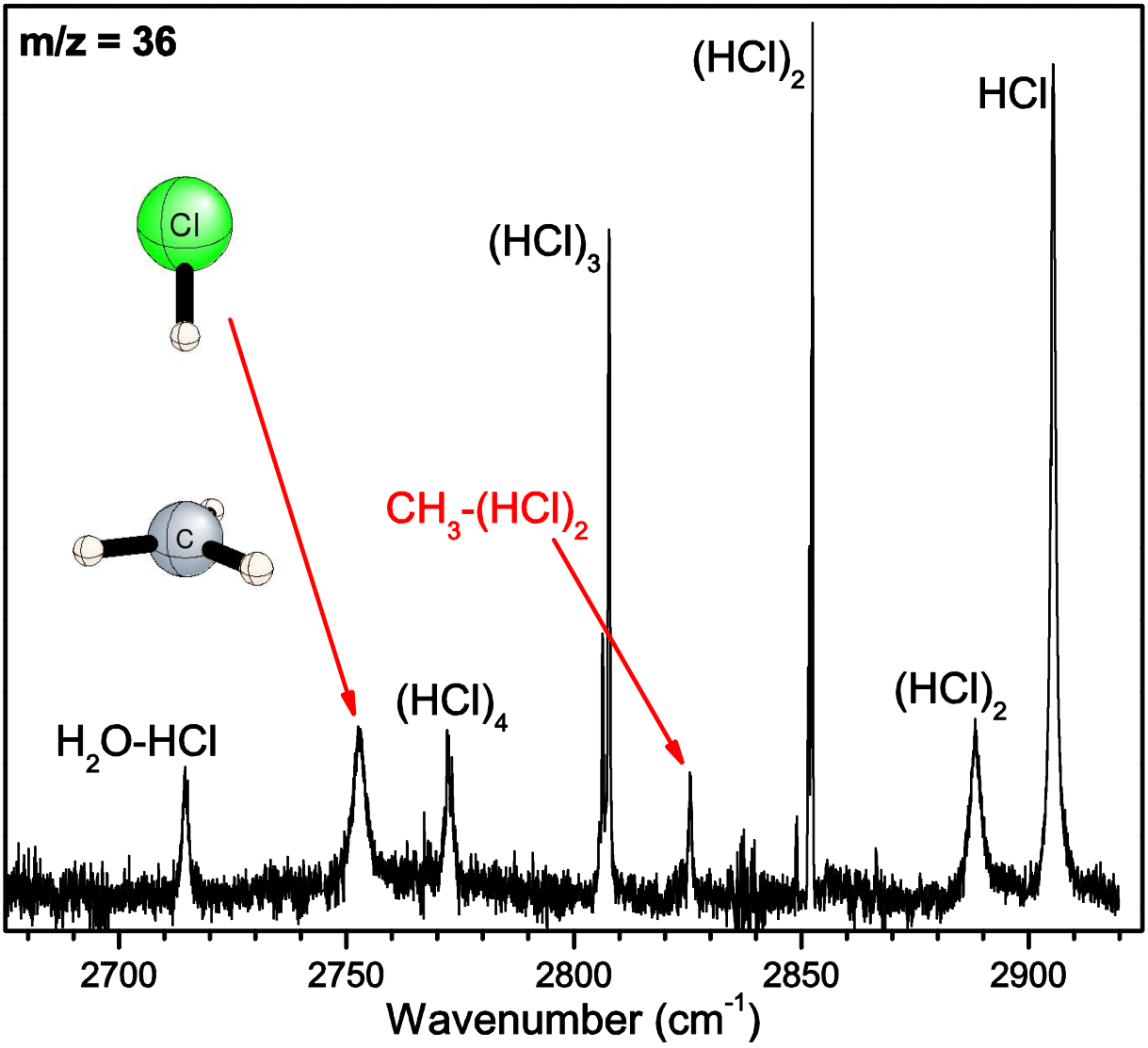

Figure 9.2: IR survey spectrum measured in the H–Cl stretching region with HCl present in the pickup cell and CH_3 radicals being generated in a hot pyrolysis source. The HCl stretch of the CH_3–HCl vdW complex was located at 2752 cm^{-1}, and it is, interestingly, the broadest feature in the spectrum. The HCl clusters were studied previous by Skvortsov, et al.,[16] and the H_2O–HCl complex was assigned by Morrison, et al.[17]

References

(1) Li, C. Y.; Agarwal, J.; Wu, C. H.; Allen, W. D.; Schaefer, H. F. *J. Phys. Chem. B* **2015**, *119*, 728-735.

(2) Buchanan, E. G.; Dean, J. C.; Zwier, T. S.; Sibert, E. L. *J. Chem. Phys.* **2013**, *138*, 064308.

(3) Thomas, P. S.; Kline, N. D.; Miller, T. A. *J. Phys. Chem. A* **2010**, *114*, 12437-12446.

(4) Thomas, P. S.; Miller, T. A. *Chem. Phys. Lett.* **2010**, *491*, 123-131.

(5) Schreiner, P. R.; Reisenauer, H. P.; Pickard, F. C.; Simmonett, A. C.; Allen, W. D.; Matyus, E.; Csaszar, A. G. *Nature* **2008**, *453*, 906-909.

(6) Schreiner, P. R.; Reisenauer, H. P. *Angew. Chem., Int. Ed.* **2008**, *47*, 7071-7074.

(7) Womack, C. C.; Crabtree, K. N.; McCaslin, L.; Martinez, O., Jr.; Field, R. W.; Stanton, J. F.; McCarthy, M. C. *Angew. Chem., Int. Ed.* **2014**, *53*, 4089-4092.

(8) Koziol, L.; Wang, Y. M.; Braams, B. J.; Bowman, J. M.; Krylov, A. I. *J. Chem. Phys.* **2008**, *128*, 204310.

(9) Kohn, D. W.; Clauberg, H.; Chen, P. *Rev. Sci. Instrum.* **1992**, *63*, 4003-4005.

(10) Merritt, J. M.; Kupper, J.; Miller, R. E. *Phys. Chem. Chem. Phys.* **2005**, *7*, 67-78.

(11) Kettwich, S. C.; Pinelo, L. F.; Anderson, D. T. *Phys. Chem. Chem. Phys.* **2008**, *10*, 5564-5573.

(12) Andrews, L.; Hunt, R. D. *J. Chem. Phys.* **1988**, *89*, 3502-3504.

(13) Zeimen, W. B.; Klos, J.; Groenenboom, G. C.; van der Avoird, A. *J. Phys. Chem. A* **2003**, *107*, 5110-5121.

(14) Monge-Palacios, M.; Espinosa-Garcia, J. *J. Phys. Chem. A* **2010**, *114*, 4418-4426.

(15) Czakó, G.; Bowman, J. M. *J. Chem. Phys.* **2012**, *136*, 044307.

(16) Skvortsov, D.; Choi, M. Y.; Vilesov, A. F. *J. Phys. Chem. A* **2007**, *111*, 12711-12716.

(17) Morrison, A. M.; Flynn, S. D.; Liang, T.; Douberly, G. E. *J. Phys. Chem. A* **2010**, *114*, 8090-8098.